Department of Information and Computer Science

On statistical theory of radar measurements

Juha Vierinen

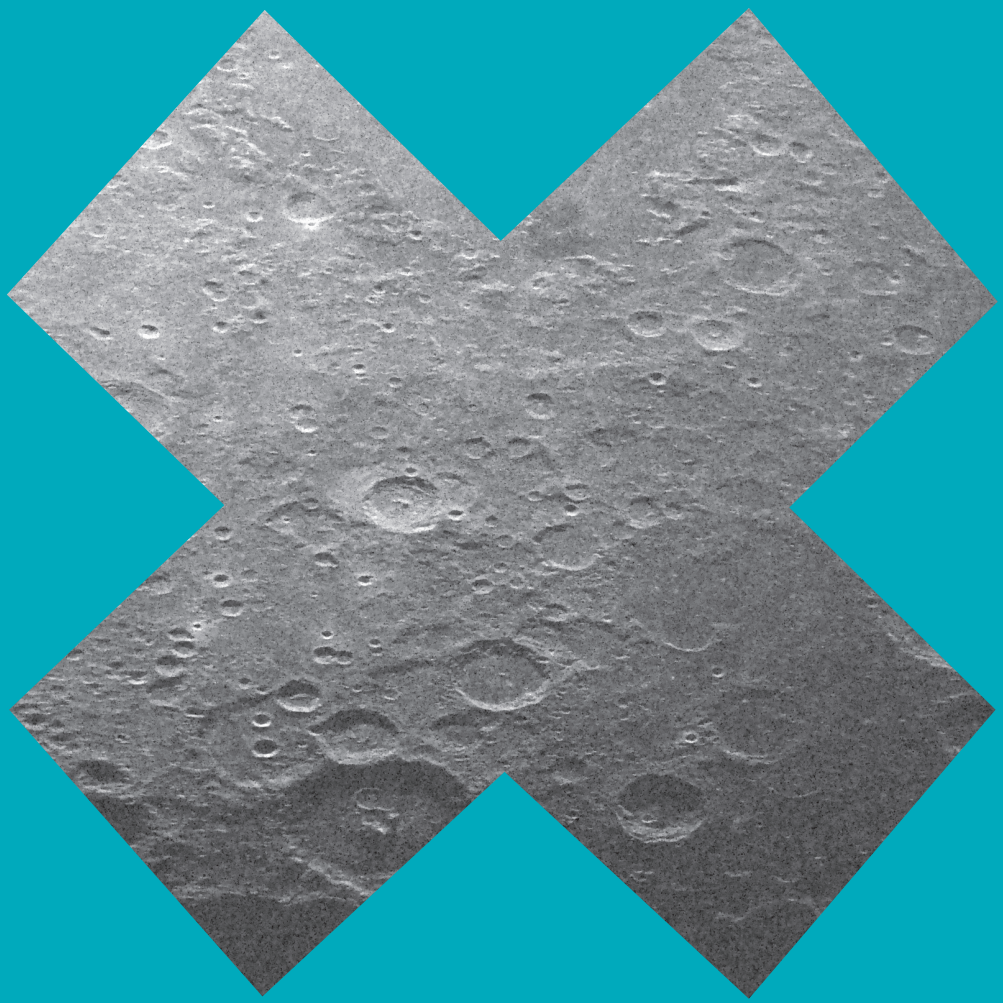

Aalto University

DOCTORAL DISSERTATIONS

Juha Vierinen On statistical theory of radar measurements Aalto University

Aalto University publication series
DOCTORAL DISSERTATIONS 115/2012

On statistical theory of radar measurements

Juha Vierinen

A doctoral dissertation completed for the degree of Doctor of Science (Technology) to be defended, with the permission of the Aalto University School of Science, at a public examination held at the Polaria lecture hall of the Sodankylä geophysical observatory on 1 October 2012 at 12 noon.

Aalto University
School of Science
Department of Information and Computer Science

Supervising professor
Prof. Erkki Oja

Thesis advisor
Prof. Markku Lehtinen

Preliminary examiners
Prof. Heikki Haario, Lappeenranta University of Technology, Finland.
Dr. Marco Milla, Radio Observatorio de Jicamarca, Peru.

Opponent
Dr. Jorge L. Chau, Radio Observatorio de Jicamarca, Peru.

Aalto University publication series
DOCTORAL DISSERTATIONS 115/2012

ISBN 978-952-60-4778-2 (printed)
ISBN 978-952-60-4779-9 (pdf)
ISSN-L 1799-4934
ISSN 1799-4934 (printed)
ISSN 1799-4942 (pdf)
http://urn.fi/URN:ISBN:978-952-60-4779-9

Unigrafia Oy
Helsinki 2012

Finland

Publication orders (printed book):
j@sgo.fi

441 697
Printed matter

Aalto University

Abstract

Aalto University, P.O. Box 11000, FI-00076 Aalto www.aalto.fi

Author
Juha Vierinen

Name of the doctoral dissertation
On statistical theory of radar measurements

Publisher School of Science

Unit Department of Information and Computer Science

Series Aalto University publication series DOCTORAL DISSERTATIONS 115/2012

Field of research Computer and Information Science

Manuscript submitted 26 April 2012 **Date of the defence** 1 October 2012

Permission to publish granted (date) 22 August 2012 **Language** English

☐ **Monograph** ☒ **Article dissertation (summary + original articles)**

Abstract

Statistical treatment of radar measurements is important as most radar measurements are corrupted by random receiver noise. In addition to this, many radar targets themselves have to be modeled as random processes. It is therefore not a coincidence that this thesis uses the framework of statistical inverse problems for modeling radar measurements.

The introductory part of this thesis first goes through some important mathematical and numerical methods that can be used to model radar measurements and to apply these models in practice. We then describe several different types of radar measurements, with emphasis on high power large aperture radars. After this, we go through several useful radar measurement models. Finally, with the help of these models, we discuss optimal experiment design -- which typically amounts to radar transmission waveform optimization.

The publications included in this thesis contain practical applications of the topics described in the introduction, including amplitude domain estimation of incoherent scatter signals, radar transmission code optimization, inverse synthetic aperture radar, and measurements of space debris.

Keywords high power large aperture radar, statistical inverse problems, radar transmission coding, geophysics, incoherent scatter radar, space debris, planetary radar

ISBN (printed) 978-952-60-4778-2 **ISBN (pdf)** 978-952-60-4779-9

ISSN-L 1799-4934 **ISSN (printed)** 1799-4934 **ISSN (pdf)** 1799-4942

Location of publisher Espoo **Location of printing** Helsinki **Year** 2012

Pages 185 **urn** http://urn.fi/URN:ISBN:978-952-60-4779-9

Aalto-yliopisto

Tiivistelmä

Aalto-yliopisto, PL 11000, 00076 Aalto www.aalto.fi

Tekijä
Juha Vierinen

Väitöskirjan nimi
Tutkamittausten tilastollisesta mallintamisesta

Julkaisija Perustieteiden korkeakoulu

Yksikkö Tietojenkäsittelytieteen laitos

Sarja Aalto University publication series DOCTORAL DISSERTATIONS 115/2012

Tutkimusala Tietojenkäsittelytiede

Käsikirjoituksen pvm 26.04.2012 **Väitöspäivä** 01.10.2012

Julkaisuluvan myöntämispäivä 22.08.2012 **Kieli** Englanti

☐ **Monografia** ☒ **Yhdistelmäväitöskirja (yhteenveto-osa + erillisartikkelit)**

Tiivistelmä

Suurin osa tutkamittauksista on hyvin kohinaisia, siksi tilastolliset menetelmät ovat tärkeässä osassa niiden analyysissä. Lisäksi monet tutkakohteet ovat luonteeltaan satunnaisia prosesseja. Tässä väitöskirjassa sovelletaan tilastollisen inversioteorian menetelmiä erilaisten tutkamittausten mallintamiseen.

Väitöskirjan johdanto käsittelee ensin eräitä tärkeitä matemaattisia ja numeerisia menetelmiä. Näitä sovelletaan tyypillisesti tutkamittausten tilastollisessa mallintamisessa ja käytännön sovellutuksissa. Tämän jälkeen esittelemme muutamia erilaisia tutkamittaustyyppejä ja mittausmalleja keskittyen erityisesti suurtehotutkiin. Käyttäen hyödyksi näitä malleja, käymme lopuksi läpi tutkamittausten tilastollisen kokeiden suunnittelun periaatteita. Tämä tyypillisesti tarkoittaa optimaalista tutkan lähetteiden suunnittelua.

Tämän väitöskirjan sisältämät julkaisut pitävät sisällään käytännön sovellutuksia väitöskirjan johdannossa esitellyistä aiheista. Julkaisut keskittyvät seuraaviin suurtehotutkamittauksia koskeviin aiheisiin: epäkoherentin sironnan amplitudin estimointi koodatuilla pulsseilla, epäkoherentin sironnan tutkamittausten lähetteiden aaltomuotojen optimointi, Kuun kartoitus suuren laskennallisen läpimitan tutkalla sekä Cosmos- ja Iridium-satelliittien törmäyksen aiheuttaman avaruusromupilven mittaukset.

Avainsanat suurtehotutkat, tilastollinen inversio, tutkakoodaus, geofysiikka, epäkoherentti sironta, avaruusromu, planetaarinen tutka

ISBN (painettu) 978-952-60-4778-2 **ISBN (pdf)** 978-952-60-4779-9

ISSN-L 1799-4934 **ISSN (painettu)** 1799-4934 **ISSN (pdf)** 1799-4942

Julkaisupaikka Espoo **Painopaikka** Helsinki **Vuosi** 2012

Sivumäärä 185 **urn** http://urn.fi/URN:ISBN:978-952-60-4779-9

Preface

During my thesis work, numerous people have helped me in various different ways. Of these people I should specially mention Prof. Markku Lehtinen, he hired me and acted as the supervisor of my thesis. He has supported me in numerous ways throughout my studies. I would also like to thank the following people, who are listed in alphabetical order. I am sure there is somebody missing from the list, you know who you are.

Pablo Cesar, V. Chandrasekar, Jorge L. Chau, Baylie Damtie, Lars Dyrud, Carl-Fredrik Enell, Jonathan Fentzke, Björn Gustavsson, Heikki Haario, Mikko Honkala, Mikko Kaasalainen, Antti Kero, Marko Laine, Sari Lasanen, Jussi Markkanen, Markku Markkanen, Derek McKay-Bukowski, Marco Milla, Erkki Oja, Mikko Orispää, Kari Pihkala, Petteri Piiroinen, Lassi Roininen, Karim. M. Kuyeng Ruiz, Esa Turunen, Thomas Ulich, Ilkka Virtanen and Petri Vuorimaa.

Most of my work wouldn't have been possible without the help of others in practical matters. I would like to thank all of the Sodankylä geophysical observatory and EISCAT staff for their support in performing many of the observations that form the basis for this thesis.

I like to the thank my parents and my brothers and sisters: Ulla, Kari, Viivi, Anne, and Taavi Vierinen. Finally, I would like to thank my family for their support and love: Pauliina, Eetu, Emil, Onni, and Piko.

Sodankylä, September 7, 2012,

Juha Vierinen

List of symbols

$\arg\max_{\mathbf{x}} f(\mathbf{x})$	Argument of the maximum
$\arg\min_{\mathbf{x}} f(\mathbf{x})$	Argument of the minimum
m, $\mathbf{m}$	A measurement
x, $\mathbf{x}$	Model parameters
ξ_t, $\boldsymbol{\xi}$	Measurement noise
$\boldsymbol{\Sigma}$	Covariance matrix of a Gaussian random vector
$\mathbf{A}$	Theory matrix of a linear problem
$\mathbf{J}$	Jacobian matrix
$\mathbf{L}$	Linear regularization operator
$\mathbf{UDV}^{\mathrm{H}}$	Singular value decomposition
$w(t)$	Window function
$z(t)$, z_t	complex timeseries
$R(t)$	Trajectory of a target
$p(\mathbf{m}\|\mathbf{x})$	Likelihood probability density function
$p(\mathbf{x}\|\mathbf{m})$	Posteriori probability density function
$p(\mathbf{x})$	Prior probability density function
$\zeta_{r,t}$	Discretized incoherent scattering process
$\mu(dx;t)$	Continuous incoherent scattering medium (Itō-measure)
ϵ_t, $\epsilon(t)$	Radar transmission waveform or envelope
$\underline{\mathbf{x}}$	Augmented complex random variable

Contents

List of Publications

This thesis consists of an overview and of the following publications which are referred to in the text by their Roman numerals.

I J. Vierinen, M. S. Lehtinen, and I. I. Virtanen. Amplitude domain analysis of strong range and Doppler spread radar echos. *Annales Geophysicae*, 26, 2419-2426, August 2008.

II J. Vierinen, M. S. Lehtinen, M. Orispää, and I. I. Virtanen. Transmission code optimization method for incoherent scatter radar. *Annales Geophysicae*, 26, 2923-2927, August 2008.

III J. Vierinen. Fractional baud-length coding. *Annales Geophysicae*, 29, 1189-1196, 2011.

IV J. Vierinen and M. S. Lehtinen. 32-cm wavelength radar mapping of the Moon. In *6th European Radar Conference, EuRAD 2009*, Rome, September 2009.

V J. Vierinen, J. Markkanen and H. Krag. High power large aperture radar observations of the Iridium-Cosmos collision. In *10th Advanced Maui Optical and Space Surveillance Techonologies Conference*, Maui, September 2009.

Author's Contribution

Publication I: "Amplitude domain analysis of strong range and Doppler spread radar echos"

The paper shows for the first time how to analyze the incoherent scatter amplitude waveform of narrow strong layers of incoherent scatter. The original idea, numerical calculations, and writing was done by me. Prof. Markku Lehtinen gave the idea of using a Fourier series to represent the time dependent incoherent scatter amplitude.

Publication II: "Transmission code optimization method for incoherent scatter radar"

The paper introduces a transmission waveform optimization method that allow searches of binary phase code groups for lag-profile inversion. The methods have been used in the design of multi-purpose transmission code groups for incoherent scatter radar. I have also used a similar optimization algorithm to search for nearly optimal amplitude and phase modulated radar transmission codes [1], lunar radar transmission codes, and also for fractional baud-length codes [2]. In addition to providing an algorithm to search for these radar codes, the paper also shows that sufficiently long random code groups [3] are nearly optimal in terms of performance, and that code optimization is needed only for shorter code groups. The paper was written based on work done mostly by me. However, the incoherent scatter autocorrelation function variance calculations were originally formulated by Prof. Markku Lehtinen, they also appear in extended form in a companion paper [4].

Publication III: "Fractional baud-length coding"

The paper introduces *fractional baud-length coding*, which is a novel radar transmission coding method that allows the amplitude domain analysis of targets with improved range resolution even when the resolution is larger than the baud-length would normally allow. This is achieved with the use of non-uniform baud-lengths that result in a transmission waveform without zeros in frequency domain. These zeros exist in all conventional uniform baud-length codes when analyzing the target at sub-baud range resolution, making the inverse problem ill-posed. The use of fractional baud-lengths avoids this problem. All of the work for this paper was done by me.

Publication IV: "32-cm wavelength radar mapping of the Moon"

The paper describes the first EISCAT lunar inverse synthetic aperture radar measurements of the Moon. This was made possible by using a long optimized binary phase code, which allowed improved effective radar transmission power with the EISCAT UHF radar. Most of the work, including experiment design, programming, radar operation, and data analysis was performed by me. The idea was initially suggested by A. P. van Eyken, who was the director of EISCAT at the time. The work was done in close collaboration with Prof. Markku Lehtinen, who had the idea of using long coded transmission pulses for the task, to significantly improve signal to noise ratio. He came up with the idea of using a Kronecker product Barker code, which was the starting point to the optimized code used in the study. The idea of using beam nulls to avoid range-Doppler North-South ambiguity was also his. Future work will include focused dual-polarization measurements of the lunar reflectivity.

Publication V: "High power large aperture radar observations of the Iridium-Cosmos collision"

The paper describes several beam-park measurements of the debris produced by the collision of the Iridium and Cosmos satellites in February 2009. As these measurements were conducted soon after the collision, they are valuable for calibrating the number of small < 10 cm diameter objects produced by the collision. The paper is mostly written by me. I

also designed and implemented the radar experiments and provided the data recording and measurement analysis software. The work was done in close collaboration with Mr. Jussi Markkanen who acted as a adviser for the work. The coherent integration part of analysis software was designed based on earlier work by Jussi Markkanen and Prof. Markku Lehtinen [5, 6]. Dr. Holger Krag provided simulations of the collision debris cloud using the MASTER debris model [7].

1. Introduction

The main theme of my research during the last five years has been the application of the statistical inverse problems framework to radar measurements and design of experiments. During my work I have developed radar measurement models and their numerical implementations with the purpose of allowing us to sense our environment more clearly.

Many of the advances in recent years in this field have been facilitated by increasingly powerful computers, wide band digital receivers, signal generators and cheap digital mass storage. This has allowed the permanent storage of continuous raw wide band receiver voltage waveforms and data analysis using software run on general purpose computers. The main consequence of this is that it has become, through the use of scientific numerical programming tools and libraries, easier to develop more precise radar target models and design more advanced measurements. This computer revolution of radio frequency signal processing is sometimes referred to as *software defined radio* [8]. The corresponding term used for radar systems is *software radar* [9].

The main contribution of this thesis lies in the introduction of novel radar measurement models and their numerical implementations. These have been used, e.g., in measurements of space debris, meteors, lunar reflectivity, and incoherent scatter from various parts of Earth's atmosphere. In addition to this, I have worked with *optimal experiment design* [10, 11], mainly in the form of designing optimal radar transmission waveforms. The main results in the field of optimal radar experiment design include *nearly perfect transmission codes* and *fractional baud-length codes*.

Experimental science requires a wide range of different tools and skills. During the course of my work, I have ventured through theoretical and practical issues ranging from formulating physical radar measurement

models to programming reliable and efficient data acquisition software for the digital receivers used to record the radar waveforms. In some cases, the numerical algorithms involved in the analysis of these waveforms needed to be written using specialized graphical accelerator cards in order to be fast enough to be able to analyze the data in a reasonable amount of time. This wide range of topics is also reflected in the contents of this thesis.

1.1 Contributions

The main contributions of this thesis can be summarized as follows:

- *Fractional baud-length coding*, which was introduced in Publication III, is a new radar transmission coding principle that for the first time makes it possible to analyze radar targets in amplitude domain with a higher range resolution than the shortest baud-length used in the radar transmission code. This is achieved by using variable sized baud-lengths.

- Several publications [12, 1, 2, 4, 13] published during the thesis work have focused on radar transmission code optimality, i.e., radar transmission waveforms that minimize the variance of various estimates that are obtained from radar measurements. This work has resulted in a robust optimization algorithm, which is presented in Publication II. This algorithm can be used to find optimal codes for several different radar measurement types. It has been used, e.g., to search for nearly optimal amplitude and phase modulated radar transmission codes [1] for coherent targets, which are in most cases only a very small fraction worse than perfect. The algorithm can also be used for searching for multipurpose [14] incoherent scatter radar transmission code groups that are nearly perfect, but contain only a small number of codes per group.

- Publication II also showed that sufficiently long purely randomly selected code groups are close to optimal in terms of incoherent scatter autocorrelation function estimation variance. While optimized code groups can be made shorter, which simplifies ground clutter removal, the use of long groups of random codes typically guarantees that the error covariance of the estimates is close to diagonal [15]. This result shows that there is no significant loss in estimation accuracy when using pseudo-

random code groups [3] for incoherent scatter measurements.

- Publication V of this thesis presents one of the few published high power large aperture radar space debris beam-park measurements that were conducted shortly after the Iridium-Cosmos satellite collision. As the measurements were done soon after the collision, the cloud was still fairly compact, making the data useful for estimating the size of the space debris cloud produced by the collision.

- Publication IV of this thesis for the first from showed that it is feasible to perform lunar inverse synthetic aperture radar measurements using the EISCAT UHF radar system. This was made possible by applying an extremely long optimized radar transmission code. These types of measurements are typically performed with the much larger Arecibo or Greenbank systems, but using methods developed in this work, such measurements can also be performed with smaller radars.

- Publication I showed for the first time how to analyze narrow and strong incoherent scattering targets in amplitude domain in cases where the incoherent scatter is overspread in range and Doppler, i.e., the backscatter amplitude changes significantly already while the transmission pulse travels through the target.

- Introduction of radar experiments and methods for simultaneously analyzing multiple different types of targets, including meteors, space debris and incoherent scatter [14, 16, 17].

- Utilizing MCMC methods for accurate analysis of various incoherent scatter radar target plasma parameters [18, 19].

- In several papers [19, 16] with my collaborators, we have for the first time applied optimal space debris and meteor head echo detection algorithms for removal of these echoes in amplitude domain, before estimating the incoherent scatter from ionospheric plasma using lag-profile inversion [20]. This significantly improves the quality of low signal to noise ratio incoherent scatter measurements, as this allows the removal weak and strong interfering echoes, while only discarding a very small amount of raw voltage samples.

- In the introduction part of this thesis, we show for the first time that a radar target estimator called the *matched filter* can be seen as a maximum a posteriori solution with a certain type a priori covariance assumption. Matched filtering, or more generally *correlation estimation*, can be seen as a form of regularization in the framework of statistical inverse problems. A similar explanation is also given for the truncated SVD method.

- The introductory part of this thesis introduces dual-polarization lag-profile inversion equations. These equations are an extension of lag-profile inversion [20] that can be used for dual-polarization radar measurements.

Most of these contributions are described in the papers included in this thesis. The rest of the contributions listed above are described in the introductory part of this thesis.

1.2 Outline of the thesis

This thesis consists of an introductory part, followed by a collection of refereed publications.

The introductory part of the thesis will first skim through the basics of probability theory and go into more detail on several types of problems that are useful in the case of radar measurements. We then go through several practical numerical methods that have been applied in the work. After this, we will shortly discuss the history of radars and give an overview of *high power large aperture* radars. This is followed by a chapter that describes various useful radar measurement models with emphasis on the contributions of the thesis. Using the introduced radar measurement models we will finally discuss several aspects of optimal radar experiment design, mainly in the form of radar transmission coding.

1.2.1 Papers not included in the thesis

During my research, I have also worked on several other interesting research topics in collaboration with my collegues. This has resulted in many publications. I will discuss some of this work in the introductory

part of the thesis, even though the publications will not be distributed as part of this thesis.

1. **J. Vierinen**, M. S. Lehtinen, J. Markkanen, and I. I. Virtanen. *Measuring space debris with phase coded aperiodic transmission sequences*. In Proc. Fifth European Conference on Space Debris, 2009.

2. M. Markkanen, **J. Vierinen**, and J. Markkanen. *Polyphase alternating codes*. Annales Geophysicae, 26, 2237-2243, 2008.

3. I. I. Virtanen, **J. Vierinen**, and M. S. Lehtinen. *Phase coded aperiodic transmission sequences*. Annales Geophysicae, 27, 2799-2811, 2009.

4. A. Kero, **J. Vierinen**, C-F Enell, I. I. Virtanen, and E. Turunen. *New incoherent scatter diagnostic methods for the heated D-region ionosphere*, Annales Geophysicae, 26, 2270-2279, 2008.

5. I. I. Virtanen, M. S. Lehtinen, T. Nygren, M. Orispää, and **J. Vierinen**. *Lag profile inversion method for EISCAT data analysis*. Annales Geophysicae, 26, 571-581, 2008.

6. M. S. Lehtinen, I. I. Virtanen, and **J. Vierinen**. *Fast comparison of IS radar code sequences for lag profile inversion*. Annales Geophysicae, 26, 2291-2301, 2008.

7. B. Damtie, M. S. Lehtinen, M. Orispää, and **J. Vierinen**. *Mismatched filtering of aperiodic quadriphase codes*. IEEE Transactions on information theory, 54, April 2008.

8. I. I. Virtanen, M. S. Lehtinen, and **J. Vierinen**. *Towards multi-purpose IS radar experiments*. Annales Geophysicae, 26, 2281-2289, 2008.

9. A. Kero, C.-F. Enell, A. Kavanagh, **J. Vierinen**, I. Virtanen, and E. Turunen. *Could negative ion production explain the polar mesosphere winter echo (PMWE) modulation in active HF heating experiments?* Geophysical Research Letters, 35, L2J102, 2008.

10. Carl-Fredrik Enell, Pekka T. Verronen, Mathew J. Beharrell, **Juha**

Vierinen, Antti Kero, Annika Seppälä, Farideh Honary, Thomas Ulich, and Esa Turunen. *Case study of the mesospheric and lower thermospheric effects of solar X-ray flares: Coupled ion-neutral modelling and comparison with EISCAT and riometer measurements*. Annales Geophysicae, 26, 2311-2321, 2008.

11. B. Damtie, M. S. Lehtinen, M. Orispää, and **J. Vierinen**. *Optimal long binary phase code-mismatched filter pairs with applications to ionospheric radars*. Bull. Astr. Soc. India, 2007.

2. Probability theory

Probability theory is a mathematical framework that is used to study uncertain quantities. This could be, e.g., the outcome of a coin toss, or the voltage of cosmic radio noise induced in a receiver. This framework is essential when analyzing nearly any type of real world measurements that contain uncertain quantities, typically in the form of measurement noise.

The importance of probability theory has long been recognized in the radar community, as random variables are needed not only for modeling measurement errors but also often as target models [21, 22, 23, 24].

As in any other field of applied mathematics, the main advances in the field of radar measurement analysis are largely driven by the exponentially growing computational capabilities of digital computers. This allows the use of more sophisticated measurement models, which in many cases can provide substantial improvements in estimation accuracy.

In this chapter, we will first briefly discuss the foundations of the theory of probability. We will then go through several topics of special importance in the case of radar measurements, including complex valued linear statistical inverse problems, Toeplitz and circulant models [25, 26], and Kolmogorov-Wiener [27] filtering. Parts of the material presented here have been influenced by the following references [28, 29].

2.1 History

Perhaps the earliest use of probability theory was for analyzing games of chance in order to gain an advantage in gambling. In addition to Cardano [30, 31], many other early mathematicians, such as Fermat and Huygens also developed probability theory through the study of games of chance. One of the first to extensively apply calculus to probability was Laplace [32]. By his time, the concept of probability was already applied for inter-

preting scientific measurements.

One of the most important practical concepts of probability theory, the least-squares solution, was developed independently by Gauss, Legendre and Adrain [33, 34, 35]. Today it is used in the heart of nearly every statistical analysis procedure.

In 1929, Kolmogorov introduced the axioms of probability theory [36], which are now considered as the foundation for modern probability theory. This set and measure-theoretic formulation of probability provides a consistent framework for mathematical inference.

2.2 The concept of probability

The following definition of the axioms of probability is based on the original Kolmogorov presentation [36]. Let Ω be a collection of elementary outcomes of a stochastic experiment and E be the set of subsets of Ω, which we will call *random events*.

I. E is a non-empty subset of the power set of Ω closed under the intersection and union of pairs of sets and under complements of individual sets, i.e., (Ω, E) is a field of sets.

II. The set E of all possible random events contains Ω.

III. Each set $A \subset E$ is associated with a non-negative real number (measure) $p(A) \geq 0$, which is called the probability of random event A.

IV. $p(\Omega) = 1$, i.e., the probability that some elementary event will occur is one.

V. If events A and B have no element in common ($A \cap B = \emptyset$), then

$$p(A \cup B) = p(A) + p(B).$$

VI. For a decreasing sequence of events

$$A_1 \supset A_2 \supset \cdots \supset A_n$$

of E, for which $\cap_n A_n = \emptyset$, the following holds:

$$\lim_{n \to \infty} p(A_n) = 0.$$

This last axiom is only needed when there are infinitely many elementary outcomes.

From these axioms, it is possible to derive the commonly used rules of probability theory.

Even though use of the most general form of probability theory requires measure theoretic formalism, the probability density function formalism is sufficient for most of the topics discussed in this thesis.

In the case of the probability density formalism, we assume that the probability of an event A can be given by applying an integrable probability density function $\pi(x)$ to the following integral:

$$p(A) = \int_A \pi(x)dx, \tag{2.1}$$

where A is the set of values of x that correspond to event A. In the rest of the introduction, we will use the notation $p(x)$ for the probability density function itself. We will also sometimes use the terms probability density function and probability distribution interchangably.

2.3 Expected value

In most situations encountered in this thesis, the probability density function $p(x) \in \mathbb{R}$ is well defined in the sense that

$$\int_\Omega p(x)dx = 1 \tag{2.2}$$

and the expected value of a function $f(x)$ is obtained by integrating over the probability density function

$$\mathrm{E}\, f(x) = \int_\Omega f(x)p(x)dx, \tag{2.3}$$

assuming the product $f(x)p(x)$ is integrable over Ω.

For example, the mean value of a variable x is defined as

$$\mathrm{E}\, x = \int_\Omega xp(x)dx. \tag{2.4}$$

Several other alternative notations exist for the expectation operator. For example in physics, the expectation operator is denoted by angle brackets $\mathrm{E}\, x = \langle x \rangle$.

2.4 Theorem of Bayes

The Bayes theorem [37, 38] is important in data analysis as it allows one to easily make use of prior information when making inferences. For

example, when estimating the ion temperature of ionospheric plasma, one typically has to make some assumption about the masses of the ions and their concentrations. This can be done by using a prior distribution of the ion concentrations.

The theorem can be derived using the formula for conditional probabilities for events A and B. Combining $p(B|A) = p(A \cap B)p(A)^{-1}$ and $p(A|B) = p(A \cap B)p(B)^{-1}$ gives us the theorem of Bayes:

$$p(B|A) = \frac{p(A|B)p(B)}{p(A)}. \tag{2.5}$$

For practical applications, the probability density function form of the Bayes theorem for vector valued random variables $\mathbf{x}$ and $\mathbf{y}$ is

$$p(\mathbf{x}|\mathbf{y}) = \frac{p(\mathbf{y}|\mathbf{x})p(\mathbf{x})}{p(\mathbf{y})}. \tag{2.6}$$

This is derived, e.g., in the textbook by Kaipio and Somersalo [28].

When solving inverse problems using the framework of probability theory, one makes use of prior information to regularize a problem that is otherwise unstable. One typical example of such a prior assumption is to assume that the solution is smooth. We will discuss this in more detail later.

2.5 Measurement model

When analyzing measurements, it is important to have a good mathematical model that describes how the measurements are produced. A statistical measurement model is a mapping of model parameters $\mathbf{x} \in X$ and measurement noise $\boldsymbol{\xi} \in \Xi$ to measurements $\mathbf{m} \in M$, in such a way that both all of these are considered as random variables. The mapping $f : X \cup \Xi \to M$ is commonly referred to as the forward theory, when is also sometimes written as

$$\mathbf{m} = f(\mathbf{x}; \boldsymbol{\xi}), \tag{2.7}$$

and in the most common cases, the measurement errors are additive:

$$\mathbf{m} = f(\mathbf{x}) + \boldsymbol{\xi}, \tag{2.8}$$

which simplifies the statistical treatment of the problem.

The task of statistical inference is to extract information about $\mathbf{x}$ from the measurements $\mathbf{m}$. Sometimes, this task of extracting information is called an *inverse problem* or a *statistical inverse problem*.

As the measurement relation typically contains random variables, a natural framework for studying inverse problems is probability theory, typically by inspecting the *a posteriori* probability distribution of the model parameters $\mathbf{x}$, given the observed measurements $\mathbf{m}$. This can be typically obtained using the Bayes formula (Eq. 2.6)

$$p(\mathbf{x}|\mathbf{m}) = \frac{p(\mathbf{m}|\mathbf{x})p(\mathbf{x})}{p(\mathbf{m})}. \tag{2.9}$$

This probability distribution contains all the information of the unknown model parameters $\mathbf{x}$. Here the term $p(\mathbf{m}|\mathbf{x})$ is called the *likelihood function*, which is the probability distribution of the measurements, given the model parameters. The likelihood function is defined using the forward theory $f(\mathbf{x};\boldsymbol{\xi})$, by assuming some probability distribution for the measurement errors $\boldsymbol{\xi}$. The term $p(\mathbf{x})$ is the *a priori* distribution of the model parameters. Finally, $p(\mathbf{m})$ is simply a scaling factor $p(\mathbf{m}) = \int_\Omega p(\mathbf{m}|\mathbf{x})p(\mathbf{x})d\mathbf{x}$ that ensures that the posterior probability distribution is scaled correctly. This scaling constant is sometimes ignored, leaving $p(\mathbf{x}|\mathbf{m}) \propto p(\mathbf{m}|\mathbf{x})p(\mathbf{x})$.

In several places in this thesis, the posteriori probability density and the likelihood function are used interchangeably. In this case, we assume so called flat priors, where we assume an infinitely wide uniform distribution as the prior density function. To avoid zero-valued probability density functions that arise with these types of improper priors, we have to use the priors in unnormalized form. This results in $p(\mathbf{m}|\mathbf{x}) \propto p(\mathbf{x}|\mathbf{m})$. In this case, the *a posteriori* and *likelihood* probability densities will, up to a constant factor, coincide.

2.5.1 Model comparison

Using the chain rule one can also write Bayes' theorem in a form that can be used for comparing several different measurement models:

$$p(\mathbf{x^{(k)}}, k|\mathbf{m}) = \frac{p(\mathbf{m}|\mathbf{x^{(k)}}, k)p(\mathbf{x^{(k)}}|k)p(k)}{p(\mathbf{m})}. \tag{2.10}$$

In this case, the joint distribution $p(\mathbf{x^{(k)}}, k)$ is substituted as $p(\mathbf{x^{(k)}}|k)p(k)$. In this equation $\mathbf{m}$ denotes the measurements, $k \in \mathbb{N}$ denotes the model, and $\mathbf{x^{(k)}}$ the corresponding model parameters of model k. This form is commonly used in multiple hypothesis testing, i.e., to study which of the many possible models k and their model parameters $\mathbf{x^{(k)}}$ best describe the measurements.

2.5.2 Estimators

Because the a posteriori probability distribution can often be very high-dimensional, it is often useful to study various aspects of $p(\mathbf{x}|\mathbf{m})$ using so called estimators, which summarize the distribution $p(\mathbf{x}|\mathbf{m})$ to a single vector, or a lower-dimensional distribution.

Assuming that the distribution has only one strong peak, it is often practical to inspect the maxima of $p(\mathbf{x}|\mathbf{m})$, which is called the *maximum a posteriori* (MAP) estimate

$$\hat{\mathbf{x}}_{\mathrm{MAP}} = \arg\max_{\mathbf{x}} p(\mathbf{x}|\mathbf{m}). \tag{2.11}$$

The equivalent estimator that only inspects the likelihood function is called the *maximum likelihood* (ML) estimator

$$\hat{\mathbf{x}}_{\mathrm{ML}} = \arg\max_{\mathbf{x}} p(\mathbf{m}|\mathbf{x}). \tag{2.12}$$

Another common estimator is the *conditional mean* (CM) estimator. When assuming a n dimensional complex-valued unknown $\mathbf{x} \in \mathbb{C}^n$ it can be written as

$$\hat{\mathbf{x}}_{\mathrm{CM}} = \int_{\mathbb{C}^n} \mathbf{x} p(\mathbf{x}|\mathbf{m}) d\mathbf{x}. \tag{2.13}$$

If the density function is well defined, unimodal, and symmetric around each coordinate axis around its peak, the maximum a posteriori and conditional mean estimators are identical, assuming that $\hat{\mathbf{x}}_{\mathrm{CM}}$ exists.

In many situations it is also advantageous to study the shape of the distribution $p(\mathbf{x}|\mathbf{m})$, but this can be difficult if the distribution has very many dimensions. A useful tool for reducing the dimensionality of $p(\mathbf{x}|\mathbf{m})$ is the so-called *marginal probability distribution*

$$p(\mathbf{x}'|\mathbf{m}) = \int_{\mathbb{C}^{n-k}} p(\mathbf{x}|\mathbf{m}) d\mathbf{x}'', \tag{2.14}$$

where $\mathbf{x}'' = \{x_i \mid i \in M\} \in \mathbb{C}^{n-k}$ are the parameters to be integrated out, and $\mathbf{x}' = \{x_j \mid j \notin M\} \in \mathbb{C}^k$ contains the remaining parameters. In practice, one or two dimensional marginal distributions are the most commonly used, as they are easiest to visualize.

2.6 Complex normal random variables

Perhaps the most important type of random variable in probability theory is the *normal random variable*. One reason for this is the central limit theorem, which states that the sample mean value of independent

identically distributed random variables with finite mean and variance approaches a random variable with a normal distribution.

Because most radar models dealing with high-frequency signals are complex valued, we will emphasize complex normal random variables. The relationship between band limited high frequency signals and complex baseband signals is explained in detail in Section 5.1.

We will first introduce *augmented complex random variables* to show connections between $2p$-variate real normal random variables with p-variate general complex normal random variables. We will then introduce a special class of random variables called *circular symmetric* complex normal random variables, which are important for radar measurement models. We will use the formalism described in [39].

In the most general case [39, 40], a p-variate complex normal random variable $\mathbf{x} \in \mathbb{C}^p$ can be represented using two real valued vectors of real normal random variables $\mathbf{x} = \mathbf{u} + i\mathbf{v}$, where $\mathbf{u} \in \mathbb{R}^p$ and $\mathbf{v} \in \mathbb{R}^p$. If we represent $\mathbf{u}$ and $\mathbf{v}$ in block form

$$\mathbf{z} = \begin{bmatrix} \mathbf{u} \\ \mathbf{v} \end{bmatrix}, \tag{2.15}$$

where $\mathbf{z} \in \mathbb{R}^{2p}$, the covariance matrix $\mathbf{\Sigma}_z = \mathrm{E}\,(\mathbf{z} - \mathrm{E}\,\mathbf{z})(\mathbf{z} - \mathrm{E}\,\mathbf{z})^{\mathrm{T}}$ describes all the possible covariance structures for $\mathbf{x}$. We can then use a linear transformation $\mathbf{T}_p \in \mathbb{C}^{2p \times 2p}$ of the form

$$\mathbf{T}_p = \begin{bmatrix} \mathbf{I}_p & i\mathbf{I}_p \\ \mathbf{I}_p & -i\mathbf{I}_p \end{bmatrix} \tag{2.16}$$

to convert $\mathbf{z}$ into a complex valued variable. Here $\mathbf{I}_p$ is a $p \times p$ identity matrix. The transform is unitary up to a constant $\mathbf{T}_p^{-1} = \frac{1}{2}\mathbf{T}_p^{\mathrm{H}}$. The conversion between vectors with real valued representation and complex valued representation is of the following form

$$\underline{\mathbf{x}} = \begin{bmatrix} \mathbf{x} \\ \overline{\mathbf{x}} \end{bmatrix} = \mathbf{T}_p\mathbf{z} \Longleftrightarrow \mathbf{z} = \begin{bmatrix} \mathbf{u} \\ \mathbf{v} \end{bmatrix} = \frac{1}{2}\mathbf{T}_p^{\mathrm{H}}\underline{\mathbf{x}}, \tag{2.17}$$

where the transformed complex valued vector contains the unconjugated and conjugated version of vector $\mathbf{x}$. This type of a representation is called an *augmented representation* and it is always denoted with an underline $\underline{\mathbf{x}} \in \mathbb{C}_*^{2p}$. If we now represent our complex valued normal random vector in *augmented form*

$$\underline{\mathbf{x}} = \begin{bmatrix} \mathbf{x} \\ \overline{\mathbf{x}} \end{bmatrix}, \tag{2.18}$$

and equivalently the *augmented mean* as

$$\underline{\boldsymbol{\mu}} = \begin{bmatrix} \boldsymbol{\mu} \\ \overline{\boldsymbol{\mu}} \end{bmatrix}, \tag{2.19}$$

we can then obtain the *augmented covariance matrix*

$$\begin{aligned} \underline{\Sigma} &= \mathrm{E}\,(\underline{\mathbf{x}} - \underline{\boldsymbol{\mu}})(\underline{\mathbf{x}} - \underline{\boldsymbol{\mu}})^{\mathrm{H}} \\ &= \begin{bmatrix} \Sigma & \widetilde{\Sigma} \\ \overline{\widetilde{\Sigma}} & \overline{\Sigma} \end{bmatrix}, \end{aligned} \tag{2.20}$$

where

$$\boldsymbol{\Sigma} = \mathrm{E}\,(\mathbf{x} - \boldsymbol{\mu})(\mathbf{x} - \boldsymbol{\mu})^{\mathrm{H}} \tag{2.21}$$

and

$$\widetilde{\boldsymbol{\Sigma}} = \mathrm{E}\,(\mathbf{x} - \boldsymbol{\mu})(\mathbf{x} - \boldsymbol{\mu})^{\mathrm{T}}. \tag{2.22}$$

The covariance matrix $\underline{\Sigma}$ must be non-negative definite Hermitian, which also implies that $\overline{\widetilde{\Sigma}}^{\mathrm{T}} = \widetilde{\Sigma}$. These type of variables that have non-zero $\widetilde{\Sigma}$ are called *generalized complex normal random variables* [39].

These definitions might at first seem redundant as it uses $\mathbb{C}_*^{2p}$ complex normal random variables, which are equivalent to $\mathbb{R}^{2p}$ real valued normal random variables $\mathbf{z}$ through a complex linear transformation. But in this way, the probability density for $\mathbf{x}$ can be written in a very compact and familiar form

$$p(\mathbf{x}) = \frac{1}{\pi^p \sqrt{|\underline{\boldsymbol{\Sigma}}|}} \exp\left(-\frac{1}{2}(\underline{\mathbf{x}} - \underline{\boldsymbol{\mu}})^{\mathrm{H}} \underline{\boldsymbol{\Sigma}}^{-1} (\underline{\mathbf{x}} - \underline{\boldsymbol{\mu}})\right). \tag{2.23}$$

Also, the fact that there are algebraically two random variables $\mathbf{x}$ and $\overline{\mathbf{x}}$ might seem confusing at first, but $\mathbf{x}$ is exactly a conjugated version of $\overline{\mathbf{x}}$ and therefore the density can be written $p(\mathbf{x})$ instead of $p(\mathbf{x}, \overline{\mathbf{x}})$. Complex normal random variables are completely characterized by $\boldsymbol{\mu}$, $\boldsymbol{\Sigma}$, and $\widetilde{\boldsymbol{\Sigma}}$. The notation $\mathbf{x} \sim \mathcal{CN}(\boldsymbol{\mu}, \boldsymbol{\Sigma}, \widetilde{\boldsymbol{\Sigma}})$ is typically used to describe such a random variable.

2.6.1 Proper complex normal random variables

When $\widetilde{\boldsymbol{\Sigma}} = 0$, the random variable is called a *proper*[1] [39] or *circular symmetric* random variable [41]. In this case the probability density is

[1] When this condition is not satisfied, the normal random variable is called *improper*.

simplified significantly and we do not need to use augmented variables or matrices

$$p(\mathbf{x}) = \frac{1}{\pi^p |\mathbf{\Sigma}|} \exp\left[-(\mathbf{x}-\boldsymbol{\mu})^{\mathrm{H}} \mathbf{\Sigma}^{-1} (\mathbf{x}-\boldsymbol{\mu})\right], \tag{2.24}$$

An important characteristic of such random variables is that they retain the circular symmetry also through complex linear transformations [42]. We will refer to a proper complex normal random variable using $\mathbf{x} \sim N(\boldsymbol{\mu}, \mathbf{\Sigma})$.

In the case of radar measurements, the measurement noise of raw voltage receiver samples can in most cases be modeled as proper complex normal random variables[2]. Therefore, we will concentrate on the theory of *proper* complex random variables, with the knowledge that we can always extend all of results to also cover improper complex normal random variables if necessary.

2.7 Statistical linear inverse problem

We will mainly discuss statistical linear models with additive *proper* complex normal random noise. For a treatment on real valued inverse problems, refer to [28].

An important type of measurement equation is the so called linear model that is linear with respect to parameters and contains a normally distributed random variable as an error term. This can be expressed using the following type of matrix equation

$$\mathbf{m} = f(\mathbf{x}; \boldsymbol{\xi}) = \mathbf{A}\mathbf{x} + \boldsymbol{\xi}, \tag{2.25}$$

where $\mathbf{A} \in \mathbb{C}^{k \times n}$ is called the *theory matrix*, $\mathbf{m} \in \mathbb{C}^k$ is the measurement vector, $\mathbf{x} \in \mathbb{C}^n$ contains the unknown model parameters, and the error is a proper complex normal multivariate random variable $\boldsymbol{\xi} \sim N(0, \mathbf{\Sigma})$. We can then write the likelihood function as

$$p(\mathbf{m}|\mathbf{x}) = \frac{1}{\pi^k |\mathbf{\Sigma}|} \exp\left[-(\mathbf{m}-\mathbf{A}\mathbf{x})^{\mathrm{H}} \mathbf{\Sigma}^{-1} (\mathbf{m}-\mathbf{A}\mathbf{x})\right], \tag{2.26}$$

which has the following maximum at the point

$$\hat{\mathbf{x}}_{\mathrm{ML}} = (\mathbf{A}^{\mathrm{H}} \mathbf{\Sigma}^{-1} \mathbf{A})^{-1} \mathbf{A}^{\mathrm{H}} \mathbf{\Sigma}^{-1} \mathbf{m}. \tag{2.27}$$

If we add a prior assumption that our unknown is a normal random variable $\mathbf{x} \sim N(0, \mathbf{\Sigma}_{\mathrm{prior}})$, the posterior probability density function is

$$p(\mathbf{x}|\mathbf{m}) = \frac{1}{\pi^{k+n} |\mathbf{\Sigma}||\mathbf{\Sigma}_{\mathrm{prior}}| p(\mathbf{m})} \exp\left[-(\mathbf{m}-\mathbf{A}\mathbf{x})^{\mathrm{H}} \mathbf{\Sigma}^{-1} (\mathbf{m}-\mathbf{A}\mathbf{x}) - \mathbf{x}^{\mathrm{H}} \mathbf{\Sigma}_{\mathrm{prior}}^{-1} \mathbf{x}\right]. \tag{2.28}$$

[2] with the exception of self-noise in lag-profile inversion

This has a maximum at the point

$$\hat{\mathbf{x}}_{\mathrm{MAP}} = \boldsymbol{\Sigma}_{\mathrm{post}} \mathbf{A}^{\mathrm{H}} \boldsymbol{\Sigma}^{-1} \mathbf{m}, \tag{2.29}$$

where

$$\boldsymbol{\Sigma}_{\mathrm{post}} = (\boldsymbol{\Sigma}_{\mathrm{prior}}^{-1} + \mathbf{A}^{\mathrm{H}} \boldsymbol{\Sigma}^{-1} \mathbf{A})^{-1}. \tag{2.30}$$

The estimator $\hat{\mathbf{x}}_{\mathrm{MAP}}$ itself is a random variable with normally distributed errors

$$\hat{\mathbf{x}}_{\mathbf{MAP}} = \mathbf{x} + \boldsymbol{\xi}', \tag{2.31}$$

where $\boldsymbol{\xi}' \sim N(0, \boldsymbol{\Sigma}_{\mathbf{post}})$. Because a normal random distribution is unimodal, the conditional mean and the maximum a posteriori estimators coincide with $\hat{\mathbf{x}}_{\mathbf{MAP}}$.

2.7.1 Stacked representation

In some cases it is numerically efficient to represent the statistical linear inverse problem with a prior covariance assumption $\boldsymbol{\Sigma}_{\mathrm{prior}}$ in an alternate form using a modified theory matrix $\widetilde{\mathbf{A}}$ that is a stacked block matrix. This modified theory matrix consists of the original theory matrix and additional, possibly sparse regularization terms $\mathbf{P}_i$ that add to the prior assumption $\boldsymbol{\Sigma}_{\mathrm{prior}}$. In many cases, constructing a prior covariance assumption is also more intuitive when it can be constructed using one small elementary block at a time.

The stacked formulation also makes it possible to use prior assumptions when using the QR decomposition method for solving statistical linear inverse problems [43]. Full covariance matrix forms that result from different combinations of sparse covariance assumptions have been studied e.g., by Roininen [44].

The stacked representation for statistical linear models is defined using modified measurements $\tilde{\mathbf{m}}$, theory matrix $\widetilde{\mathbf{A}}$ and errors $\tilde{\boldsymbol{\xi}}$

$$\tilde{\mathbf{m}} = \widetilde{\mathbf{A}}\mathbf{x} + \tilde{\boldsymbol{\xi}}, \tag{2.32}$$

which expands in stacked form to

$$\begin{bmatrix} \mathbf{m} \\ \mathbf{0} \\ \vdots \\ \mathbf{0} \end{bmatrix} = \begin{bmatrix} \mathbf{A} \\ \mathbf{P}_1 \\ \vdots \\ \mathbf{P}_n \end{bmatrix} \mathbf{x} + \begin{bmatrix} \boldsymbol{\xi} \\ \boldsymbol{\xi}_1 \\ \vdots \\ \boldsymbol{\xi}_n \end{bmatrix}, \tag{2.33}$$

where $\mathbf{A}$, $\mathbf{m}$ and $\boldsymbol{\xi}$ are the original the theory matrix, measurement vector and measurement errors. The vector $\mathbf{0} = (0, \cdots, 0)^{\mathrm{T}} \in \mathbb{C}^{N \times 1}$ is a zero

vector and $\boldsymbol{\xi}_\mathbf{i}$ are multinormal errors with $\mathrm{E}\,\boldsymbol{\xi}_\mathbf{i}\boldsymbol{\xi}_\mathbf{i}^{\mathrm{H}} = \mathbf{I}$. We also define the modified measurement error covariance matrix

$$\widetilde{\boldsymbol{\Sigma}} = \begin{bmatrix} \boldsymbol{\Sigma} & \mathbf{0}' & \dots & \mathbf{0}' \\ \mathbf{0}' & \mathbf{I} & \dots & \mathbf{0}' \\ \vdots & & \ddots & \\ \mathbf{0}' & \dots & \mathbf{0}' & \mathbf{I} \end{bmatrix}, \tag{2.34}$$

where $\mathbf{0}' = \mathbf{0}\mathbf{0}^{\mathrm{T}}$. We also require that the stacked form regularization terms $\mathbf{P}_i$ are related with the prior covariance assumption with the following relation

$$\boldsymbol{\Sigma}_{\mathrm{prior}}^{-1} = \sum_{i=1}^{n} \mathbf{P}_i^{\mathrm{H}} \mathbf{P}_i, \tag{2.35}$$

where each of the stacked priors $\mathbf{P}_i$ can be a relatively sparse matrix, but the equivalent prior covariance $\boldsymbol{\Sigma}_{\mathrm{prior}}$ can be a full matrix.

Using the modified measurement equations, we now obtain the maximum likelihood estimate

$$\begin{aligned} \hat{\mathbf{x}}_{\mathrm{ML}} &= (\widetilde{\mathbf{A}}^{\mathrm{H}} \widetilde{\boldsymbol{\Sigma}}^{-1} \widetilde{\mathbf{A}})^{-1} \widetilde{\mathbf{A}}^{\mathrm{H}} \widetilde{\boldsymbol{\Sigma}}^{-1} \tilde{\mathbf{m}} \\ &= (\mathbf{A}^{\mathrm{H}} \boldsymbol{\Sigma}^{-1} \mathbf{A} + \boldsymbol{\Sigma}_{\mathrm{prior}}^{-1})^{-1} \mathbf{A}^{\mathrm{H}} \boldsymbol{\Sigma}^{-1} \mathbf{m} \end{aligned}, \tag{2.36}$$

which is equivalent to the maximum a posteriori estimate with the prior assumption that $\mathbf{x} \sim N(0, \boldsymbol{\Sigma}_{\mathrm{prior}})$. Thus, the stacked form representation also suggests an alternative interpretation of the linear statistical inverse problem with a prior assumption. It is equivalent to adding new "virtual" zero valued measurements to the model. This result can also be generalized to include non-zero mean prior assumptions by using the measurements to define the mean value.

2.7.2 Prior assumptions and bias

Prior assumptions are sometimes required in radar measurement models, although this can usually be avoided through the use of careful experiment design. If prior assumptions have to be made, one should take special care as they can also introduce bias. In practice, prior assumptions should be introduced only in situations where the maximum likelihood estimate is unstable, i.e., the measurements do not provide enough information about the unknown variables.

In statistics, bias is defined using the expected value of the estimator

$$\mathrm{Bias}[\hat{\mathbf{x}}] = \mathrm{E}\,\hat{\mathbf{x}} - \mathbf{x}, \tag{2.37}$$

where $\hat{\mathbf{x}}$ is the estimator and $\mathbf{x}$ is the true value of the unknown.

We will only examine the case of linear theory with Gaussian errors and possibly a Gaussian prior assumption, which was discussed in Section 2.7. In this case, assuming zero mean measurement errors, the bias for a maximum a posteriori estimator is

$$\mathbf{b} = \mathbf{x} - (\mathbf{A}^{\mathrm{H}}\mathbf{\Sigma}^{-1}\mathbf{A} + \mathbf{\Sigma_{prior}}^{-1})^{-1}\mathbf{A}^{\mathrm{H}}\mathbf{\Sigma^{-1}}\mathbf{A}\mathbf{x}. \tag{2.38}$$

In essence, this is the expected value of the systematic error introduced by the prior assumptions.

In this thesis, we will show that several commonly used radar estimators and signal processing methods can be interpreted in the framework of statistical inverse problems as maximum a posteriori estimators with a prior assumption of the unknown radar target.

2.7.3 Complex to real transformation

As discussed in the previous section, a p-variate complex normal variable is equivalent to a $2p$-variate real normal random variable through a linear transformation. However, in the framework of signal processing theory, it is often easier to formulate and analyze a problem using complex valued theory. If the model requires the use of the more general augmented complex random variables, it is numerically more efficient to convert the problem into a real valued problem. In the case of statistical linear inverse problems, the problem can be transformed from a complex valued problem into a real valued problem using linear transformations.

Consider first a complex linear statistical inverse problem with complex normal errors

$$\mathbf{m} = \mathbf{A}\mathbf{x} + \boldsymbol{\xi}, \tag{2.39}$$

where $\mathbf{A} \in \mathbb{C}^{m\times n}$ and $\boldsymbol{\xi} \sim \mathcal{C}N(0, \mathbf{\Sigma}, \widetilde{\mathbf{\Sigma}})$. This can be converted into augmented form

$$\underline{\mathbf{m}} = \underline{\mathbf{A}\mathbf{x}} + \underline{\boldsymbol{\xi}} \tag{2.40}$$

which expands to

$$\begin{bmatrix} \mathbf{m} \\ \overline{\mathbf{m}} \end{bmatrix} = \begin{bmatrix} \mathbf{A} & \mathbf{0} \\ \mathbf{0} & \overline{\mathbf{A}} \end{bmatrix} \begin{bmatrix} \mathbf{x} \\ \overline{\mathbf{x}} \end{bmatrix} + \begin{bmatrix} \boldsymbol{\xi} \\ \overline{\boldsymbol{\xi}} \end{bmatrix} \tag{2.41}$$

and using the inverse transform $\mathbf{T}^{-1}$ shown in Section 2.6, we can transform the problem into a real valued linear problem

$$\mathbf{m}' = \mathbf{A}'\mathbf{x}' + \boldsymbol{\xi}',$$

which expands to

$$\frac{1}{2}\mathbf{T}_m^{\mathrm{H}}\underline{\mathbf{m}} = \left(\frac{1}{2}\mathbf{T}_m^{\mathrm{H}}\underline{\mathbf{A}}\mathbf{T}_n\right)\left(\frac{1}{2}\mathbf{T}_n^{\mathrm{H}}\underline{\mathbf{x}}\right) + \left(\frac{1}{2}\mathbf{T}_m^{\mathrm{H}}\underline{\boldsymbol{\xi}}\right), \tag{2.42}$$

from where we directly obtain the real valued theory measurement vectors $\mathbf{m}' \in \mathbb{R}^{2m}$ and theory matrix $\mathbf{A}' \in \mathbb{R}^{2m\times 2n}$. The real valued covariance matrix $\boldsymbol{\Sigma}' \in \mathbb{R}^{2m\times 2m}$ is obtained using the expected value of $\mathrm{E}\,\underline{\boldsymbol{\xi}}\underline{\boldsymbol{\xi}}^{\mathrm{H}} = \underline{\boldsymbol{\Sigma}}$ with the help of the formula for the augmented covariance matrix in Eq. 2.20

$$\mathbf{m}' = \frac{1}{2}\mathbf{T}_m^{\mathrm{H}}\underline{\mathbf{m}} = \begin{bmatrix}\mathrm{Re}\{\mathbf{m}\}\\ \mathrm{Im}\{\mathbf{m}\}\end{bmatrix} \tag{2.43}$$

$$\mathbf{A}' = \frac{1}{2}\mathbf{T}_m^{\mathrm{H}}\underline{\mathbf{A}}\mathbf{T}_n = \begin{bmatrix}\mathrm{Re}\{\mathbf{A}\} & -\mathrm{Im}\{\mathbf{A}\}\\ \mathrm{Im}\{\mathbf{A}\} & \mathrm{Re}\{\mathbf{A}\}\end{bmatrix} \tag{2.44}$$

$$\boldsymbol{\Sigma}' = \frac{1}{4}\mathbf{T}_m^{\mathrm{H}}\underline{\boldsymbol{\Sigma}}\mathbf{T}_m = \begin{bmatrix}\mathrm{E}\,\mathrm{Re}\{\boldsymbol{\xi}\}\mathrm{Re}\{\boldsymbol{\xi}^{\mathbf{T}}\} & \mathrm{E}\,\mathrm{Re}\{\boldsymbol{\xi}\}\mathrm{Im}\{\boldsymbol{\xi}^{\mathbf{T}}\}\\ \mathrm{E}\,\mathrm{Im}\{\boldsymbol{\xi}\}\mathrm{Re}\{\boldsymbol{\xi}^{\mathbf{T}}\} & \mathrm{E}\,\mathrm{Im}\{\boldsymbol{\xi}\}\mathrm{Im}\{\boldsymbol{\xi}^{\mathbf{T}}\}\end{bmatrix}. \tag{2.45}$$

These can then be solved using formulas for real valued statistical inverse problems. This also allows us to treat complex valued problems using real valued analysis in cases where this is beneficial.

This type of a transformation is more important for complex problems with errors that are not proper complex random variables. Problems with proper complex normal errors can be efficiently solved as such using the more straightforward proper complex valued random variable theory.

2.7.4 Tikhonov regularization

The Tikhonov regularization method [45] is a widely used scheme for solving ill-posed problems. Instead of minimizing the least squares $\|\mathbf{A}\mathbf{x}-\mathbf{m}\|^2$, the idea is to minimize the following modified sum of squares

$$\hat{\mathbf{x}}_{\mathbf{t}} = \arg\min_{\mathbf{x}} \|\mathbf{A}\mathbf{x}-\mathbf{m}\|^2 + \|\mathbf{L}\mathbf{x}\|^2, \tag{2.46}$$

where $\mathbf{L}$ is a suitably formed operator. This can be, e.g., used to enforce smoothness of the solution. This can be shown to have a minimum point at [28]

$$\hat{\mathbf{x}}_{\mathbf{t}} = (\mathbf{L}^{\mathrm{H}}\mathbf{L} + \mathbf{A}^{\mathrm{H}}\mathbf{A})^{-1}\mathbf{A}^{\mathrm{H}}\mathbf{m}. \tag{2.47}$$

The most simple form of regularization utilizes a scaled identity matrix $\mathbf{L} = \delta\mathbf{I}$, where $\delta \in \mathbb{R}$ is a suitably chosen regularization parameter.

All forms of Tikhonov regularization are equivalent to a maximum a posteriori estimator of a statistical linear inverse problem with diagonal

measurement error covariance $\mathbf{\Sigma} = \alpha\mathbf{I}$ and a priori covariance structure

$$\mathbf{\Sigma}_{\text{prior}}^{-1} = \frac{1}{\alpha}\mathbf{L}^{\text{H}}\mathbf{L}, \tag{2.48}$$

which is evident from Equation 2.30. However, the statistical linear inverse problem formulation is more general, as it allows an arbitrary covariance structure $\boldsymbol{\xi} \sim N(0, \mathbf{\Sigma})$ for the measurement errors.

2.7.5 Truncated singular value decomposition

Another often used method for regularizing ill-posed problems is the *truncated singular value decomposition* (TSVD) method [46]. The intuitive idea behind the method is that if the measurements do not provide enough information about the unknowns, we remove poorly determined basis vectors from the theory to improve the stability of the solution.

In order to get a statistical perspective of the problem, we will show how the TSVD estimator can be understood as a maximum a posteriori estimator for a statistical linear inverse problem with a certain type of prior assumption about the unknown parameter vector $\mathbf{x}$.

The basic idea behind singular value decomposition is to first represent the theory matrix of a statistical linear inverse problem

$$\mathbf{m} = \mathbf{A}\mathbf{x} + \boldsymbol{\xi} \tag{2.49}$$

using the singular value decomposition

$$\mathbf{A} = \mathbf{U}\mathbf{D}\mathbf{V}^{\text{H}}, \tag{2.50}$$

where $\mathbf{D} = \text{diag}\,(d_1, \ldots, d_n)$ contains the singular values. The matrices $\mathbf{U}$ and $\mathbf{V}$ contain the left and right singular vectors respectively. They are unitary, i.e., $\mathbf{U}^{\text{H}}\mathbf{U} = \mathbf{U}\mathbf{U}^{\text{H}} = \mathbf{I}$ and $\mathbf{V}^{\text{H}}\mathbf{V} = \mathbf{V}\mathbf{V}^{\text{H}} = \mathbf{I}$.

Using the singular value decomposition, the maximum likelihood matrix equations (Eq. 2.27) solution with the assumption that the errors are proper complex Gaussian with a diagonal covariance of the form $\text{E}\,\boldsymbol{\xi}\boldsymbol{\xi}^{\text{H}} = \mathbf{I}$ can now be written as

$$\hat{\mathbf{x}}_{\text{ML}} = (\mathbf{A}^{\text{H}}\mathbf{A})^{-1}\mathbf{A}^{\text{H}}\mathbf{m} = \mathbf{V}\mathbf{D}^{-1}\mathbf{U}^{\text{H}}\mathbf{m}. \tag{2.51}$$

However, the term $\mathbf{D}^{-1} = \text{diag}\left(d_1^{-1}, \ldots, d_n^{-1}\right)$ is unstable if it has elements that are very small, and in the worst case it cannot be formed if one of the elements is zero. The idea behind the truncated value method is to modify the singular value matrix $\mathbf{D}^{-1}$ and set $d_i^{-1} = 0$ for singular values that are below a certain threshold $|d_i| < c$

$$\mathbf{D}_c^{+} = \text{diag}\left(d_1^{-1}, \ldots, d_i^{-1}, 0, \ldots, 0\right) \tag{2.52}$$

and then solve the least squares equation with the modified singular value matrix $\mathbf{D}_c^+$

$$\hat{\mathbf{x}}_{\mathrm{TSVD}}(c) = \mathbf{V}\mathbf{D}_c^+\mathbf{U}^{\mathrm{H}}\mathbf{m}, \tag{2.53}$$

which is the TSVD estimator, where $c > 0 \subset \mathbb{R}$ is a suitably selected regularization parameter. In traditional inverse problems literature this parameter is selected by inspecting the so called *L-curve* [47], which results when plotting the singular values in decreasing order. This however is a fairly heuristic method.

The truncated singular value decomposition method can also be interpreted as a statistical linear inverse problem with a certain type of a prior assumption about the unknown $\mathbf{x}$. To show this, first consider again the familiar maximum a posteriori estimator for a statistical linear inverse problem with a prior assumption $\mathbf{x} \sim N(0, \mathbf{\Sigma_p})$, which is defined as

$$\hat{\mathbf{x}}_{\mathbf{MAP}} = (\mathbf{A}^{\mathrm{H}}\mathbf{\Sigma}^{-1}\mathbf{A} + \mathbf{\Sigma_p}^{-1})^{-1}\mathbf{A}^{\mathrm{H}}\mathbf{\Sigma}^{-1}\mathbf{m}. \tag{2.54}$$

We also assume that $\boldsymbol{\xi} \sim N(0, \mathbf{I})$. Note that $\mathbf{\Sigma}$ need not be $\mathbf{I}$, as we can whiten the noise by using a transformation of the form $\mathbf{\Lambda}^{-\frac{1}{2}}\mathbf{E}^{\mathrm{H}}$, where $\mathbf{E}\mathbf{\Lambda}\mathbf{E}^{\mathrm{H}}$ is the eigenvalue decomposition of $\mathbf{\Sigma}$.

We now *constructively* express the prior covariance matrix using an eigenvalue decomposition for conjugate symmetric matrices

$$\mathbf{\Sigma_p}^{-1} = \mathbf{V}\mathrm{diag}\,(s_1, ..., s_n)\,\mathbf{V}^{\mathrm{H}} = \mathbf{V}\mathbf{\Lambda}\mathbf{V}^{\mathrm{H}}, \tag{2.55}$$

where $\mathbf{V}$ is intentionally selected to be the matrix containing the right singular vectors of the singular value decomposition of $\mathbf{A}$. Using the guess, we can now get a very simple version of the maximum a posteriori estimator

$$\mathbf{x}_{\mathbf{MAP}} = \mathbf{V}(\mathbf{D}\mathbf{D}^{\mathrm{H}} + \mathbf{\Lambda})^{-1}\mathbf{D}^{\mathrm{H}}\mathbf{U}^{\mathrm{H}}\mathbf{m} = \mathbf{V}\mathbf{D}^{\dagger}\mathbf{U}^{\mathrm{H}}\mathbf{m}, \tag{2.56}$$

where

$$\mathbf{D}^{\dagger} = \mathrm{diag}\left(\frac{\overline{d_1}}{|d_1|^2 + s_1}, ..., \frac{\overline{d_n}}{|d_n|^2 + s_n}\right). \tag{2.57}$$

By comparing $\mathbf{D}^{\dagger}$ and $\mathbf{D}_c^+$, we observe that if

$$s_i = \begin{cases} 0 & \text{when} \quad |d_i| > c \\ \infty & \text{otherwise} \end{cases}, \tag{2.58}$$

then the truncated SVD estimator would coincide with the maximum a posteriori estimator. To examine what the prior assumption in this case is, let us examine the distribution of linearly transformed unknowns

$$\mathbf{y} = \mathbf{V}^{\mathrm{H}}\mathbf{x}, \tag{2.59}$$

which would have the following form of covariance matrix

$$\mathrm{E}\,\mathbf{y}\mathbf{y}^{\mathrm{H}} = \mathbf{\Lambda}^{-1} = \mathrm{diag}\left(s_1^{-1}, \ldots, s_n^{-1}\right), \tag{2.60}$$

which corresponds to a prior density of the form

$$p(\mathbf{y}) = \prod_i \frac{1}{\pi s_i^{-1}} \exp\left(-\frac{|y_i|^2}{s_i^{-1}}\right), \tag{2.61}$$

where y_i is an element of the transformed vector $\mathbf{y}$. This means that the truncated SVD estimator can be obtained when applying an improper prior in transformed coordinates $\mathbf{V}^{\mathrm{H}}\mathbf{x}$. While it is not possible to form a normalized density function for this type of a prior assumption, it is possible to inspect the unnormalized distribution, and it is possible to form a maximum a posteriori estimator, which has a maximum point corresponding to $\mathbf{x}_{\mathrm{MAP}}$. This prior has an infinite variance (flat prior) for the transformed coordinates with corresponding singular values that are larger than the threshold, and a Dirac delta shaped distribution centered at zero for transformed coordinates with corresponding singular values that are lower than the threshold.

This prior assumption also suggests a more general approach to truncated SVD that could be taken. Instead of setting the prior assumption $s_i = \infty$ when $|d_i| < c$, one could use a much smaller finite value, i.e., regularize less, and still maintain some of the information at transformed coordinate points that would be otherwise completely ignored.

2.7.6 Correlation estimator

There are many cases, especially in the traditional radar pulse decompression methodology, where unknown variables are estimated by multiplying the measurements with the conjugate transpose of the theory matrix. In a certain sense, this can be understood as correlating the measurements with the theory. The advantages of this method are two-fold: it is stable and it is also very efficient to implement numerically. However, as with Tikhonov regularization and truncated SVD, the method also in most cases results in bias. In this section we will show how the correlation estimator can be understood as a maximum a posteriori estimator with a certain type of prior assumption about the unknown parameter vector $\mathbf{x}$.

Consider a linear measurement equation of the form

$$\mathbf{m} = \mathbf{A}\mathbf{x} + \boldsymbol{\xi}. \tag{2.62}$$

Assuming $\boldsymbol{\xi}$ is zero mean proper Gaussian random vector with covariance

$$\mathrm{E}\,\boldsymbol{\xi}\boldsymbol{\xi}^{\mathrm{H}} = \mathbf{\Sigma} = \sigma^2\mathbf{I} \tag{2.63}$$

the maximum likelihood estimator is

$$\mathbf{x}_{\mathbf{ML}} = (\mathbf{A}^{\mathrm{H}}\mathbf{A})^{-1}\mathbf{A}^{\mathrm{H}}\mathbf{m}. \tag{2.64}$$

Now if the theory is orthogonal

$$\mathbf{A}^{\mathrm{H}}\mathbf{A} = \alpha\mathbf{I} \tag{2.65}$$

with $\alpha \in \mathbb{R}$, the maximum likelihood estimator can be simplified to

$$\mathbf{x}_{\mathbf{ML}} = \alpha^{-1}\mathbf{A}^{\mathrm{H}}\mathbf{m}, \tag{2.66}$$

which is basically correlating the measurements with the theory. There is no need to calculate the covariance matrix $(\mathbf{A}^{\mathrm{H}}\mathbf{A})^{-1}$, which is a huge advantage numerically. There are several practical examples where this is true: deconvolution using a perfect radar transmission code, or a discrete Fourier transform model.

Now if $\mathbf{A}^{\mathrm{H}}\mathbf{A} \neq \alpha\mathbf{I}$, but one still insists on estimating the unknown parameters using the same efficient formula

$$\mathbf{x}_{\mathbf{CE}} = \alpha^{-1}\mathbf{A}^{\mathrm{H}}\mathbf{m}, \tag{2.67}$$

the resulting estimator is biased and the result does not correspond to a maximum likelihood estimator, and α is more of a scaling factor. We will call this approach the *correlation estimator*. Spectral estimation using the *Lomb-Scargle* periodogram [48] is performed in this way. The matched filter [49] approach to deconvolving radar transmission envelopes is another example of a situation where this approximation is used (either intentionally, or by coincindence).

The correlation estimator $\mathbf{x}_{\mathbf{CE}}$ can also be understood as the maximum a posteriori estimator of a statistical linear inverse problem with a prior assumption that the unknown $\mathbf{x}$ is a proper Gaussian random variable $\mathbf{x}$. To show this, consider the singular value decomposition of the theory matrix

$$\mathbf{A} = \mathbf{U}\mathbf{D}\mathbf{V}^{\mathrm{H}}, \tag{2.68}$$

where $\mathbf{D} = \mathrm{diag}\,(d_1, ..., d_n)$ and $d_i \in \mathbb{C}$. We then assume that there is some "magic" prior $\mathbf{\Sigma_p}$ that results in a maximum a posteriori solution that is equivalent to the correlation estimator. Writing this prior using an eigenvalue decomposition for symmetric matrices

$$\mathbf{\Sigma_{prior}}^{-1} = \mathbf{V}\mathrm{diag}\,(s_1, ..., s_n)\,\mathbf{V}^{\mathrm{H}} = \mathbf{V}\mathbf{\Lambda}\mathbf{V}^{\mathrm{H}} \tag{2.69}$$

using the same orthonormal matrix $\mathbf{V}$ as in the singular value decomposition of $\mathbf{A}$, we get the following form of the maximum a posteriori estimator

$$\mathbf{x}_{\mathbf{MAP}} = \mathbf{V}(\mathbf{D}\mathbf{D}^{\mathrm{H}} + \sigma^2\mathbf{\Lambda})^{-1}\mathbf{D}^{\mathrm{H}}\mathbf{U}^{\mathrm{H}}\mathbf{m}. \tag{2.70}$$

Now, if $\mathbf{D}\mathbf{D}^{\mathrm{H}} + \sigma^2\mathbf{\Lambda} = \alpha\mathbf{I}$, then in fact

$$\mathbf{x}_{\mathbf{MAP}} = \alpha^{-1}\mathbf{A}^{\mathrm{H}}\mathbf{m}, \tag{2.71}$$

which has the same form as the correlation estimator $\mathbf{x}_{\mathrm{CE}}$, and the underlying "hidden" prior is

$$\mathbf{\Sigma}_{\mathbf{prior}} = \mathbf{V}\mathrm{diag}\left(\frac{\sigma^2}{\alpha - |d_1|^2}, \ldots, \frac{\sigma^2}{\alpha - |d_n|^2}\right)\mathbf{V}^{\mathrm{H}}, \tag{2.72}$$

as long as $\alpha \geq |d_i|^2$ for all squares of singular values. If this requirement is not satisfied, there is no underlying covariance assumption, because a covariance matrix has to have non-negative real valued eigenvalues. In this case, the resulting estimator does not have an interpretation of a prior covariance assumption. In the case where $\alpha = |d_i|^2$ the prior distribution is improper, as it has an infinitely wide variance prior distribution on this axis. This corresponds to a flat or non-informative prior in the corresponding axis. Still, it is possible to, e.g., study the bias of the estimator, which is

$$\mathbf{b} = \mathbf{x} - \alpha^{-1}\mathbf{A}^{\mathrm{H}}\mathbf{x}. \tag{2.73}$$

In the case of stationary radar targets, the bias is often studied for a radar target consisting of a single point $\mathbf{x} = (0, \ldots, 0, 1, 0, \ldots, 0)^{\mathrm{T}}$. The artefacts caused by the estimator bias are called range sidelobes in this case.

When the theory is sufficiently orthogonal ($\mathbf{A}^{\mathrm{H}}\mathbf{A} \approx \alpha\mathbf{I}$), the correlation estimator is a good first order approximation of the maximum likelihood, or a weakly regularized maximum a posteriori estimate. But it is important to be aware of what type of a prior assumption or bias is associated with this estimator.

2.8 Toeplitz models

When a matrix has constant values along its diagonals $A_{i,j} = A_{i+1,j+1}$, it is called a Toeplitz operator [25, 26]. This type of an operator is nearly ubiquitous in radar measurement theory. For example, consider the following discretized convolution equation

$$m_t = \sum_r \sigma_r \epsilon_{t-r} + \xi_t, \tag{2.74}$$

which can be used to describe backscatter from a range spread coherent target. Here the unknown convolved variables are represented with σ_r, the convolution kernel or the radar transmission envelope is ϵ_t, and the last term $\xi_t \in \mathbb{C}$ is the measurement error. This equation can be described with a Toeplitz form linear theory matrix:

$$\mathbf{m} = \mathbf{A}\mathbf{x} + \boldsymbol{\xi}, \tag{2.75}$$

or

$$\begin{bmatrix} m_1 \\ m_2 \\ m_3 \\ \vdots \\ m_{m+n-1} \end{bmatrix} = \begin{bmatrix} \epsilon_1 & 0 & \dots & 0 & 0 \\ \epsilon_2 & \epsilon_1 & \dots & \vdots & \vdots \\ \epsilon_3 & \epsilon_2 & \dots & 0 & 0 \\ \vdots & \epsilon_3 & \dots & \epsilon_1 & 0 \\ \epsilon_{m-1} & \vdots & \dots & \epsilon_2 & \epsilon_1 \\ \epsilon_m & \epsilon_{m-1} & \vdots & \vdots & \epsilon_2 \\ 0 & \epsilon_m & \dots & \epsilon_{m-2} & \vdots \\ 0 & 0 & \dots & \epsilon_{m-1} & \epsilon_{m-2} \\ \vdots & \vdots & \vdots & \epsilon_m & \epsilon_{m-1} \\ 0 & 0 & 0 & \dots & \epsilon_m \end{bmatrix} \begin{bmatrix} \sigma_1 \\ \sigma_2 \\ \sigma_3 \\ \vdots \\ \sigma_m \end{bmatrix} + \begin{bmatrix} \xi_1 \\ \xi_2 \\ \xi_3 \\ \vdots \\ \xi_{m+n-1} \end{bmatrix} \tag{2.76}$$

In addition to range spread coherent targets, also range and Doppler overspread targets can be modeled with a convolution model [20, 21].

Toeplitz matrices are also important as measurement errors are almost always characterized with a covariance matrix of Toeplitz form. In addition to this, incoherent scatter from a volume filled with independent scatterers can be assumed to be a stochastic process characterized by a covariance matrix of this form [20, 4, 22]. Stochastic processes characterized by this type of a covariance matrix are called weakly stationary, or wide sense stationary processes [50].

Toeplitz matrices can also be used to represent arbitrarily high dimensional convolutions, so the same considerations also apply for two dimensional convolutions that are commonly encountered in image processing.

2.9 Circulant model

Circulant matrices are a special class of Toeplitz matrices that have both numerical and analytic properties that make them useful. This section will give some of the important results described in more detail in [25], or even more detail in [26] or [51].

Circulant matrices $\mathbf{C} \in \mathbb{C}^{n \times n}$ have the property that

$$C_{k,j} = c_{j-k} \bmod n, \tag{2.77}$$

i.e., each row is cyclically shifted by one compared to the previous row

$$\mathbf{C} = \begin{bmatrix} c_0 & c_{n-1} & \dots & c_2 & c_1 \\ c_1 & c_0 & c_{n-1} & & c_2 \\ \vdots & c_1 & c_0 & \ddots & \vdots \\ c_{n-2} & & \ddots & \ddots & c_{n-1} \\ c_{n-1} & c_{n-2} & \dots & c_1 & c_0 \end{bmatrix}. \tag{2.78}$$

Furthermore, all circulant matrices have an eigenvalue decomposition of the form

$$\mathbf{C} = \mathbf{U}\mathbf{\Psi}\mathbf{U}^{\mathrm{H}}, \tag{2.79}$$

where $\mathbf{U}$ is a discrete Fourier transform matrix with $\omega_n = e^{-2\pi i/n}$

$$\mathbf{U} = \frac{1}{\sqrt{n}} \begin{bmatrix} \omega_n^{0\cdot 0} & \omega_n^{0\cdot 1} & \dots & \omega_n^{0\cdot(n-1)} \\ \omega_n^{1\cdot 0} & \omega_n^{1\cdot 1} & \dots & \omega_n^{1\cdot(n-1)} \\ \vdots & \vdots & \ddots & \vdots \\ \omega_n^{(n-1)\cdot 0} & \omega_n^{(n-1)\cdot 1} & \dots & \omega_n^{(n-1)\cdot(n-1)} \end{bmatrix} \tag{2.80}$$

and $\mathbf{\Psi} = \operatorname{diag}(\psi_1, \dots, \psi_n)$ is a diagonal matrix containing the discrete Fourier transform of the first row of the circulant matrix $\mathbf{C}$

$$\psi_m = \sum_{k=0}^{n-1} c_k e^{-2\pi i m k/n}. \tag{2.81}$$

The matrix $\mathbf{U}$ is unitary, i.e., $\mathbf{U}\mathbf{U}^{\mathrm{H}} = \mathbf{U}^{\mathrm{H}}\mathbf{U} = \mathbf{I}$. This has several implications:

1. The matrix multiplication of two circulant matrices commutes $\mathbf{C}\mathbf{D} = \mathbf{D}\mathbf{C}$. If $\mathbf{C} = \mathbf{U}\mathbf{\Psi}_{\mathbf{c}}\mathbf{U}^{\mathrm{H}}$ and $\mathbf{D} = \mathbf{U}\mathbf{\Psi}_{\mathbf{d}}\mathbf{U}^{\mathrm{H}}$, then

$$\mathbf{C}\mathbf{D} = \mathbf{U}\mathbf{\Psi}_{\mathbf{c}}\mathbf{U}^{\mathrm{H}}\mathbf{U}\mathbf{\Psi}_{\mathbf{d}}\mathbf{U}^{\mathrm{H}} = \mathbf{U}\mathbf{\Psi}_{\mathbf{c}}\mathbf{\Psi}_{\mathbf{d}}\mathbf{U}^{\mathrm{H}}, \tag{2.82}$$

   where $\mathbf{\Psi}_{\mathbf{c}}\mathbf{\Psi}_{\mathbf{d}}$ is the product of two diagonal matrices, which commutes and is a diagonal matrix, and thus $\mathbf{C}\mathbf{D}$ is also a circulant matrix.
2. The sum of two circulant matrices is a circular matrix of the form

$$\mathbf{C} + \mathbf{D} = \mathbf{U}(\mathbf{\Psi}_{\mathbf{c}} + \mathbf{\Psi}_{\mathbf{d}})\mathbf{U}^{\mathrm{H}}. \tag{2.83}$$

3. The inverse of a circular matrix is

$$\mathbf{C}^{-1} = \mathbf{U}{\mathbf{\Psi}_{\mathbf{c}}}^{-1}\mathbf{U}^{\mathrm{H}}, \tag{2.84}$$

   and $\mathbf{C}$ is non-singular if $\psi_m \neq 0$ for all m.

These are essentially the properties of discrete Fourier transformed sequences, which is not a coincidence, as $\mathbf{U}$ and $\mathbf{U}^{\mathrm{H}}$ correspond to the forward and inverse discrete Fourier transform operators.

2.9.1 Additivity of spectral information

Consider a block matrix that consists of stacked circulant matrices

$$\mathbf{C} = \begin{bmatrix} \mathbf{C}_1 \\ \vdots \\ \mathbf{C}_n \end{bmatrix} = \begin{bmatrix} \mathbf{U}\boldsymbol{\Psi}_1\mathbf{U}^{\mathrm{H}} \\ \vdots \\ \mathbf{U}\boldsymbol{\Psi}_n\mathbf{U}^{\mathrm{H}} \end{bmatrix}, \tag{2.85}$$

where $\mathbf{C}_i \in \mathbb{C}^{N\times N}$. These types of stacked circulant matrices are often encountered in radar models where the unknown radar target is constant over multiple radar transmission pulses, i.e., the convolution measurement is repeated multiple times and the unknowns do not change during this time. The statistical analysis of such models requires operations of the form $\mathbf{C}^{\mathrm{H}}\mathbf{C}$ and $\mathbf{C}^{\mathrm{H}}\mathbf{m}$, where $\mathbf{m} \in \mathbb{C}^{Nn}$ is a vector. Because of the diagonalization property of circulant matrices, these turn out to have relatively simple solutions of the form

$$\mathbf{C}^{\mathrm{H}}\mathbf{C} = \mathbf{U}\left(\sum_{i=1}^{n} |\boldsymbol{\Psi}_i|^2\right)\mathbf{U}^{\mathrm{H}} \tag{2.86}$$

and

$$\mathbf{C}^{\mathrm{H}}\mathbf{m} = \mathbf{U}\left(\sum_{i=1}^{n} \overline{\boldsymbol{\Psi}_i}\mathbf{M}_i\right) \tag{2.87}$$

where $\boldsymbol{\Psi}_i$ is a diagonal matrix containing the discrete Fourier transform of the first row of $\mathbf{C}_i$ and $\mathbf{M}_i$ is a diagonal matrix containing the discrete Fourier transform of the ith block of vector $\mathbf{m}$ of size N.

It should be noted that similar spectral additivity also applies to arbitrary repeated measurements where the singular value decomposition of the repeated measurement has the same left and right hand vectors.

2.9.2 Kolmogorov-Wiener filtering

One important application for circulant matrices is in filtering. Consider first a standard statistical linear inverse problem

$$\mathbf{m} = \mathbf{A}\mathbf{x} + \boldsymbol{\xi} \tag{2.88}$$

with a Toeplitz form theory matrix $\mathbf{A} = \mathbf{U}\hat{\mathbf{A}}\mathbf{U}^{\mathrm{H}}$ and error covariance matrix $\boldsymbol{\xi} = \mathbf{U}\hat{\boldsymbol{\Sigma}}\mathbf{U}^{\mathrm{H}}$. Here $\hat{\mathbf{A}} = \operatorname{diag}(\hat{a}_1, \ldots, \hat{a}_n)$ is the discrete Fourier transform of the first row of the theory matrix $\mathbf{A}$ and $\hat{\boldsymbol{\Sigma}} = \operatorname{diag}(\hat{\sigma}_1, \ldots, \hat{\sigma}_n)$ is

the Fourier transform of the first row of the error covariance matrix $\mathbf{\Sigma}$. In general, in this section all matrices marked with a hat will be diagonal matrices with the frequency domain representation of the circulant matrix on the diagonal.

Because all of the matrices involved are of Toeplitz form, the maximum likelihood can be reduced to a very simple form

$$\begin{aligned}
\mathbf{x_{ML}} &= (\mathbf{A\Sigma}^{-1}\mathbf{A})^{-1}\mathbf{A}^{\mathrm{H}}\mathbf{\Sigma}^{-1}\mathbf{m} && (2.89)\\
&= (\mathbf{U\hat{A}}^{\mathrm{H}}\mathbf{U}^{\mathrm{H}}\mathbf{U\hat{\Sigma}}^{-1}\mathbf{U}^{\mathrm{H}}\mathbf{U\hat{A}U}^{\mathrm{H}})^{-1}\mathbf{U\hat{A}}^{\mathrm{H}}\mathbf{U}^{\mathrm{H}}\mathbf{U\hat{\Sigma}}^{-1}\mathbf{U}^{\mathrm{H}}\mathbf{m} && (2.90)\\
&= \mathbf{U\hat{A}}^{-1}\mathbf{U}^{\mathrm{H}}\mathbf{m} && (2.91)\\
\mathbf{U}^{\mathrm{H}}\mathbf{x_{ML}} &= \mathbf{\hat{A}}^{-1}\mathbf{U}^{\mathrm{H}}\mathbf{m} && (2.92)
\end{aligned}$$

This essentially means that the maximum likelihood estimator is division in frequency domain. It is important to notice that the only matrix operation involved is multiplication with $\mathbf{U}^{\mathrm{H}}$ and $\mathbf{U}$, and these correspond to the forward and inverse discrete Fourier transforms. This type of a maximum likelihood estimator of a convolution problem is called the *inverse filter*.

The error covariance of the inverse filter estimator is a circulant matrix of the form

$$\mathbf{\Sigma_{post}} = (\mathbf{A}^{\mathrm{H}}\mathbf{\Sigma}^{-1}\mathbf{A})^{-1} = \mathbf{U\hat{\Sigma}}(\mathbf{\hat{A}\hat{A}}^{\mathrm{H}})^{-1}\mathbf{U}^{\mathrm{H}}. \quad (2.93)$$

Now if one were to assume a priori that the unknown x is also a normal random variable with a circulant covariance matrix

$$\mathbf{\Sigma}_{\mathrm{prior}} = \mathbf{U\hat{\Sigma}_{prior}}\mathbf{U}^{\mathrm{H}}, \quad (2.94)$$

then our MAP estimator can be obtained as

$$\begin{aligned}
\mathbf{x_{MAP}} &= (\mathbf{A}^{\mathrm{H}}\mathbf{\Sigma}^{-1}\mathbf{A} + \mathbf{\Sigma}_{\mathrm{prior}}^{-1})^{-1}\mathbf{A}^{\mathrm{H}}\mathbf{\Sigma}^{-1}\mathbf{m} && (2.95)\\
&= \mathbf{U}((\mathbf{\hat{A}}^{\mathrm{H}}\mathbf{\hat{A}} + \mathbf{\hat{\Sigma}\hat{\Sigma}}_{\mathrm{prior}}^{-1})^{-1}\mathbf{\hat{A}}^{\mathrm{H}})\mathbf{U}^{\mathrm{H}}\mathbf{m}, && (2.96)
\end{aligned}$$

where the central term

$$(\mathbf{\hat{A}}^{\mathrm{H}}\mathbf{\hat{A}} + \mathbf{\hat{\Sigma}\hat{\Sigma}}_{\mathrm{prior}}^{-1})^{-1}\mathbf{\hat{A}}^{\mathrm{H}} \quad (2.97)$$

contains only diagonal matrices containing the freqeuency domain representation of the theory and covariance matrices.

This type of MAP estimators were for the first time introduced by Kolmogorov [27] and Wiener [52], and this solution is typically referred to as a *Kolmogorov-Wiener filter*. The continuous frequency domain estimator is typically represented in the following form

$$\hat{x}_{\mathrm{MAP}}(f) = \frac{\overline{\hat{a}}(f)\hat{m}(f)}{|\hat{a}(f)|^2 + \frac{\hat{\sigma}^2(f)}{\hat{\sigma}_p^2(f)}}, \quad (2.98)$$

where all of the Toeplitz operators and unknowns are represented in their Fourier domain form. This estimator also corresponds to Tikhonov regularization for Toeplitz formed theory and covariance matrices.

3. Numerical methods

All radar measurement analysis problems can be seen as statistical problems that involve inspection of the *a posteriori* probability density function $p(\mathbf{x}|\mathbf{m})$ of the model parameters, given the measurements. Due to the data-intensive nature of radar measurements, computational performance of the numerical methods used to inspect $p(\mathbf{x}|\mathbf{m})$ plays an important role.

In this chapter, we will discuss several important numerical methods that can be applied to radar measurement problems. We will only give an overview of the methods and try to give an idea of what their strengths and weaknesses are. We won't go into very specific details or underlying proofs of these methods, since they can be found in the supplied references.

3.1 Fast Fourier Transform

Perhaps the single most important numerical algorithm for radar data analysis is the Fast Fourier Transform (FFT) [53]. It is an efficient algorithm for computing the discrete Fourier transform

$$\hat{x}_k = \sum_{t=0}^{N-1} x_t e^{-\frac{2\pi i}{N} kt} \qquad k = 0, \ldots, N-1, \tag{3.1}$$

and its inverse

$$x_t = \frac{1}{N} \sum_{k=0}^{N-1} \hat{x}_k e^{\frac{2\pi i}{N} kt} \qquad t = 0, \ldots, N-1. \tag{3.2}$$

Here $\hat{x}_k$ is the frequency domain representation of the discrete time signal x_t.

The main advantage of FFT is that it is has a very slowly growing computational complexity. Complex-valued vectors of length N can be forward or inverse transformed in $5N \log_2 N$ floating point operations [54] instead

of the $\mathcal{O}(N^2)$ complexity of a more naive discrete Fourier transform implementation. Because of this, a common optimization recipe for numerical algorithms is to attempt to utilize the FFT in some way.

The different applications of FFT are too numerous to exhaustively list here. On pages 2 and 3 in Brigham [55] there are 78 different topics in physics, mathematics and engineering where FFT can be applied, but this is just the tip of the iceberg. In the case of signal processing and statistical analysis of radar measurements, the method can be used to e.g., implement an efficient convolution operation, perform spectral analysis, perform beamforming, or to approximate Toeplitz-formed matrix operations. In addition to calculating a discrete Fourier transform, FFT can also be used to approximate many related transforms such as the discrete Fourier transform with non-uniformly spaced times and frequencies in arbitrary dimensions [56].

The FFT algorithm has been used ubiquitously in the underlying work for this thesis. In Section 5.3 we will show how it can also be used to perform a grid search for the Doppler shift parameter of a moving point-like target. In Section 5.6.1 we will show how a wide band linear chirped transmission target backscatter maximum likelihood estimator can be obtained with FFT. The algorithm can also be used to efficiently calculate the variance of radar target estimates [57, 4, 12].

3.2 Linear problems

Linear statistical problems are ones that can be described using the following type of matrix equation

$$\mathbf{m} = \mathbf{A}\mathbf{x} + \boldsymbol{\xi}, \tag{3.3}$$

where $\mathbf{m}$ and $\mathbf{x}$ are the measurement and model parameters vectors. The theory matrix $\mathbf{A}$ relates the model parameters with the measurements. The measurement errors $\boldsymbol{\xi}$ are often assumed to be normal random variables $\boldsymbol{\xi} \sim N(0, \boldsymbol{\Sigma})$.

While the matrix equations given in Section 2.7 can be directly used to solve these types of problems, they are not necessarily optimal in many practical cases. Often the theory matrix has some sort of properties that can be used to efficiently compute the maximum a posteriori estimator, and possibly the posteriori covariance matrix too. For example, if the linear theory matrix is Toeplitz-formed, it is possible to diagonalize the

theory using FFT and transform the problem into vector operations, reducing the complexity from $\mathcal{O}(N^3)$ to $\mathcal{O}(N \log N)$ with very little or no approximation errors.

When the theory matrix has a lot of rows and relatively small amount of columns (parameters), one efficient algorithm for estimating the maximum a posteriori parameters is the QR decomposition method [58]. The method also has the advantage that it can be calculated using a small number of theory matrix rows at a time if necessary, which reduces the amount of required run-time memory. Parameters can also be marginalized out on the fly, which makes the method applicable also to Kalman filtering type problems [43].

If the theory matrices are very large, but relatively sparse, one can resort to iterative methods to solve the problem [59]. In this case, there is only need to repeatedly evaluate $\mathbf{Au}$ or $\mathbf{A}^{\mathrm{H}}\mathbf{v}$ in each iteration, where $\mathbf{u}$ and $\mathbf{v}$ are arbitrary vectors. These operations are typically relatively efficient if the theory matrix is sparse.

If the theory matrix is sufficiently close to orthogonal, the correlation estimator $\hat{\mathbf{x}} = c^{-1}\mathbf{A}^{\mathrm{H}}\mathbf{m}$ discussed in Section 2.7.6 is relatively efficient computationally. This type of an approach is in fact relatively popular in radar signal processing, and it is essentially what a typical radar *correlator* does, although this matrix operation is typically implemented using FFT. There is no need to calculate the posteriori covariance matrix, which typically is much more dense than the theory matrix. However, one should be aware of the bias introduced if the theory is not close to orthogonal, $\mathbf{A}^{\mathrm{H}}\mathbf{A} \neq c\mathbf{I}$. We will discuss the resulting bias more in Section 5.5.2.

3.3 Non-linear inverse problems

In some cases, typically when fitting a physical theory to radar measurements, the measurement model

$$\mathbf{m} = f(\mathbf{x}; \boldsymbol{\xi}) \tag{3.4}$$

cannot be represented in linear form. In some cases it is possible to linearize the problem and use methodology from linear inverse problems to study the posterior probability density $p(\mathbf{x}|\mathbf{m})$. Another possibility is to use some other means to study the underlying probability distribution $p(\mathbf{x}|\mathbf{m})$, e.g., by using an optimization algorithm to search for the peak

of the distribution, or by using Monte-Carlo methods to estimate the full shape of the distribution.

In radar measurements, non-linear problems are typically encountered when fitting a physical theory to the measurements. A plasma parameter fit to the estimated incoherent scatter autocorrelation function is one example of such a problem.

3.3.1 Linearized model

Assume that our model is described by an analytic complex valued function $f : \mathbb{C}^k \to \mathbb{C}^n$ and the measurement equation is of the form

$$\mathbf{m} = f(\mathbf{x}) + \boldsymbol{\xi}, \tag{3.5}$$

where $\xi \sim N(0, \mathbf{\Sigma})$. It is possible to approximate the equation by linearizing f using a first order Taylor series expansion around some point $\mathbf{x_0}$

$$f(\mathbf{x}) \approx f(\mathbf{x_0}) + \mathbf{J}\mathbf{x}, \tag{3.6}$$

where $\mathbf{J}_{i,j} = \frac{\partial f_i}{\partial \mathbf{x}_j}$ is the Jacobian of $f(\mathbf{x})$ evaluated at $\mathbf{x}_0$. This results in the following linear measurement equation

$$\mathbf{m} - f(\mathbf{x_0}) = \mathbf{J}\mathbf{x} + \boldsymbol{\xi}, \tag{3.7}$$

which has the following maximum likelihood solution

$$\hat{\mathbf{x}} = (\mathbf{J}^{\mathrm{H}}\mathbf{\Sigma}^{-1}\mathbf{J})^{-1}\mathbf{J}^{\mathrm{H}}\mathbf{\Sigma}^{-1}(\mathbf{m} - f(\mathbf{x_0})). \tag{3.8}$$

This however only applies around the point $\mathbf{x}_0$ and therefore $\hat{\mathbf{x}}$ is not necessarily the true maximum likelihood estimator. In order to obtain an improved estimate, we can iteratively solve the problem around the previous estimate:

$$\hat{\mathbf{x}}_{\mathbf{n+1}} = \left(\mathbf{J_n}^{\mathrm{H}}\mathbf{\Sigma}^{-1}\mathbf{J_n}\right)^{-1}\mathbf{J_n}^{\mathrm{H}}\mathbf{\Sigma}^{-1}(\mathbf{m} - f(\hat{\mathbf{x}}_\mathbf{n})), \tag{3.9}$$

where $\mathbf{J}_n$ is the Jacobian of $f(\mathbf{x})$ at $\hat{\mathbf{x}}_\mathbf{n}$. This algorithm is known as the Gauss-Newton algorithm. A variation of this is the Levenberg-Marquardt algorithm [60]

$$\hat{\mathbf{x}}_{\mathbf{n+1}} = \left(\mathbf{J_n}^{\mathrm{H}}\mathbf{\Sigma}^{-1}\mathbf{J_n} + \lambda_n \mathrm{diag}\left(\mathbf{J_n}^{\mathrm{H}}\mathbf{\Sigma}^{-1}\mathbf{J_n}\right)\right)^{-1}\mathbf{J_n}^{\mathrm{H}}\mathbf{\Sigma}^{-1}(\mathbf{m} - f(\hat{\mathbf{x}}_\mathbf{n})), \tag{3.10}$$

where $\lambda_n \in \mathbb{R}^+$ is a regularization parameter used to control the convergence of the iteration. Notice that this also corresponds to a prior covariance assumption of the unknown parameters $\mathbf{x}$. The posteriori errors can also be estimated in a similar way

$$\mathbf{\Sigma_{post}} = \left(\mathbf{J_n}^{\mathrm{H}}\mathbf{\Sigma}^{-1}\mathbf{J_n}\right)^{-1}. \tag{3.11}$$

It should be noted that the error covariance matrix estimated in this way is not necessarily a very good one if the true underlying probability distribution is not close to a unimodal Gaussian distribution. Also, it is possible that the iteration procedure converges into a local maximum of the possibly multimodal probability density function, resulting in incorrect MAP or ML estimators.

3.3.2 Optimization algorithms

Optimization algorithms are algorithms that attempt to maximize or minimize the value of a function. They can readily be applied to maximize the posteriori density $p(\mathbf{x}|\mathbf{m})$ in order to find a maximum a posteriori estimate. In fact, the iteration given in the previous section is one such algorithm. Other examples are *simulated annealing* [61], the *Nelder-Mead* algorithm [62], and *differential evolution* [63].

One of the largest problems when applying optimization algorithms to non-linear models with multimodal distributions is that they can converge to a local maximum of the probability distribution. Many of the algorithms are designed to avoid this, but unless the algorithms are repeated infinitely many times at different random initial positions, there is still a possibility that this can happen.

Selecting a good initial approximation is one way to minimize the risk of converging to a local minimum. However, this requires good knowledge of what the *unknown* parameters are, which is not always the case. Another possibility is to combine a simple grid search with some optimization algorithm. Inspecting the residuals $\|f(\hat{\mathbf{x}}_{\mathrm{MAP}}) - \mathbf{m}\|^2$ can also give some idea of how good the fit is. However, there is no guaranteed method to completely avoid converging to a local minimum in practice. Most of the radar measurement problems that involve fitting a non-linear theory into measurements are inherently multimodal, with a large number of local maxima of the probability density.

3.3.3 Markov chain Monte-Carlo

Markov chain Monte-Carlo (MCMC) [64] methods can be used to randomly draw samples $\mathbf{x}^{(i)}$ from an arbitrary density $\pi(\mathbf{x})$. This density is typically either the likelihood function $p(\mathbf{m}|\mathbf{x})$ or more commonly the posteriori probability density $p(\mathbf{x}|\mathbf{m})$. These samples can then be used to estimate marginal probability densities using histograms, or to produce

conditional mean estimates by sample averaging

$$\hat{\mathbf{x}}_{\mathrm{CM}} = \int \mathbf{x} p(\mathbf{x}|\mathbf{m}) d\mathbf{x} \approx \frac{1}{N} \sum_{i=1}^{N} \mathbf{x}^{(i)}. \tag{3.12}$$

The method can also be used as an optimization algorithm, to search for the peak of the distribution.

Perhaps the most common form of MCMC is the Metropolis-Hastings sampling method [65], which is a very general algorithm that allows much freedom when implementing it [66]. Improvements, such as the Delayed Rejection Adaptive Metropolis-Hastings (DRAM) [67] method allow the study of more complicated distribution shapes with higher sampling efficiencies. A variant of the algorithm also exists for sampling from multiple different models [68, 69], which can be used from model comparison.

The only necessary prequisite for the Metropolis-Hastings algorithm is that one can evaluate the density $c\pi(\mathbf{x})$ up to some constant $c \in \mathbb{R}$. This constant is canceled out in each step of the algorithm, so it doesn't need to be known. One also needs define a proposal distribution $q(\mathbf{x}, \mathbf{x}')$, which provides proposal samples $\mathbf{x}'$ when our current sample in the chain is $\mathbf{x}$. The choice of this function can be fairly arbitrary. One fairly commonly used proposal distribution is the *random walk* distribution $q(\mathbf{x}, \mathbf{x}') = q(\mathbf{x} - \mathbf{x}')$, where $\mathbf{x}' = \mathbf{x} + \boldsymbol{\xi}$, and $\boldsymbol{\xi}$ is a small random increment to $\mathbf{x}$.

Finally, the probability that we accept the proposed jump from $\mathbf{x}$ to $\mathbf{x}'$ is defined as

$$\alpha(\mathbf{x}, \mathbf{x}') = \min\left(\frac{\pi(\mathbf{x}')q(\mathbf{x}', \mathbf{x})}{\pi(\mathbf{x})q(\mathbf{x}, \mathbf{x}')}, 1\right). \tag{3.13}$$

Using these definitions, the algorithm can then be summarized as follows:

- Initialize $\mathbf{x}^{(j)}$ to some arbitrary value.
- Repeat for $j \in \{2, \ldots, N\}$.
- Generate $\mathbf{x}'$ from the proposal distribution $q(\mathbf{x}^{(j)}, \cdot)$.
- Generate u from uniform distribution $\mathcal{U}(0, 1)$.
- If $u < \alpha(\mathbf{x}^{(j)}, \mathbf{x}')$, then set $\mathbf{x}^{(j+1)} = \mathbf{x}'$.
- Else set $\mathbf{x}^{(j+1)} = \mathbf{x}^{(j)}$.
- The samples $\{\mathbf{x}^{(1)}, \ldots, \mathbf{x}^{(N)}\}$ are samples from $\pi(\mathbf{x})$. Typically a fraction

of the samples in the beginning are ignored.

Most of the difficulties with the method arise from finding a proposal distribution $q(\mathbf{x}, \mathbf{x}')$ that results in an efficient sampling from the distribution $\pi(\mathbf{x})$. Another difficulty with the MCMC methods is that they are not as fast as optimization methods.

The MCMC method has been used for example in [19] to study the full distribution of plasma parameters.

4. High Power Large Aperture Radars

4.1 History

After the theoretical prediction of the existence of electromagnetic waves by James Clerk Maxwell in 1864, Heinrich Hertz was the first to confirm them in 1887. He also noticed experimentally that electromagnetic waves are reflected from certain materials [70].

In 1904, Christian Hülsmeyer was the first to successfully build a device (called "Telemobiloskop") for detecting ships using a simple spark gap transmitter. The system could detect ships at distances of up to 3 km. Hülsmeyer also designed a system for ranging targets using triangulation and the intensity of the return. Despite successful public demonstrations of the Telemobiloskop, Hülsmeyer failed to attract commercial interest and his invention was forgotten.

In 1925, Appleton and Barnett [71] used the interference between the ground wave and the ionospheric reflection of BBC transmissions to prove the existence of an ionized layer in Earth's atmosphere, which had been hypothesized earlier by Lodge, Kennelly and Heaviside [72]. In the next year, Breit and Tuve [73] used the time of flight of pulsed 4.3 MHz radio transmissions to infer the reflection altitude of the conducting layer in the ionosphere. Nowadays, this type of radar soundings are routinely performed by instruments called ionosondes all around the world. Instead of using a single frequency, these instruments typically cover a wide band of different frequencies between 0 and 30 MHz in order to determine the electron density profile of the ionosphere. We will discuss an ionospheric chirp sounding model in Section 5.6.1.

Radar devices were also actively developed for military purposes since the late 1920s and all major countries utilized radar systems in the second

world war, mainly for aircraft surveillance. The acronym RADAR itself originates from the name of a US military program and comes from the words Radio Detection And Ranging.

Today radar and sonar instruments are widespread and part of everyday life. They are used for everything between mapping the rings of Saturn [74] to measuring the content of the soil beneath our feet [75]. For a broad overview on different uses of radars, refer to [76] or [77].

4.2 Operating principles

In general, a radar system can be thought of as a collection of arbitrarily positioned transmitters $\epsilon_i(t)$ and receivers $m_i(t)$ which can modify and record the electromagnetic field with the intention of gaining information about the medium Ω in which the electromagnetic waves propagate. Examples of several different types of radar systems are shown in Fig. 4.1.

A radar with shared transmitter and receiver antenna is perhaps the most common type of radar. Most radars also have a narrow beam, which makes it possible to measure a small region of space at one moment of time. The most common radar measurement consists of repeated pulsed transmissions, which scatter from the medium, and are subsequently measured with a receiver that determines the scattering power and determines the distance of the scatterer using the time delay between transmission and reception. In addition to time of delay and scattering power, there are also many other parameters that can typically be measured with a radar system. These include e.g., the Doppler spectrum of the scattering, scattering power at different polarizations, and the time of delay between different polarizations.

Radar systems can also have receivers located apart from the transmitter. An ionospheric tomography measurement [78] is one such example. This measurement is done using multiple ground based receiver antennas that measure the transmitted signal from a satellite. The receivers then determine the relative time difference between different ray paths and then reconstruct a two or three dimensional map of the ionospheric index of refraction, which is related with electron density and tropospheric moisture content [79]. The receivers can also determine the accurate orbit of the satellite.

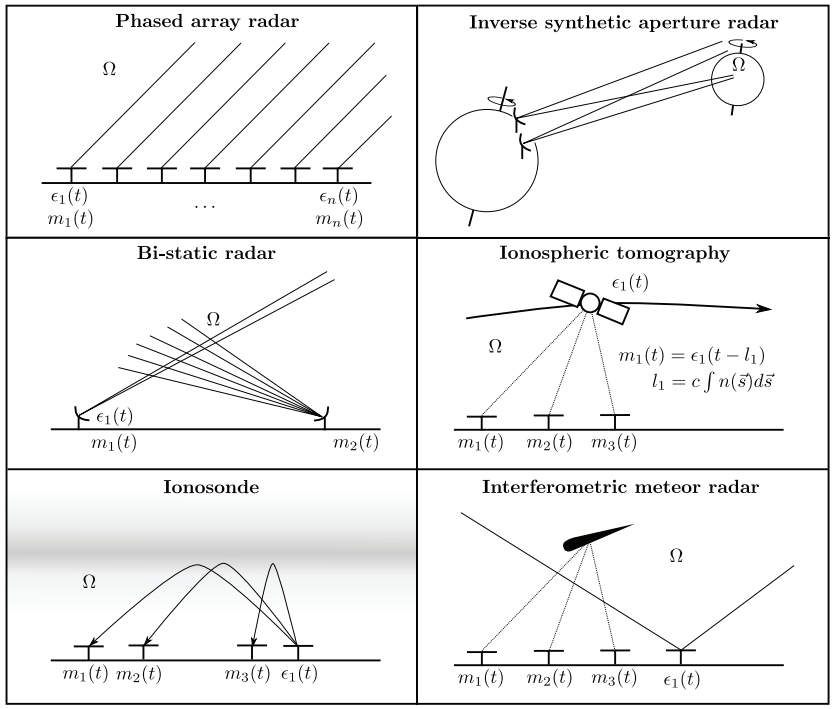

Figure 4.1. Conceptual diagrams of several different types of radars. *Top left:* A modern phased array radar with control over the signal going into each of the antenna elements, allowing the most flexibility in terms of, e.g., beam stearing and interferometry. *Top right:* An example of an inverse synthetic aperture radar where the measured object (the Moon) and the observe (on Earth) is moving with respect to each other. This movement is used to allow high resolution imaging of the object by simulating a huge antenna with the help of the relative movement of the observer and the target. *Middle left:* High power large aperture radars typically have narrow beam widths. They can also have external receiving antennas observing the common volume, possibly at multiple locations simultaneously if phase array receivers are used. *Middle right:* An ionospheric tomography measurement is made with a transmitter on a satellite and ground based receivers measuring the signal delay caused by ionospheric refraction along the ray path. *Bottom left:* An ionosonde consists of a transmitter and one or more receivers measuring the reflection height at multiple different frequencies. *Bottom right:* An interferometric meteor radar has a wide transmitter beam and multiple receiving antennas, which allow meteor trail position determination using echo arrival time difference between receivers.

4.3 High power large aperture radars

High power large aperture radars, which are the main topic of this thesis, were first envisioned as instruments that can measure the incoherent scatter from free electrons in the Earth's ionosphere, the sun, and also to obtain echoes from various planetary targets [80]. The first experimental measurement of ionospheric incoherent scatter was soon thereafter reported by Bowles [81], and many of the other goals were also soon realized when the Jicamarca Radio Observatory [82] and the Arecibo Ionospheric Observatory [83] were built. Both these radars are still the largest of their kind in the world, and they have contributed much to our knowledge of Earth's atmosphere and space. The Jicamarca radar located in Peru has a square shaped phased array antenna field with dimensions of 300×300 m. The Arecibo Ionospheric Observatory in Puerto Rico has a spherical dish with a diameter of 305 meters.

Since the early days, many more high power large aperture radars have been built in various places around the world: These include the Millstone Hill, Svalbard, Tromsø UHF, Tromsø VHF, Kharkov, Irkutsk, MU, Sondrestrom, PROUST, Poker Flat, and Resolute Bay radars. There are also various large radars of comparable size around the world used for space surveillance purposes. The most recently built Poker Flat and Resolute Bay radars are digital phased array radars, which allow fast beam steering and allow 3D imaging of the ionosphere. Some of the listed radars are shown in Fig. 4.2.

As the name already suggests, high power large aperture radars are radars with large antenna aperture and large transmission powers. As the beam width of an antenna is typically a reciprocal of collecting area, these radars also have fairly narrow beams. They also typically transmit fairly long coded pulses in order to increase the average transmitted power. In some bi-static planetary radar applications the transmission can be continuous. Transmission powers, aperture sizes and beam widths are listed in Table 4.1 for many of the worlds high power large aperture radars.

While the primary purpose of most high power large aperture radars is the study of ionospheric plasma, they can also be used for a large variety of other uses, including meteor [84, 85], space debris [5, 6], planetary [86], and lower atmospheric [87] studies.

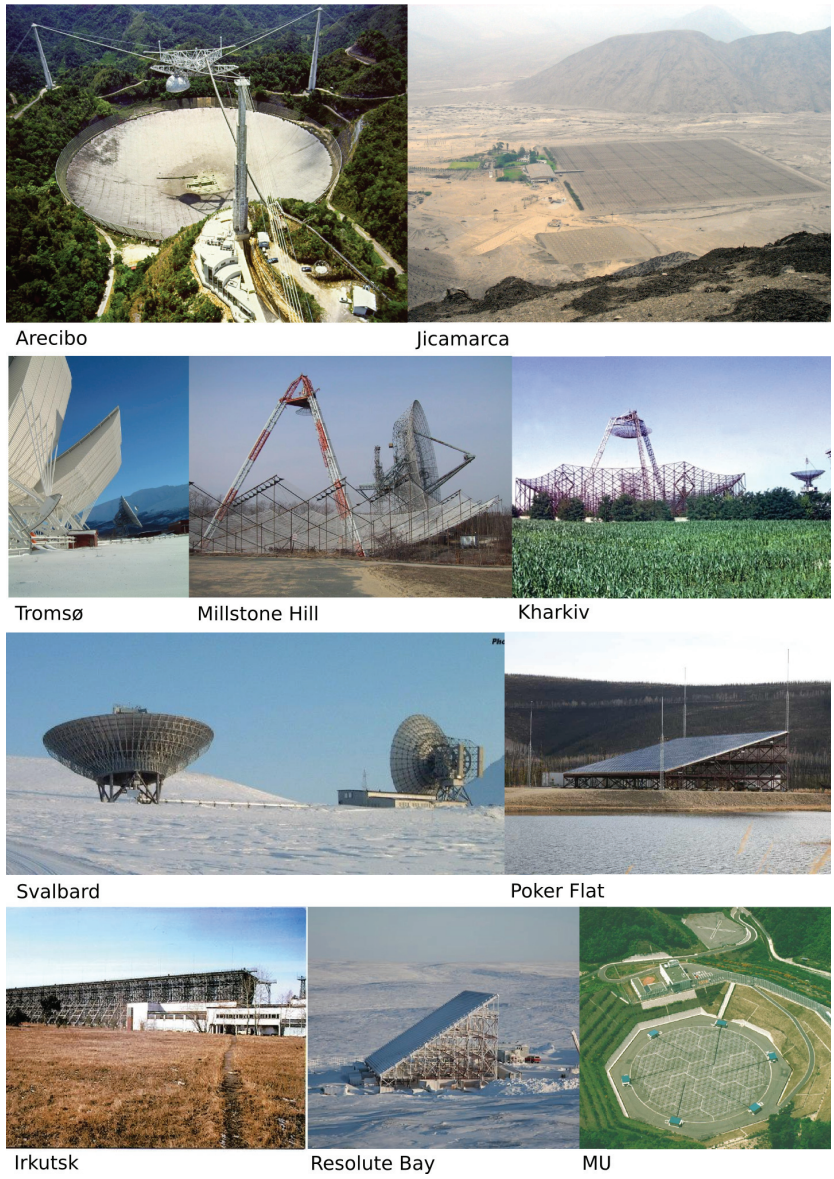

Figure 4.2. High-power large aperture radar systems of the world. Photograph credits: Arecibo (NAIC), Jicamarca (JRO), Tromsø (EISCAT), Svalbard (Tony van Eyken), Millstone Hill (MIT Haystack), Kharkiv (Institute of Ionosphere, Kharkov), Poker Flat and Resolute Bay (Craig Heinsleman).

Name	Frequency (MHz)	Antenna size (m)	Gain (dBi)	Power (MW)	Beam width (deg)
Jicamarca[1]	49.92	300×300	43	2	1
Arecibo	430	305	60	2.5	$\frac{1}{6}$
Arecibo[2]	2380	305	71	1	
Millstone Hill[3]	440	68	45.5	2.5	0.6
Millstone Hill	440	46	42.5	2.5	1.2
Svalbard[3]	500	42	45	1	0.6
Svalbard	500	32	42.5	1	2
Tromsø UHF	929	32	48	2	0.5
Tromsø VHF	224	120×40	46	1.5	0.6×1.7
Søndrestrøm	1290	32	49	3.5	0.5
Poker Flat[1]	449	30×30	43	2	1
Resolute Bay[1]	449	30×30	43	2	1
Kharkiv	158	100	42	2	1.3
Irkutsk	158	246×12.2	38	3.2	0.5×10
MU[1]	46.5	103	32	1	3.6

[1] Phase array

[2] S-band transmitter mainly used for planetary radar.

[3] Fixed zenith antenna.

Table 4.1. A list of the specifications for several high power large aperture radars in the world.

4.4 Incoherent scatter from ionospheric plasma

One of the first applications of high power large aperture radars was the measurement of the incoherent scattering from the electrons [80] of the Earth's ionosphere moving in random thermal motion. The movements of the electrons within the plasma are influenced by the heavier ions, which results in a unique double humped spectrum observed for incoherent scattering from the E- and F-regions of the ionosphere. The theory that relates the backscatter spectrum to the various plasma parameters was formulated by several authors [88, 89, 90, 91, 92, 93]. For a good overview of the theory incoherent scattering from ionospheric plasma, refer to [94].

This theory can then be used to infer various plasma parameters from incoherent scatter spectrum measurements. In typical situations, one can measure electron density, ion temperature, electron temperature and bulk velocity [95, 96]. These measurements, however, typically rely on various assumptions on ion composition. For a study on the information content of incoherent scatter spectrum measurements, refer to [97].

4.5 Meteor echoes

Each year 2000 to 200000 tons of micrometeors burn up in Earth's atmosphere (see [98] and references therein). These mostly consist of interplanetary dust separated from comets or asteroids. Radars can be used both for astronomical [99, 100] and atmospheric studies [101, 102] of these meteors. While most of the meteor radar work has been done with relatively small interferometric radar systems [103], there has recently been a interest in using high power large aperture systems for meteor studies [104, 85, 84].

Due to the narrow beam width and higher frequencies, most high power large aperture radars do not directly observe meteor trail echoes that are routinely observed using meteor radars [103]. Instead, they observe the ionized plasma in the direct vincinity of the ablating meteor itself, which is often called a meteor head echo. This allows more direct measurements of the ablation process [105], as well as better trajectory measurements using interferometric or multistatic means [106, 85].

In some cases, the detection rates (up to 2000 detections per hour with the EISCAT VHF system) are actually so high that they cause serious problems for D-region ionospheric measurements unless removed during

the processing [19]. As a byproduct of this removal, it is possible to obtain measurements of meteor head echoes. However, most of the echoes measured with high power large aperture radars are monostatic detections, which do not allow unambiguous orbital elements measurements. Still, it is possible to perform statistical studies of interactions with meteors and the atmosphere.

4.6 Space debris

Space debris is an ever growing environmental problem occurring in space [107]. After over 50 years of rocket launches, our near space is littered with approximately 10^6 objects larger than 1 cm in diameter, weighing a total of 5500 tons [108]. As the atmosphere is very thin in near-Earth space, these objects do not deorbit very quickly, causing danger to Earth-orbiting spacecraft for tens or hundreds of years to come.

Once these objects are in space, there is also a probability that they will eventually collide with each other and create even more debris. As the probability of in-flight collisions increases as a function of debris in orbit, a catastrophic collisional cascade process that renders regions of near-Earth space unusable is a real risk. This scenario is often referred to as the Kessler syndrome [109]. Recent simulations suggest that some orbital regimes have already passed the critical point where random collisions between space objects will increase the number of objects even if no new space launches would be made [110].

High power large aperture radars are important for statistical measurements of low earth orbit[1] space debris as they are more sensitive than space surveillance radars, which can typically only track objects that are larger than 10 cm in diameter. High power large aperture radars, on the other hand, can detect and track Earth orbiting objects that are larger than 1 cm in diameter [5].

Most of the measurements performed with non-military high power large aperture radars are so called beam-park measurements [111] where the antenna is positioned at a fixed pointing. During a 24-hour period, while the Earth rotates around its axis, a representative statistical sample of debris is measured, containing information on orbital elements of the debris. The time of day provides information about the longitude of the ascending node, while the Doppler shift gives information about the incli-

[1] 300-3000 km

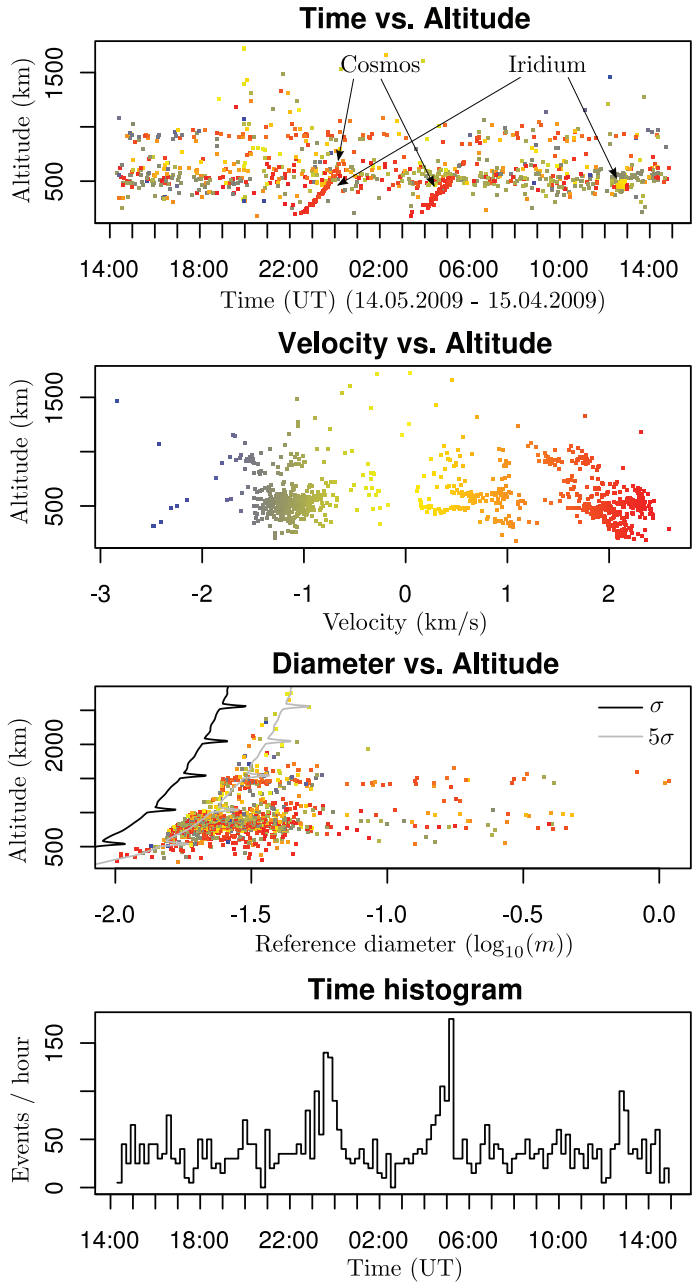

Figure 4.3. A monostatic beam-park space debris measurement on 14-15.05.2009 using the Tromsø 930 MHz incoherent scatter radar. Each point in the figure represents a detection of space debris above the radar. The Doppler velocity of the target is represented using color, which can be determined from the Velocity vs. Altitude plot. The radar beam was pointed towards west at a zenith angle of 22.7°.

nation of the object [111]. An example measurement produced at EISCAT after the collision of the Iridium and Cosmos satellites is shown in Fig 4.3. This measurement is also part of Publication V of this thesis.

The sensitivity of a radar for detecting space debris is strongly determined by the frequency of the radar. A large fraction of the objects in space are < 5 cm sized objects, meaning that the dominant scattering mechanism is Rayleigh scattering [6] where the backscatter power increases proportionally to the sixth power of the object diameter $P \propto d^6$. In this sense, the most sensitive radars for space debris work are the Arecibo, Søndrestrøm and EISCAT UHF radars, as they have the shortest wavelengths. Still, a large number of space objects can be detected with all high power large aperture radars.

4.7 Planetary radar

Planetary radar is a field of research that involves using radars to study objects in our solar system. These include the Sun, planets and their moons, comets and asteroids [80, 86]. The advantage of using a radar is the ability to control the signal that is used to illuminate the target. This allows measurements of various properties of targets through the use of time of delay, polarization and Doppler shift. Planetary radar measurements have been used, e.g., to determine and refine orbital elements and spin vectors, to study surface and subsurface composition, and to study the shape and topography of planetary objects [112, 86, 113].

Most of the planetary radar work has been conducted with various Earth based radar systems, such as Arecibo, Goldstone and VLA, but recently space probes have also been used to conduct radar measurements of various targets, such as the Moon [114], Venus [115, 116] and Mars [117].

Ground based planetary radar measurements typically involve measuring the same and opposite circular returns of the backscatter to determine the surface reflecticity and roughness [86, 118, 119]. Because the targets are typically far away, the spatial resolution is obtained by combining rotational Doppler shift and time of delay. The resulting range-Doppler or delay-Doppler images of the targets are not completely ambiguous, as several different parts of a rotating object can result in identical Doppler shift and round-trip delay.

In Publication IV of this thesis, we describe the first EISCAT UHF lunar imaging measurements. In this study we investigated the feasibility

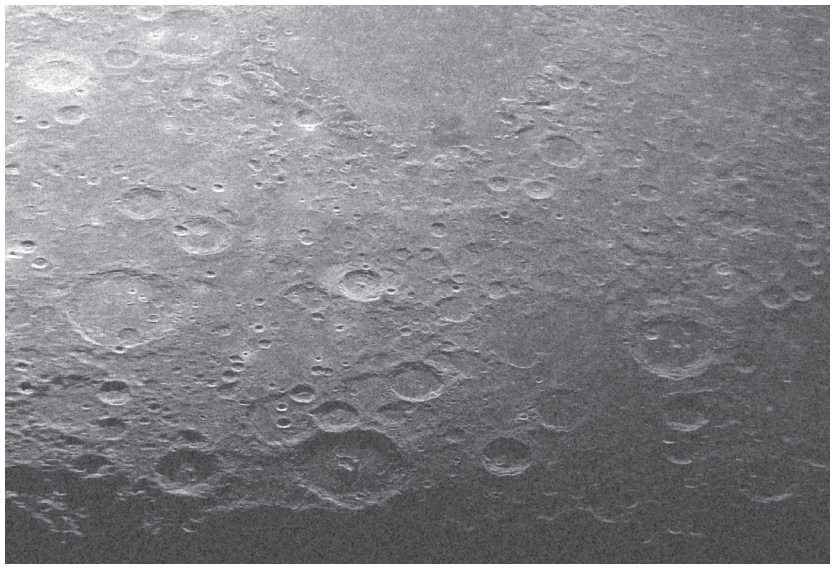

Figure 4.4. An inverse synthetic aperture radar image of the Moon, obtained with the EISCAT Tromso UHF radar.

of using a relatively small Earth-based radar system for lunar imaging measurements. For this study, we had to utilize longer pulse codes and use the beam nulls to mitigate Doppler north-south ambiguous echoes. A range-Doppler image obtained with the EISCAT UHF radar in 2008 is shown in Fig. 4.4. These are also the first 930 MHz lunar opposite circular reflectivity images. Further work is in progress to obtain opposite and same circular focused images of the Moon using this frequency.

5. Radar measurement models

In this chapter we will first go through the basic concepts of *baseband signals* and radar *transmission envelopes* as prequisites. We will then go through three of the most important different radar target models:

- Point-like target with trajectory
- Range spread radar target
- Range and Doppler spread radar target

We will also describe a *random scattering model* that can be used to model and characterize incoherent beam-filling radar targets.

5.1 Baseband signal

Radar measurement models deal with complex baseband signals, even though the actual radar signals themselves are real valued. This is merely due to convenience as most signals are band-limited and concentrated around the carrier frequency. Complex baseband signals allow representing a high frequency real-valued signal with a narrow band signal centered around the carrier frequency. A complex baseband signal is sometimes also referred to as an IQ signal

$$z_{\mathrm{bb}}(t) = I(t) + iQ(t), \tag{5.1}$$

the real part represented with $I(t) \in \mathbb{R}$ and the complex part with $Q(t) \in \mathbb{R}$. This section will describe what these signals mathematically are, and how they can be formed.

Consider a real-valued bandlimited high frequency signal $z(t) \in \mathbb{R}$. Because it is real-valued, it has a conjugate symmetric Fourier transformed

representation $\hat{z}(\omega) = \overline{\hat{z}(-\omega)} \in \mathbb{C}$. If all of the relevant spectral information is contained only within a narrow band $\omega \in B$ centered at $\omega_0 \in \mathbb{R}$, it is often convenient to deal with a band-limited signal $z_{\mathrm{bb}}(t) \in \mathbb{C}$ containing only the band of interest, which is shifted in frequency to zero.

To see how $z_{\mathrm{bb}}(t)$ can be obtained, let us consider the Fourier transform of our high frequency real valued signal $z(t)$, which is defined as

$$\hat{z}(\omega) = \int_{-\infty}^{\infty} z(t) e^{-i\omega t} dt. \tag{5.2}$$

We can first obtain a signal containing the band of interest by integrating over either the positive or negative frequencies within the band of interest $B = (\omega_0 - \Delta\omega/2, \omega_0 + \Delta\omega/2)$, where $\Delta\omega \leq 2|\omega_0|$. We will call this signal the *carrier band* complexified signal

$$z_{\mathrm{c}}(t) = \frac{1}{2\pi} \int_{\omega \in B} \hat{z}(\omega) e^{i\omega t} d\omega. \tag{5.3}$$

The signal $z_{\mathrm{c}}(t) \in \mathbb{C}$ is complex-valued, as we omit the conjugate symmetric half of the spectrum. The resulting signal $z_{\mathrm{c}}(t)$ is now a band limited signal still centered around the original frequency, hence the name carrier band signal. This signal is complex valued, as the opposite frequencies have been filtered out and the spectrum of the signal is not conjugate symmetric around zero anymore. The information within the band of interest is still retained, as the opposite side of the spectrum is merely a conjugated mirror image, allowing reconstruction of the real-valued band-limited signal. In practice, a window function $w(\omega)$ with localized time and frequency domain response is used in this filtering operation, and thus a more realistic representation would be

$$z_{\mathrm{c}}(t) = \frac{1}{2\pi} \int_{-\infty}^{\infty} w(\omega) \hat{z}(\omega) e^{i\omega t} d\omega. \tag{5.4}$$

It should also be noted that obtaining $z_{\mathrm{c}}(t)$ from $z(t)$ is simply a convolution operation. Now, in order to obtain the complex band limited *baseband* signal $z_{\mathrm{bb}}(t)$ that is centered around zero, we simply modulate the signal with the center frequency ω_0

$$z_{\mathrm{bb}}(t) = z_{\mathrm{c}}(t) e^{-i\omega_0 t}. \tag{5.5}$$

This can then be sampled at a rate corresponding to the bandwidth of B with $\Delta t \geq 1/\Delta\omega$

$$z_n = z_{\mathrm{bb}}(n\Delta t), \tag{5.6}$$

and the Nyquist-Shannon sampling theorem [120] guarantees that the discretized sequence $z_n \in \mathbb{C}$, $n \in \mathbb{Z}$ retains the information within $z_{\mathrm{bb}}(t)$.

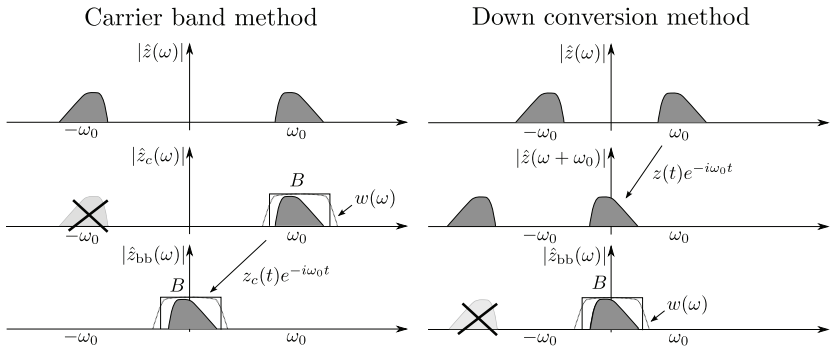

Figure 5.1. Two alternative methods for producing a baseband signal $z_{\mathrm{bb}}(t)$ from a real valued high frequency signal $z(t)$. The *carrier band* method first band-pass filters the band of interest on one side of the spectrum, resulting in the *carrier band* signal $z_{\mathrm{c}}(t)$. Then the remaining band is translated around 0 to obtain the baseband signal $z_{\mathrm{bb}}(t)$. In the *down conversion* method, the signal is first modulated and then filtered.

In practice, baseband signals are often obtained by a combination of analog and digital down conversion steps. For sufficiently low carrier frequencies, the baseband conversion can be done completely digitally using analog-to-digital converter samples. The device performing this type of digital processing is called a *digital down converter* [121] in engineering literature. The steps associated with this approach are nearly identical to the above presentation, except that the signal is first modulated to zero frequency and then band-pass filtered and discretized. We will refer to this alternative approach as the *downconversion method*, while the method described earlier in this section will be referred to as the *carrier band method*. The two alternative ways of forming a baseband signal $z_{\mathrm{bb}}(t)$ are depicted in Fig. 5.1.

In wide band applications, such as the LOFAR radio telescope [122], multiple different frequencies can be simultaneously downcoverted using a so called polyphase filterbank. This is essentially a combination of a filter and an FFT, which simultaneously performs downconversion on all the discrete Fourier transform frequencies on the positive or negative half of the spectrum, and produces narrow band IQ samples of all of these frequencies. This also has advantages in terms of beamforming, as beamforming (digital delay) can be approximated with a multiplication with a complex constant over a narrow frequency band.

5.1.1 Carrier band signals

A useful fact is that the *carrier band* complexified signal $z_{\mathrm{c}}(t)$ can also be discretized with the same sample rate as the baseband signal without loss of information. While this form might not be convenient when formulating radar measurement models, it could be useful as an intermediate signal in large scale phased array receivers. This form can be used to reduce the number of processing steps as the band-limiting and time delays required for beam forming can be combined within the same filtering operation

$$z_{\mathrm{c}}(t-\tau) = \frac{1}{2\pi}\int_{-\infty}^{\infty} e^{-i\tau\omega} w(\omega)\hat{z}(\omega)e^{i\omega t}d\omega = \frac{1}{2\pi}\int_{-\infty}^{\infty} w_\tau(\omega)\hat{z}(\omega)e^{i\omega t}d\omega, \quad (5.7)$$

where the time delay τ and band limiting performed by $w(\omega)$ are combined as a single filter $w_\tau(\omega) = e^{-i\tau\omega}w(\omega)$. Beam forming by summation of different antenna signals $z_{\mathrm{c}}^n(t-\tau_n)$ with different delays τ_n can also be done with the carrier band signals and the final base band signal can be modulated only after the beam forming

$$z_{\mathrm{bb}}(t) = e^{-i\omega_0 t}\sum_n z_{\mathrm{c}}^n(t-\tau_n). \quad (5.8)$$

This way there is only need for one modulator in the whole signal processing chain.

5.2 Transmission envelope

The waveform transmitted by a radar, which we will refer to as the *transmission envelope*, is an important factor in radar experiment design. It is one of the easiest ways to control the error variance of estimated quantities in a radar measurement. The transmission envelope determines the range and Doppler resolution, as well as the range extent of the parameters that can be estimated. A poorly chosen transmission waveform can even prevent certain quantities from being estimated.

When describing radar measurement models, we will denote a baseband transmission envelope with $\epsilon(t) \in \mathbb{C}$ when we are dealing with continuous waveforms, or $\epsilon_t \in \mathbb{C}$ when we are dealing with discretized models. In all measurement models presented in this thesis, the transmission envelope will be a baseband signal with amplitude linearly proportional to the amplitude transmitted by the radar. When the radar is not transmitting, the envelope has an amplitude of zero.

Typically, the constraints apply to the maximum bandwidth, and maximum and mean transmission power. The mean transmission power is often referred to as the *duty-cycle*. Often there is also a lower and upper limit to the transmission pulse length and the pulse repetition interval. The transmission pulse repetition time is also referred to as the *inter-pulse period* (IPP). Most high power radars also allow only transmission of constant amplitude pulses and rely only on phase coding, most commonly binary phase coding. However, some high power large aperture radars can transmit pulses that contain amplitude modulation, e.g., the recently installed waveform generator at the Millstone Hill incoherent scatter radar allows amplitude modulation.

In practical applications, it is often important that the transmission waveform actually transmitted by the radar is known. This is because real-world transmission hardware never actually transmits the analytic waveform that it has been programmed to send. Limitations in power supplies often cause droop in the transmitted signal power and phase chirping also occurs. Magnetron transmitters used in low end weather radars have significant frequency drift in the center frequency of the transmission pulse [76]. It is therefore a good practice to coherently record the actual transmitted waveform and use this when analyzing the measurements.

5.2.1 Types of transmission envelopes

While a transmission envelope can essentially be an arbitrary waveform in theory, there are practical reasons to study more restricted waveforms. The reason for this is two-fold:

1. Radar transmission hardware often imposes limitations to what can be transmitted and which types of waveforms can be synthesized.

2. A more restricted set of waveforms sometimes makes it easier to study the theoretical performance of waveforms, such as in the case of alternating codes [21, 123].

That being said, radar transmission hardware is developing in a direction that allows more flexible use of different types of transmission codes, which often translates to improved radar measurements.

We will only shortly discuss the various different types of transmission

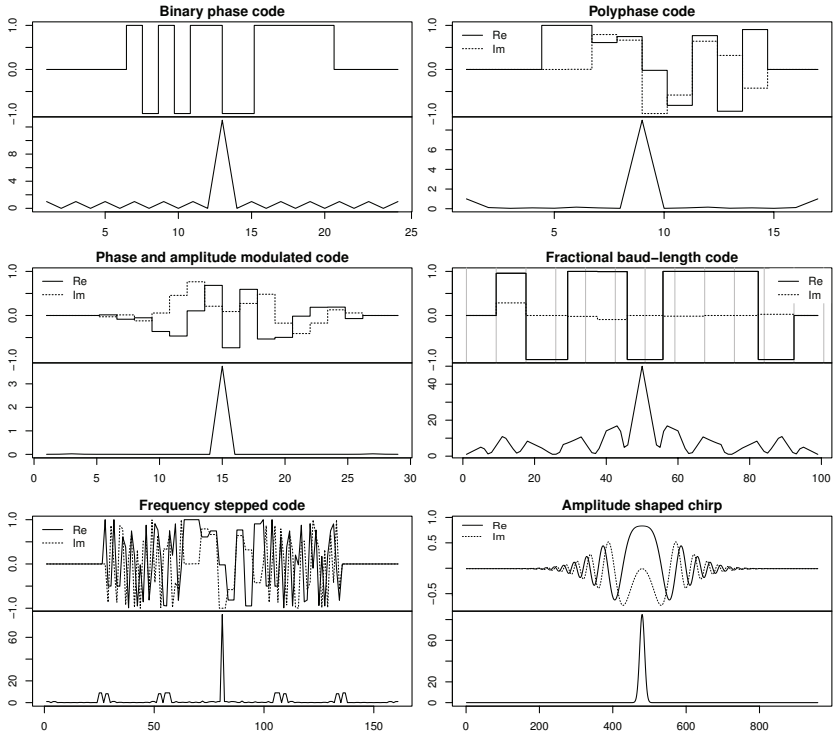

Figure 5.2. Examples of different codes accompanied with their autocorrelation functions. The autocorrelation function is mainly relevant for the performance of the codes for range-spread coherent target deconvolution, as it is the inverse of the row of the posterior covariance matrix for the inverse filter errors. It is also the response of a matched filter.

waveforms in this section and focus on the implications of transmission envelopes to radar target estimation error variance in chapter 6, after first introducing various radar measurement models later on in this chapter. Examples of the transmission envelope types, which are discussed later on in this section, are shown in Fig. 5.2.

Pulse codes

Pulse codes are transmission envelopes that consist of concatenated constant length pulses with constant phase and amplitude. General pulse codes of length L can be represented in this form:

$$\epsilon(t) = \sum_{n=1}^{L} \int \phi_n \delta(t - nl - \tau) b(\tau, l) d\tau, \tag{5.9}$$

where $\delta(t)$ is the Dirac delta function and

$$b(\tau, l) = \begin{cases} 1 & \text{when} \quad \tau \in [0, l) \\ 0 & \text{otherwise} \end{cases} \tag{5.10}$$

is a boxcar function of length l, which corresponds to the baud length. The phase and amplitude of the baud is determined by $\phi_n \in \mathbb{C}$.

In practice, these waveforms are also convolved with the transmitter and antenna impulse response $p(t)$ as the waveform would otherwise have infinite bandwidth. This can be modeled by replacing the boxcar $b(t,l)$ with the filtered boxcar

$$b_p(t,l) = \int b(t-\tau,l)p(\tau)d\tau \tag{5.11}$$

in Equation 5.9. However, the impulse response of the transmitter is often assumed to be fairly short and the contribution of $p(t)$ is often assumed to be fairly minimal.

The most common type of pulse codes are *binary phase codes*, which are of constant amplitude and have only two possible phases $\phi_n \in \{-1,1\}$, assuming that the amplitude is normalized to one. These types of codes can be transmitted with nearly all high power large aperture radars in the world, including the EISCAT radars. There are many different types of binary phase codes known to be optimal for various types of radar targets. Examples include alternating codes [21, 124, 125], Barker codes [126], and complementary codes [127]. Binary phase codes have also been recently studied for variance of deconvolved range spread target estimates [128, 129].

Polyphase codes are a generalization of binary phase codes that allow ϕ_n to be an arbitrary complex number on the unit circle $\phi_n^\omega = e^{-i\omega}$ with $\omega \in [0, 2\pi)$. However, typically the phases are restricted to a set of N distinct equally spaced phases $\phi_n = e^{-2\pi i c_n/N} = \rho^{c_n}$ and $c_n \in \{0,\ldots,N-1\}$. In this case ρ is the Nth root of unity. These types of codes were recently used by us to describe a class of optimal phase codes for incoherent scatter radar called *polyphase alternating codes* [123], which is a generalization of binary phase alternating codes [21, 125] that allow for more freedom when selecting the code lengths. Polyphase variants of Barker codes [130, 131] and complementary codes also exist [132]. We have recently also conducted a search for optimal quadriphase codes that minimize variance of deconvolved range-spread target estimates [133].

While pulse codes with *amplitude modulation*, i.e., $|\phi_n| \in [0, a_{\max}] \subset \mathbb{R}$, are not that often discussed in the literature, allowing arbitrary amplitudes has some interesting theoretical benefits. In a recent study [1], I showed that with the combination of phase and amplitude modulation it is possible to obtain very close to perfect finite length transmission codes in terms of estimation variance of coherent range spread targets. It was

also shown that amplitude modulation is required for finite length perfect transmission codes. Since then, it has been shown that perfect codes can also be analytically designed, if amplitude modulation is allowed [134]. Amplitude modulation for incoherent scatter has been studied in the case of incoherent scatter measurements in Publication II, which is included in this thesis. Recently amplitude modulation has also been proposed for use with the Arecibo incoherent scatter radar [135].

Fractional baud-length code

Fractional baud-length codes were introduced in Publication III. Fractional baud-length codes are otherwise similar to the standard phase codes presented above, with the exception that the pulse length can vary from pulse to pulse. Fractional baud-length codes can also be represented as a sum of boxcars

$$\epsilon(t) = \sum_{n=1}^{L} \int \phi_n \delta \left(t - \sum_{k=1}^{n-1} l_k - \tau \right) b(\tau, l_n) d\tau, \tag{5.12}$$

where l_n is a pulse with variable length. The codes are uniquely defined by the pulse lengths l_n and the complex amplitude of each pulse ϕ_n.

Fractional baud-length codes have several advantages when analyzing radar targets at resolutions smaller than the smallest pulse length $\min(l_k)$, assuming that the transmit and receive bandwidths are large enough.

Frequency stepped transmission envelope

A frequency stepped phase code can be seen as concatenated phase codes $\epsilon_n(t)$ in separate frequency channels

$$\epsilon(t) = \sum_{n=1}^{N_f} e^{-2\pi i f_n t} \epsilon_n(t), \tag{5.13}$$

where $f_n \in \mathbb{R}$ is the center frequency of each code $\epsilon_n(t)$.

This scheme has several advantages. First of all, the effective bandwidth of the transmission code is determined by the bandwidth of the summed channels if analyzed as one transmission waveform, allowing high resolution target estimation. Also, if the bands of the different transmission channels do not overlap, the transmission codes can be filtered into separate channels and treated separately, allowing for a possibility to perform low resolution target estimation, e.g., in the case of interference in some parts of the spectrum.

A frequency stepped fractional baud-length code was used in a recent EISCAT lunar imaging measurement. In this experiment, several different transmission envelopes were sent one after another at increasing

center frequencies. This allowed us to transmit effectively at 2.5 MHz bandwidth, even though the single band limit was only 1 MHz. Thus, allowing improved range resolution, and also allowing the use of only part of the bandwidth at the Sodankylä receiver, which has a narrow band interference filter due to nearby cellular phone base station interference.

Frequency chirped code

One popular transmission code that is not a pulse code per se, is the frequency chirp code

$$\epsilon(t) = A(t) \exp\left(-i\omega(t)\right), \tag{5.14}$$

where $A(t)$ is the amplitude envelope and $\omega(t) \in \mathbb{R}$ is a smooth function. Typically a linear chirp is used

$$\epsilon(t) = A(t) \exp\left(-2\pi i \left(\omega_0 + \frac{1}{2}\omega_1 t\right) t\right), \tag{5.15}$$

where ω_0 is the frequency at $t = 0$ and ω_1 is the frequency change rate, or chirp rate. The amplitude shaping envelope $A(t)$ can be used to shape spectral shape, or alternatively it can be used to shape the autocorrelation function of the transmission envelope and remove range sidelobes. An example of such a weighting is a Gaussian envelope

$$\epsilon(t) = \frac{1}{\sqrt{2\pi l^2}} \exp\left(-\frac{(t-t_0)^2}{2l^2}\right) \exp\left(-2\pi i \left(\omega_0 + \frac{1}{2}\omega_1 t\right) t\right), \tag{5.16}$$

which is shown in Fig. 5.2.

Chirped waveforms are widely used in radars in various different ways [76]. They are most common in surveillance radars, weather radars, and ionosondes. By a clever usage of the properties of ionospheric plasma, they have also been used for ionospheric plasma line measurements [136].

5.3 Point-like target with trajectory

In the previous Sections we have described baseband signals and different types of radar transmission envelopes. In the rest of this Chapter, we will use these definitions to describe different radar target models. We will start with the point-like target model, and then continue to beam filling targets.

A point-like radar target model is used to describe targets that have a very narrow range extent. Examples of these types of targets include space debris, satellites, and meteor head echoes. Point-like targets are fairly well researched radar targets. For example, Skolnik [76] includes a

fairly lengthy discussion on the topic. However, these books concentrate on air-surveillance radar measurements of airplanes, while high power large aperture radars are typically used for measuring space objects and meteors. These measurements differ from air surveillance measurements in several aspects: the target radial velocities are fairly large[1], the transmission pulses are typically very long[2], and the main source of clutter is the ionosphere. Most of the literature also concentrates on incoherent (power domain) integration for target detection, while we focus on the maximum likelihood detection of radar targets, which is equivalent to coherent integration in the radar literature.

In this section, we will describe two different radar models for a point-target: an *accurate model* suitable for precise target parameter fitting, and a fast approximative model, which is suitable for target detection and coarse parameter estimation. We will first describe the accurate model and then develope the coarse model based on it. The point-like target model is loosely similar to the one given by Markkanen [5, 6], with the exception that we also consider the possible Doppler spread of a point-target. We also consider the use of the non-uniform time and frequency step Fast Fourier Transform approximation [56] to solve the fast grid search instead of simple concatenation of echoes.

The unfiltered continuous time radar echo $m(t)$ from a point-like target with a trajectory can be written as

$$\begin{aligned} m(t) &= \epsilon(t - R(t))A(t)\exp\{i\phi R(t)\} + \xi(t) \\ &= f(t) + \xi(t) \end{aligned} \tag{5.17}$$

using the monochromatic incident wave approximation. The term $\epsilon(t - R(t))$ is the round-trip time of flight delayed transmission envelope, the backscatter amplitude is $A(t)$, the radar wavelength dependent coefficient is $\phi = 2\pi f_{\text{radar}}$, the radar receiver noise $\xi(t)$, and the round-trip time of flight radial trajectory is $R(t)$.

The radial trajectory $R(t)$ is the transmitter-target-receiver distance in round-trip time of flight, measured at the time when the echo is received. If the target is moving very fast, then the speed of light needs to be taken into account in order to accurately determine the true radial trajectory of the target at instant of time t, as the target has scattered the transmission envelope approximately at time $t - R(t)/2$ instead of t. However, this correction can be performed with a separate step.

[1] 0-72 km/s

[2] duty cycles between 5-25 %

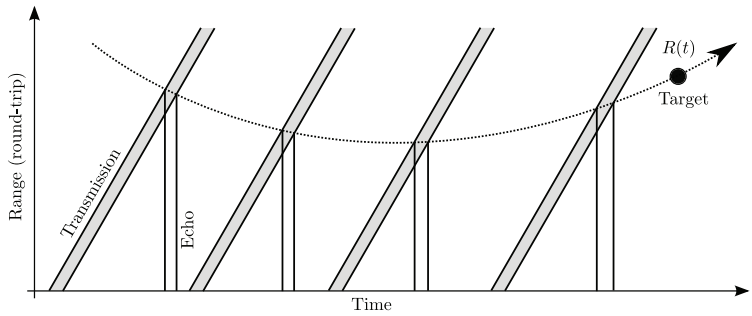

Figure 5.3. An example of a point-like target radar measurement. In this example the target is coherently measured using four transmission pulses. The radial trajectory is exaggerated.

The amplitude envelope $A(t) \in \mathbb{C}$ describes the variation of the target backscatter amplitude as a function of time. This includes beampattern variation and possible target rotation induced variations in complex backscatter coefficient. This can include both variations in radar cross-section, and also variations in phase caused by rotation of a target larger than the wavelength.

It should be perhaps noted that the measurement equation 5.17 holds also over multiple transmission pulses. When there is no transmission, the transmission envelope has an amplitude of zero $|\epsilon(t)| = 0$. The number of transmission pulses that can be included in the same model, in practice, depends on the characteristics of the radial trajectory and the radar beam width. For example, in typical space debris measurements a 0.1 s time interval can still be included in the same model (this corresponds to 10-100 transmission pulses with the EISCAT UHF radar). An example measurement is shown in Fig. 5.3.

5.3.1 Discretization

In a digital receiver the measured signal is first filtered (convolved) with the combined analog and digital receiver filter $w(t)$, and then discretized at sample intervals of Δt, which typically corresponds to the inverse of the filter bandwidth

$$m_n = (w * m)(n\Delta t). \tag{5.18}$$

In typical EISCAT space debris measurements, the actual transmitted waveform is also measured using the same digital receiver coherently

$$\epsilon_n = (w * \epsilon)(n\Delta t). \tag{5.19}$$

Measuring the actual transmitted waveform has the advantage that any high power amplifier artefacts, such as amplitude droop, phase chirping, or frequency offset can be taken into account correctly in the measurement model.

Assuming that the filter width is contained in the sampled bandwidth, the Nyquist-Shannon sampling theorem [120] then guarantees that $(w * \epsilon)(t - \tau)$ can be reconstructed from ϵ_n, where τ is an arbitrary delay. This can be done by e.g., upsampling the measured waveform.

5.3.2 Model parametrization

When fitting a model to radar measurements, one typically parametrizes $R(t)$ and $A(t)$ in some way. In the case of space debris measurements, one typically considers fairly short integration periods, where a sufficient model for $R(t)$ is a low order polynomial, e.g., a second order Taylor series expansion

$$R(t) = r_0 + r_1(t - t_0) + \frac{1}{2} r_2 (t - t_0)^2. \tag{5.20}$$

The target backscatter amplitude $A(t)$ is assumed to be a sufficiently narrow band signal, which can be approximated with a Fourier series with N_B adjacent frequencies:

$$A(t) = \sum_{k=\lfloor -(N_B-1)/2 \rfloor}^{\lfloor (N_B-1)/2 \rfloor} a_k \exp\{ik\Delta\omega t\}. \tag{5.21}$$

This type of model is suitable for detection of targets where only a few Fourier components are sufficient to cover the typical bandwidth of the target. The model presented here differs from that presented by Markkanen [5, 6] in respect that we allow $A(t)$ to be a Fourier series instead of a constant, which is equivalent to the case where there is only one term in the Fourier series expansion with $k = 0$.

The radar target is thus determined by the parameters defining the radial trajectory $R(t)$ and the amplitude of the target $A(t)$. These parameters can also be combined in a vector, which would be $\boldsymbol{\theta} = (r_0, r_1, r_2, a_1, \ldots, a_{N_b})$ for the above parametrisation.

The above parametrisation is not the only possible one. For targets with longer integration times and more irregular trajectories higher order or piecewise polynomials can be used for the trajectory $R(t)$. The target amplitude $A(t)$ can also be parametrized in a way that takes into account the rotation ω_r and precession ω_p rate of the target. This can also be done with the help of a periodic function Fourier series representation, but we

will not go into the details here.

5.3.3 Discretized parametric model

With the help of the parametrized model for $R(t)$ and $A(t)$, we can then represent the measurements m_n with the help of measured transmission envelope ϵ_n.

$$m_n = (w * f)(n\Delta t) + (w * \xi)(n\Delta t) \tag{5.22}$$

In most cases, it is possible to approximate this with

$$m_n = \epsilon_{\mathrm{round}(n - R(n\Delta t)/\Delta t)} A(n\Delta t) \exp\{i\phi R(n\Delta t)\} = f_n(\boldsymbol{\theta}) + \xi_n, \tag{5.23}$$

here the approximative model function is denoted with $f_n(\boldsymbol{\theta})$, as it depends on the model parameters $\boldsymbol{\theta}$. This approximation requires that

- Both $A(t)$ and $\exp\{i\phi R(t)\}$ can be taken out of the convolution by $w(t)$ without significantly altering $f(t)$. This requires $A(t)\exp\{i\phi R(t)\}$ to be sufficiently narrow band.

The first requirement is nearly always satisfied, and the second criteria can be satisfied by selecting a large enough sample rate. Otherwise one must resort to evaluating the forward theory $(w * f)(t)$ in a more tedious way, which includes the effect of filtering the model function $f(t)$ by $w(t)$.

The filtered and discretized measurement errors $\xi_n = (w*\xi)(t+n\Delta t)$ are assumed to be identically distributed proper complex Gaussian normal random variables. In most cases, when the filter length is matched to the sample interval, the errors can be assumed to be independent (i.e., the error covariance matrix is diagonal $\mathrm{E}\,\xi_n\overline{\xi_{n'}} = \sigma^2\delta_{n,n'}$).

If we also join the discretized measurements in a vector $\mathbf{m} = (m_1, \ldots, m_N)$, the likelihood function for the measurements can now be written as

$$p(\mathbf{m}|\boldsymbol{\theta}) = \prod_{n=1}^{N} \frac{1}{\pi\sigma} \exp\left\{-\frac{1}{\sigma^2}|m_n - f_n(\boldsymbol{\theta})|^2\right\}, \tag{5.24}$$

or equivalently as

$$p(\mathbf{m}|\boldsymbol{\theta}) = \frac{1}{\pi^N\sigma^N} \exp\left\{-\frac{1}{\sigma^2}\|\mathbf{A}(\boldsymbol{\theta}) - \mathbf{m}\|^2\right\}, \tag{5.25}$$

where the theory matrix $\mathbf{A}(\boldsymbol{\theta})$ is a vector of the model function $f_n(\boldsymbol{\theta})$ evaluated for specific parameter values $\boldsymbol{\theta}$

$$\mathbf{A}(\boldsymbol{\theta}) = (f_1(\boldsymbol{\theta}), \ldots, f_N(\boldsymbol{\theta})). \tag{5.26}$$

The tricky part in the case of moving point-targets is the search for the peak of the distribution in Equation 5.25. This is due to the fact that the distribution is highly multimodal. Provided a sufficiently good initial guess for the parameters $\boldsymbol{\theta}$, this can be done using a combination of a grid search and an optimization algorithm. However, it is not possible to perform such a search when there is a vast amount of radar measurements, which mostly do not contain radar targets. Therefore, it is important to have a fast approximative method that can provide a good initial guess for the parameters.

5.3.4 Fast approximative model

In real world applications, a fast approximative method for evaluating and inspecting the likelihood function given in Equation 5.25 is needed in order to detect targets. This can be achieved by approximatively performing a exhaustive grid-search of the logarithmic likelihood with the help of FFT. The algorithm given here is a slight modification of the original FastGMF algorithm described by Markkanen [6], the main difference is the use of the non-uniform fast Fourier transform [56], which is a more accurate approximation than a simple concatenation of the vectors.

The algorithm relies on several key points: first of all, we assume that the target Doppler spread is negligible and that the target is point-like, i.e., $A(t) = a \in \mathbb{R}$. Also assume that the target trajectory is described by a polynomial $R(t) = r_0 + r_1 t + \frac{1}{2} r_2 t^2$ (again in round-trip time units, when measured at the receiver).

Additionally, we assume that the target moves slow enough that the echo can be assumed to be a Doppler shifted copy of the transmission envelope, i.e., the effect of range migration does not affect the value of the discretized transmission envelope

$$\epsilon_{\mathrm{round}(n - R(n\Delta t)/\Delta t)} \approx \epsilon_{\mathrm{round}(n - r_0/\Delta t)}. \tag{5.27}$$

Using this approximation, we now can write the measurement model as

$$m_n = \epsilon_{\mathrm{round}(n - r_0/\Delta t)} c \exp\left\{ i\phi \left(r_1 n\Delta t + \frac{1}{2} r_2 (n\Delta t)^2 \right) \right\}, \tag{5.28}$$

where $c = a \exp\{i\phi r_0\}$ or

$$m_n = f'_n(\boldsymbol{\theta}) c, \tag{5.29}$$

where $f'_n(\boldsymbol{\theta})$ is the fast approximative forward model, which can be written in vector form as $\mathbf{f}(\boldsymbol{\theta})a = (f'_1(\boldsymbol{\theta}), \ldots, f'_N(\boldsymbol{\theta}))c$, where $\boldsymbol{\theta} = (r_1, r_2)$. The

likelihood function for this fast approximative theory can be written as

$$p(\mathbf{m}|\boldsymbol{\theta}, c) = \frac{1}{\pi^N \sigma^N} \exp\left\{-\frac{1}{\sigma^2}\|\mathbf{f}(\boldsymbol{\theta})c - \mathbf{m}\|^2\right\}, \tag{5.30}$$

which has a peak for parameter c at

$$\hat{c} = (\mathbf{f}(\boldsymbol{\theta})^{\mathrm{H}}\mathbf{f}(\boldsymbol{\theta}))^{-1}\mathbf{f}(\boldsymbol{\theta})^{\mathrm{H}}\mathbf{m} = \frac{\mathbf{f}(\boldsymbol{\theta})^{\mathrm{H}}\mathbf{m}}{\|\mathbf{f}(\boldsymbol{\theta})\|^2} \tag{5.31}$$

for any given parameter vector $\boldsymbol{\theta}$. To determine how to find the peak of the distribution for the rest of the parameters $\boldsymbol{\theta}$, we observe that the sum of squares term can be factored as

$$\|\mathbf{f}(\boldsymbol{\theta})c - \mathbf{m}\|^2 = \|\mathbf{m}\|^2 + \left||c|\|\mathbf{f}(\boldsymbol{\theta})\| - \frac{\overline{c}^0\mathbf{f}(\boldsymbol{\theta})^{\mathrm{H}}\mathbf{m}}{\|\mathbf{f}(\boldsymbol{\theta})\|}\right|^2 - \left|\frac{\mathbf{f}(\boldsymbol{\theta})^{\mathrm{H}}\mathbf{m}}{\|\mathbf{f}(\boldsymbol{\theta})\|}\right|^2, \tag{5.32}$$

where $c^0 = c/|c|$. The second term is zero when $c = \hat{c}$ and the third term is independent of c. Thus, the maximum likelihood parameters $\hat{\boldsymbol{\theta}}$ are obtained by maximizing

$$\hat{\boldsymbol{\theta}} = \arg\max_{\boldsymbol{\theta}} \left|\mathbf{f}(\boldsymbol{\theta})^{\mathrm{H}}\mathbf{m}\right|^2 \tag{5.33}$$

and

$$\hat{c} = \frac{\mathbf{f}(\hat{\boldsymbol{\theta}})^{\mathrm{H}}\mathbf{m}}{\|\mathbf{f}(\hat{\boldsymbol{\theta}})\|^2}. \tag{5.34}$$

Fast grid search

The approximative model results in a fairly straightforward maximum likelihood solution, which also suggests an efficient numerical method for performing a grid search of parameter vector $\hat{\boldsymbol{\theta}}$.

In practice, there is a pretty good idea of what is a valid range of values for the parameters $r_0 \in R_0 \subset \mathbb{R}, r_1 \in R_1 \subset \mathbb{R}$, and $r_2 \in R_2 \subset \mathbb{R}$. Therefore, it makes sense to inspect the problem in terms of a Bayesian a posteriori estimation problem with the posteriori density

$$p(\boldsymbol{\theta}|\mathbf{m}, c) \propto p(\mathbf{m}, c|\boldsymbol{\theta})p(\boldsymbol{\theta})p(c), \tag{5.35}$$

where $p(\boldsymbol{\theta})$ is the prior density for the parameters and $p(c)$ is the prior distribution for the target scattering amplitude. We will assume that $p(c)$ is uniformly distributed over all values in $\mathbb{C}$. However, we will assume that the prior $p(\boldsymbol{\theta})$ is uniformly distributed in $R_0 \times R_1 \times R_2$, and elsewhere zero. Therefore, our search needs search through only $R_0 \times R_1 \times R_2$, and the posteriori density is up to a constant the same as the likelihood function within these bounds.

The search algorithm (Algorithm 1) that searches for the maximum a posteriori performs a grid search with a grid in $R_0 \times R_1 \times R_2$. In typical

high power large aperture radar measurements, there are several thousand values of r_0, several values for r_2 and several thousand values for r_1. The efficiency of the algorithm results from the fact that the vector dot product $\mathbf{f}(\boldsymbol{\theta})^{\mathrm{H}}\mathbf{m}$ can be efficiently calculated for all of the grid values of r_2 simultaneously using FFT with the NFFT approximation. Typically radar duty-cycles are 5-25%, which means that only 5-25% of the measurement vector actually needs to be used in the NFFT evaluation of $\mathbf{f}(\boldsymbol{\theta})^{\mathrm{H}}\mathbf{m}$ for each grid point of r_0, as the rest of the values are analytically zero because the transmission envelope is zero.

Algorithm 1 Fast grid search algorithm for point-targets

for each data block $\mathbf{m} = (m_{b+1}, \ldots, m_{b+B})$ **do**
  for each range gate in search grid $r_0 \in R_0' \subset R_0$ **do**
    for each acceleration in search grid $r_2 \in R_2' \subset R_2$ **do**
      Perform a grid search over possible values of r_1 using NFFT to simultaneously evaluate $\left|\mathbf{f}(\boldsymbol{\theta})^{\mathrm{H}}\mathbf{m}\right|^2$ for all possible values of $r_1 \in R_1' \subset R_1$.
      if new peak of the posteriori density is found **then**
        Store peak parameter values $\hat{\boldsymbol{\theta}} = (\hat{r}_0, \hat{r}_1, \hat{r}_2)$
      end if
    end for
  end for
end for

One key feature of the algorithm is that it is trivial to parallelize. The three for loops can all be parallelized with minimal communication necessary. The only requirement is that all parallel nodes of execution need to be able to access the measurement vector $\mathbf{m}$. This makes it possible to use both GPU accelerated parallelization and computer cluster parallelization, and this has also been implemented in practice.

5.4 Random scattering model

The previous section discussed targets that were point-like. A radar target that is spread in range requires a different type a radar model. We will approach this problem by initially introducing a random scattering model that can be used to characterize and represent radar targets that consists of a large number of independent scatterers within the radar measurement volume. As an example, we will then show how this scat-

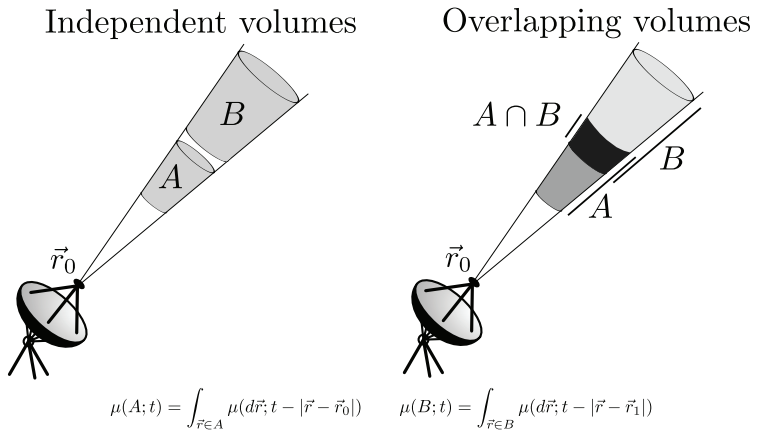

Figure 5.4. Scatter from volumes A and B. A point in space is denoted by $\vec{r}$, which in this case is scaled to time of round-trip flight.

tering model can be physically derived in the case of weather radar. In the following sections, we will then use these definitions to develope various radar measurement models for targets with long and short scattering correlation times.

The Itō measure [137] is an important concept for modeling beam filling incoherent radar targets. This mathematical construct, that is used to integrate random processes, can be used to describe the radar receiver induced voltage of the incoherent scatter originating from a volume of space that has dimensions larger than the radar wavelength, and contains a large enough number of uncorrelated scatterers that are stationary in time with respect to their range and Doppler distribution. An example of such a radar target is ionospheric plasma measured using an incoherent scatter radar. Another example is the distribution of rain drops measured using a weather radar. A random scattering model that utilizes the Itō measure was first presented by Lehtinen [21]. A similar model is also known in the signal processing and communications community as the *wide sense stationary uncorrelated scattering* medium [138, 22].

The random baseband signal received from a scattering volume $A \in \mathbb{R}^3$ at time instant $t \in \mathbb{R}$ is denoted with the measure function $\mu(A;t) \in \mathbb{C}$. This can be thought of as the received complex baseband voltage from scattering integrated over a volume of space. The measure function $\mu(A;t)$ can also be thought of as a wide sense stationary stochastic process in time [50].

5.4.1 Independent volumes

If the volumes do not overlap (i.e., $A \cap B = \emptyset$), the expected value of the conjugated cross-product $\mathrm{E}\,\mu(A;t)\overline{\mu(B;t')}$ of the received voltage is zero

$$\mathrm{E}\,\mu(A;t)\overline{\mu(B;t')} = 0, \forall t, t', \tag{5.36}$$

which essentially means that the scattering from the disjoint volumes is uncorrelated.

The physical intuition behind this is that the physical scatterers within two disjoint volumes have radial trajectories which are different. Due to the fact that their positions are random, the conjugated cross product consists of cross products of scattering from individual scatterers with random phases uniformly distributed between $[0, 2\pi]$. If we denote the locations of the individual scatterers within volume A at time t with $\vec{x}^A_{n,t}$, and the locations of individual scatterers within volume B at time $t + \tau$ with $\vec{x}^B_{m,t+\tau}$, we can express the conjugated cross-product of scattering from a continuous wave as

$$\mathrm{E} \sum_n \sum_m a^A_n \exp\left(-ik|\vec{0} - \vec{x}^A_{n,t}|\right) a^B_m \exp\left(ik|\vec{0} - \vec{x}^B_{m,t+\tau}|\right) = 0, \tag{5.37}$$

where $\vec{0}$ is the location of the radar. The terms a^A_n and a^B_m denote the amplitude of the scattering originating from each scatterer. Due to the random locations of the scatterers, assuming that the volume is significantly larger than k, the two exponential terms become two different independent unit magnitude random complex numbers with phases uniformly distributed between $[0, 2\pi]$, from which it follows that the expected value of each of the cross-products is already zero.

The above reasoning applies, e.g., disjoint volumes containing rain droplets measured with weather radar. The general idea also applies to disjoint volumes containing refractive index fluctuations within ionospheric plasma measured with incoherent scatter radar, although the details are more complicated in this case, as the we cannot consider the scattering from refractive index fluctuations as individual isolated scatterers per se.

5.4.2 Additivity

For two disjoint volumes $A \cap B = \emptyset$, the combined scattering from volumes A and B is the sum of the scattering from the individual volumes

$$\mu(A \cup B; t) = \mu(A; t) + \mu(B; t). \tag{5.38}$$

This is simply a consequence of the fact that radar echoes received simultaneously are summed together.

5.4.3 Structure function

The conjugated cross-product between the scattering from two infitesimal volumes $d\vec{r}$ and $d\vec{r}'$ is defined as

$$\mathrm{E}\,\mu(d\vec{r};t)\overline{\mu(d\vec{r}';t')} = X(\vec{r},t-t')\delta(\vec{r}-\vec{r'})d\vec{r}d\vec{r'}, \tag{5.39}$$

where $X(\vec{r},\tau)$ is the *structure function* of the Itō-measure. The expected value of the structure function is non-zero only when the volumes overlap, which is a consequence of Eq. 5.36. This is the function that is typically measured with incoherent scatter radar. This can also be understood as the *autocorrelation function* of the wide sense stationary [50] target backscatter process originating from the scattering volume, and its shape depends on the underlying physics of the scattering process.

The physical reasoning for this is that only the scattering originating from the same individual scatterers within a volume results in a non-zero mean conjugated cross-product for scattering from a continuous wave.

5.4.4 Overlapping volumes

To determine what is the expected scattering from two overlapping volumes $\mathrm{E}\,\mu(A;t)\overline{\mu(B;t')}$, we use the fact that

$$\mu(A;t) = \int_{\vec{r}\in A} \mu(d\vec{r};t), \tag{5.40}$$

and then

$$\begin{aligned} E\mu(A;t)\overline{\mu(B;t')} &= \int_{\vec{r}\in A}\int_{\vec{r'}\in B} \mathrm{E}\,\mu(d\vec{r};t)\overline{\mu(d\vec{r'};t')} \\ &= \int_{\vec{r}\in A}\int_{\vec{r'}\in B} X(\vec{r};t-t')\delta(\vec{r}-\vec{r'})d\vec{r}d\vec{r'} \end{aligned} \tag{5.41}$$

which simplifies to

$$\mathrm{E}\,\mu(A;t)\overline{\mu(B;t')} = \int_{\vec{r}\in A\cap B} X(\vec{r};t-t')d\vec{r}. \tag{5.42}$$

This can be understood as the autocorrelation function of the scattering from the overlapping volume $A\cap B$.

5.4.5 Monostatic volume

In the case of a monostatic radar measurement, a natural scattering volume arises when we investigate the volume in space that the transmitted

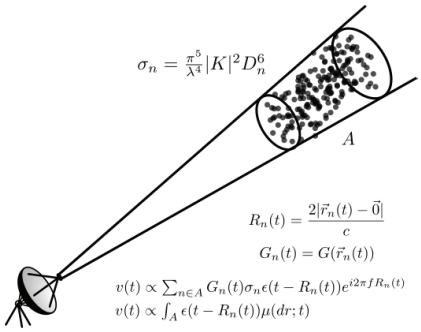

Figure 5.5. A conceptual drawing of incoherent scattering from a volume of rain drops in the case of weather radar.

radio wave has travelled through between two instants of time. This way we can reduce the three-dimensional volume $d\vec{r} \in \mathbb{R}^3$ definition with a one-dimensional coordinate system $r \in \mathbb{R}$. With a highly directive antenna, most of the contribution to the scattering is obtained from the main lobe of the radar antenna beam, and thus the dimensions of the scattering volume in the transverse direction to r can be assumed to be the dimensions of the main lobe of the antenna beam. This is shown in Fig. 5.4.

A similar approach can also be often taken in the case of multistatic radar measurements, but the antenna gains and their relationship with the geometry are trickier to determine.

5.4.6 Example: Monostatic weather radar

As a simple physical motivation for the purely mathematical random incoherent scattering model, we will show how the physically derived incoherent scatter from rain drops in the case of a weather radar can be shown to be equivalent with the random scattering model presented in the previous section.

If we ignore ground clutter, the weather radar target consists of randomly located rain droplets within the radar beam. With the help of several convenience functions, we can present the complex baseband voltage received by a monostatic radar. We first define the round-trip time of flight for the radar target, ignoring any refractive index variations within the path of flight

$$R_n(t) = \frac{2|\vec{r}_n(t) - \vec{r}_0|}{c}. \tag{5.43}$$

Here $\vec{r}_n(t)$ is the position of the nth rain droplet at time instant t and $\vec{r}_0$ is the location of the receiver. To simplify the equations, we will use a one-dimensional coordinate system for range. We also assume that the

trajectories of the individual rain droplets are randomly distributed and of the form $R_n(t) = v_n t + r_n$, where v_n and r_n are random variables with distributions $v_n \sim \pi_v(v, r)$ and $r_n \sim \pi_r(r)$.

The rain droplets are assumed to be small enough that the scattering mechanism can be assumed to be Rayleigh scattering [139]. Using the formula for Rayleigh scatter from dielectric spheres, we get the following scattering cross-section for the rain droplets

$$\sigma_n = \frac{\pi^5}{\lambda^4}|K|^2 D_n^6. \tag{5.44}$$

Here the most significant parameter is the diameter of the nth rain drop D_n^6.

As this example deals with monostatic radar, the antenna gain can be assumed to depend only on the angular distance of the scatterer from the center of the beam $G(\vec{r}_n(t)) = G(\phi_n^1(t), \phi_n^2(t)) = G_n(t)$.

We now get the following equation for the backscattered voltage received from rain drops within a certain volume. Here I_A denotes the set of indices n that correspond to rain drops located volume $A \subset \mathbb{R}^3$, ignoring the scaling factor that arises from the radar hardware[3]

$$\mu(A; t) \propto \sum_{n \in I_A} G_n(t)\sigma_n \epsilon(t - R_n(t)) e^{i2\pi f R_n(t)}, \tag{5.45}$$

where $\epsilon(t)$ is the radar transmission envelope.

We can now examine the expected value of $\mathrm{E}\,\mu(A; t)$, which is

$$\mathrm{E}\,\mu(A; t) = \sum_{n \in I_A} G_n(t)\sigma_n \epsilon(t - R_n(t)) \int_{r \in (r_0, r_1)} e^{i2\pi f(vt+r)} \pi_v(v, r)\, \pi_r(r)\, dr dv \approx 0, \tag{5.46}$$

Where the interval (r_0, r_1) corresponds to volume A along the beam axis. As the phase of each individual scatterer is approximately uniformly distributed between $(0, 2\pi]$, and integral term evaluates to approximately zero. This relies on the fact that $\pi_r(r)$ is sufficiently evenly distributed.

When we examine $\mathrm{E}\,\mu(A; t)\overline{\mu(B; t')}$, we rely on the the property that all cross-products between different rain droplets have a zero mean value, and the only non-zero term arises from the self products between the same rain droplets

$$\mathrm{E}\,\mu(A; t)\overline{\mu(B; t')} \propto \mathrm{E} \sum_{n \in I_{A \cap B}} G_n^2(t)\sigma_n^2 \epsilon(t - R_n(t))\overline{\epsilon(t' - R_n(t'))} e^{i2\pi f v_n (t - t')}. \tag{5.47}$$

[3] including e.g., transmission power and receiver filters.

Now, assuming that the radar cross sections and number density of droplets are random variables distributed as $\sigma_n \sim \pi_\sigma(\sigma, r)$ and $n \sim \pi_n(n, r)$ we can get the following form for the expected value of the second moment:

$$\mathrm{E}\,\mu(A;t)\overline{\mu(B;t')} = \int_{r\in A\cap B} \epsilon(t-r)\overline{\epsilon(t'-r)}X(r,t-t')dr, \tag{5.48}$$

where

$$X(r,t-t') = G^2 \iiint \sigma\pi_\sigma(\sigma,r)n\pi_n(n,r)\pi_v(v,r)e^{i2\pi f v(t-t')}d\sigma dn dv, \tag{5.49}$$

where the beam factor G^2 is defined with the help of the beam gain in the transverse dimensions θ_1 and θ_2

$$G^2 = \iint G^2(\theta_1,\theta_2)d\theta_1 d\theta_2. \tag{5.50}$$

It should also be noted, that the structure function can have a more complicated form. For example, the radar cross-sections of the individual rain droplets could also be dependent on velocity for example $\sigma \sim \pi_\sigma(\sigma, v)$, or all of the parameters could be modeled using a joint probability density function $(\sigma, n, v, r) \sim \pi(\sigma, n, v, r)$.

5.5 Coherent range spread target

Coherent range spread targets are targets with complex backscatter amplitude that does not significantly change during a certain time interval. In terms of the random target scattering model, the target is assumed to have a constant structure function in time

$$X(\vec{r}, t-t') = \sigma(\vec{r}) \text{ when } |t-t'| < T \tag{5.51}$$

over some time interval T, which is longer than the radar transmission pulse. This is typically assumed to be one or several interpulse periods, depending on the characteristics of the target. Examples of these types of radar targets include: tropospheric, stratospheric and mesospheric echoes, meteor trails, lunar echoes, weather radar returns, and the D-region of the ionosphere.

We will present two different schemes for estimating range spread coherent radar targets. The first we will call *inverse filtering*, and the second we will call *matched filtering*. These two approach have several fundamental differences, mainly that inverse filtering can be viewed as a sidelobe-free maximum likelihood estimator of the target backscattering coefficient, while the matched filtering approach is a biased estimator,

which can result in range sidelobe artefacts, which are dependent on the radar transmission envelopes used to estimate the target. However, there are specific cases where these two approaches in fact coincide with each other, i.e., with certain types of radar transmission envelopes the matched filtering approach is identical to the inverse filtering approach.

5.5.1 Inverse filtering

Inverse filtering is simply a maximum likelihood estimator of the complex target backscatter coefficient, which can often be obtained using filtering, when certain conditions are met. The deconvolution analysis has some resemblance to the one presented by Lehtinen [129, 134]. However, we will use continuous time, allow for different range resolutions, and allow multiple transmission envelopes.

The amplitude domain measurement equations for n transmission envelopes $\epsilon_n(t)$ convolved with a coherent target $\sigma(r) \in \mathbb{C}$ and filtered with the receiver filter $w(t)$ are

$$\begin{aligned} m_1(t) &= (w * \epsilon_1 * \sigma)(t) + (w * \xi_1)(t) \\ \vdots &\qquad\qquad \vdots \\ m_n(t) &= (w * \epsilon_n * \sigma)(t) + (w * \xi_1)(t) \end{aligned}, \tag{5.52}$$

with $*$ representing a convolution, and the scattering volume given in one-dimensional round-trip time along beam axis. In this case $\sigma(r)$ is equivalent to the amplitude domain backscatter $\mu(r, t)$, and not the structure function. Because of the long correlation time, we can assume that $\sigma(r) = \mu(r, t) = \mu(r, t')$ when $|t - t'| < T$.

The set of convolution equations can also be written in frequency domain using multiplications

$$\begin{aligned} \hat{m}_1(\omega) &= \hat{w}(\omega)\hat{\epsilon}_1(\omega)\hat{\sigma}(\omega) + \hat{w}(\omega)\hat{\xi}_1(\omega) \\ \vdots &\qquad\qquad \vdots \\ \hat{m}_n(\omega) &= \hat{w}(\omega)\hat{\epsilon}_n(\omega)\hat{\sigma}(\omega) + \hat{w}(\omega)\hat{\xi}_n(\omega) \end{aligned}. \tag{5.53}$$

Here $\hat{m}_i(\omega)$, $\hat{w}(\omega)$, $\hat{\epsilon}_i(\omega)$, $\hat{\sigma}(\omega)$, and $\hat{\xi}_i(\omega)$ are the Fourier transforms of the measurements, the receiver impulse response, transmission envelopes, the unknown range dependent backscatter coefficient, and measurement noise.

If our transmission envelope is a pulse coded transmission waveform, it can be described as a convolution of a boxcar $\hat{b}(\omega)$, the transmitter impulse response $\hat{p}(\omega)$ and the pulse code $\hat{\epsilon}'(\omega)$ consisting of Dirac deltas

$$\hat{\epsilon}_i(\omega) = \hat{b}(\omega)\hat{p}(\omega)\hat{\epsilon}'_i(\omega). \tag{5.54}$$

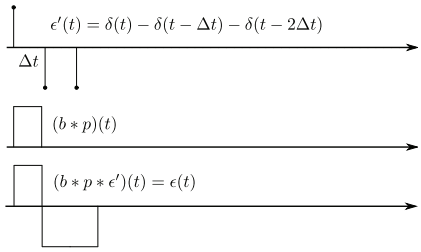

Figure 5.6. The decomposition of the pulsed transmission envelope into a boxcar $b(t)$, transmitter impulse response $p(t)$ and elementary impulse code $\epsilon'(t)$, which is a sum of Dirac delta functions multiplied with the phases and amplitudes of the individual pulse code bauds – in this example this is a 3-bit Barker code $+--$.

This is depicted in Fig. 5.6.

The measurement equations cannot be directly solved by dividing with $\hat{\epsilon}(\omega)$ as there are always zeros in the frequency domain representation of $\hat{b}(\omega)$. However, we can solve the equations of the unknown target convolved with the receiver impulse response, the boxcar function and the transmitter impulse response $\hat{\sigma}'(\omega) = \hat{b}(\omega)\hat{w}(\omega)\hat{p}(\omega)\hat{\sigma}(\omega)$. This gives us a modified set of measurement equations

$$\begin{aligned} \hat{m}_1(\omega) &= \hat{\epsilon'}_1(\omega)\hat{\sigma}'(\omega) + \hat{w}(\omega)\hat{\xi}_1(\omega) \\ \vdots &\qquad\qquad \vdots \qquad . \\ \hat{m}_n(\omega) &= \hat{\epsilon'}_n(\omega)\hat{\sigma}'(\omega) + \hat{w}(\omega)\hat{\xi}_n(\omega) \end{aligned} \tag{5.55}$$

Thus, our unknown is now the target convolved with the receiver and transmitter impulse response, and the boxcar that has the length of one baud of the pulse code

$$\hat{\sigma}'(\omega) = \hat{w}(\omega)\hat{b}(\omega)\hat{p}(\omega). \tag{5.56}$$

Typically $\hat{w}(\omega)$ is selected to be $\hat{b}(\omega)$ and $\hat{p}(\omega)$ is sufficiently narrow band, so that

$$\hat{w}(\omega)\hat{b}(\omega)\hat{p}(\omega) \approx \hat{b^2}(\omega), \tag{5.57}$$

and our unknown is basically convolved with a boxcar convolved with itself, resulting in a triangular impulse response in range. However, increasing the length of the receiver impulse response $\hat{w}(\omega)$ can be used to reduce the range resolution even further.

The posteriori measurement errors can be obtained by considering the linear measurement equation for the maximum likelihood estimator of $\hat{\sigma}'(\omega)$

$$\hat{\boldsymbol{\sigma}}_{\mathbf{ML}} = (\hat{\mathbf{A}}^{\mathrm{H}}\hat{\boldsymbol{\Sigma}}^{-1}\hat{\mathbf{A}})^{-1}\hat{\mathbf{A}}^{\mathrm{H}}\hat{\boldsymbol{\Sigma}}^{-1}\hat{\mathbf{m}}, \tag{5.58}$$

where

$$\hat{\mathbf{A}} = \begin{bmatrix} \operatorname{diag}\left(\hat{\epsilon}'_1(\omega)\right) \\ \vdots \\ \operatorname{diag}\left(\hat{\epsilon}'_n(\omega)\right) \end{bmatrix} = \begin{bmatrix} \hat{\mathbf{A}}_1 \\ \vdots \\ \hat{\mathbf{A}}_n \end{bmatrix} \tag{5.59}$$

and

$$\hat{\mathbf{\Sigma}} = \begin{bmatrix} \hat{\mathbf{\Sigma}}_\mathbf{1} & \mathbf{0} & \dots & \mathbf{0} \\ \mathbf{0} & \hat{\mathbf{\Sigma}}_\mathbf{2} & \dots & \mathbf{0} \\ \vdots & & \ddots & \\ \mathbf{0} & \dots & \mathbf{0} & \hat{\mathbf{\Sigma}}_\mathbf{n} \end{bmatrix}, \tag{5.60}$$

where $\hat{\mathbf{\Sigma}}_\mathbf{i} = \operatorname{diag}\left(|\hat{w}(\omega)|^2 \mathrm{E}\left\{|\hat{\xi}_i(\omega)|^2\right\}\right)$ and $\hat{\mathbf{m}} = (\hat{m}_1(\omega), \dots, \hat{m}_n(\omega))^{\mathrm{T}}$.

As the matrices involved are diagonal matrices, the posterior covariance can be written as

$$\begin{aligned} \hat{\mathbf{\Sigma}}_\mathbf{post} &= (\hat{\mathbf{A}}^{\mathrm{H}} \Sigma^{-1} \hat{\mathbf{A}})^{-1} \\ &= \left(\textstyle\sum_{i=1}^n \hat{\mathbf{A}}_i^{\mathrm{H}} \hat{\mathbf{\Sigma}}_i^{-1} \hat{\mathbf{A}}_i\right)^{-1} \\ &= \left(\textstyle\sum_{i=1}^n \operatorname{diag}\left(|\hat{w}(\omega)|^{-2} \mathrm{E}\left\{|\hat{\xi}_i(\omega)|^{-2}\right\} |\hat{\epsilon}'_i(\omega)|^2\right)\right)^{-1}. \end{aligned} \tag{5.61}$$

Now assuming that the measurement noise is white, we get $\mathrm{E}\,|\hat{\xi}_i(\omega)|^2 = s$, and

$$\hat{\mathbf{\Sigma}}_\mathbf{post} = \operatorname{diag}\left(\frac{s|\hat{w}(\omega)|^2}{\sum_{i=1}^n |\hat{\epsilon}'_i(\omega)|^2}\right). \tag{5.62}$$

and by Plancherel's theorem, we obtain the time (or range) domain estimation variance for the target:

$$\operatorname{Var} \sigma'(r) = \frac{s}{2\pi} \int_{-\pi}^{\pi} \frac{|\hat{w}(\omega)|^2}{\sum_{i=1}^n |\hat{\epsilon}'_i(\omega)|^2} d\omega. \tag{5.63}$$

In other words, the variance of the target backscatter amplitude estimate depends on the sum of the Fourier transforms of the delta-train of the transmission codes $\epsilon'_n(t)$ and the receiver filter $w(t)$. It also depends on the receiver noise s, but this is simply a constant, which is unaffected by the codes of the receiver filter. A code optimization procedure will thus have to consider only the receiver filter, and the transmission codes.

5.5.2 Matched filtering

Perhaps the most commonly used method for estimating radar target backscatter is the *matched filtering* approach [49], which is equivalent to the *correlation estimator* discussed in Section 2.7.6. Again, if we consider multiple measurements of the same unknown $\sigma(t)$, we have the following

set of measurement equations

$$\begin{aligned} m_1(t) &= (\epsilon_1 * \sigma)(t) + \xi_1(t) \\ \vdots &\qquad\quad \vdots \qquad\quad , \\ m_n(t) &= (\epsilon_n * \sigma)(t) + \xi_n(t) \end{aligned} \tag{5.64}$$

and we again assume that $\xi_i(t)$ are equally distributed wide sense stationary random processes. We can represent this in frequency domain using

$$\begin{aligned} \hat{m}_1(\omega) &= \hat{\epsilon}_1(\omega)\hat{\sigma}(\omega) + \hat{\xi}_1(\omega) \\ \vdots &\qquad\quad \vdots \qquad\quad . \\ \hat{m}_n(\omega) &= \hat{\epsilon}_n(\omega)\hat{\sigma}(\omega) + \hat{\xi}_n(\omega) \end{aligned} \tag{5.65}$$

We can also write the theory matrix for these measurement equations

$$\hat{\mathbf{A}} = \begin{bmatrix} \operatorname{diag}\left(|\hat{\epsilon}_1(\omega)|^2\right) \\ \vdots \\ \operatorname{diag}\left(|\hat{\epsilon}_n(\omega)|^2\right) \end{bmatrix} = \begin{bmatrix} \hat{\mathbf{A}}_1 \\ \vdots \\ \hat{\mathbf{A}}_n \end{bmatrix}, \tag{5.66}$$

and the correlation estimator of $\hat{\sigma}(\omega)$ is then

$$\hat{\boldsymbol{\sigma}}_{\mathrm{CE}} = \hat{\mathbf{A}}^{\mathrm{H}}\hat{\mathbf{m}} + \hat{\mathbf{A}}^{\mathrm{H}}\hat{\boldsymbol{\xi}}, \tag{5.67}$$

or without matrix formalism

$$\hat{\sigma}_{\mathrm{CE}}(\omega) = \left(\hat{\sigma}(\omega)\sum_{i=1}^{n}|\hat{\epsilon}_i(\omega)|^2\right) + \sum_{i=1}^{n}\overline{\hat{\epsilon}_i(\omega)}\hat{\xi}_i(\omega), \tag{5.68}$$

which is the target $\hat{\sigma}(\omega)$ convolved with the sum of the autocorrelation functions of the transmission envelopes $\epsilon_i(t)$. This sum can be made a single peaked autocorrelation function with e.g., complementary codes [140], or using perfect codes [134]. The noise term is a sum of the noise terms convolved with the conjugated transmission envelopes $\hat{\epsilon}_i(t)$.

5.6 Coherent range spread target with uniform Doppler shift

In the case of inverse synthetic aperture radar measurements of the Moon, we can assume that, during one transmission pulse, the radar target has a uniform Doppler shift over the whole range extent. For longer periods of time this assumption of course does not apply, as it is the non-uniformity of the Doppler shift that we use when making a range-Doppler map of the target. However, during short periods of time this approximation is valid, and this has the advantage that we can use radar transmission coding and analysis that resembles that of a coherent target with no Doppler shift.

This is exactly the idea behind the lunar range-Doppler measurements presented in Publication IV, which used long coded pulses to increase signal to noise ratio.

Consider a coherent radar target with constant complex target backscatter amplitude at each range during the time that the transmission pulse travels through the target. If this target also has a uniform Doppler shift, we obtain the following measurement equation, assuming a monochromatic incident wave

$$m(t) = \xi(t) + \int \epsilon(t-r)\sigma(r)\exp(i\nu(t-r))dr, \tag{5.69}$$

where $m(t)$ is the measured voltage at the receiver, $\epsilon(t)$ is the radar transmission envelope, $\sigma(r)$ is the target backscatter envelope, ν is the target Doppler shift, and r is range in round-trip time of flight.

If we then multiply the measurements with $\exp(-i\nu t)$, we obtain

$$m(t)\exp(-i\nu t) = \exp(-i\nu t)\xi(t) + \int \epsilon(t-r)\sigma(r)\exp(i\nu r)dr, \tag{5.70}$$

or

$$m'(t) = \xi'(t) + \int \epsilon(t-r)\sigma'(r)dr, \tag{5.71}$$

which is equivalent to a range spread coherent target and can be analyzed in the same way. The only exception is that the unknown target backscatter amplitude is of the form $\sigma'(r) = \sigma(r)\exp(i\nu r)$, but this can be corrected after first estimating $\sigma'(r)$ and then multiplying with $\exp(-i\nu t)$. If $\xi(t)$ is white noise, i.e., $\mathrm{E}\,\xi(t)\overline{\xi(t')} = s\delta(t-t')$, then $\xi'(t)$ is uneffected by multiplication with $\exp(-i\nu t)$.

5.6.1 Wide band chirped transmission

Wide band linear chirped transmission waveforms are commonly used in ionospheric chirp sounders. Because the transmission is essentially continuous and covers a wide range of frequencies with different propagation characteristics, a conventional coherent spread target model with transmission envelope cannot be used, as it would only apply in a narrow band. The target is also assumed not to contain any Doppler shift.

A continuous linear chirped transmission can be expressed as

$$\epsilon(t) = A\exp\{i2\pi(f_0 + 0.5f_1 t)t\}, \tag{5.72}$$

where A is the amplitude of the transmission, f_0 is the initial frequency and f_1 is the rate of frequency increase. While the transmission cannot

be continuous for an infinitely long period, it can in practice be 30 s to several minutes in the case of an ionosonde sounding.

The radar measurement equation $m(t)$ can be expressed using $\sigma(r)$ as the complex backscatter coefficient, the term $b(t)$ includes interference signals, such as radio transmissions and $\xi(t)$ is the noise entering the receiver. Range r is indicated as round-trip time $r = 2R/c$

$$m(t) = b(t) + n(t) + \int \sigma(r)\epsilon(t-r)dr. \tag{5.73}$$

Multiplying this with the normalized conjugate of the transmission envelope $\exp\{-i2\pi(f_0+0.5f_1t)t\}$ and ignoring effects near the beginning of the transmission, we get

$$m(t)\exp\{-i2\pi(f_0+0.5f_1t)t\} = m'(t) = A\int \sigma'(r)\exp\{-i2\pi f_1 rt\}dr + \xi'(t) \tag{5.74}$$

where the modified target backscatter coefficient is

$$\sigma'(r) = \sigma(r)\exp\{-i2\pi(f_0 - 0.5f_1r)r\} \tag{5.75}$$

and the chirped interference and noise term is

$$\xi'(t) = \exp\{-i2\pi(f_0+0.5f_1t)t\}(b(t)+n(t)). \tag{5.76}$$

If we now exchange some variables, and set $r = r'/f_1$ and use $\sigma''(r) = \sigma'(r/f_1)$ we can see the Fourier transform relation between $\sigma''(r')$ and $m'(t)$

$$m'(t) = \xi'(t) + \frac{A}{f_1}\int \sigma''(r')\exp\{-i2\pi r't\}dr'. \tag{5.77}$$

If we discretize $m(t)$, e.g., by simple boxcar filtering that results in a bandwidth of $B = (\Delta t)^{-1}$

$$m'_k = \frac{1}{\Delta t}\int_{k\Delta t}^{(k+1)\Delta t} m(t)dt, \tag{5.78}$$

we can approximate the Fourier transform as

$$m_t = \xi_t + \frac{A}{f_1}\sum_{r=0}^{N-1}\sigma_r\exp\{-2\pi irt/N\}, \tag{5.79}$$

where σ_r consists of the integrated backscatter from one range gate. The range resolution is determined by the frequency resolution, which on the other hand is determined by the length of the discrete Fourier transform and the bandwidth of m_t. Time of propagation range is translated from frequency with

$$R(r) = \frac{c\Delta f r}{2f_1}, \tag{5.80}$$

where $\Delta f = (N\Delta t)^{-1}$ is the frequency of the Fourier vector, and f_1 is the chirp frequency rate of the sounding.

If we consider a sequence of measurements $(m_{t+t0}, \ldots, m_{t+t0+N})$ of length N, we can write Eq. 5.79 in matrix form

$$\mathbf{m} = \mathbf{F}\mathbf{x} + \boldsymbol{\xi} \tag{5.81}$$

with the help of the discrete Fourier transform matrix $\mathbf{F}$. Here $\omega_N = e^{-2\pi i/N}$

$$\mathbf{F} = \frac{A}{f_1}\begin{bmatrix} \omega_N^{0\cdot 0} & \omega_N^{0\cdot 1} & \ldots & \omega_N^{0\cdot(N-1)} \\ \omega_N^{1\cdot 0} & \omega_N^{1\cdot 1} & \ldots & \omega_N^{1\cdot(N-1)} \\ \vdots & \vdots & \ddots & \vdots \\ \omega_N^{(N-1)\cdot 0} & \omega_N^{(N-1)\cdot 1} & \ldots & \omega_N^{(N-1)\cdot(N-1)} \end{bmatrix}. \tag{5.82}$$

We now assume that ξ_t is noise dominated and zero mean. This is in fact not always true. In the case of ionosonde soundings, a broadcast radio station can often be much stronger than the background noise signal. We however ignore this.

Because our theory matrix $\mathbf{F}$ is orthonormal and the covariance matrix $\boldsymbol{\Sigma} = E\boldsymbol{\xi}\boldsymbol{\xi}^{\mathrm{H}} = \alpha\mathbf{I}$ is assumed to be constant diagonal, the maximum a posteriori estimator for parameters $\boldsymbol{\sigma}$ can be significantly simplified

$$\hat{\boldsymbol{\sigma}} = (\mathbf{F}^{\mathrm{H}}\boldsymbol{\Sigma}^{-1}\mathbf{F})^{-1}\mathbf{F}^{\mathrm{H}}\boldsymbol{\Sigma}^{-1}\mathbf{m} = \mathbf{F}^{\mathrm{H}}\mathbf{m}, \tag{5.83}$$

where $\mathbf{F}^{\mathrm{H}}\mathbf{m}$ is merely an inverse discrete Fourier transform of $\mathbf{m}$. Also, the posteriori covariance matrix

$$\boldsymbol{\Sigma}_p = (\mathbf{F}^{\mathrm{H}}\boldsymbol{\Sigma}^{-1}\mathbf{F})^{-1} = \frac{\alpha f_1^2}{A^2 N}\mathbf{I} \tag{5.84}$$

of the errors is diagonal, meaning that the errors of the estimated backscatter coefficient of the neighbouring ranges is not correlated. The variance of the estimates is proportional to the square of the chirp rate f_1^2 and inversely proportional to the transmitted power A^2 and analysis vector length N.

Example: Sodankylä ionosonde

Fig. 5.7 shows an example ionogram analyzed from a single transmission of the Sodankylä "Alpha wolf" ionosonde. The signal was received with a single linear component magnetic loop antenna and the data was recorded using a USRP2 digital receiver device sampling a 10 MHz band between 0.5 and 10.5 MHz. Each column of the ionogram is an estimate of $10\log_{10}|\sigma_r|^2$ using Eq. 5.83 at a narrow band in frequency during the chirp.

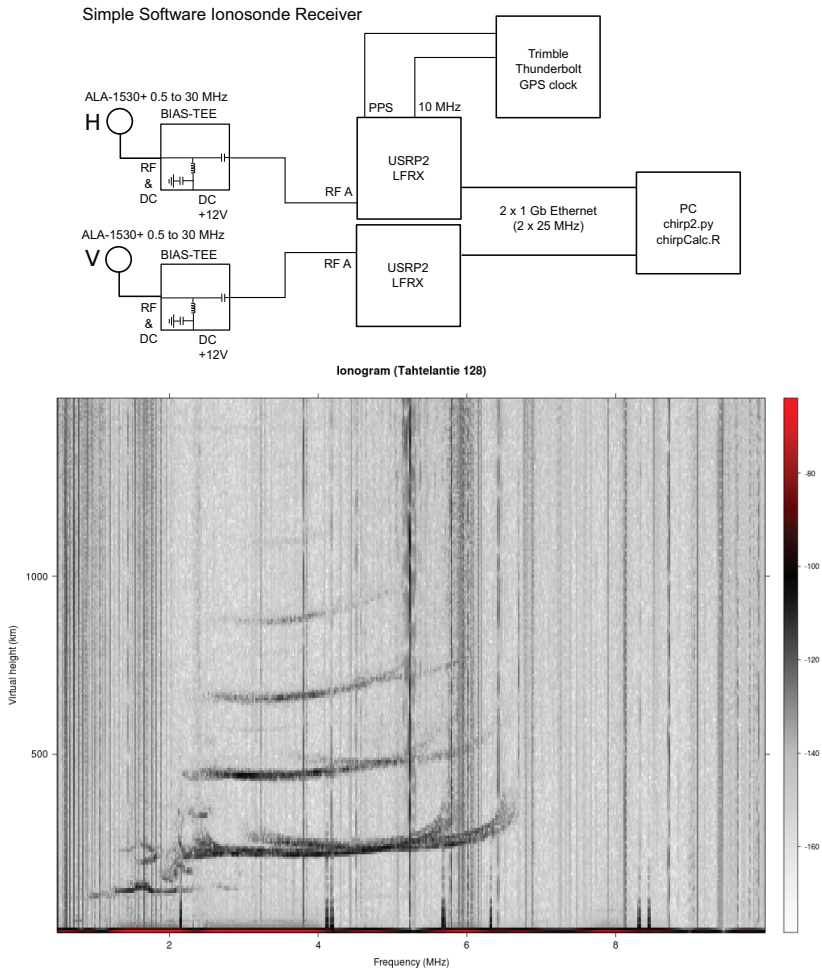

Figure 5.7. Above: The simple software ionosonde receiver. Below: Example ionogram produced from the Sodankylä chirp ionosonde located ≈ 1 km away from the receiver.

Ionosonde considerations

Even though the variance of the measurements is proportional to f_1^2, the range resolution is inversely proportional to f_1. Even though increasing N both increases range resolution and reduces variance, it is not possible to increase N above a certain limit, because the ionospheric refractive index changes strongly as a function of frequency and the target backscatter cannot be considered to be constant over a wide band of frequencies. Also, the ionosphere itself changes as a function of time, and cannot be assumed to be stationary for extremely long periods of time. This sets a lower limit to f_1, as an ionogram is assumed to be a sounding of a stationary ionosphere over a wide band of frequencies.

Strong constant frequency interference, e.g., from broadcast stations, can be included in this analysis scheme by encoding this information in $\mathbf{\Sigma}$, by first estimating the average power of the band of interest and using it in Equation 5.83.

5.7 Range and Doppler spread target

In the previous sections we have discussed radar models with correlation times that are significantly longer than the time that the pulse travels through the medium. These targets were called coherent targets. The opposite to this, is a target that has temporal backscatter correlation times shorter than the time T that the pulse, or group of pulses, travels through the target. In this case, the scattering structure function $X(\vec{r}, t-t') \neq X(\vec{r}, 0)$ from a volume of space is not constant when $|t-t'| < T$. These types of targets are commonly referred to as incoherent targets, or range and Doppler spread targets.

A classic examples of this type of a radar target is the F-region of the ionosphere, where the decorrelation times are typically measured in hundreds of microseconds. This is a time that is often shorter than the radar transmission pulse. While echoes from the D-region of the ionosphere, and from rain droplets measured with a weather radar, typically are coherent over the time that a transmission pulse travels through the medium, on longer timescales they also can be considered incoherent. In these cases, the backscatter structure function (or autocorrelation function) is not anymore constant over several milliseconds – or typically over many radar interpulse periods.

There are several ways that one can analyze range and Doppler spread

targets. First we will present an amplitude domain method for analyzing sufficiently narrow layers of incoherent scatter, which was introduced in Publication I and Publication III in this thesis. We will then discuss a power domain estimation method called *lag-profile inversion* [20], and discuss several extensions to this method.

5.7.1 Amplitude domain method

Using discretized time and range, and assuming that our receiver impulse response is sufficiently close to a boxcar function that is matched to the sample rate, the direct theory for a signal measured from a radar receiver can be expressed as a sum of the range lagged transmission envelope multiplied by the target backscatter amplitude

$$m_t = \sum_{r \in R} \epsilon_{t-r}\, \zeta_{r,t} + \xi_t. \tag{5.85}$$

Here $m_t \in \mathbb{C}$ is the measured baseband raw voltage signal, $R = \{R_{\min}, ..., R_{\max}\} \subset \mathbb{N}$ is the target range extent, $\epsilon_t \in \mathbb{C}$ is the transmission modulation envelope, and $\xi_t \in \mathbb{C}$ is measurement noise consisting of thermal noise and sky-noise from cosmic radio sources. The range and time dependent target backscatter coefficient $\zeta_{r,t} \in \mathbb{C}$ is assumed to be discretized in such a way that the time dependent behaviour is properly sampled. The measurement noise is assumed to be a zero mean complex Gausian white noise with variance $\mathrm{E}\, \xi_t \overline{\xi_{t'}} = \delta_{t,t'}\, \sigma^2$. Ranges r are defined in round-trip time at one-sample intervals, t also denotes time in samples. By convention, we apply a range dependent constant $\frac{r}{2}$ delay to t in $\zeta_{r,t}$, so that the range dependent backscatter amplitude is $\zeta_{r,t}$ instead of $\zeta_{r,t-\frac{r}{2}}$. Fig. 5.8 depicts backscatter from three range gates probed with two transmission samples.

We can further regularize the problem by assuming that $\zeta_{r,t}$ is a band limited process, e.g., by assuming that the target backscatter can be modeled using a B-spline [141], as was done in Publication III. Our model parameters will consist of N_s control points that model the backscatter at each range of interest. The frequency domain characteristics are defined by the spacing of the knots and the order of the spline n. Using the definition of B-splines, the target backscatter $\zeta_{r,t}$ is modeled using the parameters $P_{r,k} \in \mathbb{C}$ as:

$$\hat{\zeta}_{r,t} = \sum_{k=0}^{N_s-1} P_{r,k} b_{k,n} \left(\frac{t-1}{L-1} \right), \tag{5.86}$$

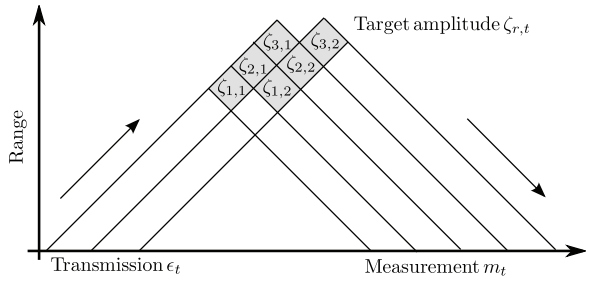

Figure 5.8. Simplified range-time diagram of backscatter from a strong narrow region (notice that this is not in round-trip time). In this example there are two transmit samples and three ranges that cause backscatter. The gray area represents the area where the backscatter of one sample originates from, assuming boxcar impulse response. A longer impulse response will cause more range spreading.

where $b_{k,n}(\cdot)$ is the B-spline basis function and coefficients $P_{r,k}$ are the control points with $k \in \{1, ..., N_s\}$. We assume that the control points are evenly spaced and that the end-points contain multiple knots in order to ensure that the second order derivatives are zero at both ends of $\hat{\zeta}_{r,t}$. Notice that we can also define a special case of one spline control point as $\hat{\zeta}_{r,t} = P_r = \zeta_r$. This corresponds to a completely coherent target.

When equation 5.86 is substituted into equation 5.85, we get

$$m_t = \sum_{r \in R} \sum_{k=0}^{N_s - 1} P_{r,k} \epsilon_{t-r} b_{k,n} \left(\frac{t-1}{L-1} \right) + \xi_t. \tag{5.87}$$

This model is linear with respect to the parameters $P_{r,k}$ and one can conveniently represent it in matrix form as

$$\mathbf{m} = \mathbf{A}\mathbf{x} + \boldsymbol{\xi}, \tag{5.88}$$

where $\mathbf{m} = [m_1, ..., m_N]^{\mathrm{T}}$ is the measurement vector, $\mathbf{A}$ is the theory matrix containing the $\epsilon_{t-r} b_{k,n}(\cdot)$ terms, $\mathbf{x} = [P_{1,1}, P_{1,2}, ..., P_{N_r,N_s}]^{\mathrm{T}}$ is the parameter vector containing the control points and $\boldsymbol{\xi} = [\xi_1, ..., \xi_N]^{\mathrm{T}}$ is the error vector with the second moment defined as

$$\mathrm{E}\, \boldsymbol{\xi} \boldsymbol{\xi}^{\mathrm{H}} = \boldsymbol{\Sigma} = \mathrm{diag}(\sigma^2, ..., \sigma^2). \tag{5.89}$$

The number of parameters is the number of ranges N_r times the number of B-spline control points N_s per range. The number of measurements $N = N_r + L - 1$ is a sum of target ranges and transmission envelope length L. As long as $N \geq N_r N_s$ and the theory matrix has sufficient rank, the problem can be solved using statistical linear inversion. In practice, the number of model parameters that can be succesfully modeled with

sufficiently small error bars depends on the signal to noise ratio. The estimation of strong range and Doppler spread echoes is shown in [13]. Fig. 5.9 shows an example theory matrix for a target range extent $N_r = 14$ with $N_s = 8$ spline guide points per range. The transmission code is a uniform baud-length 13-bit Barker code with baud length $l_j = 10$.

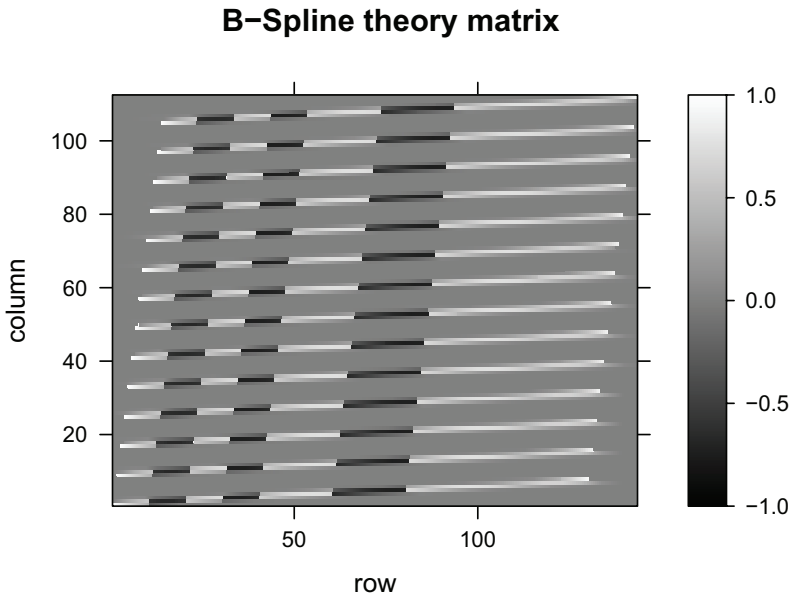

Figure 5.9. A theory matrix for a range and Doppler spread target with $N_r = 14$ range gates and $N_s = 8$ B-spline guide points per range. The code is a simple 13-bit Barker code with 10 samples per baud. The matrix is transposed.

The probability density for Eq. 5.88 can be written as:

$$p(\mathbf{m}|\mathbf{x}) \propto \exp\left(-\frac{1}{2\sigma^2}\|\mathbf{m} - \mathbf{A}\mathbf{x}\|^2\right) \tag{5.90}$$

and assuming constant-valued priors, the maximum *a posteriori* (MAP) estimator, i.e., the peak of $p(\mathbf{m}|\mathbf{x})$ is at point

$$\mathbf{x}_{\mathrm{MAP}} = (\mathbf{A}^{\mathrm{H}}\mathbf{A})^{-1}\mathbf{A}^{\mathrm{H}}\mathbf{m} \tag{5.91}$$

and the *a posteriori* covariance is:

$$\mathbf{\Sigma_p} = \sigma^2(\mathbf{A}^{\mathrm{H}}\mathbf{A})^{-1}. \tag{5.92}$$

5.7.2 Lag-profile inversion

The lag-profile inversion is a maximum likelihood estimator of the incoherent scatter autocorrelation functions at a user defined range resolution. The analysis is performed on lagged products of the measured raw

voltage radar echoes [20, 142] using linear-least squares methods. For a good description of the method, refer to Virtanen [20]. We will only give a brief description of the method here.

Consider the measurement equation for range and Doppler spread targets, but in this case using multiple different radar transmission envelopes indexed with c:

$$m_t^c = \sum_{r \in R} \epsilon_{t-r}^c \, \zeta_{r,t} + \xi_t. \tag{5.93}$$

We then take conjugated self-products of these measurements with a lag τ. These can be organized as

$$m_t^c \overline{m_{t+\tau}^c} = \sum_{r \in R} \epsilon_{t-r}^c \overline{\epsilon_{t-r+\tau}^c} \, \sigma_r^\tau + \xi_t', \tag{5.94}$$

where $\sigma_r^\tau = \mathrm{E}\, \zeta_{r,t} \overline{\zeta_{r,t+\tau}}$, and ξ_t' is a zero-mean noise term, which is dominated by the receiver noise in the case of low signal to noise ratio measurements. In the case of high signal to noise ratio measurements, this will also have significant zero mean contributions from the incoherent scatter cross-products $\zeta_{r,t} \overline{\zeta_{r',t+\tau}}$, where $r \neq r'$.

In more concise form, the lag-product equations can be stated as

$$m_t^{c,\tau} = \sum_{r \in R} \epsilon_{t-r}^{c,\tau} \sigma_r^\tau + \xi_t', \tag{5.95}$$

which is equivalent to the measurement equation for coherent (stationary) range-spread radar targets. For each lag τ, the measurement equations are different, as the ambiguity functions $\epsilon_{t-r}^{c,\tau}$ depend on the lag (and also transmission envelope). The equation is linear, i.e., the relationship between the unknown σ_r^τ and the measurements $m_t^{c,\tau}$ can be represented in matrix

$$\mathbf{m^{c,\tau}} = \mathbf{W^{c,\tau}} \boldsymbol{\sigma^\tau} + \boldsymbol{\xi'}, \tag{5.96}$$

where the measurement vector $\mathbf{m^{c,\tau}}$ spans over all time indices that contribute to the unknown $\boldsymbol{\sigma^\tau}$.

Typically, we assume the target scattering autocorrelation function to be constant over a certain integration period, i.e., we assume that many different measurements c contain the same unknown. We can add these into our equation by simply stacking the measurements:

$$\begin{bmatrix} \mathbf{m^{1,\tau}} \\ \mathbf{m^{2,\tau}} \\ \vdots \\ \mathbf{m^{c,\tau}} \end{bmatrix} = \begin{bmatrix} \mathbf{W^{1,\tau}} \\ \mathbf{W^{2,\tau}} \\ \vdots \\ \mathbf{W^{c,\tau}} \end{bmatrix} \boldsymbol{\sigma^\tau} + \boldsymbol{\xi''} \tag{5.97}$$

In addition to this, we can also combine several different lag measurements, if we assume that the autocorrelation function is indentical at these lags $\sigma_r^{\tau'} = \sigma_r^{\tau} = \sigma_r^{\tau+1} = \cdots = \sigma_r^{\tau+n}$:

$$\begin{bmatrix} \mathbf{m^{c,\tau}} \\ \mathbf{m^{c,\tau+1}} \\ \vdots \\ \mathbf{m^{c,\tau+n}} \end{bmatrix} = \begin{bmatrix} \mathbf{W^{c,\tau}} \\ \mathbf{W^{c,\tau+1}} \\ \vdots \\ \mathbf{W^{c,\tau+n}} \end{bmatrix} \boldsymbol{\sigma}^{\boldsymbol{\tau'}} + \boldsymbol{\xi''} \tag{5.98}$$

In a similar way, we can also decrease the range resolution from the nominal sample rate by assuming that n range gates have the same backscattering autocorrelation $\sigma_{r'}^{\tau} = \sigma_r^{\tau} = \sigma_{r+1}^{\tau} = \cdots = \sigma_{r+n}^{\tau}$. This allows analysis with different range resolutions at different altitudes, e.g., using a fine resolution in the E-region where the scale height is small, and a more coarse resolution in the top-side of the F-region where the signal to noise ratio is much smaller and the scale height is large.

While the equations can be solved using frequency domain methods, this is not necessarily always ideal, as incoherent scatter radar measurements often contain strong signals that can interfere with the much weaker incoherent scatter signal. In these cases it is useful to be able to remove the individual echoes from the raw voltage data, and analyze the problem using linear theory matrices. This also has the advantage that different range and lag resolutions can be used at different regions. Also, issues such as missing measurements due to ground clutter can be more optimally dealt with by using linear theory matrices than by using simple filtering methods.

5.7.3 Dual polarization lag-profile inversion

The lag-profile inversion idea can also be extended to dual-polarization measurements. Such a measurement can be used for several different purposes. Polarization can be used to measure the propagation and scattering effects [143, 144]. The most common use of dual-polarization measurements in incoherent scatter is the measurement of Faraday-rotation, which can be used to obtain absolutely calibrated electron densities from the ionosphere, independent of received power.

Polarization can also be used for transmission coding [145], although it has not been commonly used. As we will see in this section, coding is also important if one wants to measure the full scattering matrix.

In this section, we will introduce dual-polarization scattering equations

and show how the full statistical scattering matrix can be estimated using lag-profile inversion.

Dual polarization scattering equation

By using the Jones representation for polarized electromagnetic plane waves, we can write the dual-polarization incoherent scattering equation in discretized form as

$$\mathbf{m_t} = \sum_r \mathbf{S_{r,t}} \boldsymbol{\epsilon}_{\mathbf{t-r}} + \boldsymbol{\xi_t}, \tag{5.99}$$

which is similar to the one-dimensional single polarization equation, except that the measurement, the transmission envelope, and the receiver noise are two-dimensional vectors $\mathbf{m_t} \in \mathbb{C}^2$, $\boldsymbol{\epsilon_t} \in \mathbb{C}^2$ and $\boldsymbol{\xi_t} \in \mathbb{C}^2$. The two components denote two orthogonal polarizations. Also, the incoherent scatter term is a 2×2 matrix $\mathbf{S_{r,t}} \in \mathbb{C}^{2\times 2}$, which can include propagation, scattering, and radar system effects.

Example: Single polarization

In the case of a monostatic circular polarization incoherent scatter radar measurement, which is not close to perpendicular to the magnetic field, the scattering matrix can be considered diagonal.

If denote the two circular polarizations with a and b, the equation for transmitting polarization a is

$$\mathbf{m_t} = \begin{bmatrix} m_t^a \\ 0 \end{bmatrix} = \sum_r \begin{bmatrix} \zeta_{r,t}^a & 0 \\ 0 & \zeta_{r,t}^b \end{bmatrix} \begin{bmatrix} \epsilon_{t-r}^a \\ 0 \end{bmatrix} + \boldsymbol{\xi_t} \tag{5.100}$$

In this case, we represent the incoherent scatter amplitude with $\zeta_{r,t}^a$ and $\zeta_{r,t}^b$. The noise is $\mathrm{E}\,\boldsymbol{\xi_t}\boldsymbol{\xi_{t'}}^{\mathrm{H}} = \begin{bmatrix} \sigma^2 & 0 \\ 0 & \sigma^2 \end{bmatrix} \delta_{t,t'}$. And the transmission code is ϵ_t^a. We use the convention that the received wave is opposite circular polarized. This simplifies to

$$m_t^a = \sum_r \zeta_{r,t}^a \epsilon_{t-r}^a + \xi_t, \tag{5.101}$$

which is the same as the monostatic single polarization $\mathbf{B}_\parallel$ field aligned circular polarization incoherent scatter equation.

If we were to transmit polarization b, we would have

$$\mathbf{m_t} = \begin{bmatrix} 0 \\ m_t^b \end{bmatrix} = \sum_r \begin{bmatrix} \zeta_{r,t}^a & 0 \\ 0 & \zeta_{r,t}^b \end{bmatrix} \begin{bmatrix} 0 \\ \epsilon_{t-r}^b \end{bmatrix} + \boldsymbol{\xi_t} \tag{5.102}$$

which simplifies to

$$m_t^b = \sum_r \zeta_{r,t}^b \epsilon_{t-r}^b + \xi_t \tag{5.103}$$

which again is the same as the monostatic single polarization $\mathrm{B}_{\parallel}$ field aligned circular polarization incoherent scatter equation. There are no cross-polarization terms in the scattering matrix, because we assume perfect isolation between the polarizations on receiver, and we assume that the propagation and scattering doesn't result in cross-polarization of the transmitted wave.

For single polarization measurement, where one only uses one polarization for transmission, one can only estimate the incoherent scatter autocorrelation function $\mathrm{E}\,\zeta^a_{r,t}\overline{\zeta^a_{r,t+\tau}}$ or $\mathrm{E}\,\zeta^b_{r,t}\overline{\zeta^b_{r,t+\tau}}$. If one were to transmit two different polarizations, it would be possible to also estimate the cross-correlation function $\mathrm{E}\,\zeta^a_{r,t}\overline{\zeta^b_{r,t+\tau}} = \sigma^{ab}_{r,\tau}$ by inspecting cross-polarization lags

$$m^a_t\overline{m^b_{t+\tau}} = \sum_r \sigma^{ab}_{r,\tau}\epsilon^a_{t-r}\overline{\epsilon^b_{t-r-\tau}} + \xi_t. \tag{5.104}$$

which is again similar to the single polarization equation, except that the inspect use lagged products between two polarizations and use the transmission waveforms of each of these polarizations.

Full scattering matrix

In the more general situation scattering, propagation, and the radar system imperfections can cause polarization cross-talk. In this case, the more appropriate scattering equation is

$$\mathbf{m_t} = \sum_r \mathbf{S_{r,t}} + \boldsymbol{\xi_t} = \sum_r \begin{bmatrix} \zeta^a_{r,t} & \nu^b_{r,t} \\ \nu^a_{r,t} & \zeta^b_{r,t} \end{bmatrix} \boldsymbol{\epsilon_{t-r}} + \boldsymbol{\xi}_t \tag{5.105}$$

There are thus four different incoherent scatter processes: $\zeta^a_{r,t}$, $\nu^a_{r,t}$, $\zeta^b_{r,t}$, and $\nu^b_{r,t}$. The measurement noise is still assumed to be uncorrelated: $\mathrm{E}\,\boldsymbol{\xi_t}\boldsymbol{\xi_{t'}}^{\mathrm{H}} = \begin{bmatrix} \sigma^2 & 0 \\ 0 & \sigma^2 \end{bmatrix} \delta_{t,t'}$.

$$\mathbf{m_t} = \sum_r \begin{bmatrix} \epsilon^a_{t-r}\zeta^a_{r,t} + \epsilon^b_{t-r}\nu^b_{r,t} \\ \epsilon^b_{t-r}\zeta^b_{r,t} + \epsilon^a_t\nu^a_{r,t} \end{bmatrix} + \boldsymbol{\xi}_t. \tag{5.106}$$

Because there are four unknowns, it is now possible to calculate 16 different second order products from these (the covariance matrix of four

variables).

$$
\begin{aligned}
m_t^{aa,\tau} &= \sum_r \epsilon_{t-r}^a \overline{\epsilon_{t-r-\tau}^a} \sigma_r^{1,\tau} + \epsilon_{t-r}^a \overline{\epsilon_{t-r-\tau}^b} \sigma_r^{2,\tau} + \\
&\quad \epsilon_{t-r}^b \overline{\epsilon_{t-r-\tau}^a} \overline{\sigma_r^{2,\tau}} + \epsilon_{t-r}^b \overline{\epsilon_{t-r-\tau}^b} \sigma_r^{3,\tau} + \xi_t^1 \\
m_t^{ab,\tau} &= \sum_r \epsilon_{t-r}^a \overline{\epsilon_{t-r-\tau}^b} \sigma_r^{4,\tau} + \epsilon_{t-r}^a \overline{\epsilon_{t-r-\tau}^a} \sigma_r^{5,\tau} + \\
&\quad \epsilon_{t-r}^b \overline{\epsilon_{t-r-\tau}^b} \sigma_r^{6,\tau} + \epsilon_{t-r}^b \overline{\epsilon_{t-r-\tau}^a} \sigma_r^{7,\tau} + \xi_t^2 \\
m_t^{ba,\tau} &= \sum_r \epsilon_{t-r}^b \overline{\epsilon_{t-r-\tau}^a} \overline{\sigma_r^{4,\tau}} + \epsilon_{t-r}^b \overline{\epsilon_{t-r-\tau}^b} \overline{\sigma_r^{6,\tau}} + \\
&\quad \epsilon_{t-r}^a \overline{\epsilon_{t-r-\tau}^a} \overline{\sigma_r^{5,\tau}} + \epsilon_{t-r}^a \overline{\epsilon_{t-r-\tau}^b} \overline{\sigma_r^{7,\tau}} + \xi_t^3 \\
m_t^{bb,\tau} &= \sum_r \epsilon_{t-r}^b \overline{\epsilon_{t-r-\tau}^b} \sigma_r^{8,\tau} + \epsilon_{t-r}^b \overline{\epsilon_{t-r-\tau}^a} \sigma_r^{9,\tau} + \\
&\quad \epsilon_{t-r}^a \overline{\epsilon_{t-r-\tau}^a} \overline{\sigma_r^{9,\tau}} + \epsilon_{t-r}^a \overline{\epsilon_{t-r-\tau}^b} \sigma_r^{10,\tau} + \xi_t^4
\end{aligned}
$$

These are still linear equations, which can be solved with generalized linear least-squares methods, albeit in this case we have 16 unknowns.

However, due to symmetry, 10 of them are unique:

$$\sigma_r^{1,\tau} = \mathrm{E}\, \zeta_t^a \overline{\zeta_{t+\tau}^a} \tag{5.107}$$

$$\sigma_r^{2,\tau} = \mathrm{E}\, \zeta_t^a \overline{\nu_{t+\tau}^b} \tag{5.108}$$

$$\sigma_r^{3,\tau} = \mathrm{E}\, \nu_t^b \overline{\nu_{t+\tau}^b} \tag{5.109}$$

$$\sigma_r^{4,\tau} = \mathrm{E}\, \zeta_t^a \overline{\zeta_{t+\tau}^b} \tag{5.110}$$

$$\sigma_r^{5,\tau} = \mathrm{E}\, \zeta_t^a \overline{\nu_{t+\tau}^a} \tag{5.111}$$

$$\sigma_r^{6,\tau} = \mathrm{E}\, \nu_t^b \overline{\zeta_{t+\tau}^b} \tag{5.112}$$

$$\sigma_r^{7,\tau} = \mathrm{E}\, \nu_t^b \overline{\nu_{t+\tau}^a} \tag{5.113}$$

$$\sigma_r^{8,\tau} = \mathrm{E}\, \zeta_t^b \overline{\zeta_{t+\tau}^b} \tag{5.114}$$

$$\sigma_r^{9,\tau} = \mathrm{E}\, \zeta_t^b \overline{\nu_{t+\tau}^a} \tag{5.115}$$

$$\sigma_r^{10,\tau} = \mathrm{E}\, \nu_t^a \overline{\nu_{t+\tau}^a} \tag{5.116}$$

and this information can be used when fitting a physical theory into the lag-product inversion results.

Now, if we are interested in $m_t^a \overline{m_{t+\tau}^b}$ lags (Faraday rotation), which is included in $\mathrm{Arg}\{\sigma_r^{4,\tau}\}$, we can use the following two equations

$$
\begin{aligned}
m_t^{ab,\tau} &= \sum_r \epsilon_{t-r}^a \overline{\epsilon_{t-r-\tau}^b} \sigma_r^{4,\tau} + \epsilon_{t-r}^a \overline{\epsilon_{t-r-\tau}^a} \sigma_r^{5,\tau} + \\
&\quad \epsilon_{t-r}^b \overline{\epsilon_{t-r-\tau}^b} \sigma_r^{6,\tau} + \epsilon_{t-r}^b \overline{\epsilon_{t-r-\tau}^a} \sigma_r^{7,\tau} + \xi_t^2 \\
m_t^{ba,\tau} &= \sum_r \epsilon_{t-r}^b \overline{\epsilon_{t-r-\tau}^a} \overline{\sigma_r^{4,\tau}} + \epsilon_{t-r}^b \overline{\epsilon_{t-r-\tau}^b} \overline{\sigma_r^{6,\tau}} + \\
&\quad \epsilon_{t-r}^a \overline{\epsilon_{t-r-\tau}^a} \overline{\sigma_r^{5,\tau}} + \epsilon_{t-r}^a \overline{\epsilon_{t-r-\tau}^b} \overline{\sigma_r^{7,\tau}} + \xi_t^3
\end{aligned}
$$

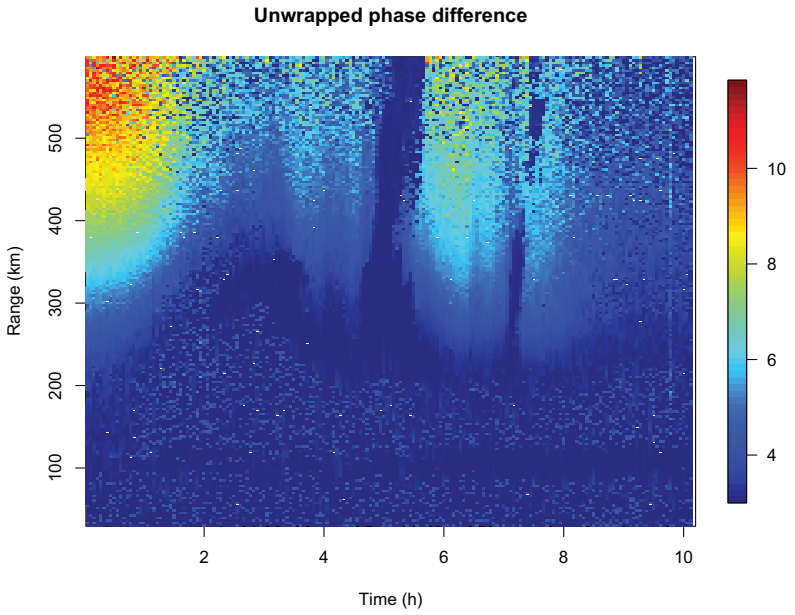

Figure 5.10. Faraday rotation measured on 13.09.2010 (starting at 22 UT) with the Jicamarca incoherent scatter radar using a dual circular polarization transmission pulses. The propagation delay between the two different modes is given in radians. The plume with zero propagation difference is scattering from equatorial spread F, which is perpendicular to the magnetic field, and has very little difference in refractive index.

as $\mathrm{Arg}(\sigma_r^{4,\tau})$ contains the information about propagation delay. This is because the Appleton-Hartree equation results in two refractive indices for two orthogonal propagation modes, which always have a circular component, unless the propagation is perpendicular to the magnetic field. Fig. 5.10 shows an example of a Faraday rotation measurement, the figure shows the propagation delay between the polarization as measured in radians $\mathrm{Arg}(\sigma_r^{4,\tau})$.

For example, the $m_t^{ab,\tau}$ can be written as a linear theory matrix using the following shorthands

$$w_{r,\tau}^t = \left[\begin{array}{cccc} \epsilon_{t-r}^a \overline{\epsilon_{t-r+\tau}^b}, & \epsilon_{t-r}^a \overline{\epsilon_{t-r+\tau}^a}, & \epsilon_{t-r}^b \overline{\epsilon_{t-r+\tau}^b}, & \epsilon_{t-r}^b \overline{\epsilon_{t-r+\tau}^a} \end{array} \right]$$

and

$$\sigma'_{r,\tau} = \left[\begin{array}{cccc} \sigma_{r,\tau}^4, & \sigma_{r,\tau}^5 & \sigma_{r,\tau}^6 & \sigma_{r,\tau}^7 \end{array} \right]^{\mathrm{T}}$$

The linear relationship between the lagged product measurements and

the unknown parameters $\mathbf{m} = \mathbf{A}\mathbf{x} + \boldsymbol{\xi}$ can now be written as:

$$\begin{bmatrix} m_1^{ab,\tau} \\ \vdots \\ m_t^{ab,\tau} \end{bmatrix} = \begin{bmatrix} w_{1,\tau}^1 & \dots & w_{r,\tau}^1 \\ \vdots & \ddots & \vdots \\ w_{1,\tau}^t & \dots & w_{r,\tau}^t \end{bmatrix} \begin{bmatrix} \sigma'_{1,\tau} \\ \vdots \\ \sigma'_{r,\tau} \end{bmatrix} + \begin{bmatrix} \xi'_1 \\ \vdots \\ \xi'_t \end{bmatrix},$$

which can be solved using standard statistical linear least squares solution methods, assuming that the transmission envelopes result in a non-singular covariance matrix.

Faster filtering solution

If the transmission waveforms ϵ_t^a and ϵ_t^b are designed in such a way that for some τ:

$$\begin{aligned} \left|\epsilon_t^a \overline{\epsilon_{t+\tau}^b}\right| &> 0 \\ \epsilon_t^a \overline{\epsilon_{t+\tau}^a} &= 0 \\ \epsilon_t^b \overline{\epsilon_{t+\tau}^b} &= 0 \\ \epsilon_t^b \overline{\epsilon_{t+\tau}^a} &= 0 \end{aligned}$$

Then our measurement equation is a convolution of Faraday rotated backscatter $\sigma_{r,\tau}^4$ and the lagged product of the transmission envelopes $\epsilon_{t-r}^a \overline{\epsilon_{t-r+\tau}^b}$:

$$m_t = \sum_r \epsilon_{t-r}^a \overline{\epsilon_{t-r+\tau}^b} \sigma_{r,\tau}^4 + \xi'_t.$$

This can be used to perform dual-polarization measurements of Faraday-rotation with very little computational resources compared to the full matrix equations.

5.7.4 Other methods

Lag-profile inversion is a fairly new method of analysing range and Doppler spread targets. However, previous methods do have certain similarities to this method. For example, the integrated correlator method used at EISCAT can be thought of as a correlation estimator of the same measurement equations that are used in lag-profile inversion. The down-side to this method, however, is that it cannot account for missing data on the raw voltage level, and thus this method is potentially more vulnerable to interfering space debris and meteor head echoes, as they have to be detected in power domain instead of amplitude domain. Also, if the transmission envelopes are not "perfect", the resulting integrated correlator dumps will have range sidelobes as bias, whereas the lag-profile inversion method can readily use the actual transmitted waveform sampled from the waveguide.

Another method for analyzing incoherent scatter targets is the so called full-profile inversion method [95, 146, 147]. This method operates directly on the averaged lag-products $m_t\overline{m_{t+\tau}}$ and makes no attempt to estimate unambiguous autocorrelation functions, but fits the full profile of ionospheric parameters using incoherent scatter theory directly to the ambiguous lag-product matrices. This method assumes that the plasma parameters that define the measured backscatter autocorrelation functions are characterized by functions that vary smoothly with altitude. This can be seen as a form of regularization. While this method is optimal in the sense that it uses all of the information optimally, the method has a drawback that one needs to assume a certain theory in advance. Also, one cannot escape the range ambiguities with full-profile inversion either. If the experiment has wide range ambiguities, this will result in poor resolution when fitting the theory to the measurements.

The principle behind lag-profile inversion is to first make an unbiased estimate of the incoherent scatter autocorrelation functions at each range gate, and then fit a theory to it. Thus, there is no reason why lag-profile inversion couldn't be used together with full-profile inversion when fitting the plasma parameters to the estimated autocorrelation functions – such processing would certainly be beneficial when fitting the incoherent scatter theory to the measured autocorrelation functions.

6. Optimal radar experiment design

The purpose of optimal experiment design is to minimize the estimation errors that are described by the *a posteriori* probability distribution of the measurement model. In the case of radar measurements there are a multitude of experiment configurations typically available in a radar system. For example, in traditional fixed antenna radar systems, one typically can modify transmission pulse intervals, transmission coding (transmission waveform) and radar pointing direction. In newer phased-array systems there are even more possibilities, such as locations of the individual antennas that comprise the aperture [22] or beam shape [148]. These factors affect the posteriori distribution of the parameters estimated from the measurements.

Traditionally, optimal experiment design [10] deals with one-dimensional optimality criteria that are derived from the posteriori error covariance matrix of the estimated parameters. One example of this is the so called A-optimality, which is the sum of the diagonal of the estimation error covariance matrix.

A more recent and less well known framework that can be applied to optimization of experiments is the *theory of comparison of experiments* [11]. This is a more powerful framework, which can be used to test if some "measurement is always as good as or better than some other experiment". In simplified terms, a measurement m_1 is better or equal to another m_2 only if one can simulate m_2 using m_1 using some transformation and possibly adding some sort of noise. The measurements are equally good if the converse is also true. In the case of linear models, one measurement is better than another measurement if all of the elements of the a posteriori covariance matrix are smaller than the elements of the posteriori covariance matrix of the other measurement. This framework is nicely demonstrated for comparison of radar transmission codes

by Lehtinen [134], where codes are characterized as being at least as good as a perfect code with some transmission power.

Traditionally, code optimality has been studied mainly from the perspective of minimizing artefacts that result from correlating the measurements with the theory matrix, which in the case of a coherent target means correlating the measurements with the transmission envelope. This is analogous to the correlation estimator discussed in Section 2.7.6. The historical reason for this is perhaps that radar measurements used to be analyzed with specialized hardware with very limited computational capabilities, which dictated the use of the less computationally demanding correlation estimate. While this sort of optimality does heuristically make sense, a more correct approach is to use the characteristics of estimation errors to determine what experiment setup is optimal.

In this section we will briefly go through some aspects of radar experiment design, which have played some role during the thesis work. These include transmission code optimization for stationary range spread targets[1], as well for range and Doppler spread targets[2]. We will also briefly discuss transmission pulse spacing without going very deep into the topic.

6.1 Range spread targets

Range spread targets can be characterized as radar targets that consist of scatterers or a scattering medium which is approximately stationary during the time when the transmission pulse travels through the medium. This has several advantages in terms of target backscatter estimation – mainly that the measurement equation can often be approximated as a convolution over the duration of one transmission pulse. Range spread targets are the most typical type of a radar target, and therefore this type of a radar target has been studied extensively in terms of experiment optimization.

The literature on traditional code optimization mostly discusses minimization of the off-diagonal elements of $\mathbf{A}^{\mathrm{H}}\mathbf{A}$ [149, 126], where the theory matrix containing the measurement equations is contained in $\mathbf{A}$, typically in the form of a convolution equation or variants of it, which also possibly take into account that the target is stationary over several interpulse periods.

[1] Also referred to as a coherent target.
[2] Also referred to as incoherent scatter target.

In terms of maximum likelihood estimation of the target backscatter estimation, it is also easy to directly inspect the covariance matrix of the measurement errors $\mathbf{\Sigma} = (\mathbf{A}^{\mathrm{H}}\mathbf{A})^{-1}$.

6.1.1 Barker codes

An important class of codes for coherent targets are so called Barker codes [126], which have the property that the off-diagonal elements of the autocorrelation function (rows of $\mathbf{A}^{\mathrm{H}}\mathbf{A}$) are always less or equal than one $|r_t| \leq 1$. There are seven known binary phase sequences with this property, with the longest code length of only 13. Recently longer polyphase Barker sequences have been found at lengths up to 77 [130, 131], and it is likely that even longer sequences can be found in the future.

Binary phase Barker codes have also been found to be optimal in terms of maximum likelihood estimation (sidelobe free decoding) of target backscatter amplitude [128, 129]. The autocorrelation function of a certain transmission code is also related with the backscatter estimation error covariance matrix, as it is the inverse of the covariance matrix $\mathbf{\Sigma}^{-1} = \mathbf{A}^{\mathrm{H}}\mathbf{A}$.

6.1.2 Complementary codes

Complementary codes [127] or Golay sequences are pairs of codes that are optimal for measuring targets. There is an underlying assumption that the target has to be stationary over the duration of two transmission pulses. In this case, the theory matrix is a set of two stacked convolution equations

$$\mathbf{A} = \begin{bmatrix} \mathbf{A_1} \\ \mathbf{A_2} \end{bmatrix}, \tag{6.1}$$

with one convolution equation $\mathbf{A}_i$ for each code. Complementary codes are optimal in the sense that the theory matrix for the target backscatter results in a diagonal covariance matrix $(\mathbf{A}^{\mathrm{H}}\mathbf{A})^{-1} = L^{-1}\mathbf{I}$, where L is the combined power of the two transmission envelopes, assuming that the measurement errors have a diagonal covariance matrix of the form $\mathbf{\Sigma} = \mathbf{I}$. In addition to this, the correlation estimate $\mathbf{A}^{\mathrm{H}}\mathbf{m}$ is also the unscaled maximum likelihood estimate for target backscatter, if the error covariance matrix is diagonal.

An example of a complementary code pair is

$$C = \{++-+-+--++, +++-+++++--\}, \tag{6.2}$$

where the two phases are represented with a plus and a minus signs.

Golay sequences are know to exist at lengths $N = 2^\alpha 10^\beta 26^\gamma$, where $\alpha, \beta, \gamma \geq 0$. Longer codes can be generated recursively from shorter complementary codes (c_1, c_2) using the follow rule

$$(c_1', c_2') = (c_1|c_2, c_1| - c_2), \tag{6.3}$$

where $|$ is the concatenation operator.

It is also possible to form polyphase complementary code pairs. In addition to this, longer groups of codes with the complementary code property can be formed, although these are perhaps not that practical, as one has to assume stationarity of the target over the whole transmission cycle of the codes.

6.1.3 Kronecker product codes

The Kronecker product construction formula is useful for forming very long transmission codes with good performance in terms of maximum likelihood estimation of a stationary target. This is a method for forming long codes from known good short codes. This is because it is easy to exhaustively search for shorter codes, while it is impossible to perform an exhaustive search for longer codes.

Consider pulse codes with phases and amplitudes determined by finite vectors $\boldsymbol{\epsilon^1} \in \mathbb{C}^p$ and $\boldsymbol{\epsilon^2} \in \mathbb{C}^q$. The Kronecker product $\boldsymbol{\epsilon^1} \otimes \boldsymbol{\epsilon^2} \in \mathbb{C}^{pq}$ of these codes is defined as

$$\boldsymbol{\epsilon^1} \otimes \boldsymbol{\epsilon^2} = \left[\epsilon_1^1 \boldsymbol{\epsilon^2}, \quad \epsilon_2^1 \boldsymbol{\epsilon^2}, \quad \cdots \quad , \epsilon_p^1 \boldsymbol{\epsilon^2}\right], \tag{6.4}$$

which has beneficial properties in terms of code construction, as it can be shown that the deconvolution estimation variance of an inverse filter for a code of this form "inherits" the variance of the codes $\boldsymbol{\epsilon^1}$ and $\boldsymbol{\epsilon^2}$. The continuous time Kronecker product code $\epsilon^{1,2}(t)$ can be seen as a convolution of the two continuous time Dirac delta spike trains $\epsilon^1(t)$ and $\epsilon^2((p+1)^{-1}t)$

$$\begin{aligned}
\epsilon^1(t) &= \sum_{i=1}^{N} \epsilon_i^1 \delta(t - i\Delta t) \\
\epsilon^2(t) &= \sum_{i=1}^{N} \epsilon_i^1 \delta(t - i\Delta t) \\
\epsilon^{1,2}(t) &= \sum_{\tau=-\infty}^{\infty} \epsilon^1(\tau)\epsilon^2((p+1)^{-1}(t-\tau))
\end{aligned}$$

An example Kronecker product code is shown in Fig. 6.1.

As the discrete Fourier transform of $\epsilon^2((p+1)t)$ is a periodic function with $p+1$ periods between 0 and 2π, we can obtain the following lower

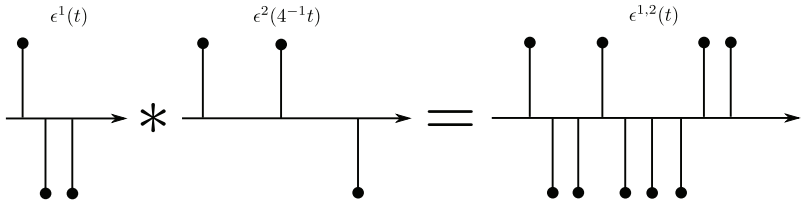

Figure 6.1. A Kronecker product code constructed from codes $\epsilon^1 = (1, -1, -1)$ and $\epsilon^2 = (1, 1, -1)$.

and upper bounds for the Kronecker product code variance

$$\begin{aligned} \int_0^{2\pi} \frac{1}{\max|\hat{\epsilon}^1(\omega)|^2 \max|\hat{\epsilon}^2(\omega)|^2} d\omega &\leq \\ \int_0^{2\pi} \frac{1}{|\hat{\epsilon}^1(\omega)|^2 |\hat{\epsilon}^2((p+1)\omega)|^2} d\omega &\leq \\ \int_0^{2\pi} \frac{1}{\min|\hat{\epsilon}^1(\omega)|^2 \min|\hat{\epsilon}^2(\omega)|^2} d\omega & \end{aligned} \tag{6.5}$$

Perhaps the most useful estimate of variance can be obtained by multiplying the variance of the two codes that form the Kronecker product. This gives a useful way of predicting the performance of a long code based on the performance of two shorter codes:

$$\int \frac{pq}{|\hat{\epsilon}^1(\omega)|^2 |\hat{\epsilon}^2((p+1)\omega)|^2} d\omega \approx \int \frac{p}{|\hat{\epsilon}^1(\omega)|^2} d\omega \int \frac{q}{|\hat{\epsilon}^2(\omega)|^2} d\omega. \tag{6.6}$$

The approximation assumes that the $\hat{\epsilon}^1(\omega)$ is constant over one cycle of $\hat{\epsilon}^1((p+1)\omega)$, therefore the approximation accuracy depends on p. The larger p is, the more accurate the approximation is. The approximation approaches the exact value when $p \to \infty$.

Kronecker product codes can be used as an initial guess for very long optimized codes. They can be used to create extremely long codes that are very close to perfect e.g., from long polyphase Barker codes [130, 131]. Optimized binary phased codes and frequency stepped codes were created using a Kronecker product code from shorter binary phase Barker codes as an initial code in the lunar mapping experiment described in Publication V.

6.1.4 Perfect and almost perfect transmission codes

Perfect codes [134] are codes that have the smallest theoretically possible estimation variance, i.e., they are equivalent to a short one-baud uncoded pulse of the same power. Such a transmission sequence has to include amplitude modulation. This can be seen by inspecting the autocorrelation function of a constant amplitude transmission envelope, which has

at least one unit amplitude sidelobe on the outer reaches of the autocorrelation function, as it is a product of two arbitrary complex numbers with a non-zero amplitude. Perfect codes are also infinitely long, but they can be made infinitely long in only one direction. Also, the amplitude of a perfect code can be designed in such a way that it decreases rapidly, in which case a truncated version of the transmission envelope is already extremely close to perfect.

Nearly perfect finite length codes were initially discovered using optimization searches for phase and amplitude modulated pulse codes [1]. In this study it was found that the estimation error variance could be made extremely small (the estimation error variance was 10^{-6} from perfect) by allowing amplitude modulation to a finite length transmission sequence. In practical applications, such codes will already be very close to optimal.

Since then, several different analytic methods have been developed for producing perfect codes. Of these, there are two noteworthy versions.

The first method transforms an arbitrary non-ideal transmission envelope into a perfect one, by scaling the frequency domain modulus to unity, and then transforming the projected perfect transmission envelope back into time domain [134]. This method involves initially selecting a radar transmission code $\epsilon(t)$ which is not perfect. This code is then Fourier transformed $\hat{\epsilon}(\omega)$, and the Fourier representation of the perfect code is obtained by scaling with $|\hat{\epsilon}(\omega)|$, the perfect code $\epsilon_p(t)$ is obtained by inverse Fourier transforming this scaled code back to time domain

$$\epsilon_p(t) = \int_{-\infty}^{\infty} \frac{\hat{\epsilon}(\omega)}{|\hat{\epsilon}(\omega)|} e^{-i\omega t} d\omega. \tag{6.7}$$

This constructive method can also be used in iterative searches for nearly perfect codes with constraints applied to the shape of the amplitude envelope [134].

Another method[3] relies on the autoregressive moving average all-pass filter design equation [150]

$$H(\omega) = \frac{\overline{a_1} + \overline{a_1} e^{-i\omega} + \overline{a_2} e^{-i2\omega} \cdots \overline{a_N} e^{-iN\omega}}{a_N + a_{N-1} e^{-i\omega} + a_2 e^{-i2\omega} \cdots a_1 e^{-iN\omega},} \tag{6.8}$$

where $a_i \in \mathbb{C}$ are autoregressive moving average filter coefficients. This design equation has by definition the property that the modulus in frequency domain is constant $|H(\omega)| = \alpha$, which guarantees that the transmission code is perfect. The perfect radar transmission code would be the impulse response of the filter in time domain. In other words, any digital

[3] Roininen 2012, publication in review

autoregressive moving average all-pass filter can be used to produce a perfect radar transmission code. This has the advantage that in some cases the transmission code has non-zero amplitude that extend to infinity only on one side. However, the disadvantage of these types of codes is that the amplitude envelope of these waveforms is typically not very flat, which is often necessary in order to maximize of duty-cycle of a high power radar transmitter.

While perfect codes have the property that they have theoretically optimal estimation error variance, they always require at least some form of amplitude modulation. This is sometimes difficult to realize in common high power amplifier designs, as there is typically some peak power that cannot be exceeded. Also, radar transmission envelopes for a monostatic radar should be as compact as possible in time, so that one can start receiving the echoes as soon as possible. Also, as there exist constant amplitude transmission codes, such as Barker codes, with only 3-15 % worse estimation error variance, the improvement obtained with perfect transmission coding is not always very significant.

6.1.5 Fractional baud-length coding

Fractional baud-length coding is a novel coding method presented in Publication III. The main goal of this method is to improve target range and Doppler estimation accuracy, which is achieved by using non-uniform baud lengths. With this method it is possible to improve the sub-baud range-resolution of phase-coded radar measurements while maintaining a narrow transmission bandwidth. By using non-uniform baud-lengths, it is possible to avoid zeros in the frequency domain representation of the transmission code, which would otherwise make sub-baud resolution impossible or extremly ill-posed. In other words, using non-uniform baud-lengths reduces the backscatter estimation error variance when analyzing the target at resolutions that are better than the minimum allowed baud-length would otherwise allow.

6.1.6 Periodically perfect codes

In certain cases when the radar target has a finite range extent and there is a possiblity of bi-static receiving and 100% duty-cycle transmit, one can use a class of codes that are perfect in terms of periodic autocorrelation. In this case, one makes use of the fact that the radar echoes are confined

into a narrow region, and that the backscatter from the previous and next transmit pulse are approximately the same. This assumption makes it possible to model the radar measurement from a single echo using a periodic convolution equation with a theory matrix of the form shown in Eq. 2.78.

There are at least two types of related codes that are optimal for this type of a measurement equation, Frank codes and Zadoff-Chu codes [151].

Asteroid measurements and lunar ISAR are examples of targets that are confined in range extent and can be approximated as stationary targets over a short period of time due to the fact that they have a bulk Doppler shift that is well known.

6.1.7 Random code groups

Random code groups were introduced by Sulzer [3] for measuring incoherent scatter autocorrelation functions with minimal sidelobes. This relied on the property that random sequences are nearly orthogonal when there are enough of them. This relies on the fact that provided with enough random codes in the measurement, the theory matrix $\mathbf{A}$ for the lag-profile measurement is orthogonal enough, i.e., $\mathbf{A}^{\mathrm{H}}\mathbf{A} \approx \alpha\mathbf{I}$. In this case, the correlation estimate discussed in Section 2.7.6 is a fairly good approximation of an unbiased maximum likelihood estimate.

When using lag-profile inversion methods for analyzing random code groups, the error variance of the lag-product estimates obtained using randomly selected code groups is very close to theorethically optimal, as was shown in Publication II of this thesis.

6.1.8 Alternating codes

Alternating codes were first introduced by Lehtinen [21]. They provide sidelobe-free decoding of the incoherent scatter autocorrelation function for inter-pulse lags, i.e., the theory matrix is orthogonal $\mathbf{A}^{\mathrm{H}}\mathbf{A} = \alpha\mathbf{I}$. In addition to this, so called *strong alternating codes* are known, which can also be used to remove the effect of receiver impulse response. Since their introduction, shorter type II alternating code groups have also been introduced by Sulzer [124].

Although the first binary phase shift keying alternating code groups were initially found using a clever exhaustive search method, a method for generating arbitrarily long sequences have since been found for both

binary phase [125] and polyphase alternating codes [123].

When inspecting the lag estimation error variance, alternating codes have been shown to be optimal, i.e.., no code groups of similar length and power, utilizing a uniform transmission amplitude have better estimation error variance [21].

The original alternating codes are known to result in strong correlations between autocorrelation function estimates in adjacent range gates when measuring a high SNR target. This, however, can be remedied by randomizing the alternating code group, i.e., by multiplying all codes in a set of alternating codes with a random phase vector, which is randomized at the beginning of each cycle [15].

6.1.9 Optimized code groups

While randomized code groups and alternating codes can be shown to be close to optimal or optimal, there are cases where one would like to utilize shorter tranmission code groups, e.g., to simplify ground clutter removal. In this case, one can use optimization algorithms to find code groups that have small estimation variance [152] and result in a short code group. This was studied in Publication II included in this thesis.

It is also possible to optimize other aspects, like, e.g., the estimation error variance of ranges where one can only measure the target with a small portion of the transmission code (lower altitudes), or in the case where different altitudes are analyzed with different range resolutions [14].

6.2 Transmission pulse spacing

Transmission pulse spacing plays an important role in radar measurements. For incoherent scatter in the E- and F-region, the decorrelation time of the target is so short that typically only intrapulse lags can be estimated. In this case, the main criteria for experiment design is the length of the transmission pulse, which has to be long enough to be able to measure long enough lags, so that the incoherent scatter autocorrelation function can be effectively measured. In the D region of the ionosphere, the correlations are longer, and pulse-to-pulse correlations need to be estimated. As the decorrelation times depend on the radar frequency, different radars typically require different timings.

In the case of monostatic radar, measurements cannot be made when transmitting. Part of the echo is also lost because of receiver protection and ground clutter before and after the transmission pulse. If equal pulse spacing is used, there will be persistent areas in range where no measurement can be made. This however can be remedied with the use of aperiodic interpulse intervals [76, 153, 154, 155, 156, 16, 17, 14, 157, 158]. In this way, the transmission pulse gap appears at different ranges, and over a sufficiently long integration time echoes can be obtained from all ranges and at a more diverse set of lags.

Uniform pulse spacing also typically suffers from what is known as the range-Doppler dilemma, which applies for radar measurements that utilize uniform interpulse periods and pulses always coded in the same way. The problem is two-fold. Decreasing the interpulse period allows better spectral width for pulse-to-pulse measurements, but at the same time decreases the unambiguous range. Inversely, increasing the interpulse period on the other hand decreases unambiguous spectral width, while it increases the unambiguous range. Typically incoherent scatter radar measurements utilize long groups of coded pulses, which can already be used to solve the range aliasing problem. Utilizing non-uniform pulse spacings also allows increased spectral resolution. Combining non-uniform spacing and radar transmission coding can be thus seen as a solution to the range-Doppler dilemma [153, 154, 155, 156, 157, 158].

7. Conclusions

This introduction has attempted to cover many important aspects related to statistical analysis of radar measurements with emphasis on the types of measurements that I have encountered during my work. This includes probability theory, numerical methods, high power large aperture radars, radar measurement models, and radar experiment optimization. The work has also included a great deal of software engineering with digital receiver hardware, radars, and numerical analysis software. Unfortunately there was not enough space to include any of this in the introduction to this thesis.

The main results of this thesis include a novel amplitude domain incoherent scatter analysis method presented in Publication I and Publication III. Publication III introduces a new type of radar transmission code that can be used to perform high resolution incoherent scatter measurements using a narrow effective transmission bandwidth. Publication II presented a stochastic optimization method that can be used for finding near-optimal radar transmission waveforms that minimize the variance of incoherent and coherent scatter radar estimates. Publication IV of this thesis presents the first EISCAT 32-cm wavelength radar mapping measurements of the Moon. Finally, Publication V presents two beam-park measurements of the Iridium-Cosmos satellite collision that occured in 2009. This event raised the public awareness of the man-made environmental problem called space debris, which can negatively affect our ability to safely operate satellites and spacecraft in the future. The EISCAT measurements shown in this thesis were one of the few publicly available measurements produced shortly after this collision.

It is evident that future radar and signal processing hardware will allow radar measurements with more receiver channels and more receiver bandwidth. Cheap solutions for data transfer and absolute timing will

also allow easier deployment of multi-static receivers. This will allow the use of multiple beams and polarization diversity. These features can be used to e.g., improve imaging of radar targets [159], or to extract physical parameters from polarization measurements [139]. Many of the possibilities that these technological advances will allow are yet to be invented. The possibility of being able to deploy a low cost sparse field of antennas has a potential to revolutionize traditional geophysical instruments, such as ionosondes and riometers.

Incoherent scatter radars of the future will be more geared towards continuous environmental monitoring, instead of the campaign based observation modes of the past. A good example of this is the new AMISR system, which operates constantly in low power mode, providing a continuous measurement of the ionosphere. Future incoherent scatter radars should also provide more than just ionospheric plasma parameters. With little extra effort, the same instrument and radar measurement modes can also be used to provide a continuous measurement of trajectories of meteors entering our atmosphere and space debris orbiting our planet.

In order to obtain the maximum amount of information from these continuous measurements, new types of general purpose radar experiments [16, 14] and flexible analysis methods [20] need to be developed. Such types of experiments and analysis methods should allow monitoring of as many regions of the ionosphere and as many types of phenomena as possible. Some care also needs to be taken in order to preserve the necessary information to allow flexible analysis of the radar measurements. Typically this can be done by storing the raw voltage samples from the radar receiver, preferably with multiple channels that provide interferometric information. Preferably the raw voltage samples should be the primary method of storing the measurements, in order to allow more sophisticated post processing of interesting events, or even allowing reprocessing of the data with methods that perhaps haven't even been developed yet.

One future challenge for high power large aperture radars is the automatic recognition of the various sporadic radar targets. The most notable ones are meteor head echoes and space debris (see Section 5.3, [5], and [6]). Another example of these types of special events are the so called naturally enhanced ion acoustic line echoes [160]. These radar targets are interesting in their own right, but they also need to be detected and removed from ionospheric measurements in order to avoid these echoes from degrading the quality of ionospheric plasma parameter measure-

ments. In terms of statistical theory, the optimal method for detecting these types of targets is Bayesian model selection. *The main challenge is to make such model selection and comparison fast enough to be used in real time*.

While polarization diversity has been used already in a few radars for over 40 years [143], most ionospheric radars still utilize only one circular polarization. Not only can polarization diversity be used to obtain information about the physical properties of the medium [139, 77], recent developments in coding theory [145] show that polarization can also be used to significantly reduce the error variance of these measurements. Section 5.7.3. of this thesis attempts to address dual polarization incoherent scatter radar measurements by extending the lag-profile inversion method [20, 142] for the case of dual polarization measurements.

Even after over 50 years history, the theory of incoherent scatter is still developing, a good example of this is that the theory of incoherent scatter for perpendicular to magnetic field pointing direction was only recently developed [161, 162]. For a radar with the capability of pointing perpendicular to the field lines, this theory also allows us to obtain more information about the plasma parameters by simultaneously pointing off perpendicular and perpendicular.

Much has already been done with ground based high power large aperture radar measurements, but there is still much more to be done. New instruments, such as AMISR and the planned EISCAT 3D, will be capable of nearly autonomous operation. These instruments will collect far more data than any of the existing systems, and a major challenge will be to extract as much useful information from these measurements as possible, in order to justify the cost of operating them.

Bibliography

[1] J. Vierinen, M. S. Lehtinen, M. Orispää, and B. Damtie, "General radar transmission codes that minimize measurement error of a static target, arxiv:physics/0612040v1." published on-line at arxiv.org, 2006.

[2] J. Vierinen, "Fractional baud-length coding," *Annales Geophysicae*, vol. 29, no. 6, pp. 1189–1196, 2011.

[3] M. Sulzer, "A radar technique for high range resolution incoherent scatter autocorrelation function measurements utilizing the full average power of klystron radars," *Radio Science*, vol. 21, no. 6, pp. 1033–1040, 1986.

[4] M. S. Lehtinen, I. I. Virtanen, and J. Vierinen, "Fast comparison of IS radar code sequences for lag profile inversion," *Annales Geophysicae*, vol. 26, no. 8, pp. 2291–2301, 2008.

[5] J. Markkanen, M. S. Lehtinen, A. Huuskonen, and A. Väänänen, *Measurements of Small-Size Debris with Backscatter of Radio Waves*. Final Report, ESOC Contract No. 13945/99/D/CD, 2002.

[6] J. Markkanen, M. Lehtinen, and M. Landgraf, "Real-time space debris monitoring with EISCAT," *Advances in Space Research*, vol. 35, no. 7, pp. 1197–1209, 2005.

[7] H. Krag, P. Beltrami-Karlezi, J. Bendisch, H. Klinkrad, D. Rex, J. Rosebrock, and T. Schildknecht, "PROOF – The extension of ESA's MASTER model to predict debris detections," *Acta Astronautica*, vol. 47, no. 2-9, pp. 687 – 697, 2000. Space an Integral Part of the Information Age.

[8] J. Mitola, *Software Radio Architecture: Object-Oriented Approaches to Wireless Systems Engineering*. John Wiley & Sons, Inc., 2002.

[9] T. Grydeland, F. D. Lind, P. J. Erickson, and J. M. Holt, "Software radar signal processing," *Annales Geophysicae*, vol. 23, no. 1, pp. 109–121, 2005.

[10] F. Pukelsheim, *Optimal Design of Experiments*. John Wiley & Sons, 1993.

[11] P. Piiroinen, *Statistical measurements, experiments and applications*. Academia Scientiarum Fennica, 2005.

[12] J. Vierinen, M. S. Lehtinen, M. Orispää, and I. I. Virtanen, "Transmission code optimization method for incoherent scatter radar," *Annales Geophysicae*, vol. 26, no. 9, pp. 2923–2927, 2008.

[13] J. Vierinen, M. S. Lehtinen, and I. I. Virtanen, "Amplitude domain analysis of strong range and Doppler spread radar echos," *Annales Geophysicae*, vol. 26, no. 9, pp. 2419–2426, 2008.

[14] I. I. Virtanen, J. Vierinen, and M. S. Lehtinen, "Phase-coded pulse aperiodic transmitter coding," *Annales Geophysicae*, vol. 27, no. 7, pp. 2799–2811, 2009.

[15] M. S. Lehtinen, A. Huuskonen, and M. Markkanen, "Randomization of alternating codes: Improving incoherent scatter measurements by reducing correlations of gated ACF estimates," *Radio Science*, vol. 32, no. 6, pp. 2271—-2282, 1997.

[16] I. I. Virtanen, M. S. Lehtinen, and J. Vierinen, "Towards multi-purpose IS radar experiments," *Annales Geophysicae*, vol. 26, no. 9, pp. 2281–2289, 2008.

[17] J. Vierinen, M. S. Lehtinen, J. Markkanen, and I. I. Virtanen, "Measuring space debris with phase coded aperiodic transmission sequences," in *Proc. Fifth European Conference on Space Debris*, 2009.

[18] A. Kero, C.-F. Enell, A. Kavanagh, J. Vierinen, I. Virtanen, and E. Turunen, "Could negative ion production explain the polar mesosphere winter echo (PMWE) modulation in active HF heating experiments?," *Geophysical Research Letters*, vol. 35, no. 23, 2008.

[19] A. Kero, J. Vierinen, C.-F. Enell, I. I. Virtanen, and E. Turunen, "New incoherent scatter diagnostic methods for the heated D-region ionosphere," *Annales Geophysicae*, vol. 26, no. 9, 2008.

[20] I. I. Virtanen, M. S. Lehtinen, T. Nygren, M. Orispaa, and J. Vierinen, "Lag profile inversion method for EISCAT data analysis," *Annales Geophysicae*, vol. 26, no. 3, 2008.

[21] M. Lehtinen, *Statistical theory of incoherent scatter measurements*. EISCAT Tech. Note 86/45, 1986.

[22] H. L. Van Trees, *Optimum Array Processing*, vol. 4. Wiley-Interscience, 2002.

[23] S. M. Rytov, Y. A. Kravtsov, and V. I. Tatarskii, *Principles of statistical radiophysics. 4. Wave propagation through random media*. Springer, 1989.

[24] V. I. Tatarskii, *Wave Propagation in a Turbulent Medium*. McGraw-Hill, 1961.

[25] R. Gray, "Toeplitz and circulant matrices: A review," 1977.

[26] A. Böttcher, B. Silbermann, and A. Y. Karlovich, *Analysis of Toeplitz Operators (Springer Monographs in Mathematics)*. Secaucus, NJ, USA: Springer-Verlag New York, Inc., 2006.

[27] A. N. Kolmogorov, "Interpolation and extrapolation," *Bulletin de l'Academie des Sciences de U.S.S.R.*, 1941.

[28] J. Kaipio and E. Somersalo, *Statistical and Computational Inverse Problems*. Springer, 2004.

[29] J. L. Mueller and S. Siltanen, *Linear and Nonlinear Inverse Problems with Practical Applications*. Manuscript in preparation, 2011.

[30] A. Hald, *Cardano and Liber de Ludo Aleae, c. 1565*, pp. 33–41. John Wiley & Sons, Inc., 2005.

[31] D. Bellhouse, "Decoding Cardano's Liber de Ludo Aleae," *Historia Mathematica*, vol. 32, no. 2, pp. 180 – 202, 2005.

[32] P.-S. Laplace, *Théorie analytique des probabilités*.

[33] C. F. Gauss, *Theoria motus corporum coelestium in sectionibus conicis solem ambientum*. 1809.

[34] A.-M. Legendre, *Nouvelles méthodes pour la détermination des orbites des cométes*. 1805.

[35] R. Adrain, "Research concerning the probabilities of the errors which happen in making observations, &c," *The Analyst*, 1805.

[36] A. N. Kolmogorov, *Grundbegriffe der Wahrscheinlichkeitrechnung*. Julius Springer, 1933.

[37] T. Bayes, "An essay towards solving a problem in the doctrine of chances," *Phil. Trans. of the Royal Soc. of London*, vol. 53, pp. 370–418, 1763.

[38] E. T. Jaynes, *Probability Theory: The Logic of Science (Vol 1)*. Cambridge University Press, Apr. 2003.

[39] P. J. Schreier and L. L. Scharf, *Statistical Signal Processing of Complex-Valued Data: The Theory of Improper and Noncircular Signals*. Cambridge University Press, 2010.

[40] B. Picinbono, "Second-order complex random vectors and normal distributions," *IEEE Transactions on Signal Processing*, vol. 44, no. 10, pp. 2637–2640, 1996.

[41] N. R. Goodman, "Statistical analysis based on a certain multivariate complex gaussian distribution (an introduction)," *The Annals of Mathematical Statistics*, vol. 34, no. 1, pp. pp. 152–177, 1963.

[42] R. G. Gallager, *Principles of Digital Communication*. Cambridge University Press, 2007.

[43] M. Orispää and M. S. Lehtinen, "Fortran linear inverse problem solver," *Inverse Problems and Imaging*, vol. 4, no. 3, 2010.

[44] L. Roininen, M. S. Lehtinen, S. Lasanen, M. Orispää, and M. Markkanen, "Correlation priors," *Inverse Problems and Imaging*, vol. 5, no. 1, 2011.

[45] A. N. Tychonoff and V. Y. Arsenin, *Solution of Ill-posed Problems*. Winston & Sons, 1977.

[46] P. Hansen and S. Christiansen, "An SVD analysis of linear algebraic equations derived from first kind integral equations," *Journal of Computational and Applied Mathematics*, vol. 12-13, no. 0, pp. 341–357, 1985.

[47] P. C. Hansen and D. P. O'Leary, "The use of the L-curve in the regularization of discrete ill-posed problems," *SIAM Journal on Scientific Computing*, vol. 14, no. 6, 1993.

[48] N. R. Lomb, "Least-squares frequency analysis of unequally spaced data," *Astrophysics and Space Science*, vol. 39, pp. 447–462, 1976. 10.1007/BF00648343.

[49] D. O. North, "An analysis of the factors which determine signal/noise discrimination in pulsed carrier systems," tech. rep., RCA Labs, Princeton New Jersey, 1943.

[50] M. B. Priestley, *Spectral Analysis and Time Series*. London: Academic Press, 1981.

[51] U. Grenander and G. Szegö, *Toeplitz forms and their applications*. California Monographs in Mathematical Sciences, Berkeley: University of California Press, 1958.

[52] N. Wiener, *Extrapolation, Interpolation, and Smoothing of Stationary Time Series*. MIT Press, 1949.

[53] J. W. Cooley and J. W. Tukey, "An algorithm for the machine calculation of complex Fourier series," *Mathematics of Computation*, vol. 19, no. 90, pp. 297–301, 1965.

[54] M. Frigo and S. Johnson, "FFTW: an adaptive software architecture for the FFT," in *Proceedings of the 1998 IEEE International Conference on Acoustics, Speech and Signal Processing*, vol. 3, pp. 1381–1384, 1998.

[55] E. O. Brigham, *The fast Fourier transform and its applications*. Upper Saddle River, NJ, USA: Prentice-Hall, Inc., 1988.

[56] J. Keiner, S. Kunis, and D. Potts, "Using NFFT 3 – a software library for various nonequispaced fast Fourier transforms," *ACM Transactions on Mathematical Software*, vol. 36, no. 4, 2008.

[57] B. Damtie, M. Lehtinen, M. Orispää, and J. Vierinen, "Optimal long binary phase code-mismatched filter pairs with applications to ionospheric radars," *Bull. Astr. Soc. India*, vol. 35, 2007.

[58] G. H. Golub and C. F. Van Loan, *Matrix computations*. Baltimore, MD, USA: Johns Hopkins University Press, 3 ed., 1996.

[59] C. C. Paige and M. A. Saunders, "LSQR: An Algorithm for Sparse Linear Equations and Sparse Least Squares," *ACM Transactions on Mathematical Software*, vol. 8, no. 1, pp. 43–71, 1982.

[60] D. W. Marquardt, "An algorithm for least-squares estimation of nonlinear parameters," *SIAM Journal on Applied Mathematics*, vol. 11, no. 2, pp. 431–441, 1963.

[61] S. Kirkpatrick, C. D. Gelatt, and M. P. Vecchi, "Optimization by Simulated Annealing," *Science*, vol. 220, no. 4598, pp. 671–680, 1983.

[62] J. A. Nelder and R. Mead, "A simplex method for function minimization," *The Computer Journal*, vol. 7, no. 4, pp. 308–313, 1965.

[63] K. V. Price, R. M. Storn, and J. A. Lampinen, *Differential Evolution, A Practical Approach to Global Optimization*. Springer, 2005.

[64] W. R. Gilks, *Markov Chain Monte Carlo in Practice: Interdisciplinary Statistics (Chapman & Hall/CRC Interdisciplinary Statistics)*. Chapman & Hall/CRC, 1 ed., Dec. 1995.

[65] W. K. Hastings, "Monte Carlo sampling methods using Markov chains and their applications," *Biometrika*, vol. 57, pp. 97–109, Apr. 1970.

[66] S. Chib and E. Greenberg, "Understanding the Metropolis-Hastings Algorithm," *The American Statistician*, vol. 49, no. 4, pp. 327–335, 1995.

[67] H. Haario, M. Laine, A. Mira, and E. Saksman, "DRAM: Efficient adaptive MCMC," *Statistics and Computing*, vol. 16, no. 4, pp. 339–354, 2006.

[68] P. J. Green, "Reversible jump Markov chain Monte Carlo computation and Bayesian model determination," *Biometrika*, vol. 82, no. 4, pp. 711–732, 1995.

[69] M. Laine, *Adaptive MCMC methods with applications in environmental and geophysical models*. Finnish Meteorological Institute, 2008.

[70] O. Klemola and A. Lehto, *Tutkatekniikka*. Otatieto, 1998.

[71] E. V. Appleton and M. A. F. Barnett, "Local reflection of wireless waves from the upper atmosphere," *Nature*, no. 115, 1925.

[72] H. Rishbeth, "Reflections in Appleton's mirror: a century of ionospheric science," *Engineering Science and Education Journal*, vol. 4, no. 4, pp. 167–175, 1995.

[73] G. Breit and M. A. Tuve, "A test of the existence of the conducting layer," *Phys. Rev.*, vol. 28, pp. 554–575, Sep 1926.

[74] R. M. Goldstein, R. R. Green, G. H. Pettengill, and D. B. Campbell, "The rings of Saturn: Two-frequency radar observations," *Icarus*, vol. 30, no. 1, pp. 104 – 110, 1977.

[75] D. J. Daniels, *Ground Penetrating Radar*. John Wiley and Sons, Inc., 2005.

[76] M. I. Skolnik, *Radar Handbook (3nd Edition)*. McGraw-Hill, 2008.

[77] J. Bech and J. L. Chau, eds., *Doppler Radar Obervations – Weather Radar, Wind Profiler. Ionospheric Radar, and Other Advanced Applications*. Intech, 2012.

[78] E. J. Fremouw, J. A. Secan, and B. M. Howe, "Application of stochastic inverse theory to ionospheric tomography," *Radio Science*, vol. 27, pp. 721–732, Oct. 1992.

[79] P. Bernhardt, C. Selcher, S. Basu, G. Bust, and S. Reising, "Atmospheric Studies with the Tri-Band Beacon Instrument on the COSMIC Constellation," in *Applications of Constellation Observing System for Meteorology, Ionosphere & Climate* (L.-C. Lee, C. Rocken, & R. Kursinski, ed.), pp. 291–, 2001.

[80] W. Gordon, "Incoherent scattering of radio waves by free electrons with applications to space exploration by radar," *Proceedings of the IRE*, vol. 46, no. 11, pp. 1824 –1829, 1958.

[81] K. L. Bowles, "Observation of vertical-incidence scatter from the ionosphere at 41 mc/sec," *Phys. Rev. Lett.*, vol. 1, pp. 454–455, Dec 1958.

[82] K. L. Bowles, "Progress report #1: Lima radar observatory," tech. rep., National Bureau of Standards, 1961.

[83] W. E. Gordon, "Arecibo ionospheric observatory," *Science*, vol. 146, no. 3640, pp. 26–30, 1964.

[84] A. Pellinen-Wannberg, "The EISCAT meteor-head method – a review and recent observations," *Atmospheric Chemistry and Physics*, vol. 4, no. 3, pp. 649–655, 2004.

[85] J. L. Chau and F. Galindo, "First definitive observations of meteor shower particles using a high-power large-aperture radar," *Icarus*, vol. 194, no. 1, pp. 23 – 29, 2008.

[86] S. J. Ostro, "Planetary radar astronomy," *Rev. Mod. Phys.*, vol. 65, pp. 1235–1279, Oct 1993.

[87] R. F. Woodman and A. Guillen, "Radar observations of winds and turbulence in the stratosphere and mesosphere," *Journal of the Atmospheric Sciences*, vol. 31, no. 2, pp. 493–505, 1974.

[88] J. P. Dougherty and D. T. Farley, "A Theory of Incoherent Scattering of Radio Waves by a Plasma," *Royal Society of London Proceedings Series A*, vol. 259, pp. 79–99, Nov. 1960.

[89] J. A. Fejer, "Radio-wave scattering by an ionized gas in thermal equilibrium," *J. Geophys. Res.*, vol. 65, 1960.

[90] J. A. Fejer, "Scattering of radio waves of an ionized gas in thermal equilibrium in the presence of a uniform magnetic field," *Canadian Journal of Physics*, vol. 39, pp. 716–+, 1961.

[91] D. T. Farley, J. P. Dougherty, and D. W. Barron, "A Theory of Incoherent Scattering of Radio Waves by a Plasma II. Scattering in a Magnetic Field," *Royal Society of London Proceedings Series A*, vol. 263, pp. 238–258, Sept. 1961.

[92] J. P. Dougherty and D. T. Farley, "A theory of incoherent scattering of radio waves by a plasma, 3. scattering in a partly ionized gas," *J. Geophys. Res.*, vol. 68, no. 19, pp. 5473–5486, 1963.

[93] D. T. Farley, "A theory of incoherent scattering of radio waves by a plasma 4. the effect of unequal ion and electron temperatures," *J. Geophys. Res.*, vol. 71, 1966.

[94] E. Kudeki and M. Milla, *Incoherent Scatter Radar — Spectral Signal Model and Ionospheric Applications*. InTech, 2012.

[95] J. M. Holt, D. A. Rhoda, D. Tetenbaum, and A. P. van Eyken, "Optimal analysis of incoherent scatter radar data," *Radio Science*, vol. 27, 1992.

[96] M. S. Lehtinen and A. Huuskonen, "General incoherent scatter analysis and GUISDAP," *Journal of Atmospheric and Terrestrial Physics*, vol. 58, no. 1-4, pp. 435 – 452, 1996.

[97] M. Vallinkoski, *Error analysis of incoherent scatter radar measurements*. EISCAT Tech. Note 89/49, 1989.

[98] L. Dyrud, D. Wilson, S. Boerve, J. Trulsen, H. Pecseli, S. Close, C. Chen, and Y. Lee, "Plasma and electromagnetic simulations of meteor head echo radar reflections," *Earth, Moon, and Planets*, vol. 102, no. 1, pp. 383–394, 2008. 10.1007/s11038-007-9189-8.

[99] D. W. R. McKinley, *Meteor science and engineering.* 1961.

[100] J. Jones, P. Brown, K. Ellis, A. Webster, M. Campbell-Brown, Z. Krzemenski, and R. Weryk, "The Canadian Meteor Orbit Radar: system overview and preliminary results," *Planetary and Space Science*, vol. 53, no. 4, pp. 413 – 421, 2005.

[101] R. G. Roper, "Globmet–the contributions of radio meteor measurements to the middle atmosphere program," *Advances in Space Research*, vol. 10, no. 10, pp. 189 – 192, 1990.

[102] B. A. Lindblad, "Meteor radar rates, geomagnetic activity and solar wind sector structure," *Nature*, vol. 273, 1978.

[103] W. K. Hocking, B. Fuller, and B. Vandepeer, "Real-time determination of meteor-related parameters utilizing modern digital technology," *Journal of Atmospheric and Solar-Terrestrial Physics*, vol. 63, no. 2-3, pp. 155 – 169, 2001.

[104] D. Janches, J. D. Mathews, D. D. Meisel, and Q. H. Zhou, "Micrometeor Observations Using the Arecibo 430 MHz Radar: I. Determination of the Ballistic Parameter from Measured Doppler Velocity and Deceleration Results," *Icarus*, vol. 145, no. 1, pp. 53 – 63, 2000.

[105] D. Janches, L. P. Dyrud, S. L. Broadley, and J. M. C. Plane, "First observation of micrometeoroid differential ablation in the atmosphere," *Geophys. Res. Lett.*, vol. 36, 2009.

[106] J. Kero, C. Szasz, A. Pellinen-Wannberg, G. Wannberg, A. Westman, and D. D. Meisel, "Determination of meteoroid physical properties from tristatic radar observations," *Annales Geophysicae*, vol. 26, no. 8, pp. 2217–2228, 2008.

[107] H. Klinkrad, *Space debris: Models and Risk Analysis*. Springer, 2006.

[108] "NASA Orbital Debris Quarterly News," January 2010.

[109] D. J. Kessler and B. G. Cour-Palais, "Collision frequency of artificial satellites: The creation of a debris belt," *Journal of Geophysical Research*, vol. 83, pp. 2637–2646, June 1978.

[110] J.-C. Liou and N. Johnson, "Instability of the present LEO satellite populations," *Advances in Space Research*, vol. 41, no. 7, pp. 1046 – 1053, 2008.

[111] R. Jehn, "Comparison of the 1999 beam-park experiment results with space debris models," *Advances in Space Research*, vol. 28, no. 9, pp. 1367 – 1375, 2001.

[112] M. Kaasalainen and L. Lamberg, "Inverse problems of generalized projection operators," *Inverse Problems*, vol. 22, no. 749, 2006.

[113] M. Kaasalainen, J. Durech, B. Warner, Y. Krugly, and N. Gaftonyuk, "Acceleration of the rotation of asteroid 1862 Apollo by radiation torques," *Nature*, vol. 446, no. 7143, 2007.

[114] B. Bussey and Mini-RF Team, "Results from the first year of Mini-RF operations on Lunar Reconnaissance Orbiter," *AGU Fall Meeting Abstracts*, pp. A7+, Dec. 2010.

[115] G. H. Pettengill, E. Eliason, P. G. Ford, G. B. Loriot, H. Masursky, and G. E. McGill, "Pioneer Venus radar results altimetry and surface properties," *J. Geophys. Res.*, vol. 85, 1980.

[116] R. S. Saunders, G. H. Pettengill, R. E. Arvidson, W. L. Sjogren, W. T. K. Johnson, and L. Pieri, "The Magellan Venus Radar Mapping Mission," *J. Geophys. Res.*, vol. 95, 1990.

[117] G. Picardi, J. J. Plaut, D. Biccari, O. Bombaci, D. Calabrese, M. Cartacci, A. Cicchetti, S. M. Clifford, P. Edenhofer, W. M. Farrell, C. Federico, A. Frigeri, D. A. Gurnett, T. Hagfors, E. Heggy, A. Herique, R. L. Huff, A. B. Ivanov, W. T. K. Johnson, R. L. Jordan, D. L. Kirchner, W. Kofman, C. J. Leuschen, E. Nielsen, R. Orosei, E. Pettinelli, R. J. Phillips, D. Plettemeier, A. Safaeinili, R. Seu, E. R. Stofan, G. Vannaroni, T. R. Watters, and E. Zampolini, "Radar Soundings of the Subsurface of Mars," *Science*, vol. 310, no. 5756, pp. 1925–1928, 2005.

[118] T. W. Thompson, "High resolution Lunar radar map at 7.5 meter wavelength," *Icarus*, vol. 36, no. 2, pp. 174–188, 1978.

[119] B. Campbell, D. Campbell, J. Margot, R. Ghent, M. Nolan, J. Chandler, L. Carter, and N. Stacy, "Focused 70-cm wavelength radar mapping of the Moon," *Geoscience and Remote Sensing, IEEE Transactions on*, vol. 45, pp. 4032–4042, Dec. 2007.

[120] C. E. Shannon, "Communication in the Presence of Noise," *Proceedings of the IRE*, vol. 37, pp. 10–21, Jan. 1949.

[121] C. Chien, *Digital radio systems on a chip: a systems approach*. Norwell, MA, USA: Kluwer Academic Publishers, 2001.

[122] M. De Vos, A. W. Gunst, and R. Nijboer, "The LOFAR Telescope: System Architecture and Signal Processing," *Proceedings of the IEEE*, vol. 97, no. 8, pp. 1431–1437, 2009.

[123] M. Markkanen, J. Vierinen, and J. Markkanen, "Polyphase alternating codes," *Annales Geophysicae*, vol. 26, no. 9, pp. 2237–2243, 2008.

[124] M. P. Sulzer, "A new type of alternating code for incoherent scatter measurements," *Radio Science*, vol. 28, pp. 995–1001, 1993.

[125] M. Markkanen and T. Nygrén, "Long alternating codes: 2. practical search method," *Radio Science*, vol. 32, no. 1, pp. 9–18, 1997.

[126] R. Barker, "Group synchronizing of binary digital systems," *Communication Theory*, pp. 273–287, 1953.

[127] M. J. E. Golay, "Complementary series," *IRE Trans. Inf. Theory*, vol. IT-7, p. 82, 1961.

[128] J. Ruprecht, *Maximum-Likelihood Estimation of Multipath Channels*. PhD thesis, Swiss federal institute of technology, 1989.

[129] M. S. Lehtinen, B. Damtie, and T. Nygrén, "Optimal binary phase codes and sidelobe-free decoding filters with application to incoherent scatter radar," *Annales Geophysicae*, vol. 22, no. 5, 2004.

[130] L. Bomer and M. Antweiler, "Polyphase Barker sequences," *Electronics Letters*, vol. 25, no. 23, pp. 1577 –1579, 1989.

[131] C. Nunn and G. Coxson, "Polyphase pulse compression codes with optimal peak and integrated sidelobes," *Aerospace and Electronic Systems, IEEE Transactions on*, vol. 45, no. 2, pp. 775 –781, 2009.

[132] R. Frank, "Polyphase complementary codes," *Information Theory, IEEE Transactions on*, vol. 26, pp. 641 – 647, Nov. 1980.

[133] B. Damtie, M. S. Lehtinen, M. Orispää, and J. Vierinen, "Mismatched filtering of aperiodic quadriphase codes," *IEEE Transactions on information theory*, vol. 54, April 2008.

[134] M. S. Lehtinen, B. Damtie, P. Piiroinen, and M. Orispää, "Perfect and almost perfect pulse compression codes for range spread radar targets," *Inverse Problems and Imaging*, vol. 3, no. 3, pp. 465–486, 2009.

[135] R. Nikoukar, *Near-optimal inversion of incoherent scatter radar measurements: coding schemes, processing techniques, and experiments*. PhD thesis, University of Illinois at Urbana-Champaign, 2010.

[136] T. Hagfors and B. Isham, "Past applications and future uses of chirped ISR plasma line observations," *Advances in Space Research*, vol. 9, no. 5, pp. 143 – 152, 1989.

[137] I. I. Gihman and A. V. Skorohod, *The Theory of Stochastic Processes I*, vol. 210. Springer, 1974.

[138] R. H. Clarke, "A statistical theory of mobile radio reception," *Bell Systems Technical Journal*, vol. 47, no. 7, pp. 957–1000, 1968.

[139] V. Bringi and V. Chandrasekar, *Polarimetric Doppler Weather Radar: Principles and Applications*. Cambridge University Press, 2001.

[140] M. G. Parker, K. G. Paterson, and C. Tellambura, *Golay Complementary Sequences*. John Wiley and Sons, Inc., 2003.

[141] C. de Boor, *A Practical Guide to Splines*. Springer-Verlag, 1978.

[142] R. Nikoukar, F. Kamalabadi, E. Kudeki, and M. Sulzer, "An efficient near-optimal approach to incoherent scatter radar parameter estimation," *Radio Science*, vol. 43, 2008.

[143] D. T. Farley, "Faraday rotation measurements using incoherent scatter," *Radio Science*, vol. 4, no. 2, pp. 143–152, 1969.

[144] B. G. Shpynev, "Incoherent scatter Faraday rotation measurements on a radar with single linear polarization," *Radio Science*, vol. 39, 2004.

[145] B. Gustavsson and T. Grydeland, "Orthogonal-polarization alternating codes," *Radio Science*, vol. 44, 2009.

[146] M. S. Lehtinen, A. Huuskonen, and J. Pirttilä, "First experiences of full-profile analysis with GUISDAP," *Annales Geophysicae*, vol. 14, pp. 1487–1495, 1997. 10.1007/s00585-996-1487-3.

[147] D. L. Hysell, F. S. Rodrigues, J. L. Chau, and J. D. Huba, "Full profile incoherent scatter analysis at Jicamarca," *Annales Geophysicae*, vol. 26, no. 1, pp. 59–75, 2008.

[148] J. L. Chau, F. R. Galindo, C. J. Heinselman, and M. J. Nicolls, "Meteor-head echo observations using an antenna compression approach with the 450 MHz Poker Flat Incoherent Scatter Radar," *Journal of Atmospheric and Solar-Terrestrial Physics*, vol. 71, no. 6, pp. 636–643, 2009.

[149] R. Turyn, *Sequences with small correlation*. Wiley, 1976.

[150] M. Lang, "Allpass filter design and applications," *Signal Processing, IEEE Transactions on*, vol. 46, pp. 2505 –2514, sep 1998.

[151] N. Levanon and E. Mozeson, *Radar Signals*. Academic Press, 2004.

[152] J. D. Sahr and E. R. Grannan, "Simulated annealing searches for long binary phase codes with application to radar remote sensing," *Radio Sci.*, vol. 28, no. 6, pp. 1053–1055, 1993.

[153] D. T. Farley, "Multiple-pulse incoherent-scatter correlation function measurements," *Radio Science*, vol. 7, no. 6, p. 661–666, 1972.

[154] S. V. Uppala and J. D. Sahr, "Spectrum estimation of moderately overspread radar targets using aperiodic transmitter coding," *Radio Science*, vol. 29, p. 611–623, 1994.

[155] S. V. Uppala and J. D. Sahr, "Aperiodic transmitter waveforms for spectrum estimation of moderately overspread targets: new codes and a design rule," *IEEE Transactions on Geoscience and Remote Sensing*, vol. 34, p. 1285–1287, 1996.

[156] J. L. Chau, D. L. Hysell, P. M. Reyes, and M. A. Milla, "Improved spectral observations of equatorial spread F echoes at Jicamarca using aperiodic transmitter coding," *Journal of Atmospheric and Solar-Terrestrial Physics*, vol. 66, pp. 1543–1548, 2004.

[157] J. Pirttilä, M. S. Lehtinen, A. Huuskonen, and M. Markkanen, "A proposed solution to the range–doppler dilemma of weather radar measurements by using the SMPRF codes, practical results, and a comparison with operational measurements," *Journal of Applied Meteorology*, vol. 44, no. 9, pp. 1375–1390, 2005.

[158] J. Pirttilä and M. Lehtinen, "Solving the range-Doppler dilemma with ambiguity-free measurements developed for incoherent scatter radars," *COST 75, Advanced Weather radar systems, International seminar*, pp. 557–568, 1999.

[159] D. L. Hysell and J. L. Chau, "Optimal aperture synthesis radar imaging," *Radio Science*, vol. 41, 2006.

[160] Y. Ogawa, S. C. Buchert, I. Häggström, M. T. Rietveld, R. Fujii, S. Nozawa, and H. Miyaoka, "On the statistical relation between ion upflow and naturally enhanced ion-acoustic lines observed with the EISCAT Svalbard radar," *J. Geophys. Res.*, vol. 116, 2011.

[161] M. P. Sulzer and S. González, "The effect of electron Coulomb collisions on the incoherent scatter spectrum in the F region at Jicamarca," *J. Geophys. Res.*, vol. 104, 1999.

[162] E. Kudeki and M. A. Milla, "Incoherent scatter spectral theories — part I : A general framework and results for small magnetic aspect angles," *IEEE Transactions on Geoscience and Remote Sensing*, vol. 49, no. 1, pp. 315–328, 2011.

Publication I

J. Vierinen, M. S. Lehtinen, and I. I. Virtanen. Amplitude domain analysis of strong range and Doppler spread radar echos. ***Annales Geophysicae*****, 26, 2419-2426, August 2008.**

Ann. Geophys., 26, 2419–2426, 2008
www.ann-geophys.net/26/2419/2008/

Annales Geophysicae

Amplitude domain analysis of strong range and Doppler spread radar echos

J. Vierinen[1], **M. S. Lehtinen**[1], **and I. I. Virtanen**[2]

[1]Sodankylä Geophysical Observatory, 99600, Sodankylä, Finland
[2]Department of Physical Sciences, University of Oulu, P.O. Box 3000, 90014, Finland

Received: 3 January 2008 – Revised: 4 April 2008 – Accepted: 4 June 2008 – Published: 6 August 2008

Abstract. We present a novel method for analyzing range and Doppler spread targets in the amplitude domain using linear statistical inversion. The result of the analysis is an estimate of the range dependent amplitude behaviour of the target backscatter during the time that the transmission passes the target. A meteor head echo and strong backscatter from artificially heated regions of the ionosphere are used to demonstrate this novel analysis method. Plans to apply amplitude-domain radar target estimation methods to more complicated noisy underdetermined targets are also briefly discussed.

Keywords. Ionosphere (Active experiments; Ionospheric irregularities; Instruments and techniques)

1 Introduction

Incoherent scatter radar targets are usually analyzed in the power domain using lag-profile or correlation based methods. For example, Virtanen et al. (2008a) discusses autocorrelation function estimation of range and Doppler spread ionospheric targets through statistical inversion. On the other hand, for targets that are spread only in range, matched filters or range sidelobe-free inverse filters have been used to analyze targets in the amplitude domain (e.g. Sulzer, 1989; Ruprecht, 1989).

Lag-profile analysis usually implies pre-defined integration times, range gates and lags to be estimated. These settings do not necessarily preserve all the information of the target. Also, lag-profile analysis inherently implies that the target backscatter is modelled as a stationary stochastic process – an assumption which is not always true.

While filter based amplitude domain decoding methods are fast and well proven, they are not suitable for all situations. For example, the matched filter suffers from range ambiguities and has an underlying assumption of a point-like target. The sidelobe-free inverse filter on the other hand does not have range ambiguity problems (Lehtinen et al., 2004; Vierinen et al., 2006), but just like the matched filter, there is an assumption that the target scattering coefficient (being defined as the ratio of target backscatter to the complex amplitude of the transmission) stays constant while the transmission pulse travels through the target. In reality this assumption is often violated. A good example is the F-region heating that is discussed later.

In this study we present a novel method for estimation of the target backscattering in the amplitude domain. To do this, we model the time evolution of the reflection amplitude for each range gate using a parametric model. For a wide target that is also Doppler spread, this results in a difficult underdetermined problem with many more parameters than measurements. But when the target is sufficiently narrow in both range and Doppler spread, the problem becomes an overdetermined linear statistical inverse problem which can be solved. We describe this analysis procedure and as an example we show how to get high spatial and temporal resolution amplitude estimates of narrow and strong radar targets, even with transmissions that are coded with bauds longer than the range resolution. The fundamental limit is set by the sample rate used to measure the echo.

The strong artificial ionospheric heating effects shown in this study were seen at the EISCAT Tromsø site on 18 October 2007 with O-mode heating during an experiment that was mainly intended for D-region studies. The heating was pointed in vertical direction with a 10 s on 10 s off modulation. The heater was operating at 5.4 MHz with an effective radiated power of 600 MW. Strong backscatter was often seen during the heater on period. The radar experiment was designed to also probe ranges up to 1100 km unambiguously by use of uneven inter pulse periods, which enabled us to also see strong heating effects in the F-region with three

Correspondence to: J. Vierinen
(juha.vierinen@iki.fi)

Published by Copernicus Publications on behalf of the European Geosciences Union.

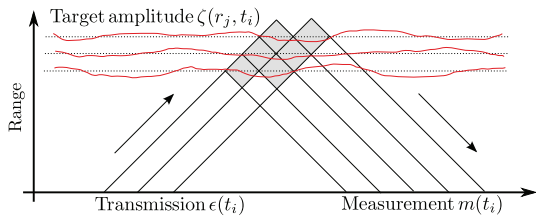

Fig. 1. Simplified range-time diagram of backscatter from a strong narrow region. In this example there are two transmit samples and three ranges that cause backscatter. The red lines visualize the changing amplitude of backscatter at each range. The gray area represents the area where the backscatter of one sample originates from (assuming boxcar impulse response).

out of four echos. In addition to the strong F-region heating effects, we also saw a strong sporadic E-layer heating, although it was less frequent and often of much shorter duration. The heating effects were seen on both UHF and VHF radars. The short transmission pulse length of 150 μs, while necessary for D-region studies, prevented us from forming a high resolution spectrum of the target, but this could be easily remedied by using a longer transmission pulse in future experiments.

2 Amplitude model of an incoherent scatter target

Using discrete time and range, the direct theory for a signal measured from a radar receiver can be expressed as a sum of range lagged transmission envelopes multiplied by the target backscatter amplitude

$$m(t_i) = \sum_j \epsilon(t_i - r_j)\, \zeta(r_j, t_i - r_j) + \xi(t_i). \tag{1}$$

Here $m(t) \in \mathbb{C}$ is the measured baseband signal (the notation $\in \mathbb{C}$ means that the signal is complex-valued), $\epsilon(t) \in \mathbb{C}$ is the transmission modulation envelope, $\zeta(r, t) \in \mathbb{C}$ is the range and time dependent target scattering coefficient and $\xi(t) \in \mathbb{C}$ is measurement noise consisting of thermal noise and sky-noise from cosmic radio sources. The measurement noise is assumed to be a zero mean complex Gausian white noise with variance $\mathrm{E}\,\xi(t_i)\,\overline{\xi(t_j)} = \delta_{i,j}\,\sigma^2$. Ranges r_j are defined in round-trip time at one sample intervals and t_i denotes time as samples.

There are many possible ways to model $\zeta(r, t)$. One possibility is to use a Fourier series in time, so our model parameters will consist of k terms of a Fourier series representation of the target scattering coefficient for each range of interest. This has the advantage that we can define the frequency characteristics that we expect to see in a target, as it is often the spectral properties that are of interest. Thus, we can express $\zeta(r, t)$ using coefficients $c_{j,k} \in \mathbb{C}$ of the series

$$\hat{\zeta}(r_j, t) = \sum_k c_{j,k} e^{i\omega_k t}, \tag{2}$$

with frequency parameters ω_k selected so that the frequency domain characteristics can be determined from the data. The backscatter amplitude of the target can thus be modelled using the parameter set $\theta = \{c_{j,k}\}$, which has $N_r \times N_f$ parameters, where N_r is the number of ranges and N_f is the number of elements in the Fourier series representation of the target amplitude. Thus, θ contains the parameters that we will attempt to infer based on the measurements.

We are left with a simple statistical parameter estimation problem, with parameters in set θ, which can be solved using statistical inversion. Using Eqs. (1) and (2), we can then write our direct theory $z(t_i, \theta)$ using the model as:

$$z(t_i, \theta) = \sum_j \sum_k \epsilon(t_i - r_j)\, c_{j,k}\, e^{i\omega_k t_i}. \tag{3}$$

We can write a likelihood function as a product of independent complex Gaussian densities, as our measurements are assumed to be distributed this way. Here D represents the set of measurements $D = \{m(t_1), \ldots, m(t_N)\}$:

$$p(D \mid \theta) = \prod_i \frac{1}{\pi\sigma^2} \exp\left\{ -\frac{|m(t_i) - z(t_i, \theta)|^2}{\sigma^2} \right\} \tag{4}$$

Normally, if the target range extent is wide, we would need many more parameters in θ than there are measurements. In this case it would be necessary either to use prior information or instead of backscatter coefficients, estimate the second order statistical properties of the target backscatter coefficients: $\sigma(r, \tau) = \mathrm{E}\,\zeta(r, t)\,\overline{\zeta(r, t+\tau)}$. This is what is done in traditional analysis using lagged product data $m(t)\,\overline{m(t+\tau)}$ to determine $\sigma(r, \tau)$ without estimating $\zeta(r, t)$.

If we are interested in a narrow region only, as depicted in Fig. 1, we can leave out all parameters that are not from ranges that are interesting to us, assuming that the backscatter from these ranges merely adds to the measurement noise. If the range we are interested in has a very strong signal compared to the surrounding ranges, this is a good assumption to make. In this case, the problem becomes easy to solve as we have more measurements than model parameters. This study focuses on narrow strong targets that fulfill this criteria.

3 Numerical details

Assuming that we know the white noise variance σ^2, our problem is a linear statistical inverse problem (Kaipio and Somersalo, 2004). We can find the maximum a posteriori parameters $\boldsymbol{\theta}_{\mathbf{MAP}}$[1] using linear algebra if we write Eqs. (1) and (3) in the form

$$\boldsymbol{m} = \boldsymbol{A\theta} + \boldsymbol{\xi}, \tag{5}$$

[1] i.e. the peak of the probability density function

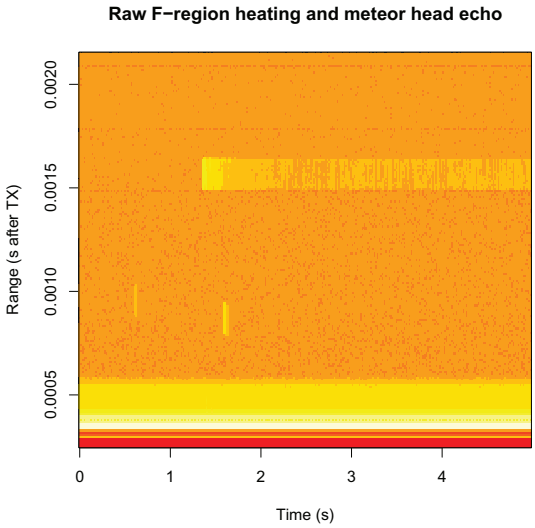

Fig. 2. Modulus of raw VHF measurements from a strong narrow layer in the F-region. Two meteor head echos can also be seen below the F-region backscatter. The strong echos below are ground clutter echos. Origin of time is the end of the TX pulse.

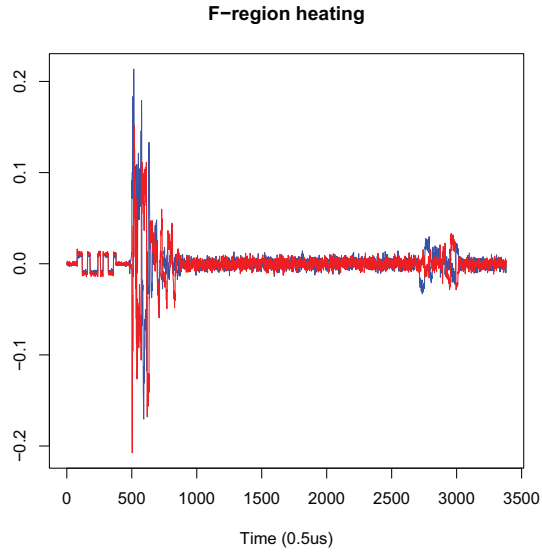

Fig. 3. Example transmission and echo from a point-like heating effect in the F-region. In this case from the EISCAT UHF signal. The transmitted signal is in the beginning of the signal, followed by ground clutter and the ionospheric echo. At around 1500 μs one can see the F-region heating related echo. The time on the x-axis is in samples which are 0.5 μs long. The red and blue represent real and complex parts of the baseband signal.

where the measurements and parameters are vectors and the theory is expressed as a matrix. The measurement vector is $\boldsymbol{m}=[m(t_1), ..., m(t_N)]^{\mathrm{T}}$ and the number of measurements $N=N_r+l-1$ is a sum of target ranges and transmission envelope length l. The parameter vector is $\boldsymbol{\theta}=[c_{1,1}, c_{1,2}, ..., c_{N_r,N_f}]^{\mathrm{T}}$, which has $N_r \times N_f$ elements. Errors are uncorrelated so $\boldsymbol{\xi} \sim N(0, \boldsymbol{\Sigma})$, with $\boldsymbol{\Sigma}=\mathrm{diag}(\sigma^2, ..., \sigma^2)$. The theory matrix $\mathbf{A}$ can be expressed using Eq. (3).

To solve this problem efficiently, we used a software package called FLIPS[2] (Orispää and Lehtinen, 2008[3]). The library uses QR-factorization via Givens rotations to solve the system of overdetermined linear equations. FLIPS can also be used to evaluate the posterior distribution of the parameters, which can be used to express errors associated with the parameters.

4 Example: F-region heating effect

During our 18 October 2007 daytime D-region heating experiment there was a sporadic E region during most of the experiment. In addition to this, we saw many strong O-mode heating related backscatter enhancements from the F-region and the sporadic E region on both VHF and UHF radars. By looking at the raw echos, shown in Fig. 2, it is evident that the heating effect was very strong and concentrated in a narrow region. By looking at the individual echos it was clear that the target was not completely coherent because the strong echo was not even close to an exact copy of the transmission pulse. An example of a transmission and the corresponding echo from the heated F-region is shown in Fig. 3.

To examine the amplitude of the F-region heating, we modelled 12 ranges 1 μs apart. Our coding, described in Virtanen et al. (2008b), used four 150 μ pulses with 10 μs bauds. The transmission envelope $\epsilon(t)$ was sampled directly from the waveguide. We modelled the range dependent amplitude using seven Fourier series parameters ω_k 6.667 kHz apart within a $\pm$20 kHz spectral area. The number of parameters was chosen so that the fit was good, while still giving residuals of correct magnitude. The signal was strong enough for us to be able to construct a decent estimate for each separate echo. Figure 4 shows the modulus of the parameters $c_{j,k}$ for each of the modelled ranges as a function of time during the 10 s heating period. This parameter plot can also be interpreted as a dynamic spectrum of the range dependent backscatter amplitude. The modelled backscatter amplitude at ranges 199.65–201.3 km during the first 100 ms of heating is shown in Fig. 5.

[2] available at http://mep.fi/mediawiki/index.php/FLIPS

[3] Orispää, M. and Lehtinen, M. S.: Fortran Linear Inverse Problem Solver (FLIPS), Inverse Problems and Imaging, in preparation, 2008.

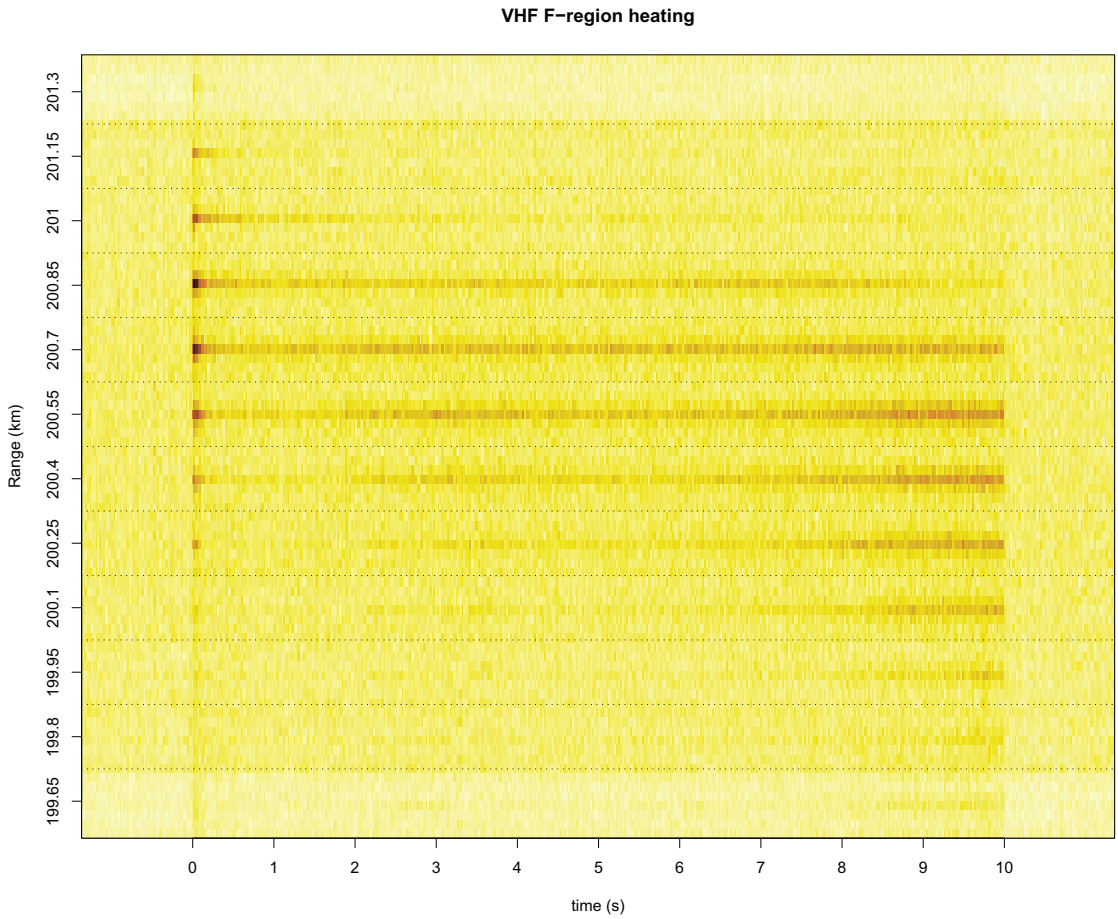

Fig. 4. Heating in the F-region at 150 m resolution from one heating period starting from 10:45:20. The temporal resolution is approximately 2.5 ms (uneven IPPs). The figure contains the modulus of one set of spectral parameters for each transmit pulse, the values are in linear scale. The values are the statistically most probable values given the measurements. Each range gate is represented with a ±20 kHz spectrum at a 6.67 kHz frequency resolution. The spectrum is dominated by one central peak. The heated layer is completely contained within a 1.8 km range interval and most of it is within a 600 m region. After recovering from the strong overshoot in the beginning, the heated region moves down at about 45 m/s during a single 10 s heating period. The spectrum seems to broaden and strengthen slightly towards the end of the heating period.

The results are similar to the ones obtained by Djuth et al. (2004), except that we have slightly worse frequency resolution due to the shorter transmission pulse. But we are able to obtain much better temporal resolution. During this experiment, we did not record plasma lines, but this same method is applicable for analyzing them, provided the plasma line bands are sampled.

5 Example: sporadic E-layer heating effect

The sporadic E region heating effect was analyzed using the same Fourier series parameters ω_k as the F-region heating in the previous section. The combined results of one 10 s heater on period are shown in Fig. 6. Compared to the F-region heating effect, both the spectrum and the layer itself is very narrow. The spectrum is so narrow that only the zero frequency component of the Fourier series has significant power – the change in amplitude is only apparent when inspecting

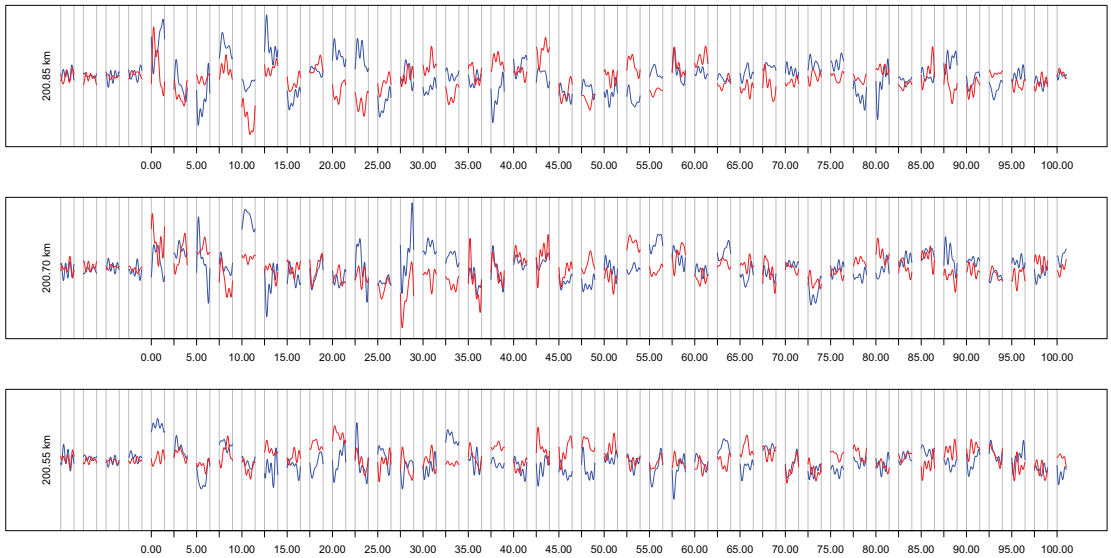

Fig. 5. Estimated backscatter amplitude from three ranges during the first 100 ms of heating. The estimate is based on the statistically most probable value of parameter vector θ given the measurements. The red and blue lines represent the real and complex parts of the baseband signal in linear scale. This F-region heating event is the same as the one in Fig. 4. The amplitude is modelled for 150 μs, which is the time that the transmission pulse travels through the range gate. Discontinuities in the figure are greater than they appear in, they are determined by the inter-pulse period, which is approximately 2.5 ms in this case.

the signal on a pulse to pulse basis, where the slow changes begin to appear.

The results from the sporadic E layer heating show variation in backscatter power during the on-period. The heating effect is mostly contained in one 150 m range gate, with a weak signal in the neighboring gates in the beginning of heating (the measurements could not be explained with only one range without causing worse residuals, which is an indication that these additional ranges are needed in the model). There is certain similarity to heating effects reported by Rietveld et al. (2002), with the exception that the ion-line spectrum obtained here is very narrow, less than 10 Hz.

In this case, the amplitude mostly contained very slow changes and one can easily see the main Doppler shift of -8 Hz by inspecting the estimated amplitude data. During the first echo received after heating on, there is a strong overshoot, which is not there any more during the next echo. In addition to this there were at least three detectable harmonics of 50 Hz, with 50 Hz the strongest of them, only approximately 10 dB lower than the main peak centered at -8 Hz. It is unclear what causes these harmonics, but we have ruled out the EISCAT VHF transmitter by inspecting the transmitter envelope sampled from the wave guide. The receiver chain also seems to be free of any of these components, as e.g. the ground clutter does not contain any of these components. Two feasible alternatives could be the heater RF or direct power transmission line modulation of the sporadic E region in the ionosphere.

6 Example: meteor echo

Meteor head echos are also one example of strong point-like radar targets. Two meteor head echos are shown in Fig. 2 below the F-region heating effect. Meteor head echos are routinely measured with high power large aperature radars such as EISCAT or Arecibo radars (e.g. Mathews et al., 1997; Pellinen-Wannberg, 2005). These measurements are usually modelled with a delayed transmission envelope multiplied by a complex sinusoid

$$m(t) = \epsilon(t - r)\,\zeta\, e^{i\omega t}. \tag{6}$$

The meteor velocity and range are then determined by finding the best fitting parameters ζ, r and ω. This is actually a good model, but it cannot describe arbitrary amplitude behaviour, and moreover it cannot be used to model range dependence very well. Typically, there is an underlying assumption of a point-like target, which results in range ambiguities for a spread target.

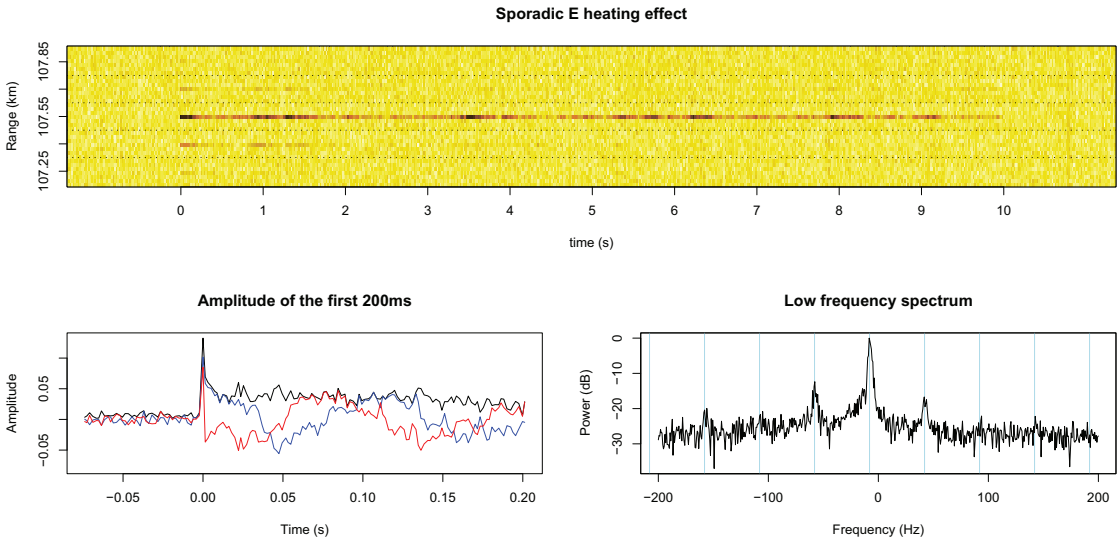

Fig. 6. Backscatter amplitude estimate of the sporadic E-region heating effect. The time is relative to the start of the 10 s O-mode heater on period. The figure above shows the modulus of the seven ±20 kHz Fourier series coefficients $c_{j,k}$ used to estimate the amplitude of each range gate during the 150 μs that the transmission pulse passes each range. The heating effect is mostly concentrated in only one range gate, with slight hints of power on the neighboring range gates, which cannot be explained by a model with only one range gate. The figure on the lower left depicts the amplitude behaviour of the first 200 ms of heating at 107.55 km. Blue is real and red is the imaginary part of the signal, the black line is the modulus of amplitude. The first echo is stronger and at a different phase than the rest of the backscattered waveform. On the lower right is the low frequency spectrum of the reflection amplitude from 107.55 km estimated over the whole 10 s heater on period. The main Doppler shift is centered at around −8 Hz. The blue vertical lines depict 50 Hz harmonics shifted by −8 Hz. It is unclear why the 50 Hz harmonics are in the received backscatter signal – but it does not seem to be caused by the EISCAT VHF TX or RX receive path. Possibilities include heater modulation or a direct modulation by ground based power transmission lines.

To demonstrate amplitude domain analysis of meteor head echos, we modelled $\zeta(r_j, t_i)$ at 9 ranges using 9 Fourier series coefficients centered around 40 kHz, which was approximately the Doppler shift of the meteor head echo. The raw voltage data was sampled at 8 MHz bandwidth. The modulus of the coefficients $c_{j,k}$ for one meteor head echo is shown in Fig. 7. The code length was 104 μs with 2 μs bauds. The backscatter amplitude is concentrated in a 100 m region with a backscatter magnitude decreasing with range. This could be a signature of the quickly vanishing trailing edge of the meteor head echo, but a more rigorous analysis would be required to verify this.

7 Discussion

We have demonstrated a method that gives very good temporal and spatial resolution for decoding strong sufficiently narrow targets. The method works with many types of radar transmissions, and can thus be run as a secondary analysis for situations where strong echos are observed. The method, although very promising, is still new and thus there remains work to be done with testing, parametrization, estimation errors, transmission code optimality, and numerical solution methods.

In this study we used a Fourier series to model the target, as it was the most straightforward one and it resulted in a linear model. Because of the small number of parameters in the series, there will certainly be some artifacts caused by this parametrization. The most notable one is that the amplitude behaviour tends to be periodic at the ends of the estimation interval, which is visible in Fig. 5. In cases where the target backscatter amplitude is sufficiently narrow band, a better parametrization for target backscatter amplitude would more likely be a complex sinusoid multiplied by a cubic spline. This would also be more suitable for meteor head echos, as this would allow more precise determination of the Doppler shift. This approach results in a non-linear statistical inverse problem which can be solved, e.g. by using MCMC (Hastings, 1970).

In addition to the examples presented in this study, there are also many other possible applications for this method. In the case of strong targets, our method will be directly

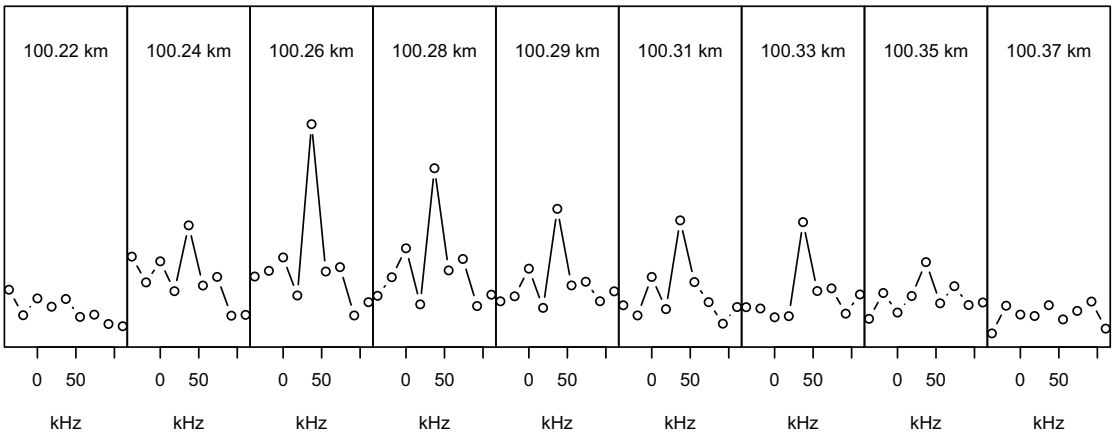

Fig. 7. The modulus of the Fourier series coefficients $c_{j,k}$. The meteor head echo is about 100 m wide and the main 40 kHz Doppler shift dominates the model.

applicable. For weak targets it is yet unknown how our method will perform, and it is a topic of future work. For example, near earth asteroids are an example of narrow radar targets that are fairly weak. Range-Doppler measurements of near earth asteroids (Hudson, 1993) are routinely used to determine the shape of the target. The range-amplitude measurement presented in this paper would offer more information than a traditional power domain range-Doppler estimate. The reason for this is that it is possible the reduce the range-amplitude estimate into a power domain range-Doppler estimate by simply taking the modulus of the Fourier domain representation of the amplitude, but this would mean discarding the phase information.

In this paper, we have not covered transmission code optimality in terms of amplitude domain inversion. In order to optimize a transmission code for a certain kind of target, one needs to calculate the covariance matrix for the parameter vector $\boldsymbol{\theta}$. In matrix form this is

$$\boldsymbol{\Sigma_p} = \sigma^2(\boldsymbol{A}^{\mathrm{H}}\boldsymbol{A})^{-1}, \tag{7}$$

where $\boldsymbol{A}$ is the theory matrix from Eq. (5) and σ^2 is the measurement noise variance. This matrix contains the transmission envelope $\epsilon(t)$ and the Fourier series terms $e^{i\omega_k t_i}$. Here $\boldsymbol{A}^{\mathrm{H}}$ is the complex conjugated transpose of the theory matrix $\boldsymbol{A}$. There are several aspects of the covariance matrix that one can optimize, but in general the errors of the parameters should be small and as independent as possible. This leads to several different code optimization criteria, such as minimization of the determinant of the error covariance matrix. Code optimization is a topic of future work.

Also, we have not yet visualized the estimation errors properly with the results, although this is pretty straightforward to do, as the problem gives a well defined Gaussian posterior covariance. This will be important when infering physical parameters from amplitude domain estimates.

It would be interesting to repeat the experiments shown in the examples with a longer transmit pulse and a higher sample rate to achieve better frequency and height resolution. The plasma lines should also be measured and analyzed using the method described here. Preferably the data should be sampled at a large enough rate to fit the whole signal.

In this work we have used a discrete time and range model. Some improvements in estimation accuracy can be expected if the model would include proper range ambiguities that also take into account the impulse response of the receiver chain.

While we have only applied this method to strong overdetermined targets, there might also be a possibility to extend this method to analyze underdetermined and weak incoherent scatter targets. It is not yet completely clear how this would be carried out. However, we plan to develop methods for a calculus of singular distributions for the target scattering coefficients, which could then be used in a further step of analysis modeling the scattering autocorrelation function as an unknown instead.

Acknowledgements. The authors thank I. W. McCrea and an anonymous referee for valuable comments. The authors would also like to thank M. Orispää for implementing FLIPS and showing how to use it. The work has been supported by the Academy of Finland (application number 213476, Finnish Programme for Centres of Excellence in Research 2006-2011). The EISCAT measurements were made with special programme time granted for Finland. EISCAT is an international assosiation supported by China (CRIRP), Finland (SA), Germany (DFG), Japan (STEL and NIPR), Norway (NFR), Sweden (VR) and United Kingdom (STFC).

Topical Editor K. Kauristie thanks I. McCrea and another anonymous referee for their help in evaluating this paper.

References

Djuth, F. T., Isham, B., Rietveld, M. T., Hagfors, T., and Hoz, C. L.: First 100 ms of HF modification at Tromsø, Norway, J. Geophys. Res., 109, A11307, doi:10.1029/2003JA010236, 2004.

Hastings, W.: Monte Carlo Sampling Methods Using Markov Chains and Their Applications, Biometrika, 57, 97–109, doi:doi:10.2307/2334940, 1970.

Hudson, R. S.: Three-dimensional reconstruction of asteroids from radar observations, Rem. Sens. Rev., 8, 195–203, 1993.

Kaipio, J. and Somersalo, E.: Statistical and Computational Inverse Problems, Springer, 2004.

Lehtinen, M. S., Damtie, B., and Nygrén, T.: Optimal binary phase codes and sidelobe-free decoding filters with application to incoherent scatter radar, Ann. Geophys., 22, 1623–1632, 2004, http://www.ann-geophys.net/22/1623/2004/.

Mathews, J., Meisel, D., Hunter, K., Getman, V., and Zhou, Q.: Very High Resolution Studies of Micrometeors Using the Arecibo 430 MHz Radar, Icarus, 126, 157–169, doi:10.1006/icar.1996.5641, 1997.

Pellinen-Wannberg, A.: Meteor head echos – observations and models, Ann. Geophys., 23, 201–205, 2005, http://www.ann-geophys.net/23/201/2005/.

Rietveld, M. T., Isham, B., Grydeland, T., Hoz, C. L., Leyser, T. B., Honary, F., Ueda, H., Kosch, M., and Hagfors, T.: HF-Pump-Induced Parametric Instabilities in the Auroral E-Region, Adv. Space Res., 29, 1363–1368, doi:10.1016/S0273-1177(02)00186-2, 2002.

Ruprecht, J.: Maximum-Likelihood Estimation of Multipath Channels, PhD thesis, Swiss federal institute of technology, 1989.

Sulzer, M. P.: Recent incoherent scatter techniques, Adv. Space Res., 9, 1989.

Vierinen, J., Lehtinen, M. S., Orispää, M., and Damtie, B.: General radar transmission codes that minimize measurement error of a static target, http://aps.arxiv.org/abs/physics/0612040v1, 2006.

Virtanen, I. I., Lehtinen, M. S., Nygren, T., Orispää, M., and Vierinen, J.: Lag profile inversion method for EISCAT data analysis, Ann. Geophys., 26, 571–581, 2008a, http://www.ann-geophys.net/26/571/2008/.

Virtanen, I. I., Lehtinen, M. S., and Vierinen, J.: Towards multi-purpose IS radar experiments, Ann. Geophys., 26, 2281–2289, 2008b, http://www.ann-geophys.net/26/2281/2008/.

Publication II

J. Vierinen, M. S. Lehtinen, M. Orispää, and I. I. Virtanen. Transmission code optimization method for incoherent scatter radar. *Annales Geophysicae*, 26, 2923-2927, August 2008.

Ann. Geophys., 26, 2923–2927, 2008
www.ann-geophys.net/26/2923/2008/

Annales Geophysicae

Transmission code optimization method for incoherent scatter radar

J. Vierinen[1], **M. S. Lehtinen**[1], **M. Orispää**[1], **and I. I. Virtanen**[2]

[1]Sodankylä Geophysical Observatory, 99600 Sodankylä, Finland
[2]Department of Physical Sciences, University of Oulu, P.O. Box 3000, 90014 Oulu, Finland

Received: 8 January 2008 – Revised: 28 May 2008 – Accepted: 29 July 2008 – Published: 24 September 2008

Abstract. When statistical inversion of a lag profile is used to determine an incoherent scatter target, the posterior variance of the estimated target can be used to determine how well a set of transmission codes perform. In this work we present an incoherent scatter radar transmission code optimization search method suitable for different modulation types, including binary phase, polyphase and amplitude modulation. We found that the combination of amplitude and phase modulation provides better performance than traditional binary phase coding, in some cases giving better accuracy than alternating codes.

Keywords. Radio science (Signal processing; Instruments and techniques)

1 Introduction

Incoherent scatter radar lag profile measurements can be deconvolved using statistical inversion with arbitrary range and time resolution as shown by Virtanen et al. (2008b). The radar transmission envelope plays an important part in determining the variance of the target autocorrelation function estimates. As the inversion is a statistical problem with a linear model, determining an optimal radar transmission waveform, i.e. one that minimizes variance, is a typical problem of optimal statistical experiment design (Pukelsheim, 1993).

Even though alternating codes are transmission sequences that are optimal in terms of posterior variance when integrated over the code transmission cycle (Lehtinen, 1986; Sulzer, 1993), shorter and only slightly less optimal code groups are beneficial in many cases where an alternating code sequence is too long. Also, a shorter code group offers more flexibility when designing radar experiments, e.g. making it easier to combine multiple different experiments in the same frequency channel and simplifying ground clutter removal. The use of short transmission codes is described in more detail in the companion paper by Virtanen et al. (2008a).

We have previously studied the target estimation variance of a coherent target where the target backscatter is assumed to stay constant while the transmission travels through the target (Vierinen et al., 2006). We found using an optimization algorithm that a combination of amplitude and arbitrary phase modulation can achieve very close to optimum coding (in most cases $\ll$1% worse than optimal in terms of normalized variance). In this study we apply a similar optimization method to find transmission codes that minimize the variance of incoherent target autocorrelation function estimates. We compare results of the optimization algorithm for several different modulation methods.

All formulas in this paper use discrete time, unless otherwise stated. All waveforms discussed are complex valued baseband signals. The ranges will be defined as round-trip time for the sake of simplicity.

2 General transmission code

A code with length L can be described as an infinite length sequence with a finite number of nonzero bauds with phases and amplitudes defined by parameters ϕ_k and a_k. These parameters obtain values $\phi_k \in \mathrm{P} \subset [0, 2\pi]$ and $a_k \in \mathrm{A} \subset \mathbb{R}^+$, where $k \in \{1, \ldots, L\} : L \in \mathbb{N}$. The reason why one might want to restrict the amplitudes to some range stems from practical constraints in transmission equipment. Usually, the maximum peak amplitude is restricted in addition to average duty cycle. Also, many systems only allow a small number of phases placed at even intervals on the unit circle, e.g. the commonly used binary phase coding has phases in $\phi_k \in \{0, \pi\}$.

Correspondence to: J. Vierinen
(juha.vierinen@iki.fi)

Published by Copernicus Publications on behalf of the European Geosciences Union.

By first defining $\delta(t)$ with $t \in \mathbb{Z}$ as

$$\delta(t) = \begin{cases} 1 & \text{when} \quad t = 0 \\ 0 & \text{otherwise,} \end{cases} \tag{1}$$

we can describe an arbitrary baseband radar transmission envelope $\epsilon(t)$ as

$$\epsilon(t) = \sum_{k=1}^{L} a_k e^{i\phi_k} \delta(t - k + 1). \tag{2}$$

We restrict the total transmission code power to be constant for all codes of equal length. Without any loss of generality, we set code power equal to code length (and thus, the number of bauds)

$$L = \sum_{t=1}^{L} |\epsilon(t)|^2. \tag{3}$$

3 Lag estimator variance

We will only discuss estimates of the target autocorrelation function $\sigma_\tau(r)$ with lags τ that are shorter than the length of a transmission code (here r is the range in round-trip time, and it is discretized by the baud length). The lags are assumed to be non-zero multiples of the baud length of the transmission code. Autocorrelation function estimation variance is presented more rigorously in the companion paper by Lehtinen et al. (2008). The variance presented there also includes pulse-to-pulse and fractional lags, taking into account target post-integration as well.

Also, we will only consider the diagonal of the covariance matrix. In terms of optimal experiment design, this corresponds to A-optimality (Pukelsheim, 1993), as the covariance matrix for an extended targets is a Toeplitz matrix.

Lag profile inversion is conducted using lagged products for the measured receiver voltage, defined for lag τ as

$$m_\tau(t) \equiv u(t)\,\overline{u(t+\tau)}, \tag{4}$$

where $u(t)$ is the measured complex baseband receiver voltage signal and $m_\tau(t)$ is the so called lagged product measurement.

As more than one code is used to perform the measurement, we index the codes with c as $\epsilon^c(t)$. For convenience, we define a lagged product of the code as

$$\varepsilon_\tau^c(t) \equiv \epsilon^c(t)\,\overline{\epsilon^c(t+\tau)}. \tag{5}$$

With the help of these two definitions, the lagged product measurement can be stated as a convolution of the lagged product of the transmission with the target autocorrelation function:

$$m_\tau^c(t) = (\varepsilon_\tau^c * \sigma_\tau)(t) + \xi_\tau(t). \tag{6}$$

The equation also contains a noise term $\xi_\tau(t)$, which is rather complicated, as it also includes the unknown target $\sigma_\tau(r)$. This term is discussed in detail, e.g. by Huuskonen and Lehtinen (1996). In the case of low SNR, which is typical for incoherent scatter measurements, the thermal noise dominates and $\xi_\tau(t)$ can be approximated as a zero mean Gaussian white noise process, with the second moment defined as

$$\mathbf{E}\,\xi_\tau(i)\,\overline{\xi_\tau(j)} = \delta(i-j)\,s^2, \tag{7}$$

where s^2 is the variance of the measurement noise.

In this case, the normalized measurement "noise power" of lag τ can then be approximated in frequency domain as

$$P_\tau \approx \int_0^{2\pi} \frac{N_c(L-\tau)}{\sum_{c=1}^{N_c} |\hat{\varepsilon}_\tau^c(\omega)|^2} d\omega, \tag{8}$$

where $\hat{\varepsilon}_\tau^c(\omega) = \mathcal{F}_D^M\{\varepsilon_\tau^c(t)\}$ is a zero padded discrete Fourier transform of the transmission envelope with transform length $M \gg L$. N_c is the number of codes in the transmission group and L is the number of bauds in a code. Each code in a group is assumed to be the same length.

For alternating codes of both Lehtinen (1986) and Sulzer (1993) type, $P_\tau = 1$ for all possible values of τ. For constant amplitude codes, this is the lower limit. On the other hand, if amplitude modulation is used, this is not the lower limit anymore, because in some cases more radar power can be used on certain lags, even though the average transmission power is the same.

To give an idea of how phase codes perform in general, Fig. 1 shows the mean lag noise power for random code groups at several different code and code group lengths. It is evident that when the code group is short and the code length is large, the average behaviour is not close to optimal. On the other hand, when there is a sufficient number of codes in a group, the performance is fairly good even for randomly chosen code groups. Thus, we only need to worry about performance of code groups with small code group length and large code length.

4 Code optimization criteria

Nearly all practical transmission code groups result in such a vast search space that there is no possibility for an exhaustive search. As we cannot yet analytically derive the most optimal codes, except in a few selected situations, we must resort to numerical means. The problem of finding a transmission code with minimal estimation variance is an optimization problem and there exist a number of algorithms for approaching this problem numerically.

A typical approach is to define an optimization criteria $f(x)$ that gives positive real valued optimality for parameter x. The optimization algorithm then finds $x_{\min}$ that minimizes $f(x)$. In the case of transmission code groups, x will contain the phase ϕ_k^c and amplitude a_k^c parameters of each code in the code group

$$x = (a_k^c, \phi_k^c) \in \mathrm{A}^{N_c L} \times \mathrm{P}^{N_c L}. \tag{9}$$

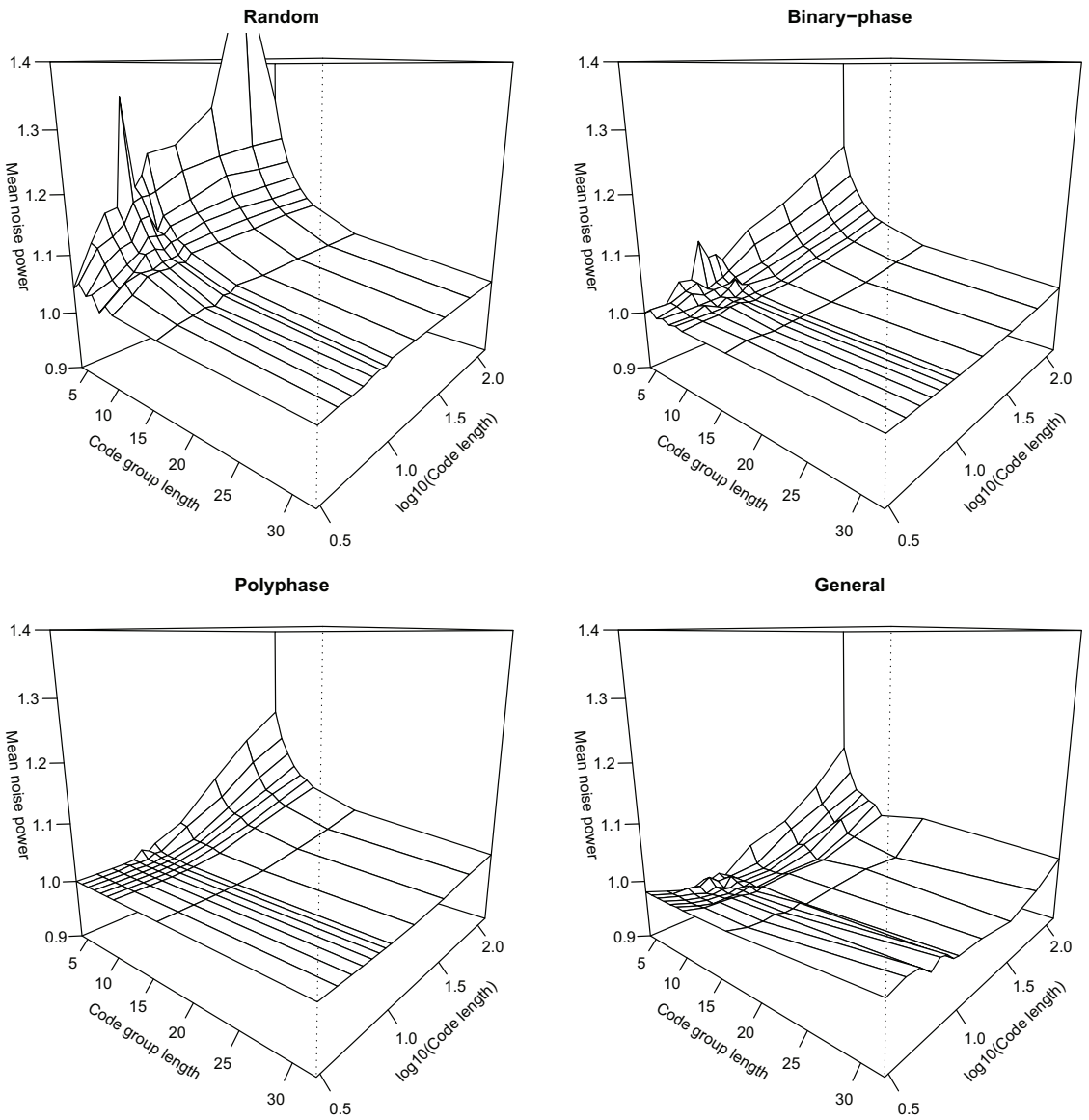

Fig. 1. The mean lag noise power for random binary phase codes, optimized binary phase codes, optimized polyphase codes and optimized amplitude $a_k \in [0, 2]$ and arbitrary phase modulated (general modulation) codes. The largest improvements are achieved for short code groups. Also, it is clear that the combination of amplitude and phase modulation provides the best lag variance.

There are many different ways to define $f(x)$ in the case of transmission code groups, but a trivial one is a weighted sum of the normalized lag power P_τ, with weights w_τ selected in such a way that they reflect the importance of that lag

$$f(x) = \sum_\tau w_\tau P_\tau. \tag{10}$$

In this paper, we set $w_\tau = 1$ for all lags. This gives each lag an equal importance. This is a somewhat arbitrary choice of weights, in reality they should be selected in a way the reflects the importance of the lag in the experiment. In practice, one can use the results of Vallinkoski (1989) in determining the weights for the lags.

5 Optimization algorithm

As our search method will also have to work with codes that have a finite number of phases, we needed an algorithm that could also work with situations were an analytic or numerical derivative of $f(x)$ cannot be defined. We developed a simple random local optimization algorithm (Lewis and Papadimitriou, 1997) for this specific task.

The random local optimization algorithm is fairly efficient at converging to a minima of $f(x)$ and it can also to some extent jump out of local minima. In practice, it is faster to restart the optimization search with a different random initial parameter set in order to efficiently locate different minima of $f(x)$.

A simplified description of our code search algorithm that searches for local minima of $f(x)$ is as follows:

1. Randomize parameters in x.
2. For a sufficient number of steps, randomize a new value for one of the elements of x and accept the change if $f(x)$ is improved.
3. Randomize all parameters x, accept the change if $f(x)$ is improved.
4. If sufficient convergence to a local minima of $f(x)$ has been achieved, save x and goto step 1. Otherwise go to step 2. The location of the minima can be further fine tuned using gradient-based methods, if a gradient is defined for $f(x)$.

In practice, our algorithm also included several tunable variables that were used in determining the convergence of $f(x)$ to a local minima. Also, the number of local minima to search for depends a lot on the number of parameters in the problem. In many cases we are sure that the global minima was not even found as the number of local minima was so vast.

Even though the algorithm that we developed seems to be fairly robust, it might be worth investigating several other optimization algorithms in the future. Two promising algorithms that might be useful are Differential Evolution (Price et al., 2005) and Simulated Annealing (Kirkpatrick et al., 1983), both of which have certain similarities to our optimization algorithm.

6 Optimization results

In order to demonstrate the usefulness of the optimization method, we searched for code groups that use three different types of modulation: *binary phase modulation*, *polyphase modulation*, and the combination of amplitude and polyphase modulation, which we shall refer to as *general modulation*. In this example, we used $a_k=1$ for the constant amplitude modulations and allowed amplitudes in the range $a_k\in[0, 2]$ for general modulation codes, while still constraining the total transmission code power in both cases to be the same.

The results are shown in Fig. 1. In this case the results are shown in terms of mean lag noise power $P=(L-1)^{-1}\sum_\tau P_\tau$. It is evident that significant improvement can be achieved when the code group length is short. For longer code groups, the optimized groups do not differ that much from random code groups. Also, one can see that optimized polyphase codes are somewhat better than binary phase codes; ultimately general phase codes are better than polyphase codes – in some cases the mean lag noise power is less than unity. The reason for this is that amplitude modulation allows the use of more power for measuring some lags, in addition to allowing more freedom in removing range ambiguities. It should also be noted, that when the code or code group length is increased, the difference between different modulation methods also becomes less significant.

7 Conclusions

We have introduced an optimization method suitable for searching transmission codes when performing lag profile inversion. General radar tranmission coding, i.e. modulation that allows amplitude and arbitrary phase shifts, is shown to perform better than plain binary phase modulation. Amplitude modulation is shown to be even more effective than alternating codes, as the amplitude modulation allows the use of more radar power in a subset of the lags.

For sake of simplicity, we have only dealt with estimation variances for lags that are non-zero multiples of the baud length, with the additional condition that the lags are shorter than the transmission pulse length. It is fairly easy to extend this same methodology for more complex situations that, e.g. take into account target post-integration, fractional or pulse-to-pulse lags. This is done by modifying the optimization criterion $f(x)$.

In all the cases that we investigated, the role of the modulation method is important when the code length is short. When using longer codes or code groups, the modulation scheme becomes less important. Also, there is less need for optimizing codes when the code group length is increased.

Further investigation of the high SNR case would be beneficial and the derivation of variance in this case would be interesting, albeit maybe not as relevant in the case of incoherent scatter radar.

Acknowledgements. This work has been supported by the Academy of Finland (application number 213476, Finnish Programme for Centres of Excellence in Research 2006-2011).

Topical Editor K. Kauristie thanks B. Damtie and two other anonymous referees for their help in evaluating this paper.

References

Huuskonen, A. and Lehtinen, M. S.: The accuracy of incoherent scatter measurements: error estimates valid for high signal levels, J. Atmos. Terr. Phys., 58, 453–463, 1996.

Kirkpatrick, S., Gelatt, C. D., and Vecchi, M. P.: Optimization by Simulated Annealing, Science, 220, 671–680, 1983.

Lehtinen, M.: Statistical theory of incoherent scatter measurements, EISCAT Tech. Note 86/45, 1986.

Lehtinen, M. S., Virtanen, I. I., and Vierinen, J.: Fast comparison of IS radar code sequences for lag profile inversion, Ann. Geophys., 26, 2291–2301, 2008, http://www.ann-geophys.net/26/2291/2008/.

Lewis, H. R. and Papadimitriou, C. H.: Elements of the Theory of Computation, Prentice Hall, Upper Saddle River, NJ, USA, 1997.

Price, K. V., Storn, R. M., and Lampinen, J. A.: Differential Evolution, A Practical Approach to Global Optimization, Springer, 2005.

Pukelsheim, F.: Optimal Design of Experiments, John Wiley & Sons, 1993.

Sulzer, M. P.: A new type of alternating code for incoherent scatter measurements, Radio Sci., 28, 1993.

Vallinkoski, M.: Error analysis of incoherent scatter radar measurements, EISCAT Tech. Note 89/49, 1989.

Vierinen, J., Lehtinen, M. S., Orispää, M., and Damtie, B.: General radar transmission codes that minimize measurement error of a static target, http://aps.arxiv.org/abs/physics/0612040v1, 2006.

Virtanen, I. I., Lehtinen, M. S., and Vierinen, J.: Towards multipurpose IS radar experiments, Ann. Geophys., 26, 2281–2289, 2008a, http://www.ann-geophys.net/26/2281/2008/.

Virtanen, I. I., Lehtinen, M. S., Nygren, T., Orispaa, M., and Vierinen, J.: Lag profile inversion method for EISCAT data analysis, Ann. Geophys., 26, 571–581, 2008b, http://www.ann-geophys.net/26/571/2008/.

Publication III

J. Vierinen. Fractional baud-length coding. ***Annales Geophysicae*****, 29, 1189-1196, 2011.**

Ann. Geophys., 29, 1189–1196, 2011
www.ann-geophys.net/29/1189/2011/
doi:10.5194/angeo-29-1189-2011

Annales Geophysicae

Fractional baud-length coding

J. Vierinen

Sodankylä Geophysical Observatory, Sodankylä, Finland

Received: 24 March 2010 – Revised: 8 February 2011 – Accepted: 6 June 2011 – Published: 30 June 2011

Abstract. We present a novel approach for modulating radar transmissions in order to improve target range and Doppler estimation accuracy. This is achieved by using non-uniform baud lengths. With this method it is possible to increase sub-baud range-resolution of phase coded radar measurements while maintaining a narrow transmission bandwidth. We first derive target backscatter amplitude estimation error covariance matrix for arbitrary targets when estimating backscatter in amplitude domain. We define target optimality and discuss different search strategies that can be used to find well performing transmission envelopes. We give several simulated examples of the method showing that fractional baud-length coding results in smaller estimation errors than conventional uniform baud length transmission codes when estimating the target backscatter amplitude at sub-baud range resolution. We also demonstrate the method in practice by analyzing the range resolved power of a low-altitude meteor trail echo that was measured using a fractional baud-length experiment with the EISCAT UHF system.

Keywords. Radio science (Ionospheric physics; Signal processing; Instruments and techniques)

1 Introduction

We have previously described a method for estimating range and Doppler spread radar targets in amplitude domain at sub baud-length range-resolution using linear statistical inversion (Vierinen et al., 2008b). However, we did not use codes optimized for the targets that we analyzed. Also, we only briefly discussed code optimality. In this paper we will focus on optimal transmission codes for a target range resolution that is smaller than the minimum allowed baud-length. We will introduce a variant of phase coding called "fractional baud-length codes" that are useful for amplitude domain inversion of range and possibly Doppler spread targets, when a better resolution than the minimum allowed radar transmission envelope baud-length is required.

The method introduced in this study differs from the Frequency Domain Interferometry (FDI) (Kudeki and Stitt, 1987) method as it does not require the target scattering to originate from a very narrow layer within the radar scattering volume. Assuming that the target is indeed a narrow enough layer, the FDI method will probably perform better in terms of range resolution. However, it is feasible to combine fractional baud-length coding with FDI to obtain a shorter decoded pulse before the interferometry step.

In radar systems there is a limit to the smallest baud length, which arises from available bandwidth due to transmission system or licensing constraints. However, the transmission envelope can be timed with much higher precision than the minimum baud length. For example, the EISCAT UHF and VHF mainland systems in Tromsø are currently capable of timing the transmission envelope at 0.1 µs resolution, but the minimum allowed baud length is 1 µs. Thus, it is possible to use transmission codes with non-uniform baud-lengths that are timed with 0.1 µs accuracy, as long as the shortest baud is not smaller than 1 µs. This principle can then be used to achieve high resolution (<1 µs) backscatter estimates with smaller variance than what would be obtained using a uniform baud-length radar transmission code with baud lengths that are integer multiples of 1 µs.

In this paper, we first derive the target backscatter amplitude estimation covariance for range and Doppler spread radar targets when estimating target parameters in amplitude domain. Then we define transmission code optimality for a given target. After this, we present two search strategies which can be used to find optimal transmission codes: an exhaustive search algorithm, and an optimization search algorithm. As an example, we study code optimality in the case of a simulated range spread coherent target. We also show an example of a real fractional baud-length coding measurement of a range spread meteor echo.

Correspondence to: J. Vierinen
(juha.vierinen@iki.fi)

Published by Copernicus Publications on behalf of the European Geosciences Union.

2 Fractional baud-length code

We will treat the problem in discrete time. The measurement sample rate is assumed to be the same as the required target range resolution.

A transmission envelope can be described as a baseband sequence of L samples. If the transmission envelope has much less bauds $N_\mathrm{b} \ll L$ than samples, it is economical to represent the transmission code in terms of bauds. In this case, the envelope can be described in terms of the lengths $l_k \in \Gamma \subset \mathbb{N}$, phases $\phi_k \in \mathrm{P} \subset [0, 2\pi)$ and amplitudes $a_k \in \Lambda \subset [0,1] \subset \mathbb{R}$ of the bauds. We can define an arbitrary transmission envelope as

$$\epsilon_\mathrm{t} = \sum_{j=1}^{N_\mathrm{b}} [t \in B_j] a_j e^{i\phi_j}, \tag{1}$$

where $[\cdot]$ is the so called Iverson bracket, which evaluates to 1 if the logical expression is true – in this case when the index "t" is within the set of indices $B_j = \{1 + \sum_{i=0}^{j-1} l_i, 2 + \sum_{i=0}^{j-1} l_i, \cdots, l_j + \sum_{i=0}^{j-1} l_i\}$ within baud j and zero otherwise (additionally, we define $l_0 = 0$). In this study, the code power is always normalized to unity $\sum_{t=-\infty}^{\infty} |\epsilon_t|^2 = 1$, which means that the variances are comparable between transmission envelopes that deliver a similar amount of radar power. The codes can also be normalized otherwise, if comparison between two envelopes of different total power is needed.

The transmission waveform definition is intentionally as general as possible. Radar specific constraints can be imposed by defining the sets Γ, P, and Λ. These will be discussed later on in Sect. 5.

3 Target estimation variance

The presentation here slightly differs from Vierinen et al. (2008b). Instead of a Fourier series, we will use B-splines to model the target backscatter.

Using discrete time and range, and assuming that our receiver impulse response is sufficiently close to a boxcar function that is matched to the sample rate, the direct theory for a signal measured from a radar receiver can be expressed as a sum of the range lagged transmission envelope multiplied by the target backscatter amplitude

$$m_t = \sum_{r \in R} \epsilon_{\mathrm{t}-r} \zeta_{r,t} + \xi_t. \tag{2}$$

Here $m_t \in \mathbb{C}$ is the measured baseband raw voltage signal, $R = \{R_\mathrm{min}, ..., R_\mathrm{max}\} \subset \mathbb{N}$ is the target range extent, $\epsilon_\mathrm{t} \in \mathbb{C}$ is the transmission modulation envelope, $\zeta_{r,t} \in \mathbb{C}$ is the range and time dependent target scattering coefficient and $\xi_t \in \mathbb{C}$ is measurement noise consisting of thermal noise and sky-noise from cosmic radio sources. The measurement noise is assumed to be a zero mean complex Gausian white noise with variance $\mathrm{E}\xi_t\overline{\xi_{t'}} = \delta_{t,t'}\sigma^2$. Ranges r are defined in round-trip time at one sample intervals, t also denotes time in samples. By convention, we apply a range dependent constant $\frac{r}{2}$ delay, so that the range dependent backscatter amplitude is $\zeta_{r,t}$ instead of $\zeta_{r,t-\frac{r}{2}}$. Figure 1 depicts backscatter from three range gates probed with two transmission samples. To simplify matters, we use overlapping triangular range gates.

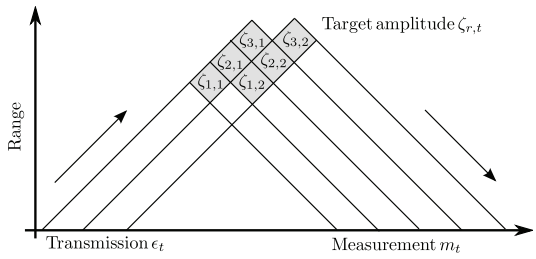

Fig. 1. Simplified range-time diagram of backscatter from a strong narrow region (notice that this is not in round-trip time). In this example there are two transmit samples and three ranges that cause backscatter. The gray area represents the area where the backscatter of one sample originates from, assuming boxcar impulse response. A longer impulse response will cause more range spreading.

3.1 Coherent target

Now if the target backscatter is constant $\zeta_{r,t} = \zeta_r$, the measurement equation becomes a convolution equation

$$m_t = \sum_{r \in R} \epsilon_{t-r} \zeta_r + \xi_t, \tag{3}$$

which is the most common measurement equation for radar targets. Assuming that the target is sufficiently extended, this can be solved by filtering the measurements with a filter that corresponds to the frequency domain inverse of the transmission envelope (Sulzer, 1989; Ruprecht, 1989). However, for a finite range extent, the filtering approach is not always optimal as it does not properly take into account edge effects, such measurements missing due to ground clutter or receiver protection. A sufficiently narrow range extent also results in smaller estimation errors. In these cases, one should use a linear theory matrix that explicitely defines the finite range extent. We will define this as a special case of the incoherent backscatter theory presented next.

3.2 Incoherent target

If the target backscatter is not constant, the range dependent backscatter $\zeta_{r,t}$ has to be modeled in some way in order to make the estimation problem solvable. One natural choice is to assume that the target backscatter is a band-limited signal, which can be modeled using a B-spline (de Boor, 1978). Our model parameters will consist of N_s control points that model the backscatter at each range of interest. The frequency domain characteristics are defined by the spacing of

the knots and the order of the spline n. Using the definition of B-splines, the target backscatter $\zeta_{r,t}$ is modeled using the parameters $P_{r,k} \in \mathbb{C}$ as:

$$\hat{\zeta}_{r,t} = \sum_{k=0}^{N_s-1} P_{r,k} b_{k,n}\left(\frac{t-1}{L-1}\right), \tag{4}$$

where $b_{k,n}(\cdot)$ is the B-spline basis function and coefficients $P_{r,k}$ are the control points with $k \in \{1,...,N_s\}$. We assume that the control points are evenly spaced and that the endpoints contain multiple knots in order to ensure that the second order derivatives are zero at both ends of $\hat{\zeta}_{r,t}$. We also define a special case of one spline control point as $\hat{\zeta}_{r,t} = P_r = \zeta_r$. This corresponds to a completely coherent target.

When Eq. (4) is substituted into Eq. (2), we get

$$m_t = \sum_{r\in R}\sum_{k=0}^{N_s-1} P_{r,k}\epsilon_{t-r} b_{k,n}\left(\frac{t-1}{L-1}\right) + \xi_t. \tag{5}$$

This model is linear in respect to the parameters $P_{r,k}$ and one can conveniently represent it in matrix form as

$$\boldsymbol{m} = \mathbf{A}\boldsymbol{x} + \boldsymbol{\xi}, \tag{6}$$

where $\boldsymbol{m} = [m_1,...,m_N]^{\mathrm{T}}$ is the measurement vector, $\mathbf{A}$ is the theory matrix containing the $\epsilon_{t-r} b_{k,n}(\cdot)$ terms, $\boldsymbol{x} = [P_{1,1}, P_{1,2},..., P_{N_r,N_s}]^{\mathrm{T}}$ is the parameter vector containing the control points and $\boldsymbol{\xi} = [\xi_1,...,\xi_N]^{\mathrm{T}}$ is the error vector with the second moment defined as

$$\mathrm{E}\boldsymbol{\xi}\boldsymbol{\xi}^{\mathrm{H}} = \boldsymbol{\Sigma} = \mathrm{diag}(\sigma^2,...,\sigma^2). \tag{7}$$

The number of parameters is the number of ranges N_r times the number of B-spline control points N_s per range. The number of measurements $N = N_r + L - 1$ is a sum of target ranges and transmission envelope length L. As long as $N \geq N_r N_s$ and the theory matrix has sufficient rank, the problem can be solved using statistical linear inversion. In practice, the number of model parameters that can be succesfully modeled with sufficiently small error bars depends on the signal to noise ratio. The estimation of strong range and Doppler spread echos is shown in Vierinen et al. (2008b). Figure 2 shows an example theory matrix for a target range extent $N_r = 14$ with $N_s = 8$ spline guide points per range. The transmission code is a uniform baud-length 13-bit Barker code with baud length $l_j = 10$.

The probability density for Eq. (6) can be written as:

$$p(\boldsymbol{m}|\boldsymbol{x}) \propto \exp\left(-\frac{1}{\sigma^2}\|\boldsymbol{m} - \mathbf{A}\boldsymbol{x}\|^2\right) \tag{8}$$

and assuming constant valued priors, the maximum a posteriori (MAP) estimate, i.e., the peak of $p(\boldsymbol{m}|\boldsymbol{x})$ is

$$\boldsymbol{x}_{\mathrm{MAP}} = (\mathbf{A}^{\mathrm{H}}\mathbf{A})^{-1}\mathbf{A}^{\mathrm{H}}\boldsymbol{m} \tag{9}$$

and the a posteriori covariance is:

$$\boldsymbol{\Sigma}_{\boldsymbol{p}} = \sigma^2(\mathbf{A}^{\mathrm{H}}\mathbf{A})^{-1}. \tag{10}$$

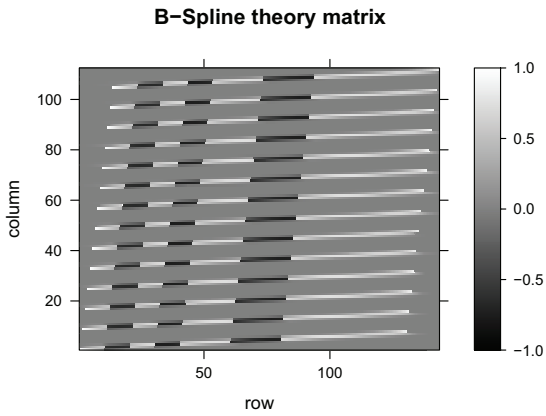

Fig. 2. A theory matrix for a range and Doppler spread target with $N_r = 14$ range gates and $N_s = 8$ B-spline guide points per range. The code is a simple 13-bit Barker code with 10 samples per baud.

3.3 Infinitely extended coherent target

In the special case of an infinitely extended coherent target ($N_s = 1$), the matrix $\mathbf{A}$ becomes a convolution operator and the problem can be efficiently solved in frequency domain and numerically evaluated using FFT (Cooley and Tukey, 1965). This case has been extensively discussed by, e.g., Lehtinen et al. (2008); Vierinen et al. (2006); Lehtinen et al. (2004) and Ruprecht (1989). The covariance matrix will be an infinitely extended Toeplitz matrix with rows[1]:

$$\Sigma_t = \lim_{M\to\infty} \frac{1}{M}\mathcal{F}_M^{-1}\left\{\left(\mathcal{F}_M\left\{\sum_{\tau=-\infty}^{\infty}\epsilon_\tau\overline{\epsilon_{\tau-t}}\right\}\right)^{-1}\right\}.$$

This result is also a fairly good approximation for a sufficiently long finite range extent, differing only near the edges. However, this result is not valid for a sufficiently narrow finite range extent or when the target also has Doppler spread. Also, it is not even possible to calculate the covariance matrix in this way for uniform baud-length codes when the baud-length is larger than the target resolution. The reason for this is that for an infinitely extended target there will be zeros in the frequency domain representation of the transmission envelope and because of this, the covariance matrix is singular. Even in the case of a finite range extent, all codes with uniform baud-length result in a theory matrix with strong linearly dependent components. An example of this is shown in Sect. 6. When using non-uniform baud-lengths the problem can be avoided, since in this way it is possible to form a code

[1]The index t refers to the column of the matrix row. Operators $\mathcal{F}_M$ and $\mathcal{F}_M^{-1}$ are the forward and reverse discrete Fourier transforms of length M. In practice the covariance can be approximated numerically with sufficiently large values of M.

without zeros in the frequency domain. This is somehwhat similar to random alias-free sampling (Shapiro and Silverman, 1960). Another analogy can be found in the use of aperiodic radar interpulse periods to overcome range-Doppler ambiguities, e.g., (Farley, 1972; Uppala and Sahr, 1994; Pirttilä and Lehtinen, 1999).

4 Code optimality

The performance of a certain code is determined by the target parameter estimation errors. These on the other hand are determined by the a posteriori covariance matrix in Eq. (10). Because we assume uniform priors, the covariance matrix is fully determined by the target model (i.e., assumed target characteristics) in theory matrix **A**. The theory matrix **A** contains the transmission envelope and therefore it affects the covariance matrix. The task of code optimization is to find a covariance matrix that produces the best possible estimates of the target.

In terms of the theory of comparison of measurements (Piiroinen, 2005), a code ϵ_1 is in every situation better than some other code ϵ_2 only if the difference of their corresponding covariance matrices $\mathbf{\Sigma_2} - \mathbf{\Sigma_1}$ is positive definite. Even though it might be feasible use this as a criterion in a code search, we chose a more pragmatic approach where we construct a function that maps the the covariance matrix to a real number $\Omega : \mathbb{R}^{N_p \times N_p} \rightarrow \mathbb{R}$ while still retaining some of the information contained in the covariance matrix. One such map is the trace of the covariance matrix $\Omega(\mathbf{\Sigma}) = \mathrm{tr}(\mathbf{\Sigma})$, which is called A-optimality in terms of optimal statistical experiment design. This has the effect of minimizing the average variance of the model parameters. We will use this criterion throughout this paper. Refer to, e.g., Pukelsheim (1993) for more discussion on optimization criteria.

For infinitely extended fully coherent targets, the trace of the covariance matrix is infinite, but one can use the diagonal value of one row of the covariance matrix. Because it is of Toeplitz form, all diagonal values are the same, and this will correspond to A-optimality.

5 Code search

The transmission envelope consisting of N_b bauds is fully described by the baud lengths $l_k \in \Gamma \subset \mathbb{N}$, phases $\phi_k \in \mathrm{P} \subset [0, 2\pi)$ and amplitudes $a_k \in \Lambda \subset [0, 1] \subset \mathbb{R}$. These form the set of parameters to optimize

$$(l_k, \phi_k, a_k) \subset \Gamma^{N_\mathrm{b}} \times \mathrm{P}^{N_\mathrm{b}} \times \Lambda^{N_\mathrm{b}}. \quad (11)$$

In addition to this, the number of bauds N_b in a code of length L need not be fixed, as this depends on the lengths of the individual bauds l_k.

For reasonably short codes with sufficiently small number of phases it might be possible to perform an exhaustive search. This consists of first determining all the different ways to divide a code of length L into bauds of lengths l_k. After this, all unique orderings of the baud-lengths and permutations of phases and amplitudes need to be traversed. The problem of determining the different combinations of baud lengths amounts to the problem of generating all integer partitions for L (Kelleher and O'Sullivan, 2009). When additional constraints to baud lengths are applied, the problem is called the multiply restricted integer partitioning problem (Riha and James, 1976). An efficient algorithm for iterating through restricted partitions has been described by Riha and James (1976).

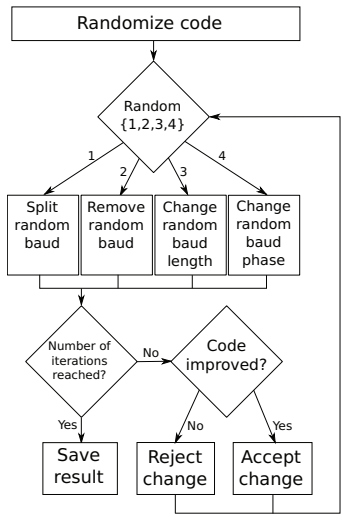

Fig. 3. Simplified block diagram of the optimization algorithm.

The exhaustive approach fails already for reasonably small problems due to the catastrophic growth of the search space. Therefore we have to resort to some optimization method in order to find optimal codes. Optimization methods have been previously used for code searches at least by Sahr and Grannan (1993), and Nikoukar (2010). Our approach for finding optimal codes is based on the simulated annealing method (Kirkpatrick et al., 1983).

The optimization procedure that we have developed can be used to find well performing non-uniform baud-length codes, given a set of constraints. The constraints are given as the set of allowed baud lengths Γ, the set of allowed phases P and the set of allowed amplitudes Λ. We have previously used a similar algorithm to optimize codes for infinitely extented coherent targets and lag-profile inversion of incoherent scatter radar (Vierinen et al., 2006, 2008a).

The main principle of the algorithm is very simple. We first randomize a code $E_0 \equiv (l_k, \phi_k, a_k, N_\mathrm{b})$ that meets the given constraints. Next, for a certain number of iterations we incrementally attempt to improve this code with small

random changes $E' = \delta E_i$. Here δ is an operator that slightly modifies E in some way, while conforming to the constraints imposed on the code. If any of these changes results in a code that is better, we then save these parameters $E_{i+1} = E'$ and continue to the next iteration. In order to reduce the chance of the algorithm from getting stuck in a local minima, we also sometimes (by a small random chance) allow changes that do not improve the code. In order to achieve convergence, the magnitude of the random changes δE is decreased as the iteration advances. The algorithm is depicted in Fig. 3. The small incremental changes that we use are:

1. Split random baud. Select a long enough baud in the code and split it into two bauds. Retain the original amplitude and phase on one of these bauds and slightly randomly modify them on the other baud.

2. Remove a random baud. Increase a randomly selected baud length.

3. Change the length of a baud. Increase the length of one randomly selected baud and decrease the length of another randomly selected baud to maintain code length.

4. Change random baud phase and amplitude. Select an arbitrary baud and slightly change phase and amplitude.

These incremental changes are designed in a way that they always conform to the criteria imposed on the transmission code. If this is not possible (i.e., if it is not possible to add a new baud), the code remains unchanged. The implementation of "slight change" depends on the constrains placed on the code. E.g., in the case of binary phase codes with constant amplitude, a 180° phase flip would correspond to a slight phase change, while the amplitudes would remain unchanged. For a polyphase code, the slight change in phase could be a small random change in the original phase $\phi'_k = \phi_k + \epsilon_\phi$, where ϵ_ϕ would be a small random number.

In order to initially randomize a code, we start with any phase code that conforms with the constraints of baud lengths, phases and amplitudes. This can be hard coded. We then perform a certain number of the same incremental changes that we use in the optimization procedure, except that we accept all of the changes.

6 Example: range spread coherent target

To demonstrate the performance of non-uniform baud-length codes when estimating a target at sub-baud resolution, we simulated an echo using a constant amplitude binary phase non-uniform baud-length code and traditional uniform baud-length constant amplitude binary phase code of the same length. In this example, we analyze a 10 sample wide target at the resolution of one sample. The non-uniform baud-length code was an optimized 11-bit code with baud lengths $\{12, 12, 12, 12, 10, 13, 10, 11, 11, 15, 12\}$ and phases $\{1, -1, 1, -1, 1, -1, 1, -1, 1, -1, -1\}$. The smallest allowed baud-length was 10 samples. For comparison we used the well known 13-bit Barker code with a baud-length of 10 samples. Both simulations had the same instance of measurement noise SNR = 3 and the same target amplitudes, which in this case was an instance of the complex Gaussian random $\mathcal{N}_{\mathbb{C}}(0, 1)$ process.

The results are shown in Fig. 4. It is evident that the non-uniform baud-length code performs better in terms of estimation errors. It is also evident that the Barker code suffers from the fact that every baud is the same length – if the range extent would have been infinite, the covariance matrix would have been singular. Now the covariance matrix is only near-singular. This is seen as large off-diagonal stripes in the 13-bit Barker code covariance matrix and correlated errors. In the case of the 11-bit fractional code the off-diagonal elements are more uniform and the variance is also smaller.

7 Example: meteor echo structure

During the 15–19 November 2009 Leonid meteor campaign, we used a set of 53 optimized fractional baud-length codes with 0.5 µs fractional resolution and 5 µs minimum baud length. The transmission pulse length was 371 µs. The data was sampled at sampled at 2 MHz sample rate. The large number of pulses, together with the fairly long baud-length allowed simultaneous analysis of space debris and the ionosphere, while not sacrificing too much in terms of meteor head echo parameter estimation accuracy. We used the EISCAT UHF radar located in Tromso, with the 32 m antenna beam pointed approximately 99 km above Peera, Finland, giving a zenith angle of about 42°. The radar peak power was approximately 1.4 MW.

During this campaign, one of the observed "strange" meteor echos was an echo at approximately 60 km. The meteor head (or the dense cloud of plasma) is first seen decelerating from about 1 km s^{-1} to 0 km s^{-1}. After this, several disjoint trail-like structures persist for nearly 2 s.

The meteor head echo was detected by searching for the maximum likelihood parameters for a single echo moving point-target model

$$m_t = \sigma \epsilon_{t-R_0} \exp\{i\omega t\} + \xi_t, \tag{12}$$

where σ is the backscatter amplitude, ω is the Doppler shift and R_0 is range (ξ_t denotes receiver noise). The maximum likelihood parameters were obtained using a grid search of the likelihood function resulting from the measurement model. This is necessary as the Doppler shift is usually significant for meteor head echos at 929 MHz with such a long pulse.

The detected echo was then analyzed using a coherent spread target model (Eq. 3), which assumes that the backscatter comes from an extended region with a uniform Doppler

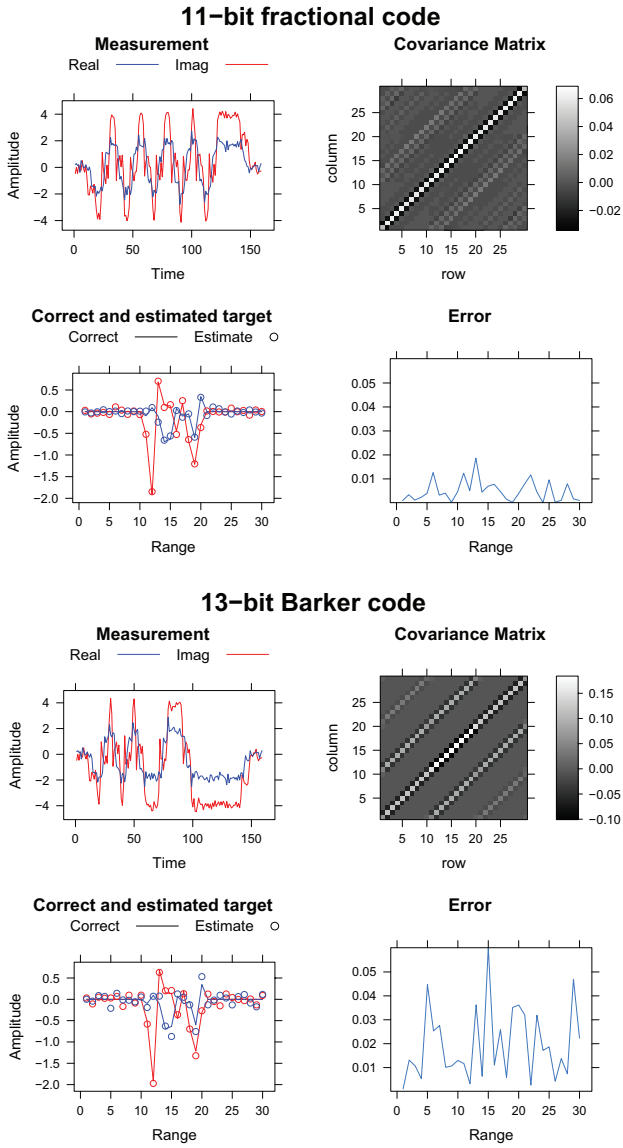

Fig. 4. Simulated coherent echo from a 11-bit non-uniform baud-length code that is 13 µs long and the smallest baud-length is 1 µs. When compared to the performance of a uniform baud-length 13-bit Barker code with 1 µs baud length, the performance is again better. The simulated target length is 10 µs and SNR = 3.

shift. The analysis resulted in the generalized linear least-squares parameter estimate for range dependent complex backscatter amplitude, which in other words is a range sidelobe-free estimate of the target backscatter. The range resolution was 0.5 µs, even though the minimum baud-length of the code was 5 µs. The Doppler shift obtained from the point-target estimate was used in the spread-target estimate – although this correction was not significant after the first 0.2 s of the echo as the Doppler shift was very close to 0.

The results in of the moving point and spread target estimates are shown in Fig. 5. The moving point-model indicates that after the initial deceleration, the trails have nearly zero

Doppler shift. The spread target results show that there are up to seven different layers separated in altitude. The strongest layer also shows range spread up to 500 m. Had a uniform baud length code with 5 µs bauds been used, the a posteriori variance would have been approximately twice larger.

This is the first time that such echos have been seen in EISCAT UHF observations. As micrometeoroids do not reach such a low altitude, one possible explanation is that this is a larger object. Perhaps a bolide. Because the altitude of this mono-static detection was obtained assuming that the target was within the main lobe of the antenna, another possible explantion is that this is a far side lobe detection of a combined meteor head and specular trail echo directly above the radar at approximately 85–90 km altitude. However, this would require the target to be approximately 45° off axis.

Meteor trail echos are not typically observed in EISCAT UHF observations as the high latitude location does not allow observing magnetic field-aligned irregularities. Also, the trail electron density is typically too small to be observed at UHF frequencies, making observation of specular trail echos unlikely.

Recent observations at Jicamarca (Malhotra and Mathews, 2009) have indicated a new type of scattering mechanism that does not yet have a physical explanation. These so called Low Altitude Trail Echos (LATE) seem to have no preference to the angle between the magnetic field and radar beam. They also have different characteristics than specular trail echos as they are typically observed only at low altitudes, usually together with head echos. Malhotra and Mathews (2009) suggest that these echos are produced as a by-product of fragmentation. Our results show that there are at least seven distinct layers, which is an indication that the meteor has fragmented multiple times. However, this event is different from those described by Malhotra and Mathews in the sense that this trail is at a much lower altitude (60–65 km) and also the trail is more long lasting. So it is difficult to say if the same scattering mechanism applies here.

8 Conclusions

In this paper, we first describe the statistical theory of estimating coherent and incoherent radar targets in amplitude domain. We then study target amplitude domain estimation variance for different codes. Using these results, we show that when sub baud-length resolution is needed, a transmission code that has non-uniform baud length results smaller estimation variance than a traditional code with uniform baud lengths. We then discuss a numerical method for finding suitable constrained transmission codes. The principles are demonstrated using simulated and real coherent radar echos.

The main application of non-uniform baud-length coding will be in cases where there is good SNR and sufficient receiver bandwidth, but a limited transmission bandwidth. Although the examples in this study only deal with coher-

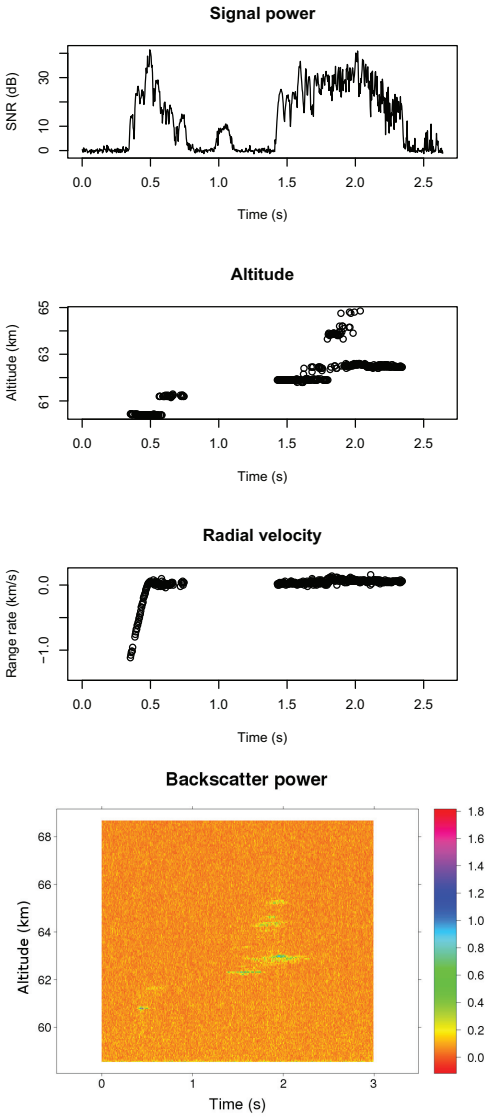

Fig. 5. A low-altitude meteor echo at 60 km seen with the EISCAT UHF radar on 19 November 2009 at 05:16 UT during a low-elevation meteor experiment. The meteor echo can been decelerating from 1 km s^{-1} down to 0, and then then echos from a trail-like structure are seen for a while. The three top panels show the results from a moving point-target model that determines the most likely range, Doppler shift and power of a point target. The fourth panel shows the range resolved backscatter power from a spread target model. After the initial head echo, many layers appear at altitudes above the initial detection. Most of the layers show 100-400 m range spread.

ent targets, the considerations also apply for amplitude domain estimation of strong range and Doppler spread (incoherent) echos, such as the ones described in Vierinen et al. (2008b). Examples of practical use cases include Lunar measurements, range spread meteor trail studies, and artificial ionospheric heating induced enhanced ion- and plasma-line echos.

Non-uniform baud-lengths are also advantageous for multi-purpose high power large aperture radar experiments where one mainly observes targets that benefit from longer baud lengths (e.g., ionospheric plasma or space debris), but where one would still want to be able to analyze strong targets at sub-baud resolution.

Although we have only studied the non-uniform baud-length coded transmission envelope performance in the case of amplitude domain target estimation, the same principles can also be applied to find optimal high resolution transmission codes for lag-profile inversion (Virtanen et al., 2008c) using estimation variance calculations that can be found e.g., in Lehtinen et al. (2008).

Acknowledgements. Editor-in-Chief M. Pinnock thanks J. Sahr and another anonymous referee for their help in evaluating this paper.

References

Cooley, J. W. and Tukey, J. W.: An algorithm for the machine calculation of complex fourier series, Math. Comput., 19, 297–301, 1965.

de Boor, C.: A Practical Guide to Splines, 114–115 pp., Springer-Verlag, 1978.

Farley, D. T.: Multiple-pulse incoherent-scatter correlation function measurements, Radio Sci., 7(6), 661–666, 1972.

Kelleher, J. and O'Sullivan, B.: Generating all partitions: A comparison of two encodings, CoRR, abs/0909.2331, 2009.

Kirkpatrick, S., Gelatt, C. D., and Vecchi, M. P.: Optimization by Simulated Annealing, Science, 220(4598), 671–680, doi:10.1126/science.220.4598.671, 1983.

Kudeki, E. and Stitt, G. R.: Frequency domain interferometry: A high resolution radar technique for studies of atmospheric turbulence, Geophys. Res. Lett., 14(3), 198–201, 1987.

Lehtinen, M. S., Damtie, B., and Nygrén, T.: Optimal binary phase codes and sidelobe-free decoding filters with application to incoherent scatter radar, Ann. Geophys., 22, 1623–1632, doi:10.5194/angeo-22-1623-2004, 2004.

Lehtinen, M. S., Virtanen, I. I., and Vierinen, J.: Fast comparison of IS radar code sequences for lag profile inversion, Ann. Geophys., 26, 2291–2301, doi:10.5194/angeo-26-2291-2008, 2008.

Malhotra, A., and Mathews, J. D.: Low-altitude meteor trail echoes, Geophys. Res. Lett., 36, L21106, doi:10.1029/2009GL040558, 2009.

Nikoukar, R.: Near-optimal inversion of incoherent scatter radar measurements: coding schemes, processing techniques, and experiments, PhD thesis, University of Illinois at Urbana-Champaign, 2010.

Piiroinen, P.: Statistical measurements, experiments and applications, Academia Scientiarum Fennica, 2005.

Pirttilä, J. and Lehtinen, M.: Solving the range-doppler dilemma with ambiguity-free measurements developed for incoherent scatter radars, COST 75, Advanced Weather radar systems, International seminar, pp. 557–568, 1999.

Pukelsheim, F.: Optimal Design of Experiments, John Wiley & Sons, 1993.

Riha, W. and James, K. R.: Algorithm 29 efficient algorithms for doubly and multiply restricted partitions, Computing, 16, 163–168, doi:10.1007/BF02241987, 1976.

Ruprecht, J.: Maximum-Likelihood Estimation of Multipath Channels, PhD thesis, Swiss federal institute of technology, 1989.

Sahr, J. D. and Grannan, E. R.: Simulated annealing searches for long binary phase codes with application to radar remote sensing, Radio Sci., 28(6), 1053–1055, doi:10.1029/93RS01606, 1993.

Shapiro, H. S. and Silverman, R. A.: Alias-free sampling of random noise, Journal of the Society for Industrial and Applied Mathematics, 8(2), 225–248, 1960.

Sulzer, M. P.: Recent incoherent scatter techniques, Adv. Space Res., 9, 153–162, 1989.

Uppala, S. V. and Sahr, J. D.: Spectrum estimation of moderately overspread radar targets using aperiodic transmitter coding, Radio Sci., 29, 611–623, 1994.

Vierinen, J., Lehtinen, M. S., Orispää, M., and Damtie, B.: General radar transmission codes that minimize measurement error of a static target, arxiv:physics/0612040v1, published on-line at arxiv.org, 2006.

Vierinen, J., Lehtinen, M. S., Orispää, M., and Virtanen, I. I.: Transmission code optimization method for incoherent scatter radar, Ann. Geophys., 26, 2923–2927, doi:10.5194/angeo-26-2923-2008, 2008a.

Vierinen, J., Lehtinen, M. S., and Virtanen, I. I.: Amplitude domain analysis of strong range and Doppler spread radar echos, Ann. Geophys., 26, 2419–2426, doi:10.5194/angeo-26-2419-2008, 2008b.

Virtanen, I. I., Lehtinen, M. S., Nygrén, T., Orispää, M., and Vierinen, J.: Lag profile inversion method for EISCAT data analysis, Ann. Geophys., 26, 571–581, doi:10.5194/angeo-26-571-2008, 2008c.

Publication IV

J. Vierinen and M. S. Lehtinen. 32-cm wavelength radar mapping of the Moon. In *6th European Radar Conference, EuRAD 2009*, Rome, September 2009.

32-cm Wavelength Radar Mapping of the Moon

Juha Vierinen [1], Markku S. Lehtinen

Sodankylä Geophysical Observatory
Tähteläntie 62, 99600 Sodankylä, Finland
[1]Juha.Vierinen@sgo.fi

***Abstract*— We present our effort for producing a high-resolution 32-cm wavelength synthetic aperture radar map of the Moon using ground based measurements with the EISCAT UHF radar. We discuss coding, decoding, Doppler north-south ambiguity mitigation, focusing, and clock error mitigation. We also show preliminary results from a test measurement.**

I. Introduction

Polarimetric radar studies of the Moon are useful as they provide a way of probing the sub-surface geochemical properties and the rock abdundance of lunar regolith [1]. Previously such maps have been produced at wavelengths of 3.8 cm [2], 70 cm [1], [3] and 7.5 m [4]. To our knowledge, the 32 cm wavelength used by the EISCAT UHF system has not been previously used for such studies. Different wavelengths probe the surface at different depths. Echo intensity also tells of the surface roughness at the radar wavelength scales [4]. Thus a 32 cm map would provide valuable information to complement space probe measurements and other previously published high resolution Lunar maps.

Most high-resolution Earth based Lunar mapping efforts have been conducted with a very narrow transmitter beam, which allows the Doppler north-south ambiguity to be avoided by beam positioning. In other cases, interferometry has been used to solve the ambiguity [4]. The EISCAT UHF transmistter antenna has a beam full width at half maximum of approximately 0.5 degrees, which illuminates the whole Moon simultaneously. Thus, there will be mixing of the north and south of the apparent Doppler equator. However, it is still possible to position the first null of the beam in such a way that ambiguous echos from the other side of the Doppler equator are sufficiently attenuated.

II. Mapping procedure

Our process is similar to previous range-Doppler mappings [5] of the Moon with the exception that we use a long coded ≈ 2 ms pulse to compensate for the small antenna gain. Also, instead of correcting the mean Lunar Doppler shift in the transmission frequency, we perform the Doppler correction in software to the recorded raw voltage data. This allows us to perform Lunar measurements without any hardware modifications to the EISCAT system.

A. Pulse compression

The instantaneous Doppler spread of the Moon is between 10-15 Hz during a typical measurement. Thus, we can assume that the target is approximately stationary during the time when the $\leq$ 2 ms transmission pulse travels through the target. The only significant factor is the slowly changing mean Doppler shift ω_t between the Moon and the observer, which can be assumed constant during one inter-pulse period.

If we assume that each range is Doppler shifted uniformly by ω and that the complex valued $\zeta_r \in \mathbb{C}$ contains the phase and backscatter amplitude for each range, the measurement equation for a single Lunar echo is:

$$m_t = \xi_t + \sum_r \epsilon_{t-r}\zeta_r \exp\left(i\omega(t-r)\right). \tag{1}$$

We denote our transmission envelope with ϵ_t, and the complex Gaussian valued measurement errors with ξ_t. By writing

$$\exp(-i\omega r)\exp(i\omega t) = \exp(i\omega(t-r)), \tag{2}$$

and replacing $\zeta'_r = \zeta_r \exp\left(-i\omega r\right)$ we can write the equation as:

$$m_t = \xi_t + \sum_r \epsilon_{t-r}\zeta'_r \exp\left(i\omega t\right). \tag{3}$$

We now divide by $\exp\left(i\omega t\right)$, set $\xi'_t = \exp\left(-i\omega t\right)\xi_t$. We arrive at:

$$m_t \exp\left(-i\omega t\right) = \xi'_t + \sum_r \epsilon_{t-r}\zeta'_r, \tag{4}$$

which is the measurement equation of a coherent target with the exception that the measurement is multiplied by a complex sinusoid. This equation is valid for a single inter-pulse period.

To estimate ζ'_r, we first multiply our measurement with the Doppler correction $\exp\left(-i\omega t\right)$, and convolve the result with the inverse filter

$$\lambda_t = \mathcal{F}_D^{-1}\left\{\frac{1}{\mathcal{F}_D\epsilon_t}\right\}_t, \tag{5}$$

which is known to be the target backscatter amplitude maximum *a posteriori estimate* in the case of high SNR (i.e., a Wiener filter with the assumption of high SNR). This can also be understood as division by the transmission envelope in frequency domain for infinitely extended aperiodic signals (here $\mathcal{F}_D$ is an infinitely extended zero-padded discrete Fourier transform). If we examine the estimation error variance for ζ'_r, we see that it is the same as that of a stationary spread target as obtained in [7], [8]. We have used the same code optimality criterion here.

On a longer time-scale, the Lunar Doppler shift changes slowly, so we have to take into account the changing Doppler shift ω_t. This is done by making the Doppler correction term a slowly chirping complex sinusoid $\exp\left(-i\omega_t t\right)$, although the

chirp rate during a single inter-pulse period is insignificant, and the frequency can be assumed constant.

After decoding, we obtain range and time (here t is the IPP index) dependent backscatter amplitude $\zeta_{r,t} + n_{r,t}$ with additional complex Gaussian noise $n_{r,t}$, which has a range dependent covariance structure from the inverse filtering step. The estimate of $\zeta_{r,t}$ can be then used to obtain an focused or unfocused range-Doppler map of the target. The unfocused map is obtained simply by making an independent power spectrum estimate for each range of $\zeta_{r,t}$.

In order to form the focused map of the target, we also have to take into account range and Doppler migration caused by Lunar libration during the integration period. We assume a spherical shape for the Moon, and with the help of the Lunar ephemeris, we calculate the corresponding Lunar coordinates and their Doppler shifts contributing to the backscatter at each range gate. This is then used to form a theory matrix A that describes the measured complex backscatter amplitude $\zeta_{r,t}$ in terms of the complex backscatter coefficients in Lunar coordinates $\sigma(x, y)$. To speed up computations, the resulting theory matrix A and error covariance matrix for $n_{r,t}$ can be assumed orthagonal ($A^H A \approx I$), so we can form our estimate by correlation $\hat{x} = A^H m$:

$$\sigma(x, y) = \frac{1}{T} \sum_{t=0}^{T} \zeta_{r(t,x,y),t} \exp\left\{i\omega_l(t, x, y)t\right\}, \qquad (6)$$

where $r(t, x, y)$ and $\omega_l(t, x, y)$ are the range gate and Doppler shift of Lunar coordinate (x, y) at time instant t.

A slightly better, but more time-consuming estimate can be obtained by using the full linear solution, with the covariance structure of $n_{r,t} \sim N(0, \Sigma)$:

$$\hat{x} = (A^H \Sigma^{-1} A)^{-1} A^H \Sigma^{-1} m, \qquad (7)$$

where vector $\hat{x}$ contains parameters $\sigma(x, y)$ and vector m contains the measurements $\zeta_{r,t}$ in such a way that the forward theory matrix A describes the measurements in terms of the parameters $m = Ax$.

III. Clock errors

For a point-like feature in a range-Doppler image, the signal can be written as:

$$s(t) = \exp(2\pi\omega i t) \exp(2\pi\omega\sigma_a i t), \qquad (8)$$

where σ_a is the Allan deviation of the clock. Here $\exp(2\pi\omega\sigma_a it)$ is the error-term, ω is the radar frequency and t is time. Heuristically, one can say that once the clock error term is off by more than $\pi/4$, our coherence is lost. Using this definition, we can define a average coherence time achievable with the clock:

$$\tau = (8\omega\sigma_a)^{-1} \qquad (9)$$

To our knowledge, the best Rb clocks available at the moment have a stability of $\sigma_a = 4 \cdot 10^{-13}$ (100 s time scale). This gives us a coherence time of 340 s. On the other hand, a typical active hydrogen maser clock has an Allance deviation of $\sigma_a = 7 \cdot 10^{-15}$ (one hour time scale), which gives us a coherence time of 19300 s. As we only have a Rb clock, we have to be able to correct the clock drift in some way if we want to achieve better than 340 s integration periods.

The clock stability directly defines the Doppler resolution. If we assume that the Moon has a Doppler spread of ω_M, and the radius of the Moon is 1738 km, our best achievable resolution in meters near the Doppler north pole is approximately

$$\Delta r = \frac{2 \cdot 1738 \cdot 10^3}{\tau\omega_M} \mathrm{m}. \qquad (10)$$

For $\omega_M = 10$ Hz and $\tau = 340$ s, we get a resolution of $\Delta r = 1022$ m. In the case of a hydrogen maser, we get $\Delta r = 18$ m.

A. Clock error recovery

In synthetic aperture radar mapping, clock errors result in smearing of the image in Doppler direction. As we are using GPS stabilized Rb clocks, we expect the clock to drift several radar wavelengths during an hour. It would be nice if there would be a way to correct clock drifts from the Lunar measurement itself.

For a point-like target it can be shown that clock errors can be recovered from the data. Assuming that the target has a certain range with a known point Doppler shift $\phi \in \mathbb{R}$ and assuming no measurement errors, the measurement of that range gate can be stated as

$$m(t) = a \exp\left\{i\phi(t + \varepsilon(t))\right\}, \qquad (11)$$

where $m(t)$ is the measurement, $a \in \mathbb{C}$ is the unknown backscatter coefficient containing both phase and magnitude, $t \in \mathbb{R}$ is time, and $\varepsilon(t) \in \mathbb{R}$ is the clock error, which we assume to be a zero-mean stochastic process, i.e., $\forall t, \mathrm{E}\,\varepsilon(t) = 0$. We arrange the terms as follows

$$-i\phi^{-1} \log m(t) - t = \varepsilon(t) - i\phi^{-1} \log a. \qquad (12)$$

In this case, we don't need to estimate a, so we can solve $\varepsilon(t)$ making use of the fact that $\int_0^\infty i\phi^{-1} \log m(t) + tdt = i\phi^{-1} \log a$, and get

$$\varepsilon(t) = -\frac{i \log m(t)}{\phi} - t + \int_0^\infty \frac{i \log m(t)}{\phi} + tdt + \frac{2\pi n}{\phi}, \qquad (13)$$

where $n \in \mathbb{Z}$. Thus, it is in theory possible to recover clock errors from noise-free data.

The Lunar map also contains similar, albeit not exactly the same, types of features. E.g., the leading edge of the Moon is nearly a point-target. And sharp shadows formed at the edges of craters are analguous. In practice, it should be possible to use some sort of prior information that promotes sharp features in the image. An example of such a prior is the total variation prior [6].

IV. Test run

To test the feasibilty of the EISCAT system for Lunar studies, we have conducted several test experiments during November 2008. We used the EISCAT Tromso UHF system in monostatic mode at full 2 MW peak power. The coded

transmission pulses were 200-1825 μs long with bauds between 1-10 μs. The duty cycle was between 2-11%, with interpulse intervals carefully selected so that the Lunar echos would fit between transmission slots during the whole experiment. The ephemeris was obtained from the NASA JPL Horizon's system.

We sampled our data at 4 MHz using a Universal Software Radio Peripheral (USRP[1]) and stored the 16-bits per sample raw voltage data to disk in baseband – all processing was done off-line to this data, so no modifications to the EISCAT system were required. We also recorded the transmission envelope from the waveguide and used it for decoding in the off-line processing stage to mitigate decoding errors caused by the non-ideal transmission waveform.

A part of a raw unfocused delay-Doppler image using 2 μs baud-length is shown in Fig. 1. The image is taken over a 600 s integration period. This is close to the limits of the capabilities of our Rb clock. The resolution is approximately 600 m in range and Doppler direction, although Doppler smearing is already expected with such a long integration time.

We used several different transmission codes with baud-lengths ranging from 1 μs to 10 μs. The transmission codes were Kroenecker product (i.e., sub-pulse coded) codes derived from the 13-bit Barker code or an optimal sub-sequence of such a code. The optimization criteria was the posterior estimation variance of stationary spread target backscatter amplitude [7], [8].

V. Future Work

We have demonstrated that the feasibility of creating a high-resolution 32-cm Lunar map with the EISCAT UHF radar. We plan to continue the work to:

- Produce a full focused map using both same and opposite sense circular polarization
- Compare results to other measurements at different wavelengths
- Investigate the possibility of long baseline interferometric measurements using the EISCAT system

VI. Conclusions

We have outlined our ongoing work to produce a high-resolution 32 cm focused polarized synthetic aperture radar map of the Moon. The main differences to previous work is that we are using coded long pulses and pointing the beam pattern nulls to produce an unambiguous range-Doppler map. We also have several ideas for correcting the clock errors to increase the coherent integration time further.

We have performed preliminary measurements to prove that a high-resolution map is feasible using EISCAT. Our goal is to proceed to measure a full focused Lunar map with same- and opposite-circular polarizations.

[1] http://www.ettus.com

References

[1] B. Campbell, D. Campbell, J. Margot, R. Ghent, M. Nolan, J. Chandler, L. Carter, and N. Stacy, "Focused 70-cm wavelength radar mapping of the Moon," *Geoscience and Remote Sensing, IEEE Transactions on*, vol. 45, no. 12, pp. 4032–4042, Dec. 2007.

[2] S. H. Zisk, G. H. Pettengill, and G. W. Catuna, "High-resolution radar maps of the lunar surface at 3.8-cm wavelength," *Earth, Moon, and Planets*, vol. 10, p. 17, 05 1974. [Online]. Available: http://dx.doi.org/10.1007/BF00562017

[3] T. W. Thompson, "High-resolution lunar radar map at 70-cm wavelength," *Earth, Moon, and Planets*, vol. 37, p. 59, 01 1987. [Online]. Available: http://dx.doi.org/10.1007/BF00054324

[4] T. W. Thompson, "High resolution Lunar radar map at 7.5 meter wavelength," *Icarus*, vol. 36, no. 2, pp. 174–188, 1978.

[5] N. J. S. Stacy, *High-resolution synthetic aperture radar observations of the moon*. Ph.D. dissertation, Cornell Univ., Ithaca, NY, 1993.

[6] J. Kaipio and E. Somersalo, *Statistical and Computational Inverse Problems*. Springer, 2004.

[7] J. Ruprecht, *Maximum-Likelihood Estimation of Multipath Channels*. PhD thesis, Swiss federal institute of technology, 1989.

[8] M. S. Lehtinen, B. Damtie, and T. Nygrén, "Optimal binary phase codes and sidelobe-free decoding filters with application to incoherent scatter radar," *Annales Geophysicae*, 2004.

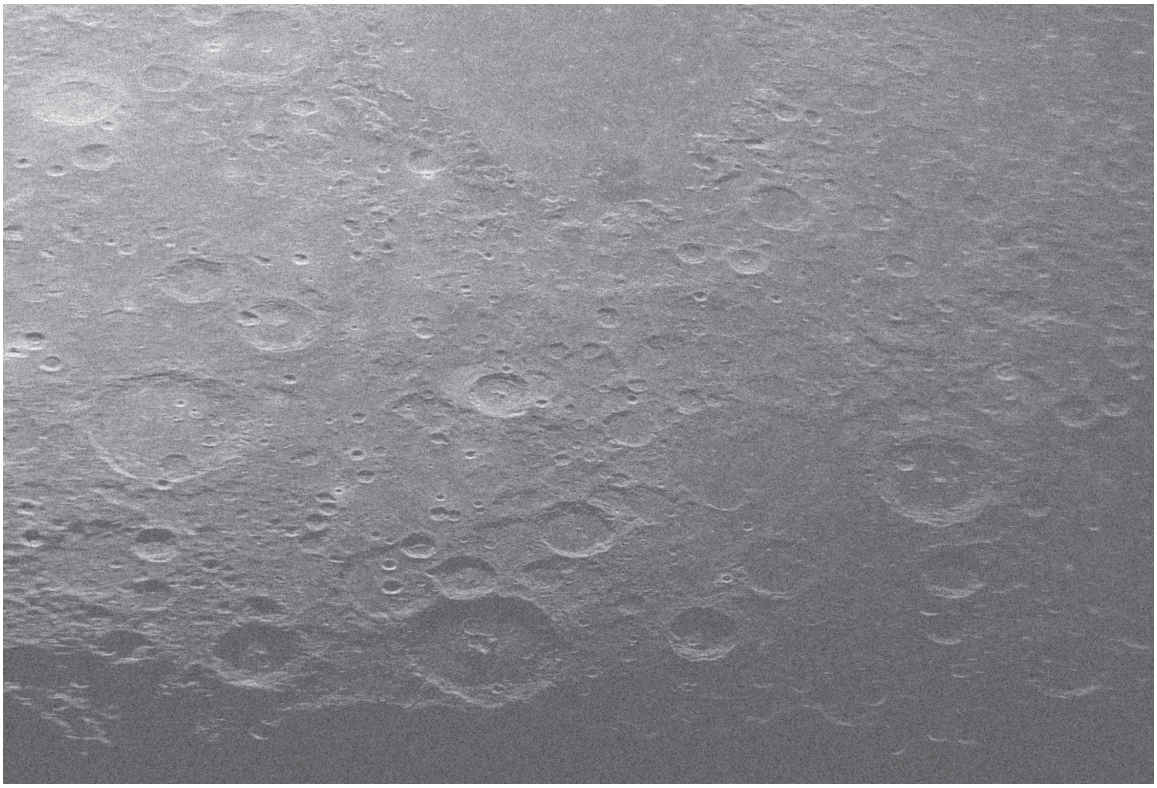

Fig. 1. An opposite sense (quasispecular or coherent scatter) circular polarized unfocused delay-Doppler image obtained with the EISCAT 926 MHz UHF system. The range resolution is approximately 600 m. Because the image is still unfocused, Doppler smearing caused by the changing range rate can be seen on the edges.

Publication V

J. Vierinen, J. Markkanen and H. Krag. High power large aperture radar observations of the Iridium-Cosmos collision. In *10th Advanced Maui Optical and Space Surveillance Techonologies Conference*, Maui, September 2009.

High Power Large Aperture Radar Observations of the Iridium-Cosmos collision

Juha Vierinen
Sodankylä Geophysical Observatory

Jussi Markkanen
EISCAT Scientific Association

Holger Krag
European Space Operations Centre

September 2, 2009

Abstract

We present results from two recent beam park radar experiments conducted with the EISCAT UHF radars in February and May 2009 to survey the debris produced by the Iridium-Cosmos satellite collision. The resulting debris is clearly visible in the measurements. The results are compared to a simulated observation produced with the ESA PROOF model. The measurements are found to agree to some extent with the model, but there are still discrepancies between the measurement and the simulation, mainly in the shape of the debris cloud and the total amount of observed debris.

1 Introduction

The European Incoherent Scatter radar facility (EISCAT) currently consists of three high power large aperture radar systems: the mainland VHF (225 MHz) and UHF (930 MHz) radars with transmitters in Tromsø, Norway, and the 500 MHz EISCAT Svalbard radar (ESR). The mainland UHF system is tri-static, with additional receivers located in Kiruna, Sweden and Sodankylä, Finland. The radars are primarily used for ionospheric studies, but since 2000 [6, 5], there has existed the capability to analyze the measurements also for space debris. For this purpose, a separate digital receiver, which we will here refer as the space debris receiver, is operated in parallel with the standard EISCAT receiver. Since 2000, the EISCAT facilities have been used several times for statistical space debris studies with co-operation with the European Space Agency.

In situ measurements of debris can be used to statistically measure < 1 cm scale debris [2]. Existing space surveillance radars can be used to track > 10 cm scale objects. Debris between 1 and 10 cm can be measured with megawatt-scale high power large aperture radars. There are two such facilities in Europe: EISCAT and TIRA [1].

After the collision of the Iridium and Cosmos satellites on 10 February 2009, we have conducted two dedicated beam-park experiments to study the debris cloud produced by the collision, one on 14 February 2009 and another on 14 May 2009. Both were conducted with the Tromsø UHF radar. In addition to this, we have recorded with the space debris receivers several standard ionospheric measurements, both before and after the collision. All our post-collision measurements show clear increase of event count at the times and altitudes when the radar beam is predicted to cross the two debris rings.

2 Analysis methods

The measurement analysis is based on a coherent integration of signals scattered from point targets. The detection algorithm is a new version of the fast generalized match function algorithm previously used at EISCAT [6, 7]. Instead

of assuming that the signal is fully coherent, the new version allows slight broadening of the backscatter spectrum due to, e.g., object rotation or insufficiently modeled acceleration.

In the detection phase our complex baseband signal model, in discretized form, is

$$m_t = \epsilon_{t-r} \sum_{k=\lfloor -(N-1)/2 \rfloor}^{\lfloor (N-1)/2 \rfloor} a_k \exp\{i(\omega + k\Delta\omega)t\} + \xi_t, \tag{1}$$

where ϵ_t is the transmission envelope, r is the target range gate, N is the number of adjacent frequency components with corresponding complex coefficients a_k, and ω is the central frequency. The term ξ_t corresponds to measurement noise, which is assumed to be complex Gaussian independent and identically distributed noise with power $\mathrm{E}\xi_t\overline{\xi_{t'}} = \delta_{t,t'}kTB$.

Our debris observations are formed by searching for the maximum likelihood estimates of parameters r, ω and a_k. This is done using a FFT-based grid search. The results of these coherent integration blocks are then combined into events, which provide an estimate of the target radial trajectory and radar cross-section. However, as the EISCAT radars are not equiped with a monopulse feed, we cannot produce an accurate radar cross-section estimate if the detection is not tri-static. Thus, the radar cross-section estimate obtained by taking the peak target signal to noise ratio along the trajectory is usually a lower bound for the true value, as the target doesn't necessarily pass through the center of the beam.

3 Radar experiments

For performing our beam-park measurements, we have used standard EISCAT ionospheric radar experiments called *beata* and *steffe*, and a newly developed space debris program called *spade* [9]. Even though the EISCAT ionospheric experiments are able to provide the unambiguous range coverage that one needs for low earth orbit space debris surveys, they have problematic gaps in range, caused by the high (10-25%) transmission duty cycle and uniform interpulse intervals. The *spade* experiment also has a high duty-cycle, but avoids the gaps in range (up to $16 \cdot 10^3$ km) by using non-uniform interpulse periods. Table 1. lists our measurements related to the Iridium-Cosmos collision.

3.1 Tri-static observations

The 14 May 2009 measurement was the first-ever tri-static space debris measurement with the EISCAT UHF system. In this case, the Tromsø transmitter was pointed eastward, above Ivalo, Finland, at 780 km height. The two 32 m receive-only antennas were also pointed to the same point. The geometry is shown in Fig. 1. This pointing direction is more beneficial than the magnetic field align direction that is normally used by EISCAT, as it gives better Doppler-inclination information. Also, multi-static detections are expected to give some information about the orbital elements as well.

We managed to get surprisingly many bi-static events with the Kiruna (16 per hour) and Sodankylä (12 per hour) systems. Some of the detections were also tri-static. This is perhaps due to the transmitter main lobe, receiver sidelobe combination, which is only about -20 dB at the first side lobe of the receiving antenna.

We also noticed that the remote receiver data quality was better than the receiver located at the transmitter, making it possible to use a smaller detection thresholds at the remotes. This can be attributed to many things: there are no missing echos because the remote sites don't transmit; there is significantly less ionospheric clutter at the remotes; and the receiver noise temperature at the remotes is lower.

4 Results

We show here only results from the two *spade*-experiments. Figs. 2. and 3. show results from the 14-15 February 2009 run, and Figs. 4. and 5. show the run on 14-15 May 2009. Simulated measurements produced with the ESA PROOF model [4] are shown alongside the real measurements.

The detection rate for the field align measurement in February was about 24 detections per hour. For the eastward, slightly lower elevation, pointing direction in May, it was about 30 detections per hour. A previous March 2006 field aligned pointing direction measurement resulted in about 17 detections per hour [8], so there is a nearly 40% increase

Date	Experiment	Radar	Pointing
14:00 14.2.2009 – 11:00 15.2.2009	spade	UHF	FA
12:00 19.2.2009 – 12:00 20.2.2009	steffe	ESR	FA
08:00 12.5.2009 – 14:00 14.5.2009	beata	UHF	FA
14:00 14.5.2009 – 15:00 15.5.2009	spade	UHF	SD

Table 1: List of beam-park experiments conducted after the Iridium-Cosmos collision. The UHF radar refers to the Tromsø 930 MHz radar and ESR refers to the Svalbard 500 MHz radar. The *beata*- and *steffe*-experiments are ionospheric experiments, which can be analyzed for space debris, although there are gaps in the range coverage. The *spade*-experiment is a new space debris radar program that gives gapless range coverage with full radar duty-cycle. The pointing direction FA means magnetic field aligned at approximately 300 km. In Tromsø, this corresponds to a pointing direction of azimuth 185.8° and elevation 77.4°. The pointing labeled SD is an eastward pointing direction shown in Fig. 1., which gives more Doppler inclination information. This corresponds to a pointing direction of azimuth 86.5° and elevation 67.3°.

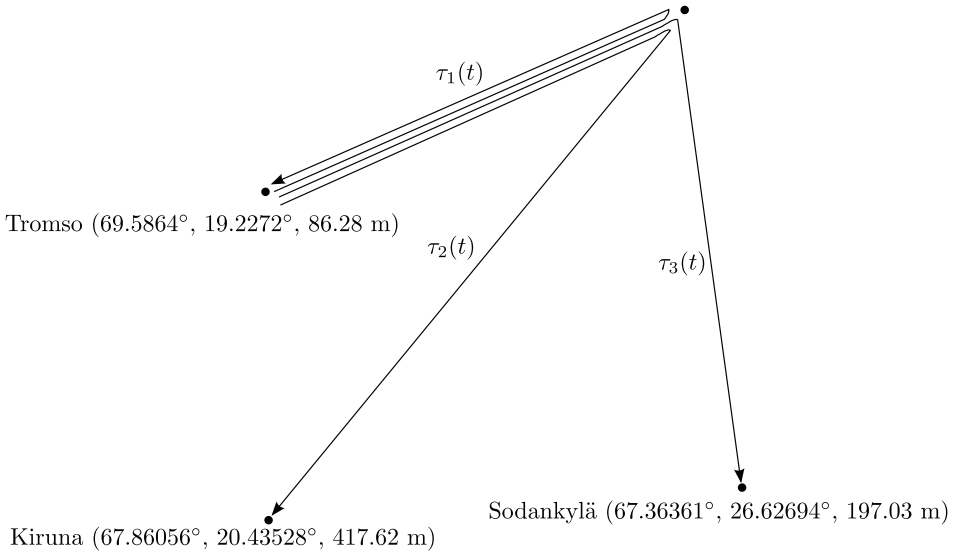

Figure 1: The geometry of the tri-static space debris experiment. All three antennas are pointed above Ivalo (69.5864°, 26.6269°) at the height of 780 km.

as a result of the Chinese anti-satellite experiment and the Iridium-Cosmos collision. However, these number are not completely comparable, as a different radar experiment, different detection algorithms and different receiver hardware were used in these two measurements.

A quick visual inspection of the results shows that the Cosmos cloud is over twice the size of the Iridium debris cloud. Also, the Cosmos cloud appears to be more spread out in range, about 100 km in February and about 500 km in May. The Iridium cloud is initially spread out to a 100 km range in February and 200 km May. The Cosmos cloud causes approximately an increase of 200-300 % compared to the background level during one 15 minute histogram bin. The Iridium cloud causes a smaller, perhaps 100-200 % increase during a 15-minute histogram bin.

When comparing the results to the simulation, the measured debris cloud is much more clumped together, both in range and time of day. The simulation also shows all in all about twice the number of detections compared to the real measurement. The model also seems to over-predict the size of the Iridium and Cosmos debris clouds. The overall of tilt and Doppler of the clouds are modeled to some extent correctly, although the shape of the clouds is quite different in the real measurement.

The reason for these discrepancies is not yet clear. One problem with the analysis is that it can only detect one target at a time. This can result in some undetected events. The mean time between detections is about 120 s, so this shouldn't cause 50% loss of data. It is more probable that there is some as-yet unidentified inconsistency in how PROOF models our new experiments.

5 Conclusions

We have performed several measurements of > 1 cm scale debris with the EISCAT radars after the Iridium-Cosmos collision to assess the shape of the produced debris cloud. All measurements detect a clear increase in debris during the two passes of the debris rings.

The measurements agree to some extent with PROOF model simulations, although there are also certain differences. The measured debris cloud is more clumped together than the model suggests. Also, the amount of detected debris in the real measurement (about 24-30 events per hour) is approximately 50% of that in the simulation. This can be partially explained by insufficient sensor modeling, which assumes a wider beam than actually used. Another possibility is unoptimal analysis, which fails to detect weaker events. However, the magnetic field aligned detection rate of 24 events per hour in the February 2009 measurement is more in line with previous measurements made in 2006 with the same radar [8], which suggests that the new analysis and radar experiment are consistent with previous ones.

6 Future Work

We plan to continue observing the time evolution of the Iridium-Cosmos debris cloud with EISCAT by analyzing all ≥ 24 h routine ionospheric measurements for space debris, and possibly performing dedicated space debris beam park observations.

In terms of data analysis, there is still work to be done, especially with the post-integration processing of detections. Currently, only one target is allowed to be observed at a time, which causes some simultaneous events to go undetected. A better post-integration algorithm is also likely to improve the sensitivity of the analysis.

The tri-static beam-park campaign is still being processed. One goal is to produce estimates for orbital elements of the multi-static detections that were found. Similar work has already been done at EISCAT for determining micrometeor orbits from tri-static measurements [3]. We have also attempted a tracking experiment for the Envisat-satellite, using low quality TLE to point the UHF antenna. The goal of this experiment was to see if EISCAT can be used for obtaining precise orbital elements.

References

[1] D. Banka, L. Leushacke, and D. Mehrholz. Beam-park-experiment-1/2000 with TIRA. *Space Debris*, 2:83–96, 2000.

[2] G. Drolshagen, H. Svedhem, E. Grün, O. Grafodatsky, and U. Prokopiev. Microparticles in the geostationary orbit (GORID experiment). *Advances in Space Research*, 23(1):123 – 133, 1999.

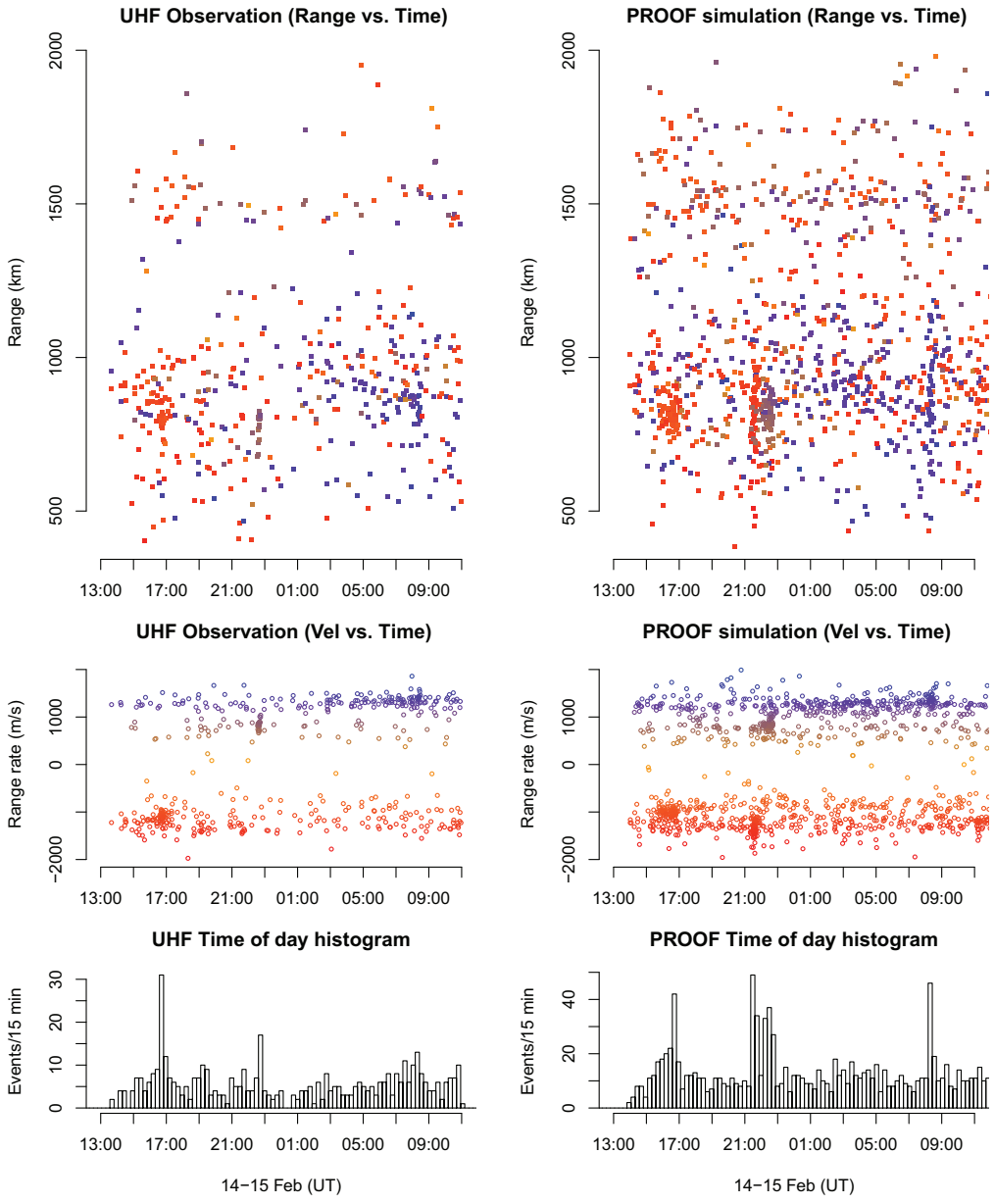

Figure 2: Detections from the 14-15 February 2009 21 h beam-park experiment. The left-hand side shows the monostatic measurement made with the Tromsø radar. The right-hand side shows the simulations produced with the PROOF tool. Doppler shifts are color-coded with colors indicated by the middle panel. The Iridium cloud passes at ≈ 08:30 and 22:00, and the Cosmos cloud passes at ≈ 16:45 and 22:45.

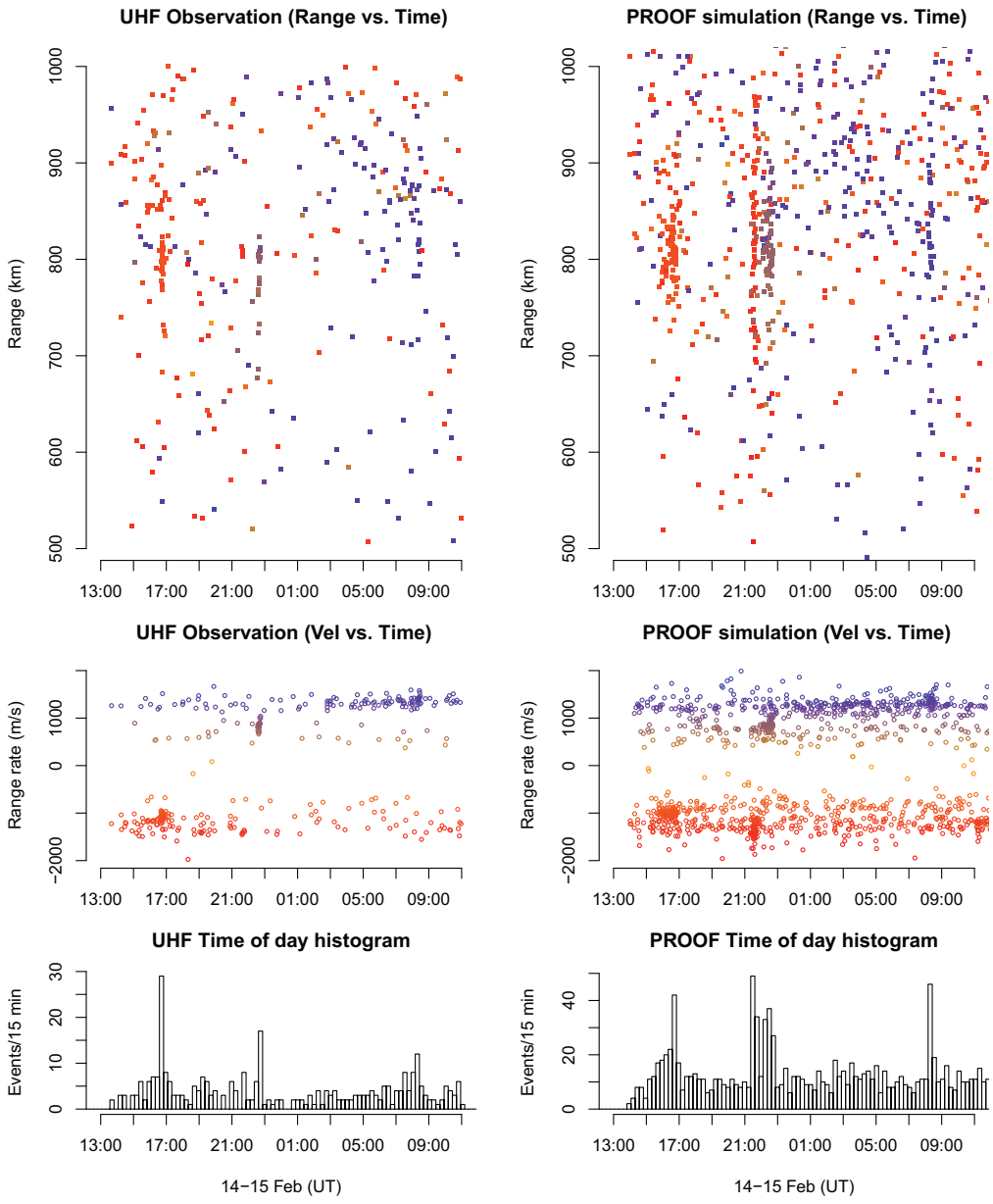

Figure 3: The same as Fig. 2., but ranges restricted to between 500 and 1000 km.

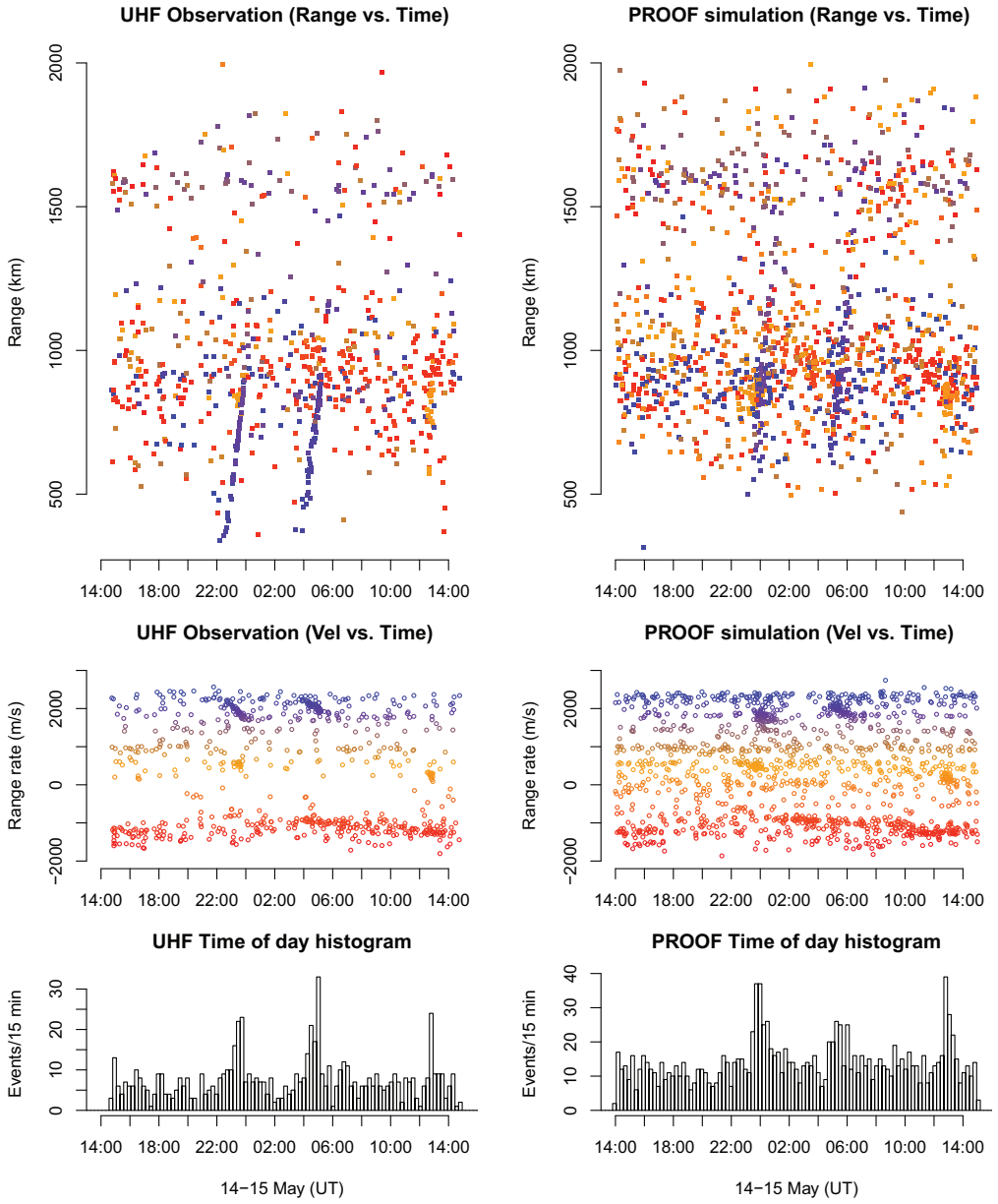

Figure 4: Detections from the 14-15 May 2009 beam-park experiment. The left-hand side shows the real monostatic measurement made with the Tromsø radar. The right-hand side shows the simulations produced with the PROOF model. The Iridium cloud passes at ≈ 00:00 and 13:00, and the Cosmos cloud passes at ≈ 00:00 and 06:00.

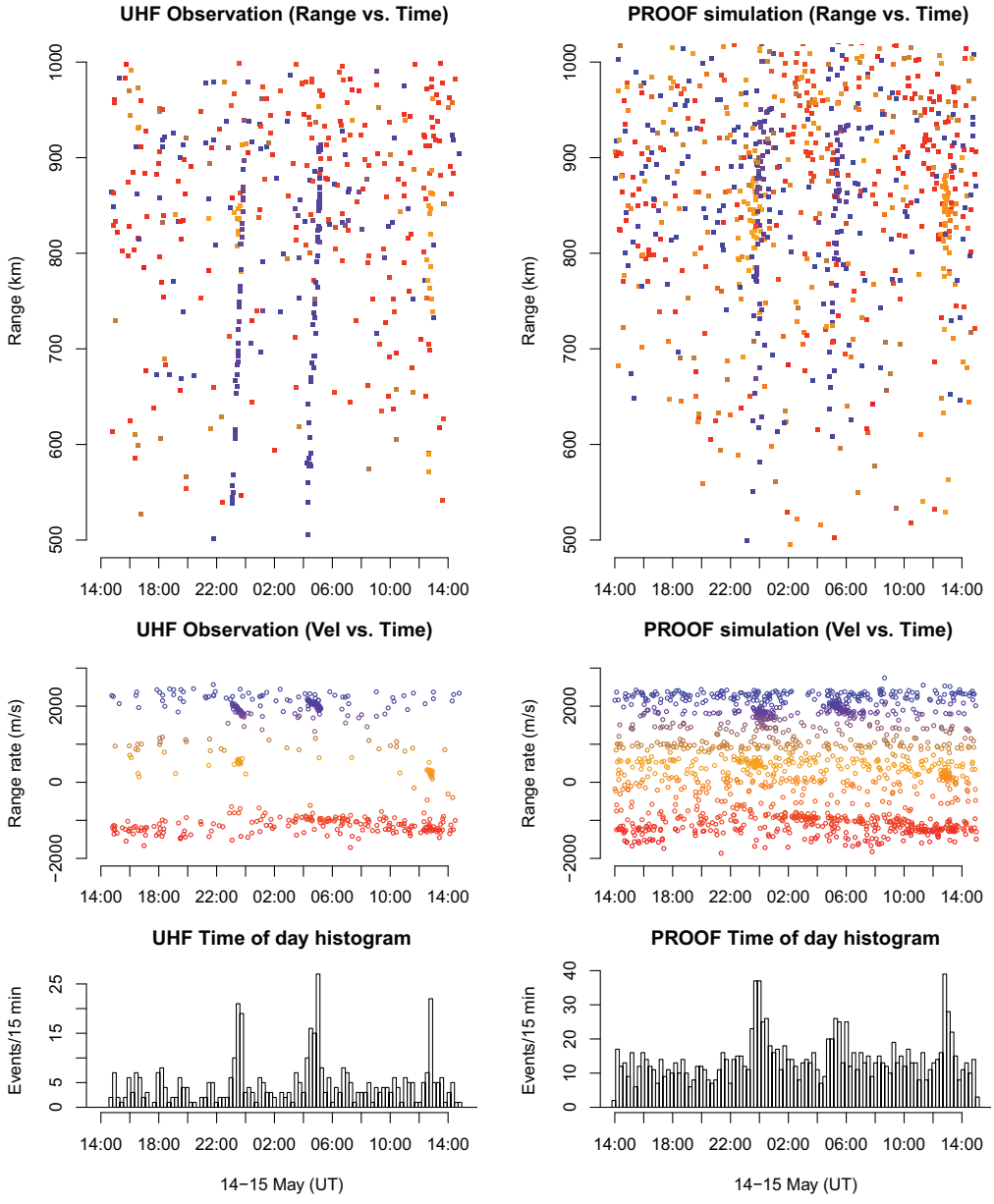

Figure 5: The same as Fig. 4., but ranges restricted to between 500 and 1000 km.

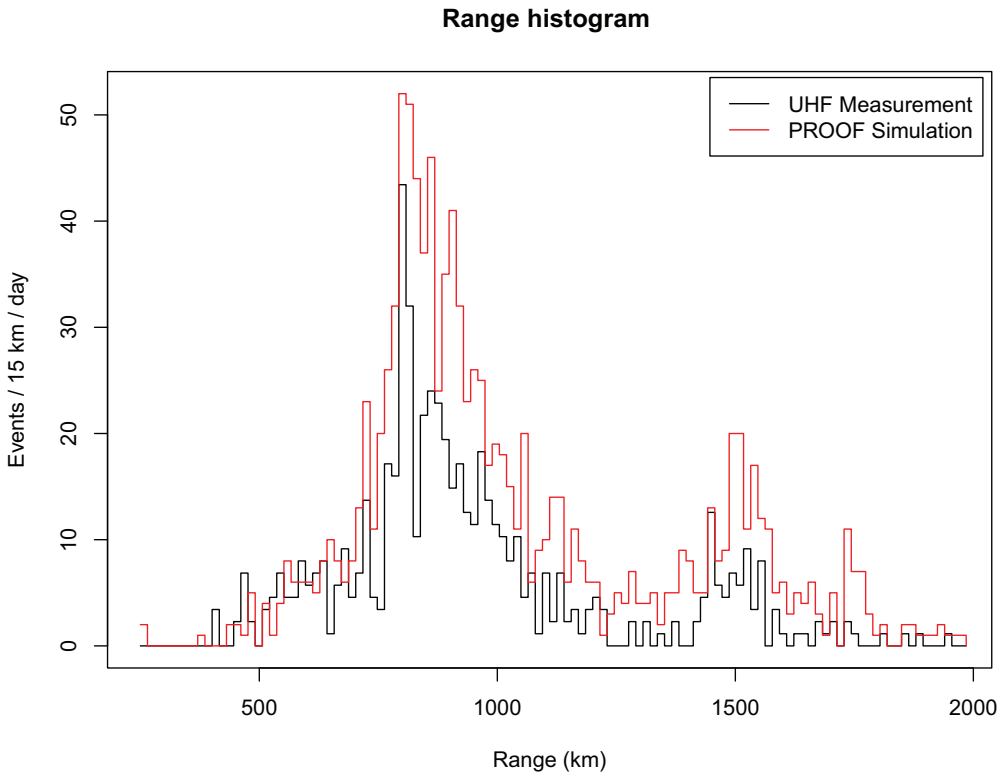

Figure 6: Range histograms for the PROOF simulation and the measured data for the 14-15 February 2009 measurement. The general shape of the measurement agrees with the simulation, although the simulation predicts significantly more detections.

[3] J. Kero, C. Szasz, A. Pellinen-Wannberg, G. Wannberg, A. Westman, and D. D. Meisel. Determination of meteoroid physical properties from tristatic radar observations. *Annales Geophysicae*, 26(8):2217–2228, 2008.

[4] H. Krag, P. Beltrami-Karlezi, J. Bendisch, H. Klinkrad, D. Rex, J. Rosebrock, and T. Schildknecht. PROOF – The extension of ESA's MASTER model to predict debris detections. *Acta Astronautica*, 47(2-9):687 – 697, 2000. Space an Integral Part of the Information Age.

[5] J. Markkanen, M. Lehtinen, and M. Landgraf. Real-time space debris monitoring with EISCAT. *Advances in Space Research*, 35:1197–1209, 2005.

[6] J. Markkanen, M. S. Lehtinen, A. Huuskonen, and A. Väänänen. *Measurements of Small-Size Debris with Backscatter of Radio Waves*. Final Report, ESOC Contract No. 13945/99/D/CD, 2002.

[7] J. Markkanen, M. S. Lehtinen, and M. Landgraf. Real-time space debris monitoring with EISCAT. *Advances in Space Research*, 35(7):1197 – 1209, 2005. Space Debris.

[8] J. Markkanen and A. van Eyken. Space debris measurements with EISCAT radars, the first 1000 (+) hours. Talk at COSPAR 2006.

[9] J. Vierinen, M. S. Lehtinen, J. Markkanen, and I. I. Virtanen. Measuring space debris with phase coded aperiodic transmission sequences. In *Proc. Fifth European Conference on Space Debris*, 2009.

Aalto-DD 115/2012

ISBN 978-952-60-4778-2
ISBN 978-952-60-4779-9 (pdf)
ISSN-L 1799-4934
ISSN 1799-4934
ISSN 1799-4942 (pdf)

Aalto University
School of Science
Department of Information and Computer Science
www.aalto.fi

BUSINESS + ECONOMY

ART + DESIGN + ARCHITECTURE

SCIENCE + TECHNOLOGY

CROSSOVER

DOCTORAL DISSERTATIONS